Emergence of Cosmic Structures around Distant Radio Galaxies and Quasars

Emergence of Cosmic Structures around Distant Radio Galaxies and Quasars

Proefschrift

ter verkrijging van
de graad van Doctor aan de Universiteit Leiden,
op gezag van de Rector Magnificus Dr. D.D. Breimer,
hoogleraar in de faculteit der Wiskunde en
Natuurwetenschappen en die der Geneeskunde,
volgens besluit van het College voor Promoties
te verdedigen op dinsdag 30 mei 2006
te klokke 14.15 uur

door

Roderik Adriaan Overzier

geboren te Rotterdam
in 1978

Promotiecommissie

Promotor:	Prof. dr. G.K. Miley
Co-promotor:	Dr. H.J.A. Röttgering
Referent:	Prof. dr. H.C. Ford (The Johns Hopkins University, USA)
Overige leden:	Dr. P.N. Best (University of Edinburgh, UK) Prof. dr. M. Franx Dr. J. Schaye Prof. dr. P.T. de Zeeuw

Dit proefschrift is tot stand gekomen met steun van

Nederlandse Organisatie voor Wetenschappelijk Onderzoek

To my parents

Front cover. *Vermeer's 'Astronomer' (Louvre, Paris) pondering the questions of the Universe. The background shows an image that was obtained with the Advanced Camera for Surveys towards the distant radio galaxy TN J1338–1942 (the green object), as part of this thesis.*

Voorkant. *Vermeer's 'Sterrenkundige' (Louvre, Parijs) buigt zich over de vragen van het heelal. De achtergrond toont een diepe opname gemaakt met de Advanced Camera for Surveys in de richting van het verre radiosterrenstelsel TN J1338–1942 (het groene object), waar dit proefschrift gedeeltelijk op gebaseerd is.*

Back cover. *Creation of the world depicted on the coffin of Amenhotep, priest of Amon (c. 1500 B.C., Thebes). The air god Sju separates the star-spangled goddess of heaven, Nut, from the earth god Geb (RMO, Leiden).*

Achterkant. *Schepping van de wereld zoals afgebeeld op de doodskist van Amenhotep, priester van Amon (c. 1500 v. Chr., Thebe). De luchtgod Sju scheidt de met sterren bezaaide hemelgodin Nut van de aardgod Geb (RMO, Leiden).*

(Cover artwork: Isa Oliveira)

Contents

Chapter 1

Introduction

1.1 Basic elements of cosmology

The complex distribution of galaxies, groups and (super-)clusters that constitutes the large-scale structure of the universe originated from small, seed fluctuations in the cosmic density field, as evidenced by the minute anisotropies observed in the cosmic microwave background (e.g. Bennett et al. 2003). These primordial fluctuations can be traced back to a (near-)Gaussian density field, consistent with the theory of inflation (Guth 1981) that predicts that the universe expanded over many orders of magnitude in size within a tiny time interval shortly after the "Big Bang", about 14 billions years ago. The geometry of the universe is believed to be dominated not by matter, but by "dark energy" (expressed by a cosmological constant, Λ) which has driven the cosmological expansion to accelerate over relatively recent times (see Carroll et al. 1992). This is confirmed by the latest studies of distant supernovae (Perlmutter et al. 1999; Riess et al. 2004). The power spectrum of the microwave background, combined with information on the spatial distribution of galaxies obtained from large galaxy redshift surveys, have placed important constraints on the cosmic matter budget, the density distribution at recombination ($z \approx 1000$), and the biasing between galaxies and the dark matter (e.g. Lahav et al. 2002; Tegmark et al. 2004). The currently favoured model for structure formation is the so-called cold dark matter model ("ΛCDM"), which explains how bound objects such as galaxies and clusters formed on increasingly larger spatial scales due to the growth of density fluctuations from gravitational instability in an expanding universe. According to such models, the universe became (re-)ionized by the first light of stars, protogalaxies and/or quasars at $z_r \sim 7 - 20$ (e.g. Loeb & Barkana 2001; Fan et al. 2002; Kogut et al. 2003). The best current observational evidence for galaxies and quasars in the early universe is found at about 1 billion years after the Big Bang ($z \sim 6 - 7$), confirming that the first galaxies and quasars developed within a couple of hundred million years (e.g. Kodaira et al. 2003; Kneib et al. 2004; Eyles et al. 2005; Bouwens et al. 2006).

1.2 Structure formation

The theoretical framework that is used to describe the formation of the large-scale structure and the galaxies it contains is based on the following two tenets (White & Rees 1978):

(i) the distribution of the dominant mass component at all scales developed purely from gravitational clustering through the collapse and merging of dark matter halos (PS; Press & Schechter 1974). The resulting hierarchy of formed structures is a consequence of the fact that most of the power of the initial mass fluctuations was at small scales.

(ii) galaxy formation is driven by the dissipation and collapse of gas in the cores of dark matter halos.

This theoretical framework aims at providing a detailed explanation of the most fundamental issues in cosmology concerning the formation and evolution of galaxies and the large-scale structure.

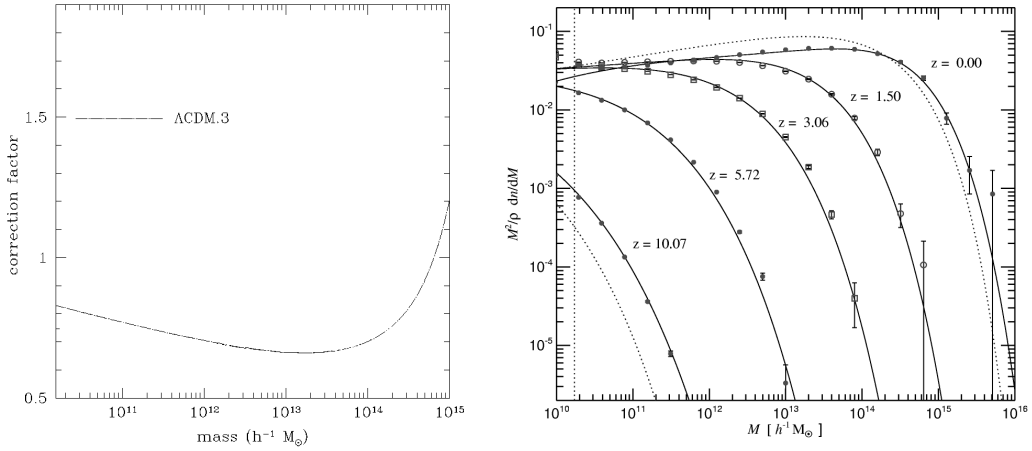

Figure 1.1 — Predictions for dark matter halo abundances in semi-analytical models and *N*-body simulations. *Left panel:* Correction factors for the halo abundance as a function of mass to be applied to the extended PS formalism as derived by Sheth & Tormen (1999) (from Somerville & Primack 1999). *Right panel:* Halo abundance as a function of redshift, plotted as the mass fraction in objects of mass *M*. Points are from the Millennium Run *N*-body simulation (Springel et al. 2005). Solid lines are the analytic fitting function from Jenkins et al. (2001). Dotted lines give the PS model predictions at the minimum and maximum redshift (taken from Springel et al. 2005).

For example, which of the galaxies observed at high redshift are the progenitors of local galaxy populations and how and when did they form? Which of the local galaxies host the remnant black holes that once powered high redshift active galactic nuclei (AGN)? What are the effects of AGN on the star formation history? How and when did clusters of galaxies form, and what role does galaxy environment play in the evolution of the galaxies themselves? The formation and evolution of structure in the universe can, in principle, be derived analytically from the power spectrum of density fluctuations, but not beyond the point where linear theory breaks down due to collapse and merging of structures that distorts the form of the fluctuation spectrum. The non-linear regime can be studied using semi-analytical approximations, or experimentally through numerical *N*-body simulations. The semi-analytic approach (White & Frenk 1991, see also Somerville & Primack 1999 for a review) is used to study the complicated feedback loops that exist between gas cooling, star formation, merging, supernovae, AGN, dust extinction, etc. The semi-analytical prescriptions for star and galaxy formation are applied to halo merger trees based on the PS formalism. The inherent hierarchical nature of the merger-tree formalism is in contrast with the dissipative monolithical collapse model in which galaxy assembly is sudden rather than gradual (Eggen et al. 1962). There is, however, mounting evidence that at least certain types of galaxies may have formed in short, massive starbursts at very high redshifts (e.g. Mobasher et al. 2005). The PS formalism was extended to relate halos of a given mass at a specific redshift, to the masses of their progenitor halos prior to that redshift (Bond et al. 1991; Bower 1991). A later modification was proposed by Sheth & Tormen (1999) in order to account for a discrepancy between the original PS formalism and results from numerical simulations leading to overpredictions in the halo abundances at small scales and underpredictions at large scales (Fig. 1.1).

The semi-analytical approach has been successful in reproducing some of the key local observables (e.g. luminosity functions, Tully-Fisher relation, sizes, colours, metallicities), but reproducing all of those simultaneously remains challenging (e.g. Kauffmann et al. 1999; Cole et al. 2000). It has been

suggested that a powerful test to discern between passively evolving galaxies that formed in a relatively early burst of short duration and galaxies that formed later through hierarchical processes, lies in the study of the shape of the *K*-band luminosity function at $z \sim 1$ (Kauffmann & Charlot 1998). Such a test was recently performed by Somerville et al. (2004) who concluded that although the hierarchical model provides a better match to the data than the monolithic model at least qualitatively, there is a quantitative disagreement between the number of (red) galaxies observed at $z \gtrsim 1.5$ and the number expected from the model. A better knowledge of galaxies at $1.5 < z < 2.5$ is of crucial importance for providing better constraints for either model.

Recent results from large *N*-body simulations coupled with semi-analytical post-processing have provided numerous predictions for the properties of the large-scale structure and galaxies over a wide redshift range (see right panel of Fig. 1.1; Springel et al. 2005, and references therein). These large ΛCDM simulations will form a navigable frame of reference for current and future observational cosmologists. For example, it is predicted that quasars at $z \sim 6$ lie in the center of very massive dark matter halos of $\sim 10^{12}\ M_{\odot}$ surrounded by many fainter galaxies, and that these halos will evolve into massive clusters of $\sim 10^{15}\ M_{\odot}$ at $z = 0$ (Springel et al. 2005). The simulations indicate that the quasar progenitors form at $z \sim 17$. The simulations are also successful in reproducing the clustering of galaxies observed in local redshift surveys, and furthermore they predict that 'baryon wiggles', reflecting the acoustic oscillations in the mass power spectrum of the ΛCDM model, should be imprinted on the galaxy distribution out to $z \sim 3$. These wiggles may be used to constrain the nature of the dark energy (Blake & Wall 2002b). The power spectrum analyses of large galaxy redshift surveys (the Two-degree Galaxy Redshift Survey and the Sloan Digital Sky Survey) have recently shown the baryonic oscillations to be present in the distribution of galaxies in the local universe (Eisenstein et al. 2005; Cole et al. 2005).

1.3 Recent advances in the study of clusters of galaxies

Despite the rapid advancements in our understanding of the evolution of galaxies concerning e.g. their star formation histories, morphologies and clustering at $z \lesssim 6$ (e.g. Papovich et al. 2004; Bouwens et al. 2004a, 2006; Giavalisco et al. 2004a; Franx et al. 2003; Barmby et al. 2004; Ferguson et al. 2004; Lotz et al. 2004, 2005; Conselice 2003; Ouchi et al. 2004; Porciani & Giavalisco 2002; Lee et al. 2005), the study of the evolution of *clusters of galaxies* has progressed at a much slower pace. Clusters of galaxies are the most massive and largest structures in the universe, that are the product of billions of years of gravitational growth. They typically have masses of $10^{14-15}\ M_{\odot}$, and contain hundreds of galaxies over a region of several Mpc across. Because mass condensations on these scales are extremely rare (Kaiser 1984), it is believed that they formed relatively late in the history of the universe and are thus even more rare at high redshifts (e.g. see Mo & White 2002). Also, clusters and their progenitors ('protoclusters'[1]) are much harder to distinguish at high redshift because the density contrast between clusters and the field decreases with lookback time, and thus the study of cluster formation is a very challenging field.

The most distant clusters known, at roughly half the Hubble time ($z \sim 1$), contain significant populations of relatively old galaxies, as well as younger star-forming galaxies (e.g. Dressler et al. 1999; van Dokkum et al. 2000; Demarco et al. 2005; Goto et al. 2005; Homeier et al. 2005; White et al. 2005; Stanford et al. 2005). Clusters have a 'red sequence', or colour-magnitude relation (CMR) consisting of massive, predominantly early-type galaxies (see Fig. 1.2). Its slope is believed to originate from a mass-metallicity relation, in the sense that more massive galaxies are better able to retain their metals and therefore appear redder than less massive galaxies (see Kodama & Arimoto and refer-

[1]See chapter 10 for a working definition.

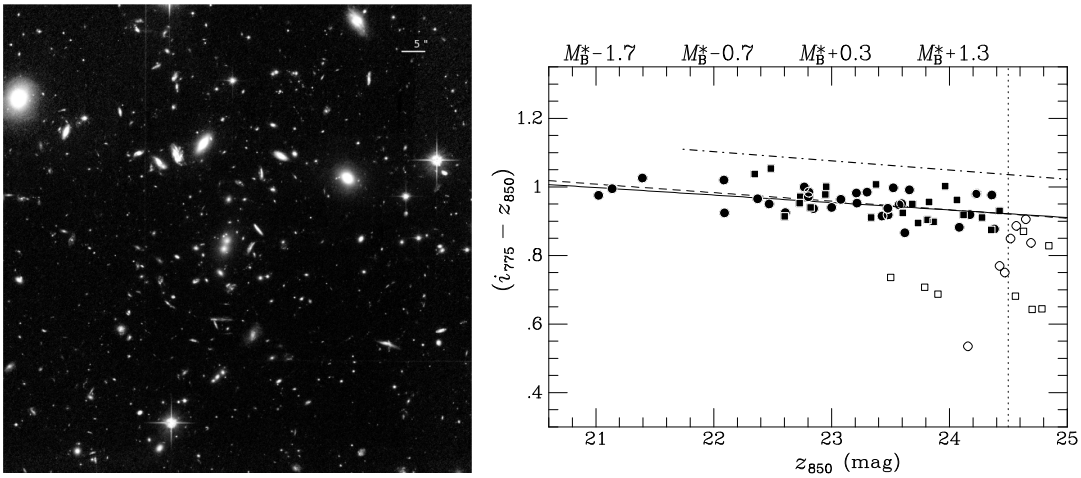

Figure 1.2 — One of the most distant and massive clusters known: Cl1252–2927 at $z = 1.24$. Left: ACS/WFC i_{775}+z_{850}-band image. Right: Color-magnitude diagram of early-type galaxies within the central 2′ of the cluster, with elliptical galaxies indicated by (filled) circles and S0 galaxies by squares. The lines indicate fits to the CMR for ellipticals only (solid line) and for all early-types (dashed). The dot-dashed line represents the relation for the Coma Cluster, transformed to these bandpasses at $z = 1.24$ assuming no evolution. The figures were taken from Blakeslee et al. (2003).

ences therein). Interestingly, some parts of clusters are remarkably old even at $z \sim 1$ as evidenced by the following. First, the tight scatter in the CMR for cluster early-types suggests formation redshifts of $z_f > 2.5$ with average luminosity-weighted ages of 2-4 Gyr (e.g. Ellis et al. 1997; Stanford et al. 1998; Stanford et al. 2005; Blakeslee et al. 2003; Mei et al. 2006). Second, analysis of the cluster morphology-density relation with HST suggests that while the relative fractions of S0s and spirals in clusters evolve strongly from $z \approx 1$ to $z \approx 0$, the elliptical fraction exhibits no significant evolution (Postman et al. 2005). It has been suggested that an excess of spiral galaxies observed at $z \sim 1$ can account for the deficit of S0 galaxies through extensive periods of merging at $z \lesssim 0.5$. Third, although many high redshift clusters ($z \gtrsim 0.5$) show signs of substructure and filamentary, diffuse X-ray emission, all clusters have hot virialized cores (core radii of a few hundred kpc) which are also traced by the distribution of the rest-frame optical stellar light, as well as the mass distribution determined from weak-lensing analysis (e.g. Jee et al. 2005a,b).

The most distant clusters currently known have been found mostly from wide-field surveys at optical (e.g. Gladders & Yee 2005) or X-ray wavelengths (e.g. Rosati et al. 1998; Mullis et al. 2005). The optical surveys can target high redshift clusters quite efficiently by looking for a cluster red sequence, provided that enough area is being surveyed to sufficient depth. However, as the 4000Å break shifts towards the near-infrared for $z \gtrsim 1.2$ the selection becomes more and more difficult. Recently, Stanford et al. (2005) discovered the second highest redshift cluster ($z = 1.41$) yet detected from a concentration of objects with high photometric redshifts. The survey data used in this detection comes from the infrared Spitzer Space Telescope, indicating the versatility of this new space telescope. The 'discovery power' of X-ray surveys becomes increasingly less with redshift, since the X-ray surface brightness profile of clusters is proportional to $(1+z)^{-4}$. Even worse, structure formation predicts that the X-ray signature of thermal gas only becomes apparent during the epoch of cluster virialization, which is believed to have occurred by $z \sim 1 - 1.5$ for the most massive clusters currently known. In the very near future, the search and study of clusters is likely to experience a significant revolution through sensitive, large area surveys targeting the Sunyaev-Z'eldovich (SZ)

signature of hot intracluster gas that scatters the photons of the CMB and modifies the incident CMB spectrum. The strength of the SZ effect is redshift independent and relies only on the presence of a hot medium above a certain mass threshold that is limited only by the sensitivity of the instruments. Large samples of galaxy groups and clusters are expected to be discovered at both low and high redshift (e.g. Laroque 2003, see Carlstrom et al. 2002 for a review) that could significantly advance the study of (massive) structure formation.

1.4 Searches and discoveries of forming clusters in the early universe

Given the relatively old ages of the stellar populations of elliptical galaxies in massive galaxy clusters at a distance of roughly half the Hubble time ($z \sim 1$), an interesting epoch of cluster formation and evolution could lie at even higher redshifts. Are such structures partially virialized at $z > 2$, and do they consist of several galaxy groups in sub-halos that eventually merge and give rise to a cluster red sequence? Do these structures lie at the nodes of filaments in the large scale structure as observed in *N*-body simulations? In any case, the progenitors of clusters must possess intense star formation. This star formation and possibly enhanced AGN activity at $z \gtrsim 2$ could be responsible for 'pre-heating' (Tozzi & Norman 2001) as well as chemical enrichment of the intra-cluster medium (e.g. Arnaud et al. 1992; Tozzi et al. 2003; Maoz & Gal-Yam 2004; Ettori 2005). Simulations predict that the ages of galaxies depend strongly on environment, with ellipticals in the most massive halos being > 1 Gyr older on average. Up to 50% of the stellar mass in these galaxies is presumably *formed* by $z \sim$4, although it was only *assembled* into a single galaxy at $z \sim 1$ (De Lucia et al. 2006).

Are we already witnessing some of these phenomena at $z \gtrsim 2$? Overdensities of galaxies have been discovered out to $z \approx 6$ (e.g. Pascarelle et al. 1996; Steidel et al. 1998, 2005; Keel et al. 1999; Kurk et al. 2000; Pentericci et al. 2000; Francis et al. 2001; Möller & Fynbo 2001; Venemans et al. 2002, 2004; Venemans et al. 2005; Shimasaku et al. 2003; Kurk et al. 2004; Ouchi et al. 2005; Stiavelli et al. 2005). These structures are all overdense compared to the field, but their derived physical properties are generally highly uncertain. These objects have estimated galaxy overdensities close to or in excess of the requirements for gravitational collapse, group- or clusterlike masses of 10^{13-15} $M_\odot$, projected sizes of several to tens of comoving Mpc, and in some cases measured velocity dispersions of several 100 km s^{-1} determined from emission line galaxies. Their topologies and masses indicate that they may constitute 'filaments', 'sheets', 'proto-groups' and 'protoclusters'. While some of these structures have been found as by-products of wide field surveys using broad or narrow band imaging and spectroscopic follow-up, in other instances, these large-scale structures were traced by a luminous or powerful radio galaxy or quasar that facilitated in pinpointing the overdense region. In the following section, we will focus on the latter group, since it forms the basis of the current thesis.

1.4.1 Probing the emergence of cosmic structures around distant radio galaxies

Luminous radio galaxies are amongst the most massive forming galaxies at high redshift ($z \gtrsim 1$). They form a bright envelope in the *K*-band Hubble redshift diagram (De Breuck et al. 2002; Rocca-Volmerange et al. 2004), indicating that radio galaxy hosts statistically have baryonic masses of up to $\sim 10^{12}$ $M_\odot$ over a wide redshift range. This is confirmed by detailed studies of individual objects. Pentericci et al. (2001) and Zirm et al. (2003) measured the stellar hosts of radio galaxies at $1 < z < 3$, finding that they often possess $r^{1/4}$-law light profiles, indicating that they are massive, passively evolving elliptical galaxies. Villar-Martín et al. (2006) presented the first rest-frame optical-near-infrared spectral energy distribution of a radio galaxy at $z = 2.5$, which suggested the existence of a reddened, evolved stellar population of age >1.8 Gyr ($z_f \gtrsim 6$) and mass $(5 \pm 2) \times 10^{11}$ $M_\odot$. The galaxy itself is embedded in a giant (> 100 kpc), perhaps rotating, nebula of emission line gas which

is a common feature in high redshift radio galaxies (e.g. van Ojik et al. 1997; Venemans et al. 2002; Reuland et al. 2003). Some radio galaxies show signs of vigorous starbursts with star formation rates as high as several hundreds to a thousand $M_\odot$ yr^{-1} (e.g. Dey et al. 1997; Papadopoulos et al. 2000; Stevens et al. 2003; Zirm et al. 2005). An example of the host galaxy of radio source MRC 1138–262 at $z = 2.16$ is shown in Fig. 1.3, showing several characteristic features of radio galaxies at rest-frame UV wavelengths (see figure caption for further details). From the study of the clustering properties of radio galaxies it has been found that they are associated with the densest environments that may be virializing at any cosmic epoch (e.g. Negrello et al. 2006, and references therein).

The theory of structure formation predicts that, in principle, the most massive galaxies at any epoch are associated with the most extreme peaks in the large-scale structure. Could distant radio galaxies trace the progenitors of the galaxy clusters seen in the local universe? If so, this would provide us with a unique tool for studying cluster formation in the early universe. Over the past decade, this hypothesis has been tested by searching for companion galaxies in the vicinity of radio sources. Many radio galaxies in the redshift range $1.5 < z < 2$ have been found to be associated with overdensities of relatively red galaxies (e.g. Sánchez & González-Serrano 1999, 2002; Thompson et al. 2000; Hall et al. 2001; Barr et al. 2003; Best et al. 2003; Wold et al. 2003; Bornancini et al. 2006), suggesting clusters of Abell richness class 0–1. In a pioneering study by Pentericci et al. (2000) and Kurk et al. (2000), a narrow-band filter was used to search for Lyα companion objects in a $7' \times 7'$ field around a radio galaxy at $z = 2.16$ using the Very Large Telescope (VLT) in Chile. Follow-up spectroscopy of a large number of candidate Lyα excess galaxies, augmented by a sample of near-infrared selected candidate Hα excess galaxies (Kurk et al. 2004) showed a large structure of galaxies within 1000 km s^{-1} of the radio galaxy. The mass of the system is $\sim 10^{14}$ $M_\odot$, estimated from the overdensity of Lyα emitters relative to the field. The radio galaxy protocluster program was expanded by means of a Large Program with the VLT to carry out similar studies towards other luminous radio galaxies in the redshift range $2.0 < z < 5.2$. The program resulted in the discovery of six new structures of Lyα galaxies with masses in the range of 10^{14-15} $M_\odot$ (Venemans et al. 2002, 2004; Venemans et al. 2005, 2006). The velocity dispersions of the systems decrease with increasing redshift, roughly as predicted for forming clusters by numerical simulations (Venemans et al. 2006). The work of Venemans et al. has provided strong evidence that distant radio galaxies are tracers of rich environments in the early universe.

1.4.2 The ACS high redshift cluster/protocluster survey

The Advanced Camera for Surveys (ACS; Ford et al. 1998) on the Hubble Space Telescope (HST) is a unique instrument for studying galaxy and cluster evolution, due to its unprecedented sensitivity, relatively wide field of view ($3\farcm4 \times 3\farcm4$), and high spatial resolution ($\sim 0\farcs1$). This has motivated an extensive program to study the properties of massive galaxy clusters in the early universe, using broad-band imaging with the HST/ACS Wide Field Channel (WFC), as part of the Guaranteed Time Observations (GTO). The survey covers a large number of X-ray selected clusters in the redshift range $0.8 < z < 1.4$ (Blakeslee et al. 2003; Mei et al. 2006; Holden et al. 2005; Postman et al. 2005; Goto et al. 2005; Jee et al. 2005a,b; Homeier et al. 2005, 2006).

The cluster program is complemented by the study of protocluster candidates around high redshift ($z > 2$) radio galaxies and quasars (Miley et al. 2004; Overzier et al. 2006a,b; Zheng et al. 2006; Zirm et al. 2005), the results of which are presented in this thesis.

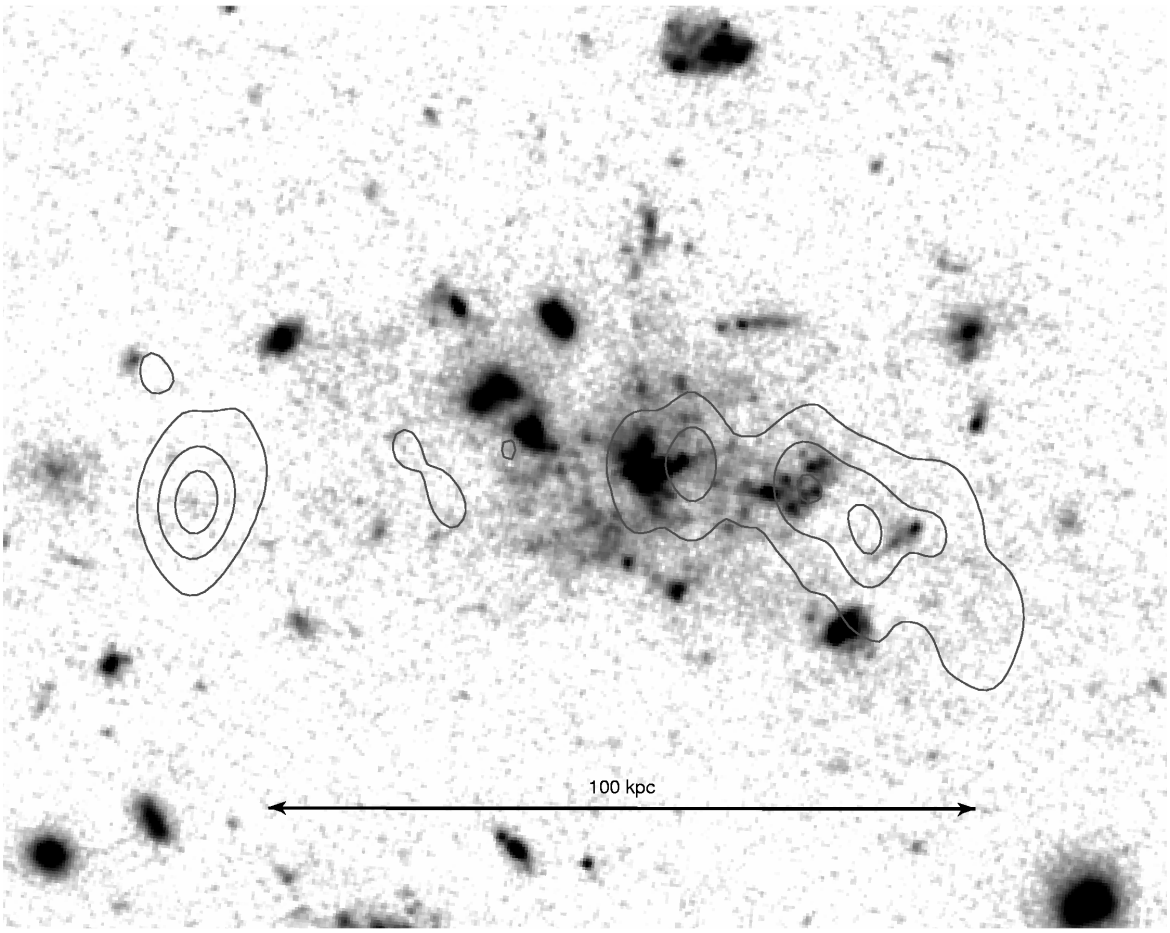

Figure 1.3 — ACS/WFC $g_{475}+I_{814}$ detail image of the radio galaxy MRC 1138–262 at $z = 2.16$. The system consists of a large (> 100 kpc) conglomeration of sub-galactic clumps embedded in a region of diffuse emission. The total star formation rate in the clumps and the diffuse component are about equal. Comparison with rest-frame optical light indicates that the mass of the UV continuum component seen in this image is only a small fraction of the total mass of the system, suggesting that the MRC 1138–262 system has elements of both monolithical and hierarchical formation (Miley et al., in prep.). Contours show the radio emission at 4.5 GHz.

1.5 This thesis

This thesis presents additional evidence for associations of star-forming galaxies that may have developed early on in the history of the universe, especially in the close vicinity of luminous active galactic nuclei (radio galaxies and quasars). These structures form an interesting class of relatively rare and massive objects. A systematic study of these structures may shed light on the origin of galaxy clusters. Here, I analyse the environments of radio galaxies at large and small scales, and study the morphological and spectral properties of several galaxy overdensities between $z = 2$ and $z = 6$ and investigate their relation to the epoch of cluster formation, and to the properties of the emerging large-scale structure in general. The structure of this thesis is as follows.

Chapter 2 – In this chapter an analysis of the angular correlation function, $w(\theta)$, of radio sources in

the 1.4 GHz NVSS and FIRST radio surveys is presented. Below $\sim 6'$ the signal is dominated by the size distribution of classical double radio galaxies. A high amplitude measured for the cosmological clustering suggests that powerful radio galaxies probe significantly more massive structures compared to normal galaxies, quasars as well as radio galaxies of average power. This is consistent with powerful radio galaxies being associated with massive galaxies in relatively rich environments at high redshift. Their clustering scalelength (r_0) at $z \sim 1$ is close to that measured for extremely red objects (EROs) associated with a population of old elliptical galaxies at similar redshifts, and we propose that EROs and radio galaxies may be the same systems seen at different evolutionary stages. Depending on the underlying model for their evolution from $z \sim 1$ to $z = 0$, the clustering of radio galaxies could be in agreement with both ΛCDM hierarchical predictions for massive early-type galaxies, and with passive evolution into a present-day population of clusters.

Chapter 3 – This chapter reports of the use of the Chandra X-ray observatory to study 5 radio galaxies at $z \sim 2-3$. The goals were to (i) study the nature of their non-thermal X-ray emission, (ii) investigate the presence of hot gas, and (iii) look for overdensities of active galaxies near high redshift radio galaxies. We detected unresolved X-ray components towards the radio nuclei, and their X-ray luminosities implied that the nuclei are surrounded by obscuring material with H I column densities of $\sim 10^{22}$ cm^{-2}. We found extended emission coincident with the radio hotspots or lobes, which can be explained by the Inverse-Compton scattering of photons that make up the cosmic microwave background (CMB). The magnetic field strengths of $\sim 100-200$ μG that we derive agree with the equipartition magnetic field strengths. The relative ease with which the lobe X-ray emission is detected is a consequence of the $(1+z)^4$ increase in the energy density of the CMB. For one of the lobes, the X-ray emission could also be produced by a reservoir of hot, shocked gas.

We detected no diffuse emission and derive upper limits of $\sim 10^{44}$ erg s^{-1}, thereby ruling out a virialized structure of cluster-size scale at $z \sim 2$. The average number of soft X-ray sources in the field surrounding the radio sources is consistent with the number density of AGN in the Chandra Deep Fields, and analysis of their angular distribution shows no evidence for rich large-scale structure associated with these radio galaxies, in contrast to what was found for the radio galaxy PKS 1138–262 at $z = 2.2$.

Chapters 4 & 5 – Here deep ACS and VLT K_S-band observations are presented of fields around the radio galaxy TN J1338–1942 at $z = 4.1$. We study in detail 12 spectroscopically confirmed companions previously found through their excess Lyα emission by Venemans et al. (2002), and conclude that the Lyα emitters (LAEs) are young (a few $\times 10^7$ yr), dust-free galaxies based on small sizes, steep UV slopes ($\beta \approx -2$) and blue UV-optical colours with star formation rates (SFRs) of < 14 $M_\odot$ yr^{-1}. We derive stellar masses of a few $\times 10^8$ M$_\odot$, and estimate the LAE AGN fraction to be minimal.

We selected 66 Lyman break galaxies (LBGs) at $z \sim 4.1$ ('g_{475}-dropouts'), six of which are in the LAE sample. Their SFRs, sizes, morphologies, UV slope-magnitude and (i_{775}–K_S) vs. K_S colour-magnitude relations are all similar to those found for LBGs in the 'field'. We quantify the number density and cosmic variance of $z \sim 4$ LBGs, and show that the field of TN J1338–1942 is richer than the average field at the $3-5\sigma$ significance. The angular distribution is highly filamentary, with about half of the objects clustered in a 4.4 arcmin^2 region that includes the radio galaxy and the brightest LBGs. The generally fainter LAEs appear to favour regions that are devoid of LBGs, while LBGs detected in the rest-frame optical (K_S) tend to lie in the richest region. This may suggest a forming age- or mass-density relation. We find an excess signal in the angular correlation function at separations of $\theta < 20''$, corresponding to the typical halo size of dark matter halos hosting bright LBGs recently shown to be statistically present in large LBG field samples. The large galaxy overdensity, its corresponding mass overdensity and the sub-clustering at the approximate redshift of TN J1338–1942 suggest the

assemblage of a $> 10^{14}$ $M_\odot$ structure, possibly a 'protocluster'.

Chapter 6 – In this chapter we focus on the properties of the host galaxy of the radio source TN J1338–1942 at $z = 4.1$. TN J1338 is the dominant galaxy in the protocluster in terms of size and luminosity and therefore seems destined to remain the brightest cluster galaxy. The high spatial resolution ACS images reveal several kpc-scale features within and around the radio galaxy. The rest-frame continuum light is aligned with the radio axis and is resolved into two clumps with luminosities of $\sim 10^9$ $L_\odot$ and sizes of a few kpc. The estimated nebular continuum, scattered light, synchrotron- and IC-scattering contributions to the aligned continuum light are only a few percent of the total observed flux which is likely dominated by forming stars with a star formation rate of ~ 200 $M_\odot$ yr^{-1}. A simple model in which the jet has triggered the star formation is consistent with the available data. A small, linear feature in the z_{850} aligned light may be indicative of a large-scale shock associated with the advance of the radio jet. The rest of the aligned light also seems morphologically consistent with star formation induced by shocks associated with the radio source, as seen in other high-z radio galaxies. An unusual feature is seen in Lyα emission. A wedge-shaped extension emanates from the radio galaxy perpendicularly to the radio axis. This "wedge" naturally connects to the surrounding asymmetric, large-scale ($\sim$100 kpc) Lyα halo. We posit that the wedge is a starburst-driven superwind. The shock and wedge are examples of feedback processes due to both the active galactic nucleus and star formation in the earliest stages of massive galaxy formation.

Chapter 7 – Here ACS observations are presented, of the most distant radio galaxy known, TN J0924–2201 at $z = 5.2$. This radio galaxy has 6 spectroscopically confirmed Lyα emitting companion galaxies, and appears to lie within an overdense region. Although the radio galaxy shows some continuum emission aligned with the radio axis, its basic properties (half-light radius and UV star formation rate) are comparable to the typical values found for Lyman break galaxies at $z \sim 4 - 5$. The Lyα emitters are sub-L^* galaxies, with deduced star formation rates of $1 - 10$ $M_\odot$ yr^{-1}. One of the Lyα emitters is only detected in Lyα, and the lack of continuum emission could be explained if the galaxy is younger than ~ 2 Myr and is producing its first stars.

Observations in $V_{606}i_{775}z_{850}$ were used to identify additional LBGs associated with this structure. In addition to the radio galaxy, there are 22 V_{606}-break galaxies with z_{850}<26.5, two of which are also in the spectroscopic sample. We compare the surface density of ~ 2 arcmin^{-2} to that of similarly selected V_{606}-dropouts extracted from the Great Observatories Origins Deep Survey (GOODS) and the Hubble Ultra Deep Field (UDF) parallel fields. We find evidence for an overdensity ($> 99\%$ confidence), based on a counts-in-cells analysis applied to the control field. The excess is suggestive of the V_{606}-break objects being associated with a forming structure around the radio galaxy.

Chapter 8 – The angular clustering has been measured from a sample of 506 i_{775} dropout galaxies obtained from deep ACS fields to study clustering at $z \sim 6$. For our largest and most complete subsample ($L \gtrsim 0.5L^*_{z=6}$), we detected clustering at $\sim 94\%$ significance. We derived a (co-moving) spatial correlation length of $r_0 = 3.6^{+1.7}_{-2.5}$ h_{72}^{-1} Mpc and bias $b = 3.6^{+1.3}_{-2.2}$, using an accurate model for the redshift distribution. No clustering could be detected in the much deeper but significantly smaller UDF sample. We compare our findings to Lyman break galaxies at $z \sim 3 - 5$ at a fixed luminosity. Our best estimate of the bias parameter implies that i_{775} dropouts are hosted by dark matter halos having masses of $\sim 10^{11}$ $M_\odot$, consistent with the typical mass of halos hosting V_{606} dropouts at $z \sim 5$. We evaluate a recent claim by Lee et al. (2005) that at $z \gtrsim 5$ star formation might have occurred more efficiently compared to that at $z = 3 - 4$. This may provide an explanation for the very mild evolution observed in the rest frame UV luminosity density between $z = 6$ and 3. Although our results are consistent with the star formation efficiency also being higher at $z \sim 6$, our errors are too large to find conclusive evidence for this.

Chapter 9 – A five square arcminute region around the luminous radio-loud quasar SDSS J0836+0054 ($z = 5.8$) hosts a wealth of associated galaxies, characterized by very red ($1.3 < i_{775} - z_{850} < 2.0$) colour. The surface density of these $z \sim 5.8$ candidates is approximately six times higher than the number expected from deep ACS fields (see chapter 8). We also find evidence for a substructure associated with one of the candidates. It has two very faint companion objects within two arcseconds, which are likely to merge. The finding supports the results of a recent simulation that luminous quasars at high redshifts lie on the most prominent dark-matter filaments and are surrounded by many fainter galaxies. The quasar and star formation activity from these regions may signal the buildup of a massive system.

Chapter 10 – This chapter attempts to provide new constraints on the scenario for the formation of galaxy clusters, based, in part, on the observational evidence presented in this thesis. The chapter is structured in 3 parts. In part I, we compile the first overview of observational evidence for overdensities of galaxies between $z = 2$ and $z = 6$. The overdensities, estimated from the number densities of star-forming galaxies (Lyα emitting galaxies and Lyman break galaxies) relative to random fields, are on the order of a few. If these structures were to collapse under the influence of their own gravity, their masses would be $\sim 10^{14}$ to 10^{15} $M_{\odot}$. Because this is comparable to the masses of clusters of galaxies in the local universe, we define the term 'protocluster' as being an object that meets the requirements for forming a bound object on the mass scale of a cluster prior to, or at, the present epoch, but which has not yet collapsed and virialized at the epoch corresponding to its observed redshift. In part II, we use simple theoretical descriptions for the growth of overdensities in a ΛCDM universe to study the evolution of the sample of candidate protoclusters compiled in part I. Using very conservative estimates of the overdensities, we find that the majority of the structures are likely to collapse within a finite time. We identify several structures as meeting the requirements for virialization at $z \approx 0.5$, whereas others are expected to have fully collapsed by the present epoch. In part III, we use a simple model for the star formation history of cluster red sequence galaxies to demonstrate that the observed star formation rates in protocluster fields can explain the build-up of the stellar mass in the red sequence galaxies of relatively nearby clusters.

References

Arnaud, M., Rothenflug, R., Boulade, O., Vigroux, L., & Vangioni-Flam, E. 1992, A&A, 254, 49

Barmby, P. et al. 2004, ApJ, 154, 97

Barr, J. M., Bremer, M. N., Baker, J. C., & Lehnert, M. D. 2003, MNRAS, 346, 229

Bennett, C. L., et al. 2003, ApJ, 148, 1

Best, P. N., Lehnert, M. D., Miley, G. K., Röttgering, H. J. A. 2003, MNRAS, 343, 1

Blake, C., & Glazebrook, K. 2003, ApJ, 594, 665

Blakeslee, J. P., et al. 2003, ApJ, 596, L143

Blumenthal, G. R., Faber, S. M., Primack, J. R., & Rees, M. J. 1984, Nature, 311, 517

Bond, J. R., Cole, S., Efstathiou, G., & Kaiser, N. 1991, ApJ, 379, 440

Bornancini, C. G., Lambas, D. G., & De Breuck, C. 2006, MNRAS, 366, 1067

Bouwens, R. J., Illingworth, G. D., Blakeslee, J. P., Broadhurst, T. J., & Franx, M. 2004, ApJ, 611, L1

Bouwens, R. J., Illingworth, G. D., Blakeslee, J. P., & Franx, M. 2005, Submitted to ApJ

Bower, R. G. 1991, MNRAS, 248, 332

Carlstrom, J. E., Holder, G. P., & Reese, E. D. 2002, ARA&A, 40, 643

Carroll, S. M., Press, W. H., & Turner, E. L. 1992, ARA&A, 30, 499

Cole, S., Aragon-Salamanca, A., Frenk, C. S., Navarro, J. F., & Zepf, S. E. 1994, MNRAS, 271, 781

Cole, S., Lacey, C. G., Baugh, C. M., & Frenk, C. S. 2000, MNRAS, 319, 168

Cole, S., et al. 2005, MNRAS, 362, 505

Conselice, C. J. 2003, ApJ, 147, 1

De Breuck, C., van Breugel, W., Stanford, S. A., Röttgering, H., Miley, G., & Stern, D. 2002, AJ, 123, 637

De Lucia, G., Springel, V., White, S. D. M., Croton, D., & Kauffmann, G. 2006, MNRAS, 366, 499

Demarco, R., Ford, H. C., Rosati, P., MPLA, 20, 1409, 2005

Dey, A., van Breugel, W., Vacca, W. D., & Antonucci, R. 1997, ApJ, 490, 698

Dressler, A., Smail, I., Poggianti, B. M., Butcher, H., Couch, W. J., Ellis, R. S., & Oemler, A. J. 1999, ApJ, 122, 51

Eggen, O. J., Lynden-Bell, D., & Sandage, A. R. 1962, ApJ, 136, 748

Eisenstein, D. J., et al. 2005, ApJ, 633, 560

Ellis, R. S., Smail, I., Dressler, A., Couch, W. J., Oemler, A. J., Butcher, H., & Sharples, R. M. 1997, ApJ, 483, 582

Ettori, S. 2005, MNRAS, 362, 110
Eyles, L. P., Bunker, A. J., Stanway, E. R., Lacy, M., Ellis, R. S., & Doherty, M. 2005, MNRAS, 364, 443
Fan, X., Narayanan, V. K., Strauss, M. A., White, R. L., Becker, R. H., Pentericci, L., & Rix, H.-W. 2002, AJ, 123, 1247
Ferguson, H. C. et al. 2004, ApJ, 600, L107
Ford, H. C., et al. 1998, Proc. SPIE, 3356, 234
Francis, P. J., et al. 2001, ApJ, 554, 1001
Franx, M. et al. 2003, ApJ, 587, L79
Giavalisco, M. et al. 2004, ApJ, 600, L103
Gladders, M. D., & Yee, H. K. C. 2005, ApJ, 157, 1
Goto, T., et al. 2005, ApJ, 621, 188
Guth, A. H. 1981, PhRvD, 23, 347
Hall, P. B., et al. 2001, AJ, 121, 1840
Holden, B. P., et al. 2005, ApJ, 626, 809
Homeier, N. L., et al. 2006, AJ, 131, 143
Homeier, N. L., et al. 2005, ApJ, 621, 651
Jee, M. J., White, R. L., Ford, H. C., Blakeslee, J. P., Illingworth, G. D., Coe, D. A., & Tran, K.-V. H. 2005, ApJ, 634, 813
Jee, M. J., White, R. L., Benítez, N., Ford, H. C., Blakeslee, J. P., Rosati, P., Demarco, R., & Illingworth, G. D. 2005, ApJ, 618, 46
Jenkins, A., et al. 2001, MNRAS, 321, 372
Kaiser, N. 1984, ApJ, 284, L9
Kauffmann, G., & Charlot, S. 1998, MNRAS, 297, L23
Kauffmann, G., Colberg, J. M., Diaferio, A., & White, S. D. M. 1999, MNRAS, 303, 188
Keel, W. C., Cohen, S. H., Windhorst, R. A., & Waddington, I. 1999, AJ, 118, 2547
Kneib, J.-P., Ellis, R. S., Santos, M. R., & Richard, J. 2004, ApJ, 607, 697
Kodaira, K., et al. 2003, PASJ, 55, L17
Kogut, A., et al. 2003, ApJ, 148, 161
Kurk, J. D., et al. 2000, A&A, 358, L1
Kurk, J. D., Pentericci, L., Overzier, R. A., Röttgering, H. J. A., & Miley, G. K. 2004, A&A, 428, 817
Lahav, O., et al. 2002, MNRAS, 333, 961
LaRoque, S. J., et al. 2003, ApJ, 583, 559
Lee, K., et al. 2005, Submitted to ApJ(astro-ph/0508090)
Loeb, A., & Barkana, R. 2001, ARA&A, 39, 19
Lotz, J., Madau, P., Giavalisco, M., Primack, J., & Ferguson, H. 2005, ApJIn Press (astro-ph/0509106)
Mobasher, B., et al. 2005, ApJ, 635, 832
Lotz, J. M., Primack, J., & Madau, P. 2004, AJ, 128, 163
Maoz, D., & Gal-Yam, A. 2004, MNRAS, 347, 951
Mei, S., et al. 2006, ApJ, In press
Miley, G. K., et al. 2004, Nature, 427, 47
Mo, H. J., & White, S. D. M. 2002, MNRAS, 336, 112
Möller, P., & Fynbo, J. U. 2001, A&A, 372, L57
Mullis, C. R., Rosati, P., Lamer, G., Böhringer, H., Schwope, A., Schuecker, P., & Fassbender, R. 2005, ApJ, 623, L85
Negrello, M., Magliocchetti, M., & De Zotti, G. 2006, MNRAS, In press (astro-ph/0602283)
Ouchi, M., et al. 2005, ApJ, 620, L1
Ouchi, M., et al. 2004, ApJ, 611, 685
Overzier, R. A., et al. 2006, ApJ, 637, 58
Overzier, R. A., et al. 2006, ApJ, Submitted
Papadopoulos, P. P., et al. 2000, ApJ, 528, 626
Papovich, C. et al. 2004, ApJ, 600, L111
Pascarelle, S. M., Windhorst, R. A., Driver, S. P., Ostrander, E. J., & Keel, W. C. 1996, ApJ, 456, L21
Pentericci, L., McCarthy, P. J., Röttgering, H. J. A., Miley, G. K., van Breugel, W. J. M., & Fosbury, R. 2001, ApJ, 135, 63
Pentericci, L., et al. 2000, A&A, 361, L25
Perlmutter, S., et al. 1999, ApJ, 517, 565
Postman, M., et al. 2005, ApJ, 623, 721
Porciani, C., & Giavalisco, M. 2002, ApJ, 565, 24
Press, W. H., & Schechter, P. 1974, ApJ, 187, 425
Reuland, M., et al. 2003, ApJ, 592, 755
Riess, A. G., et al. 2004, ApJ, 607, 665
Rocca-Volmerange, B., Le Borgne, D., De Breuck, C., Fioc, M., & Moy, E. 2004, A&A, 415, 931
Rosati, P., della Ceca, R., Norman, C., & Giacconi, R. 1998, ApJ, 492, L21
Sánchez, S. F., & González-Serrano, J. I. 1999, A&A, 352, 383
Sánchez, S. F., & González-Serrano, J. I. 2002, A&A, 396, 773
Sheth, R. K., & Tormen, G. 1999, MNRAS, 308, 119
Shimasaku, K., et al. 2003, ApJ, 586, L111
Somerville, R. S., & Primack, J. R. 1999, MNRAS, 310, 1087
Somerville, R. S., et al. 2004, ApJ, 600, L135
Spergel, D. N., et al. 2003, ApJ, 148, 175
Springle, V. et al. 2005, Nature, 435, 629
Stanford, S. A., Eisenhardt, P. R., & Dickinson, M. 1998, ApJ, 492, 461
Stanford, S. A., et al. 2005, ApJ, 634, L129
Steidel, C. C., Adelberger, K. L., Dickinson, M., Giavalisco, M., Pettini, M., & Kellogg, M. 1998, ApJ, 492, 428
Steidel, C. C., Adelberger, K. L., Shapley, A. E., Erb, D. K., Reddy, N. A., & Pettini, M. 2005, ApJ, 626, 44
Stevens, J. A., et al. 2003, Nature, 425, 264
Stiavelli, M., et al. 2005, ApJ, 622, L1
Tegmark, M., et al. 2004, PhRvD, 69, 103501
Thompson, D., Aftreth, O., & Soifer, B. T. 2000, AJ, 120, 2331
Tozzi, P., Rosati, P., Ettori, S., Borgani, S., Mainieri, V., & Norman, C. 2003, ApJ, 593, 705
van Dokkum, P. G., Franx, M., Fabricant, D., Illingworth, G. D., & Kelson, D. D. 2000, ApJ, 541, 95
van Ojik, R., Röttgering, H. J. A., Miley, G. K., & Hunstead, R. W. 1997, A&A, 317, 358
Venemans, B. P., et al. 2002, ApJ, 569, L11
Venemans, B. P., et al. 2004, A&A, 424, L17
Venemans, B. P., et al. 2005, A&A, 431, 793
Venemans, B. P. 2006, Astronomische Nachrichten, 327, 196
Villar-Martín, M., et al. 2006, MNRAS, 366, L1
Wold, M., Armus, L., Neugebauer, G., Jarrett, T. H., & Lehnert, M. D. 2003, AJ, 126, 1776
White, S. D. M., & Rees, M. J. 1978, MNRAS, 183, 341
White, S. D. M., et al. 2005, A&A, 444, 365
Zheng, W., et al. 2006, ApJ, In press
Zirm, A. W., Dickinson, M., & Dey, A. 2003, ApJ, 585, 90
Zirm, A. W., et al. 2005, ApJ, 630, 68

Chapter 2

The spatial clustering of radio sources in NVSS and FIRST; implications for galaxy clustering evolution

Abstract. We have measured the angular correlation function, $w(\theta)$, of radio sources in the 1.4 GHz NVSS and FIRST radio surveys. Below $\sim 6'$ the signal is dominated by the size distribution of classical double radio galaxies, an effect underestimated in some previous studies. We model the physical size distribution of FRII radio galaxies to account for this excess signal in $w(\theta)$. The amplitude of the true cosmological clustering of radio sources is roughly constant at $A \simeq 1 \times 10^{-3}$ for flux limits of 3–40 mJy, but has increased to $A \simeq 7 \times 10^{-3}$ at 200 mJy. This can be explained if powerful (FRII) radio galaxies probe significantly more massive structures compared to radio galaxies of average power at $z \sim 1$. This is consistent with powerful high-redshift radio galaxies generally having massive (forming) elliptical hosts in rich (proto-)cluster environments. For FRIIs we derive a spatial (comoving) correlation length of $r_0 = 14 \pm 3\ h^{-1}$ Mpc. This is remarkably close to that measured for extremely red objects (EROs) associated with a population of old elliptical galaxies at $z \sim 1$ by Daddi et al. (2001). Based on their similar clustering properties, we propose that EROs and powerful radio galaxies may be the same systems seen at different evolutionary stages. Their r_0 is $\sim 2\times$ higher than that of QSOs at a similar redshift, and comparable to that of bright ellipticals locally. This suggests that r_0 (comoving) of these galaxies has changed little from $z \sim 1$ to $z = 0$, in agreement with current ΛCDM hierarchical merging models for the clustering evolution of massive early-type galaxies. Alternatively, the clustering of radio galaxies can be explained by the galaxy conservation model. This then implies that radio galaxies of average power are the progenitors of the local field population of early-types, while the most powerful radio galaxies will evolve into a present-day population with r_0 comparable to that of local rich clusters.

R. A. Overzier, H. J. A. Röttgering, R. B. Rengelink & R. J.Wilman
Astronomy & Astrophysics, **405**, 53 (2003)

2.1 Introduction

In striking contrast with the extremely high level of isotropy observed in the temperature of the cosmic microwave background (see e.g. de Bernardis et al. 2000), galaxies are not distributed throughout the Universe in a random manner. According to the gravitational theory of instability the present structures originated from tiny fluctuations in the initial mass density field. This has shaped the *large-scale structure* of the Universe, which consists of vast empty regions (*voids*), and strings of dark and luminous matter (*walls*) where billions of galaxies are found.

The clustering properties of galaxies can be quantified using statistical techniques, such as methods of nearest neighbour, counts in cells, power spectra, and correlation functions (see Peebles 1980,for an in-depth mathematical review). In particular the two-point correlation function is a simple, but powerful tool that has become a standard for studying large-scale structure. The clustering of cosmological objects can be characterized by their spatial correlation function, which has the form $\xi(r) = (r/r_0)^{-\gamma}$ where r_0 is the present-day correlation length and $\gamma \simeq 1.8$ for objects ranging from clusters to normal galaxies (see Bahcall & Soneira 1983, for a review). The local population of galaxies is a relatively unbiased tracer of the underlying matter distribution, with $r_0 = 5.4\ h^{-1}$ Mpc derived from galaxies in the early CfA redshift survey by Davis & Peebles (1983), however more recent low-redshift surveys show that the clustering of galaxies depends strongly on luminosity and/or morphological type. For example, local $L \gtrsim L_*$ ellipticals represent spatial structures that are much more strongly clustered with $r_0 \simeq 7 - 12\ h^{-1}$ Mpc (e.g. Guzzo et al. 1997; Willmer et al. 1998; Norberg et al. 2002). From deep, magnitude-limited redshift samples it has been found that the comoving correlation length of galaxies declines with redshift, roughly as expected from simple gravitational theory (e.g. CFRS, Le Fèvre et al. 1996; Hawaii K, Carlberg et al. 1997; CNOC2, Carlberg et al. 2000; CFDF, McCracken et al. 2001). In contrast to this, the clustering strength of quasars appears to vary little over $0 \lesssim z \lesssim 2.5$. Croom et al. (2001) found an approximately constant amplitude of $\sim 5\ h^{-1}$ Mpc from $\sim 10,000$ quasars in the 2dF QSO Redshift Survey. Likewise, Daddi et al. (2001, 2002) found that the (comoving) correlation length of massive elliptical galaxies also shows little evolution with redshift. They find $r_0 = 12 \pm 3\ h^{-1}$ Mpc for a population of extremely red objects (EROs) at $z \sim 1$ (see also McCarthy et al. 2001; Roche et al. 2002; Firth et al. 2002), which are consistent with being the passively evolving progenitors of local massive ellipticals (e.g. Dunlop et al. 1996; Cimatti et al. 1998, 2002; Dey et al. 1999; Liu et al. 2000). Color selection methods such as Lyman-break (Steidel et al. 1995) and narrow-band imaging techniques are providing statistical samples of very high redshift galaxies, allowing us to study large-scale structure at even earlier epochs. Lyman-break galaxies have correlation lengths as high as $r_0 \simeq 3\ h^{-1}$ Mpc even at $z \sim 3 - 4$, and are thought to be associated with (mildly) biased star-forming galaxies (e.g. Adelberger 2000; Ouchi et al. 2001; Porciani & Giavalisco 2002).

Studying clustering as a function of redshift and galaxy type may provide important constraints on some long-standing problems in cosmology concerning galaxy formation and evolution. For example, which of the galaxies observed at high redshift are the progenitors of local galaxy populations, and which of the local galaxies host the remnant black holes that once powered high redshift active galactic nuclei (AGN)? Two common views on how structures observed at high redshifts may be related to structures observed today are represented by (i) *the galaxy conservation model* (e.g. Fry 1996; Tegmark & Peebles 1998) in which it is assumed that galaxies formed very early in a monolithic collapse (e.g. Eggen et al. 1962) and have evolved passively with a decreasing star formation rate since $z \sim 2$, and (ii) *the hierarchical merging model* (e.g. Mo & White 1996) in which it is assumed that the most luminous galaxies formed more recently in massive dark

matter haloes that have grown hierarchically by the merging of less massive galaxies and their haloes. Kauffmann & Charlot (1998) computed the evolution of the observed K-band luminosity function for both the monolithic case and the hierarchical case, and found that by a redshift of ~ 1 these models differ greatly in the abundance of bright galaxies they predict. Likewise, the validity of these models can be tested by comparing predictions for galaxy clustering from numerical simulations or (semi-)analytic theory (e.g. Kauffmann et al. 1999b; Moustakas & Somerville 2002; Mo & White 2002,and references therein) with the observed clustering of a population of galaxies. In the case of pure monolithic collapse galaxy clustering is dictated by the evolution of galaxy bias under the rules of gravitational perturbation theory, but without the extra non-linear effects arising from galaxy mergers. Such a scenario can be thought of as a baseline model for the clustering of the matter as probed by galaxies situated in average mass haloes. However, in the hierarchical case the evolution of galaxy bias is much more complex, since galaxies are no longer conserved quantities (Kauffmann et al. 1999b). Comparing their observations to model predictions Daddi et al. (2001) find that such a scenario best explains the clustering evolution of massive ellipticals out to $z \sim 1$.

Radio surveys can make an important contribution to this study: the use of magnitude-limited surveys for finding high redshift objects is usually a cumbersome task, while any flux density limited sample of radio sources contains objects at redshifts of $z \sim 0 - 5$ (Dunlop & Peacock 1990). Powerful extra-galactic radio sources, or AGN in general, result from the fuelling of a supermassive blackhole (e.g. Rees 1984, 1990), and there is evidence that the host galaxies of these high-redshift AGN are associated with some of the most massive structures in the early Universe (e.g. McCarthy 1988; Crawford & Fabian 1996; Röttgering et al. 1996; Best et al. 1998; Pentericci et al. 1999; Venemans et al. 2002). Moreover, because powerful AGN were far more numerous at $z \sim 1 - 2$ than today, radio surveys can be used to probe a population of massive galaxies in the epoch of galaxy formation.

Despite initial concerns that any cosmological clustering of radio sources may be undetectable due to the relatively broad redshift distribution washing out the signal (e.g. Webster & Pearson 1977; Griffith 1993), Kooiman et al. (1995) detected strong clustering of bright radio sources in the 4.85 GHz 87GB survey. Cress et al. (1996) made a thorough analysis of clustering at the mJy-level. Using the 1.4 GHz FIRST survey (see also Magliocchetti et al. 1998) they obtained the first high-significance measurement of clustering from a deep radio sample, allowing them to investigate the separate contributions of both AGN and starburst galaxies (but see Wilman et al. 2003). Further results on the statistics of radio source clustering have been presented by Loan et al. (1997) and Rengelink (1998), who based their analysis on the 4.85 GHz Parkes-MIT-NRAO survey and the 325 MHz WENNS survey, respectively. In high-resolution surveys such as FIRST, large radio sources can become resolved in several components, thereby spuriously contributing to the cosmological clustering signal. Cress et al. (1996) and Magliocchetti et al. (1998) outlined the basic steps involved in separating the signal due to this effect from the true cosmological clustering, although the angular size distribution of radio sources at the mJy level is still largely unconstrained.

Since the individual redshifts of the radio sources are generally not known, one usually only measures the two-dimensional clustering by means of the angular two-point correlation function (ACF), $w(\theta)$. However, the *redshift distribution* of the survey can be used to constrain r_0. Using this so-called Limber inversion technique (Limber 1953; Rubin 1954; Phillipps et al. 1978; Peebles 1980), radio sources from the above surveys are typically found to have $r_0 \approx 5 - 15\ h^{-1}$ Mpc. Rengelink (1998) and Rengelink & Röttgering (1999) pointed out that this broad range in r_0 measured can be explained by a scenario in which powerful radio sources have a larger r_0 than less powerful radio sources. This

would be highly consistent with the mounting evidence that powerful radio galaxies are the high-redshift progenitors of local cD-galaxies residing in massive environments that are hence strongly clustered. Here, we will further explore the hypothesis of Rengelink et al. by investigating the clustering of radio sources in a number of flux-limited subsamples taken from the 1.4 GHz NRAO VLA Sky Survey (see also Blake & Wall 2002a,b), the largest existing 1.4 GHz survey to date, containing $\sim 1.8 \times 10^6$ radio sources down to a flux density limit of ~ 2.5 mJy at $45''$ (FWHM) resolution (Condon et al. 1998). We also present new results on clustering using the latest release of the FIRST survey, carefully taking into account the contribution of multiple-component radio sources, which we found to be severely underestimated in earlier analyses.

The outline of this article is as follows: in Sect. 2 we describe our methods for measuring the ACF. In Sect. 3 we describe the NVSS and FIRST radio surveys, and in Sect. 4 we present measurements of the angular clustering of the sources in these surveys and construct a simple model of the angular size distribution of radio sources. We derive an estimate of r_0 as a function of flux density limit in Sect. 5. In Sect. 6 we compare our results with the results found for other populations of galaxies taken from literature, and discuss how the combined measurements relate to current theories on galaxy formation and evolution. The main conclusions are summarized in Sect. 7.

2.2 The angular correlation function

The galaxy angular two-point correlation function, $w(\theta)$, is defined as the excess probability, over that expected for a Poissonian distribution, of finding a galaxy at an angular distance θ from a given other galaxy (e.g. Peebles 1980):

$$\delta P = n[1 + w(\theta)]\delta\Omega, \tag{2.1}$$

where δP is the probability, n is the mean surface density and $\delta\Omega$ a surface area element. The ACF of a given sample of objects can be estimated as follows. For each object, determine the angular distances to all other objects, then count the number of objects in each angular distance interval, denoted by $DD(\theta)$. As we want to calculate the *excess* probability of finding a galaxy at a certain distance from another galaxy due to clustering, we compare the observed distribution, $DD(\theta)$, with the expected distribution of distances, $RR(\theta)$, calculated from large artificial catalogues of randomly placed sources. We note that several variants of $w(\theta)$-estimators exist in literature, of which the methods proposed by Hamilton (1993) and that of Landy & Szalay (1993) (see Blake & Wall 2002b, for application of this estimator to NVSS) are generally considered to be the most robust. We follow Rengelink (1998) and Wilman et al. (2003) and use the Hamilton estimator

$$w(\theta) = \frac{4n_D n_R}{(n_D - 1)(n_R - 1)} \frac{DD(\theta) \cdot RR(\theta)}{DR(\theta) \cdot DR(\theta)} - 1, \tag{2.2}$$

where n_D and n_R are the number of sources in the data and random catalogues, respectively, and the numerical factor $4n_D n_R/(n_D - 1)(n_R - 1)$ normalizes the pair counts. This estimator additionally makes use of the cross-correlation between data and random catalogues, $DR(\theta)$, to minimize effects due to large-scale fluctuations in the mean galaxy density. We estimate $w(\theta)$ by averaging over the $w(\theta)$ computed using 16 different random catalogues, each containing the same number of sources as the data catalogue to minimize the errors in $DR(\theta)$ and $RR(\theta)$ (a similar result can be obtained by constructing a single random catalogue that vastly exceeds the size of the data catalogue). Poissonian errors on the binned values of $w(\theta)$ are estimated by $\delta w(\theta) = \sqrt{[1 + w(\theta)]/DD(\theta)}$. Alternatively, errors can be computed using the so-called bootstrap resampling method of Ling et al. (1986). In this method, the standard deviation in $w(\theta)$ found among a large number of pseudo-random resamples of the original dataset is used as a measure of the error in $w(\theta)$. However, we found that fitting a model to $w(\theta)$ (see Sect. 2.4) using (i) Poissonian errors, and (ii) bootstrap errors gives results that are consistent

within the errors of the fitted parameters. Therefore, given the unprecedented volumes of the radio surveys we use the first method instead of the relatively expensive bootstrap technique.

2.3 Survey descriptions and data selection

2.3.1 The NRAO VLA Sky Survey

The NRAO VLA Sky Survey (NVSS) is the largest radio survey that currently exists at 1.4 GHz. It was constructed between 1993 and 1998 (Condon et al. 1998), and covers ~ 10.3 sr of the sky north of $\delta = -40^\circ$ ($\sim 82\%$ of the sky). Fig. 2.1 indicates the coverage of the NVSS. With a limiting flux density of ~ 2.5 mJy ($5\sigma_{rms}$) and an angular resolution of $45''$ (FWHM), the NVSS contains about 1.8×10^6 sources, and is considered to be 99% complete at a flux density limit of 3.4 mJy (Condon et al. 1998). The NVSS is based on 217,446 snapshot observations (of mostly 23 seconds) using the VLA in D- and DnC-configuration. These snapshots were then combined to produce a set of $4^\circ \times 4^\circ$ datacubes containing Stokes I, Q, and U images. A source catalogue was extracted by fitting the images with multiple elliptical Gaussians. Since the angular resolution of the NVSS ($\theta \approx 45''$ FWHM) is well above the median angular size of extragalactic radio sources ($\theta \sim 10''$), most sources in the catalogue are unresolved ($\gtrsim 95\%$ for $3 < S_{1.4} < 10$ mJy). The main NVSS data products have been made publicly available for the use of the astronomical community, and can be obtained from the NRAO website[1].

2.3.2 NVSS data selection

To optimize our catalogue for measuring the true cosmological clustering of radio sources, we have carried out a detailed examination of the NVSS source catalogue to identify and correct regions that may spuriously contribute to $w(\theta)$:

(i) The edge of the survey just a few arcminutes south of $\delta = -40^\circ$ follows an irregular pattern with right ascension. We select the region $\delta \geq -40^\circ$ to ensure that the boundary of the survey is straight.

(ii) The survey area is known to contain six hexagonal gaps due to missing snapshot observations that we masked from the catalogue by excluding rectangular regions of $2^\circ \times 2^\circ$ fully covering each gap. The regions are listed in Table 2.1.

(iii) We constructed a map of the NVSS source density as a function of position on the sky by applying an equal-area projection to the catalogue and plotting filled contours of the number of objects in $1^\circ \times 1^\circ$ non-overlapping cells covering the survey area. This map is shown in Fig. 2.1. The scaling of the greyscale was chosen so that underdense regions of 2σ below the mean density are black, and overdense regions of 2σ above the mean are white. Radio emission from the region of the galactic plane, as evidenced by a continuous chain of large white areas in Fig. 2.1, is dominated by the large population of galactic radio sources that consists mostly of supernova remnants and H II regions. In Fig. 2.4 we plot the rms-noise level as a function of galactic latitude, where the rms-noise level in each latitude bin is the average of the locally determined rms-noise values listed for every source entry in the NVSS catalogue. The rms-noise level is found to peak at $b = 0^\circ$ due to the overcrowding of galactic sources, but falls off to a relatively constant level of ~ 0.48 mJy beam^{-1} for $|b| \gtrsim 10^\circ$. We decided to exclude the region of the galactic plane that is bounded by $|b| = 10^\circ$, which was chosen so that the large overdense regions in Fig. 2.1 are all fully masked and the rms-noise is at a relatively constant level.

(iv) Further inspection of Fig. 2.1 reveals that some regions are associated with a significant increase in the local source density. From contour maps of these areas it was found that bright and/or extended sources are sometimes accompanied by significant numbers of spurious sources due to a side-effect of the fitting algorithm used to extract the sources, and, in some cases, due to side-lobe contamination. From the

[1] http://www.cv.nrao.edu/nvss/

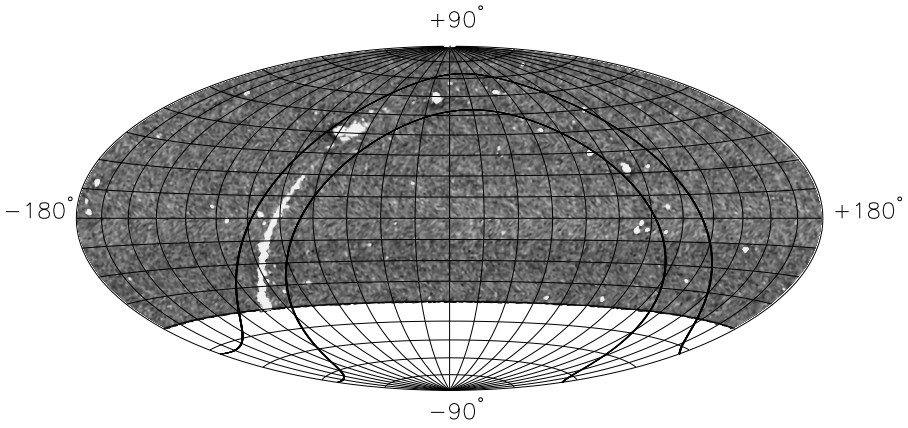

Figure 2.1 — Aitoff map of the NVSS source density. Scales run from 2σ below (black) to 2σ above the mean source density (white). The region of the galactic plane with $|b| < 10°$ is indicated by solid lines. Besides the expected enhancement of the source density due to the large population of galactic radio sources, the NVSS catalogue suffers from large numbers of spurious sources around bright or extended sources (white regions), as well as an overall decrease in the source density below $\delta = -10°$ (see the greyscale change at $\delta = -10°$). See text and Table 2.1 for details.

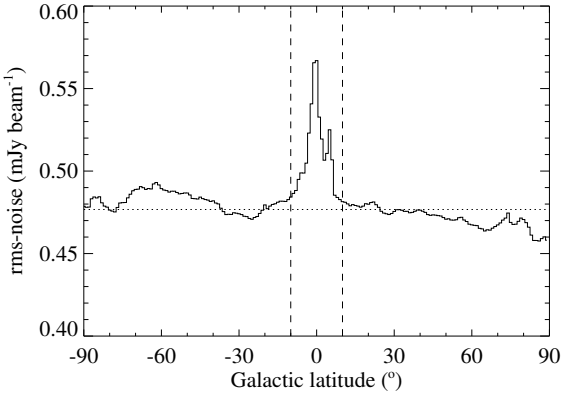

Figure 2.4 — The rms-noise level as a function of galactic latitude. The average rms-noise level of the survey is ~ 0.48 mJy beam^{-1}. Dotted lines enclose the region $|b| < 10°$.

catalogue we excluded rectangular regions of mostly $1° \times 1°$ in size centered on each of these sources (larger regions of up to $2° \times 2°$ were required in some cases). The excluded regions are listed in Table 2.1. No regions of $\geq 2\sigma$ underdensities were found.

(v) Most of the NVSS observations were conducted using the VLA in D-configuration, but the regions $\delta \leq -10°$ and $\delta \geq +78°$ were observed using the hybrid DnC-configuration to counterbalance projection effects which result from foreshortening of the north-south *uv*-coverage range. Fig. 2.2 shows the NVSS source density as a function of declination for various flux-limited sub-samples. Below the flux density limit of 10 mJy, the use of the DnC-configuration has caused a significant decrease in sensitivity leading to a drop in the source density of $\gtrsim 10$ percent (see also Fig. 2.1). As this will inevitably cause spurious signal in the ACF, we selected only the regions observed in D-configuration for measuring $w(\theta)$ below flux density limits of 10 mJy.

Table 2.2 lists the final regions and the number of sources in them for various flux density limited subsamples.

2.3.3 The FIRST Survey

The Faint Images of the Radio Sky at Twenty centimeters (FIRST) survey (Becker et al. 1995) is another 1.4 GHz VLA survey, which was started in 1993 and is still under construction. Using the VLA in B-configuration it will ultimately cover $\sim 10,000$ square degrees of the northern Galactic cap, matching the survey area of the Sloan Digital Sky Survey. Given the large coverage

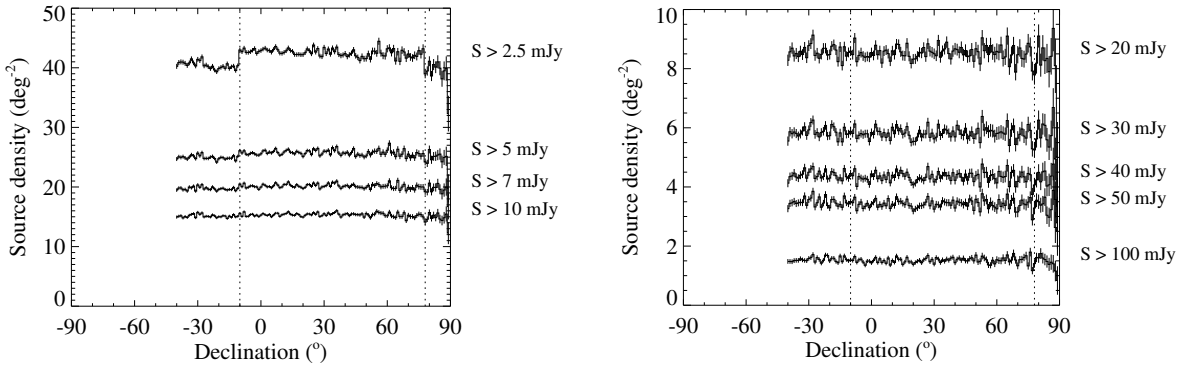

Figure 2.2 — The NVSS source density as a function of declination for various flux-limited sub-samples. Below ~ 10 mJy beam^{-1} the source density is non-uniform due to changes in the configuration of the VLA at $\delta = -10^\circ$ and $\delta = +78^\circ$ (dotted lines).

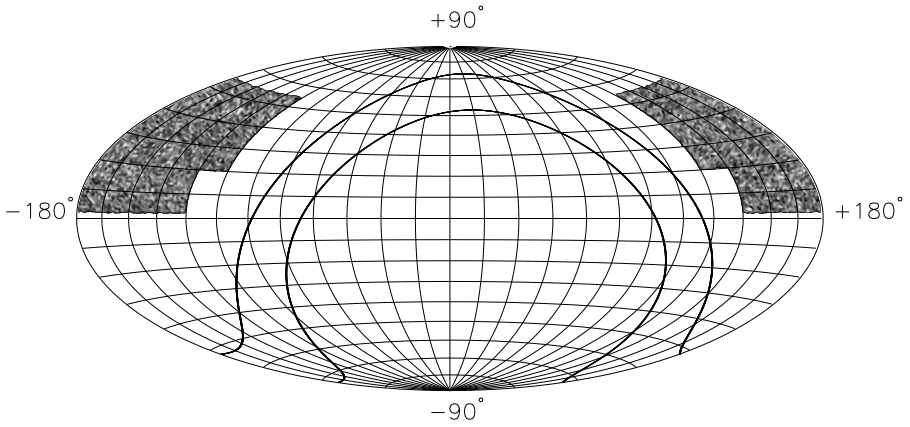

Figure 2.3 — Aitoff map of the FIRST source density. Scales run from 2σ below (black) to 2σ above (white) the mean source density. The region of the galactic plane with $|b| < 10^\circ$ is indicated by solid lines.

of FIRST, its sensitivity is unprecedented: with a limiting flux density of ~ 1 mJy ($5\sigma_{rms}$) and an angular resolution of $5\farcs4$ (FWHM) the catalogue contains about 100 sources per square degree with a completeness level of $\sim 95\%$ at 2 mJy (Becker et al. 1995).

We have obtained the publicly available 2001 October 15 version of the source catalogue[2], which has been derived from the 1993 through 2001 observations, and covers about 8,565 square degrees of the sky. About 4% of the 771,076 sources in the catalogue are flagged as possible side-lobes, which we exclude from the catalogue. We set the lower flux density limit of the catalogue to 3 mJy, the limiting flux density of the NVSS survey. Finally, we select the regions $+2^\circ \leq \delta \leq +20^\circ$ and $9^h \leq \alpha \leq 16^h$, $+20^\circ \leq \delta \leq +55^\circ$ and $8^h \leq \alpha \leq 17^h$ from the catalogue, by requiring a relatively uniform source density and a simple geometric form. This area covers $\sim 5,538$ square degrees and contains 188,885 sources. As for the NVSS, we construct a map of the FIRST surface density (Fig. 2.3), and plot the source density as a function of declination (Fig. 2.5). For the selected region we found no suspicious features in the catalogue. The number of sources in various FIRST subsamples are listed

[2]http://sundog.stsci.edu/

Table 2.1 — Regions of the NVSS catalogue that were masked because of missing snapshot observations and overdense regions associated with bright or extended sources. Overdense regions at $|b| < 10^\circ$ are not listed here since we excluded this area from the catalogue as a whole.

RA (J2000)	DEC (J2000)	Remark
$15^h38^m00^s - 15^h43^m00^s$	$-05^\circ00'00'' - -06^\circ00'00''$	Missing snapshot
$09^h54^m00^s - 10^h00^m00^s$	$-11^\circ45'00'' - -12^\circ45'00''$	Missing snapshot
$09^h54^m00^s - 10^h00^m00^s$	$-25^\circ00'00'' - -26^\circ00'00''$	Missing snapshot
$04^h25^m00^s - 04^h30^m00^s$	$-37^\circ45'00'' - -38^\circ45'00''$	Missing snapshot
$18^h17^m00^s - 18^h22^m00^s$	$-16^\circ00'00'' - -17^\circ00'00''$	Missing snapshot
$18^h02^m00^s - 18^h07^m00^s$	$-23^\circ30'00'' - -24^\circ30'00''$	Missing snapshot
$01^h34^m00^s - 01^h42^m00^s$	$+32^\circ30'00'' - +33^\circ50'00''$	3C 48
$03^h16^m48^s - 03^h21^m48^s$	$+40^\circ00'42'' - +43^\circ00'42''$	Perseus A
$03^h17^m00^s - 03^h27^m00^s$	$-36^\circ20'00'' - -38^\circ20'00''$	Fornax A
$04^h35^m05^s - 04^h39^m05^s$	$+29^\circ10'12'' - +30^\circ10'12''$	3C 123
$05^h18^m00^s - 05^h26^m00^s$	$-35^\circ40'00'' - -37^\circ20'00''$	PKS 0521–36
$05^h31^m17^s - 05^h39^m17^s$	$-06^\circ23'00'' - -04^\circ23'00''$	M42
$05^h38^m00^s - 05^h46^m00^s$	$-01^\circ20'00'' - -02^\circ40'00''$	3C 147.1
$05^h40^m36^s - 05^h44^m36^s$	$+49^\circ21'07'' - +50^\circ21'07''$	3C 147
$05^h52^m00^s - 05^h56^m00^s$	$-04^\circ20'00'' - -05^\circ40'00''$	TXS 0549–051
$07^h05^m00^s - 07^h25^m00^s$	$+74^\circ20'00'' - +75^\circ20'00''$	3C 173.1
$09^h15^m05^s - 09^h21^m05^s$	$-12^\circ50'24'' - -11^\circ20'24''$	Hydra A
$12^h16^m00^s - 12^h23^m00^s$	$+05^\circ00'00'' - +06^\circ30'00''$	NGC 4261
$12^h26^m07^s - 12^h32^m07^s$	$+01^\circ18'00'' - +02^\circ48'00''$	3C 273
$12^h26^m50^s - 12^h34^m50^s$	$+11^\circ23'24'' - +13^\circ23'24''$	M87
$13^h11^m00^s - 13^h15^m00^s$	$-22^\circ30'00'' - -21^\circ30'00''$	MRC 1309–216
$13^h21^m00^s - 13^h27^m00^s$	$+31^\circ20'00'' - +32^\circ20'00''$	NGC 5127
$14^h07^m00^s - 14^h15^m00^s$	$+51^\circ40'00'' - +52^\circ40'00''$	3C 295
$16^h49^m11^s - 16^h53^m11^s$	$+04^\circ29'24'' - +05^\circ29'24''$	Hercules A
$17^h18^m00^s - 17^h24^m00^s$	$-01^\circ40'00'' - -00^\circ20'00''$	3C 353
$18^h26^m00^s - 18^h34^m00^s$	$+48^\circ00'00'' - +49^\circ40'00''$	3C 380
$19^h22^m00^s - 19^h26^m00^s$	$-28^\circ45'00'' - -29^\circ45'00''$	TXS 1921–293

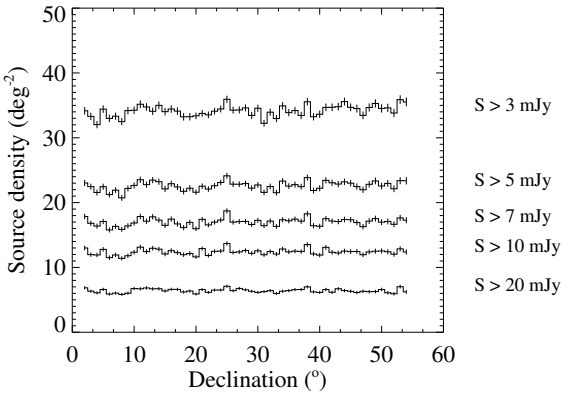

Figure 2.5 — The FIRST source density as a function of declination for various limiting flux densities.

in Table 2.2.

Table 2.2 — NVSS and FIRST subsamples.

NVSS		
S_{low}	Region	Sources
3 mJy	$+10^\circ \le b \le +45^\circ$, $-5^\circ \le \delta \le +70^\circ$	210,530
5 mJy	$\|b\| \ge 10^\circ$, $-10^\circ \le \delta \le +78^\circ$	507,608
7 mJy	$\|b\| \ge 10^\circ$, $-5^\circ \le \delta \le +70^\circ$	351,079
10 mJy	$\|b\| \ge 10^\circ$	433,951
20 mJy	$\|b\| \ge 10^\circ$	242,599
30 mJy	$\|b\| \ge 10^\circ$	165,45
40 mJy	$\|b\| \ge 10^\circ$	123,769
50 mJy	$\|b\| \ge 10^\circ$	97,753
60 mJy	$\|b\| \ge 10^\circ$	79,738
80 mJy	$\|b\| \ge 10^\circ$	56,903
100 mJy	$\|b\| \ge 10^\circ$	43,294
200 mJy	$\|b\| \ge 10^\circ$	17,015
FIRST		
3 mJy	$+2^\circ \le \delta \le +20^\circ$ and $9^h \le \alpha \le 16^h$	188,885
	$+20^\circ \le \delta \le +55^\circ$ and $8^h \le \alpha \le 17^h$	
5 mJy	" "	124,974
7 mJy	" "	94,099
10 mJy	" "	68,560

2.4 The angular clustering of radio sources

2.4.1 The ACF of $S > 10$ mJy NVSS sources

Following the procedures described in Sect. 2.2 we compute $w(\theta)$ for the $S > 10$ mJy NVSS subsample. Distances between data and/or random positions are initially measured in bins of $0'.5$, and rebinned in bins of constant logarithmic spacing to analyse the data. We fit the data using a weighted χ^2-minimization routine, and we determine the 1σ errors from the covariance matrix.

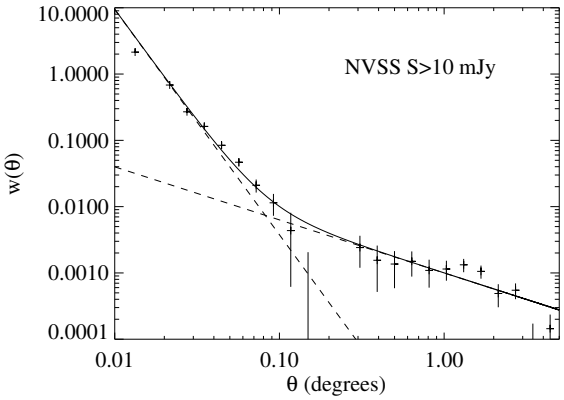

Figure 2.6 — The ACF of $S > 10$ mJy NVSS sources. The power-law fits described in the text are indicated.

The results are shown in Fig. 2.6. We find that two power-laws are needed to describe the full range of our measurements. Fitting the data

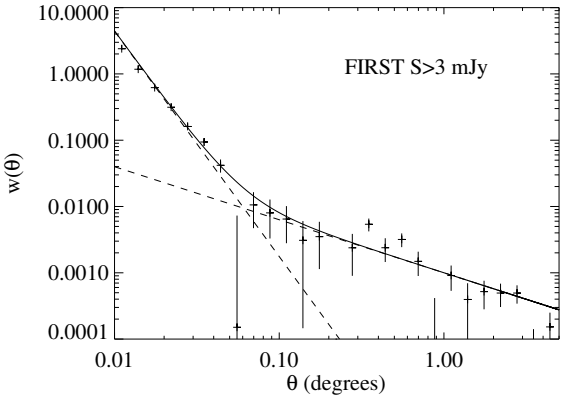

Figure 2.7 — The ACF of $S > 3$ mJy FIRST sources. The power-law fits described in the text are indicated.

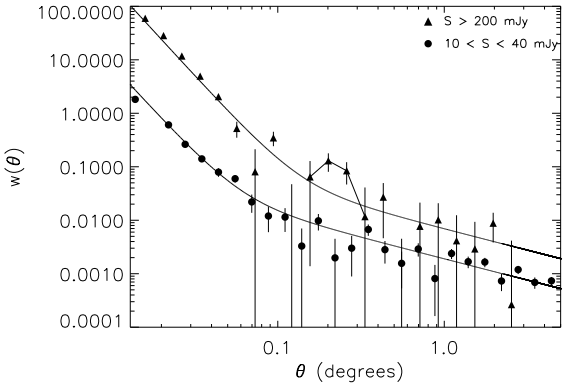

Figure 2.8 — ACFs for the flux density intervals $10 < S < 40$ mJy and $S > 200$ mJy. The power-law fits to the data described in the text are overplotted. Because of an unexplained 'bump' in the $S > 200$ mJy signal at $0.1 \lesssim \theta \lesssim 0.3$ (connected points), the small- and large-scale correlation functions were fitted separately over the ranges $\theta \leq 0.1$ and $\theta \geq 0.3$, respectively.

with a power-law ACF $w(\theta) = A\theta^{1-\gamma}$ (e.g. Peebles 1980) at angular scales of $\theta \lesssim 6'$ gives a slope of $\gamma = 4.4 \pm 0.2$, while at $\theta \gtrsim 6'$ we find a slope of $\gamma = 1.7 \pm 0.1$. The latter value is consistent with the slope of the empirical power-law of $\gamma \simeq 1.8$ found for the cosmological clustering of objects ranging from normal galaxies to clusters (see Bahcall & Soneira 1983,for a review). However, at small angular scales the power-law is much steeper, presumably caused by the enhancement of $DD(\theta)$ due to the decomposition of large radio galaxies into their separate radio components (see Sect. 2.4.2 & Sect. 2.4.4; see also Blake & Wall 2002a). If we fit the data simultaneously with a double power-law correlation function of the form $w(\theta) = B\theta^{1-\gamma_B} + A\theta^{1-\gamma_A}$ with fixed slopes of $\gamma_B = 4.4$ and $\gamma_A = 1.8$, we find amplitudes of $B = (1.5 \pm 0.2) \times 10^{-6}$ and $A = (1.0 \pm 0.2) \times 10^{-3}$. The double power-law fit is indicated in Fig. 2.6.

2.4.2 The effect of multiple component radio sources and the ACF of FIRST

Although the median angular size of radio sources is $\sim 10''$ (e.g. Condon et al. 1998), radio sources can have sizes of up to several arcminutes. At angular scales comparable to the size of these large radio galaxies, the true cosmological $w(\theta)$ can become confused or even dominated by resolving these galaxies into their various radio components, such as lobes, hot spots and cores. The angular scale at which the size distribution of radio galaxies begins to dominate $w(\theta)$ is indicated by the clear break around $6'$. Earlier studies attempted to correct $w(\theta)$ for the contribution of multi-component radio sources by means of component combining algorithms. For example, Cress et al. (1996) calculated the ACF for the FIRST survey considering all sources within $1'.2$ of each other as a single source. The analysis of the FIRST data was repeated by Magliocchetti et al. (1998), who removed double sources using an algorithm based on the $\theta \propto \sqrt{S}$ relation of Oort et al. (1987) and flux ratio statistics of the components of genuine doubles. They found values of $\gamma = 2.5 \pm 0.1$, and $A = (1.0 \pm 0.1) \times 10^{-3}$ for flux density limits between 3 and 10 mJy. Comparing their results to our measurement for the NVSS presented in Fig. 2.6, we conclude that despite the efforts of these authors it is likely that a residual contribution from large radio galaxies remained. Fitting the data over the whole range of θ with a *single* power-law explains the apparently high value of $\gamma \simeq 2.5$ reported for the clustering of FIRST radio sources.

Here, we present new measurements from the

FIRST survey. Our reasons for repeating the work of Cress et al. (1996) and Magliocchetti et al. (1998) are threefold. Firstly, the FIRST catalogue has almost doubled in size, enabling a better statistical measure of $w(\theta)$. Secondly, the clear break found in the ACF of the NVSS enabled us to isolate the signal due to true clustering from the signal due to the size distribution of radio galaxies. A similar analysis can be applied to the FIRST data. Thirdly, we found large-scale gradients in the NVSS source density below a flux density limit of 10 mJy (see Sect. 2.3.2). The FIRST data can be used to verify and complement the results from the NVSS for 3–10 mJy.

In Fig. 2.7 we present our measurements for the ACF from the $S > 3$ mJy FIRST subsample. As for the NVSS, we see a clear break in $w(\theta)$ due to the presence of multi-component radio sources. Fitting the measurements with our double power-law model yields $\gamma_B = 4.1 \pm 0.2$ and $B = (2.7 \pm 0.3) \times 10^{-6}$, and $\gamma_A = 1.9 \pm 0.2$ and $A = (1.0 \pm 0.3) \times 10^{-3}$. Note that the break in $w(\theta)$ in this sample occurs at $\theta \sim 4'$ compared to $\theta \sim 6'$ for $S > 10$ mJy in NVSS (see Fig. 2.6). Blake & Wall (2002a) show that this is due to a $1/\sigma$ dependency (σ being the surface density of radio sources) of the amplitude of $w(\theta)$ at small angular scales, simply because the weight of pair-counts due to large radio galaxies increases as the surface density decreases (see their equation 4).

We conclude that the cosmological $w(\theta)$ of $S > 10$ mJy NVSS sources and $S > 3$ mJy FIRST sources, as determined by our analysis, are consistent with having the canonical clustering power-law slope of $\gamma \simeq 1.8$, and an amplitude of $A \simeq 1 \times 10^{-3}$.

2.4.3 $w(\theta)$ as a function of flux density limit

To investigate angular clustering as a function of flux density limit, we calculate $w(\theta)$ for all NVSS and FIRST subsamples listed in Table 2.2. We obtain the amplitudes of $w(\theta)$ by fitting the data with the double power-law model $w(\theta) = B\theta^{1-\gamma_B} + A\theta^{1-\gamma_A}$, fixing the slopes at $\gamma_B = 4.4$ and $\gamma_A = 1.8$. However, because the signal for the $S > 200$ mJy subsample is affected by a 'bump' at $\theta \sim 0.^\circ2$ (see Fig. 2.8), we obtained the amplitudes for this subsample by fitting the small- and large-scale correlation functions separately with power-laws $w(\theta) = B\theta^{-3.4}$ for $\theta \leq 0.^\circ1$ and $w(\theta) = A\theta^{-0.8}$ for $\theta \geq 0.^\circ3$, respectively. The measured amplitudes and their 1σ errors are listed in Table 2.3. The values of both B and A are found to increase with increasing flux density limit of the subsamples. The increase in B can be explained by the $1/\sigma$-dependency of the small-scale correlation function that is dominated by double or multiple component radio sources (see Sect. 2.4.2). From this point onward, we will be only concerned with the amplitude A that is believed to be dominated by the true cosmological clustering. In Fig. 2.9 we have plotted the amplitude of the cosmological $w(\theta)$ as a function of flux density limit. For comparison, we have indicated the results from the 325 MHz WENSS and 4850 MHz GB6 surveys (Rengelink 1998; Rengelink & Röttgering 1999) by extrapolating to 1.4 GHz using a power law spectrum, $S_\nu \propto \nu^{-\alpha}$, with spectral index $\alpha = 0.8$. Between 3 and 40 mJy the amplitude is approximately constant within the errors and has an (unweighted) average of $\sim 1.2 \times 10^{-3}$. From $50 - 100$ mJy the amplitude is $\sim 2\times$ higher, and

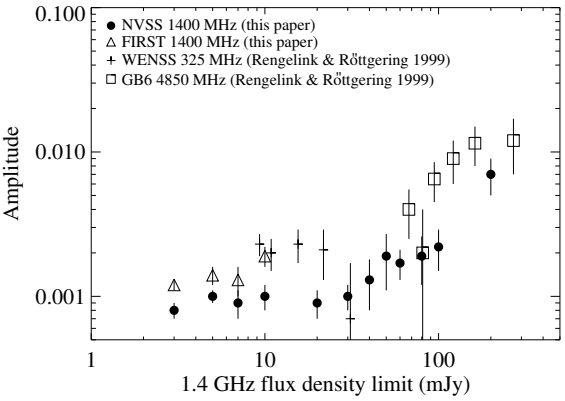

Figure 2.9 — The amplitude of the cosmological ACF ($\gamma = 1.8$) of NVSS and FIRST as a function of 1.4 GHz flux density limit. For comparison, we have indicated the results for the WENSS and GB6 surveys from Rengelink (1998) and Rengelink & Röttgering (1999).

Table 2.3 — Amplitudes and 1σ errors of the double power-law correlation function $w(\theta) = B\theta^{-3.4} + A\theta^{0.8}$ as a function of flux density limit.

S_{lim}	NVSS		FIRST	
	$10^6 \times B$	$10^3 \times A$	$10^6 \times B$	$10^3 \times A$
3 mJy	0.7 ± 0.1	0.8 ± 0.1	0.7 ± 0.1	1.2 ± 0.1
5 mJy	1.0 ± 0.1	1.0 ± 0.1	1.0 ± 0.1	1.4 ± 0.2
7 mJy	1.2 ± 0.1	0.9 ± 0.2	1.2 ± 0.1	1.3 ± 0.3
10 mJy	1.5 ± 0.1	1.0 ± 0.2	1.4 ± 0.1	1.9 ± 0.3
20 mJy	2.6 ± 0.2	0.9 ± 0.2	–	
30 mJy	4.1 ± 0.1	1.0 ± 0.2	–	
40 mJy	4.4 ± 0.1	1.3 ± 0.5	–	
50 mJy	8.3 ± 0.2	1.9 ± 0.8	–	
60 mJy	6.8 ± 3.0	1.7 ± 0.4	–	
80 mJy	8.4 ± 0.2	1.9 ± 0.7	–	
100 mJy	19 ± 1	2.2 ± 0.7	–	
200 mJy	30 ± 1	6.6 ± 1.8	–	

it has increased by another factor of $\sim 2-3$ at 200 mJy. These measurements indicate a trend of increasing clustering amplitude with increasing flux density limit. However, one has to keep in mind that the sources in the brighter subsamples are also included in the subsamples with lower limiting flux densities. Therefore, we also compute $w(\theta)$ for sources that lie in the flux *interval* $10 < S < 40$ mJy. The results are shown in Fig. 2.8 together with $w(\theta)$ found for $S > 200$ mJy. The amplitude $A = (6.6 \pm 1.8) \times 10^{-3}$ that we measure for $S > 200$ mJy is significantly higher than the amplitudes measured at lower flux densities. This is consistent with Rengelink (1998) and Rengelink & Röttgering (1999) who found $A = (11.5 \pm 3.5) \times 10^{-3}$ for $S_{1.4} \geq 160$ mJy in the GB6 survey and Loan et al. (1997) who estimated that A has a value between 0.005 and 0.015 for $S_{1.4} > 100 - 270$ mJy from the combined 87GB and PMN surveys (Fig. 2.9).

We would like to make the following remarks: (i) Rengelink (1998) and Rengelink & Röttgering (1999) measured $w(\theta)$ from WENSS and GB6 by excluding the first $5'$ and $10'$, respectively. We have used our routines to measure $w(\theta)$ for their catalogues as well (not shown here). The amplitudes and slopes we find are consistent with their values, and we find no evidence for a contribution of multi-component sources at the smallest angular scales allowed by these surveys.
(ii) Below 10 mJy the amplitudes for the NVSS and FIRST data are consistent with $A \simeq 1.1 \times 10^{-3}$. However, at 10 mJy the amplitude is $\sim 2\times$ higher for FIRST than for the NVSS. This is curious since the NVSS and FIRST surveys probe radio sources at exactly the same frequency. Blake & Wall (2002b) give a very nice demonstration (see their Fig. 3) of the most probable cause. The resolution of FIRST is ten times higher than that of NVSS, and therefore the average flux density of a single NVSS source is only equal to the *sum* of all its possibly resolved components in FIRST. Sources that appear in NVSS with integrated fluxes just above a given flux density limit can thus be missed in FIRST. Therefore, we consider NVSS to be more optimal than FIRST for measuring the clustering of extra-galactic radio sources. Furthermore, if we compute $w(\theta)$ for only those NVSS sources that lie in the region covered by FIRST, we find an amplitude of $A = (1.7 \pm 0.3) \times 10^{-3}$. This is consistent with the results found for the 10 mJy FIRST sample, suggesting that cosmic variance of clustering may be an additional factor contributing to the difference in amplitudes measured for the total NVSS area and FIRST. Future work might show that the region covered by FIRST is especially rich in large-scale structures.
(iii) In the 200 mJy subsample we find an unexpected increase in the correlation signal at $\theta \approx 0.^\circ 2$ (indicated by the connected points in Fig. 2.8). We investigate two possibilities. *(1) Sidelobes*: Cress et al. (1996) found a bump in $w(0.^\circ 1)$ for $S > 3$ mJy sources in FIRST, and found that it was caused by sidelobe contamination. However, if sidelobes are responsible for boosting the correlation function at $\theta \sim 0.^\circ 2$ in the $S > 200$ mJy NVSS sample, these sidelobes themselves also must have minimum peak fluxes of 200 mJy. It is highly unlikely that such bright sidelobes have found their way into the NVSS catalogue, without being masked in Sect. 2.3.2. Also, we have visually inspected the contour maps of several tens of source pairs ($S > 500$ mJy) that contribute to $w(\theta)$ at $\theta \sim 0.^\circ 2$. In all cases the pairs consisted of unresolved peaks

without signs of diffuse, extended emission or side-lobe contamination. *(2) Radio galaxies with large angular sizes*: the position of the bump near the break in $w(\theta)$ suggests that it may somehow be related to the size distribution. Conveniently, Lara et al. (2001) have constructed a sample of 84 large angular size ($\theta \geq 4'$) radio galaxies from the NVSS at $\delta \geq +60^\circ$ and a total integrated flux density of ≥ 100 mJy. Candidates were pre-selected by visual inspection of the NVSS maps, and confirmed or rejected following observations at higher resolution. If the bump is caused by $\sim 12'$-sized radio galaxies, then given the 2-Mpc linear size cutoff of large radio galaxies (see Schoenmakers et al. 2001), these galaxies must lie at $z \lesssim 0.1$. It is unlikely that such a large, relatively nearby source with, among other emission, two radio components each with a peak flux of ≥ 200 mJy would have been missed by their selection criteria. Lara et al. (2001) determined angular sizes by either measuring the maximum distance between 3σ contours, or by the distance between peaks at the source extremes. Also, sizes were measured along the 'spine' of a source if significant curvature was present. To investigate how many of these sources could actually contribute to $w(\theta)$ at $\sim 12'$ we redetermine the angular sizes of the sources of Lara et al. (2001). We find that none of these sources consists of ≥ 2 components of ≥ 200 mJy of $\sim 12'$ separation. On the other hand, if we extrapolate the clustering power-law derived at larger scales to $\theta = 0.^\circ 2$ we find that the bump translates into $\sim 10\times$ the number of pairs expected. Even allowing for the much larger area of NVSS, the possibility that the bump is caused by large radio galaxies as in the sample of Lara et al. (2001) is therefore unlikely.

Unfortunately, the exact origin of this feature remains unclear. We realize, however, that this bump is situated at a crucial angular scale for our measurements. Therefore, we have obtained the amplitudes B and A by fitting $w(\theta)$ on both sides of the bump with a single power-law. Under the condition that the effect that causes the bump is not responsible for enhancing $w(\theta)$ at $\theta \gtrsim 0.^\circ 3$, this will enable us to derive an estimate for the amplitude for the cosmological clustering. At $\theta \gtrsim 0.^\circ 3$ $w(\theta)$ is consistent with the classical $\gamma = 1.8$ power-law clustering model.

2.4.4 Modelling the angular size distribution of radio galaxies

2.4.4.1 The model

The steepening of the slope of $w(\theta)$ at small angular scales is presumably related to multi-component sources spuriously enhancing the true clustering pair counts at small θ. To demonstrate the reality of this assumption, we create a simple model for the angular size distribution of radio galaxies in the NVSS, that is able to account for this extra signal contributing to $w(\theta)$. We model the physical size distribution of sources in our $S > 10$ mJy NVSS sample, and use their redshift distribution to obtain the angular size distribution. Because we know the angular resolution of the NVSS, this model can then be used to estimate the fraction of sources likely to be resolved. It is essential to separate sources that are resolved into a single, elongated object from sources that are resolved into a number of components, since only the latter would produce extra pair counts. Here, we assume that the majority of surplus pair counts arise from resolving the two edge-brightened radio lobes of FRII-type radio galaxies (see Fanaroff & Riley 1974), and we estimate that the fraction of FRIIs at 10 mJy is $\sim 40\%$ from Wall & Jackson (1997) (assuming a spectral index of $\alpha = 0.8$ to extrapolate to 1.4 GHz).

Several groups have investigated the median physical sizes of FRII radio galaxies as a function of redshift and radio luminosity by parameterizing the linear size as $D \propto (1+z)^{-n} P^m$, where P is the radio luminosity (for a review see Blundell et al. 1999). Results using different samples of radio galaxies vary from no size evolution at all (e.g. Nilsson et al. 1993), to size evolution depending only on redshift (e.g. Kapahi et al. 1987), and size evolution depending on both redshift and luminosity with contradictory results (e.g. Oort et al. 1987; Barthel

& Miley 1988; Singal 1993). We use the results of Neeser et al. (1995) who found the following linear size–redshift relation from a spectroscopically complete sample of FRII radio galaxies:

$$D \propto (1+z)^{-1.7\pm0.5} \quad (\text{for } \Omega_M = 1 \text{ and } \Omega_\Lambda = 0), \tag{2.3}$$

and remark that no intrinsic correlation was found between D and P ($P^m \simeq 1$ with $m = 0.06 \pm 0.09$). This observed linear-size evolution may be related to evolution of the confining intergalactic medium, or to evolution of the radio galaxy itself, but the exact underlying physical mechanism is unknown (see Neeser et al. 1995).

For the purpose of our model, we place simulated sources in small redshift intervals ($\Delta z = 0.01$) in the range $0 \leq z \leq 5$, and assume that their mean physical size evolves with redshift according to equation 2.3. We set the total number of input sources equal to the estimated number of $S > 10$ mJy FRIIs in our NVSS sample ($\sim 40\% of 434,000$), and calculate the number of sources in each redshift interval from the redshift distribution, $N(z)$, using the formalism of Dunlop & Peacock (1990) (see Sect. 2.5 for details). We then assume that in each redshift interval sizes are normally distributed. We take a mean size of 500 kpc and a standard deviation of 250 kpc at $z \simeq 0$, chosen so that the resulting physical size distribution roughly resembles the distribution of projected linear sizes versus redshift as it is given by Blundell et al. (1999) for three complete samples of FRII radio galaxies from the 3C, 6C, and 7C radio surveys. The resulting physical size distribution is shown in Fig. 2.10, where we plot filled contours of the source density in the linear size-redshift plane to illustrate the underlying redshift distribution. We have also indicated the minimum physical size that is theoretically required for a source to become resolved as a function of redshift, given by the NVSS resolution of $45''$ (FWHM). We would like to remark at this point that the distribution of sizes in our model beyond redshifts of $z \sim 3$ should not be taken too seriously as it is based on a straight extrapolation from measurements made at redshifts $0 \lesssim z \lesssim 2$, and does not take into account the fact that at these high redshifts most sources will be extremely young and are thus likely to be very small. However, as can be seen from Fig. 2.10, our modeled size distribution falls below the NVSS resolution already at $z \sim 1$. Taking smaller sizes at higher redshifts will have no effect on the modeled size distribution of resolved sources that we want to derive here.

Assuming $\Omega_M = 1$ we calculate the angular size distribution associated with our model. We construct 10 such models, and average them to get our final model of the angular size distribution of the sample. This model is presented in Fig. 2.11. Although the mean angular size is $\sim 10''$ in agreement with Condon et al. (1998), sizes are found to extend up to several arcminutes beyond the resolution of the NVSS (indicated by the dotted line).

2.4.4.2 Results

We now compare the number of surplus pairs expected from resolved FRII sources in the model, $DD_{mod}(\theta)$, to the actually measured pair counts at angular scales of $\theta \lesssim 6'$. At these scales, the measured pair counts consist of both pair counts due to clustering and pair counts due to doubles, so

$$DD_{tot}(\theta) = DD_{gal}(\theta) + DD_{dbl}(\theta). \tag{2.4}$$

To extract $DD_{dbl}(\theta)$ from the total counts, $DD_{tot}(\theta)$, we calculate $DD_{gal}(\theta)$ by assuming that the galaxy ACF as measured above the break in $w(\theta)$ can be extrapolated to angular scales of $\theta \lesssim 6'$:

$$w_{gal}(\theta) = 1.0 \times 10^{-3}\theta^{-0.8} = DD_{gal}(\theta) \cdot F(\theta) - 1, \tag{2.5}$$

where $F(\theta) = 4 \cdot RR(\theta)/[DR(\theta)]^2$, the part of the Hamilton estimator that is relatively independent of the presence of doubles. Since we now know both $DD_{tot}(\theta)$ and $DD_{gal}(\theta)$, we can subtract them to get a measure of the counts arising from the double sources: $DD_{dbl}(\theta)$. The final step is to rebin the modeled number of pair

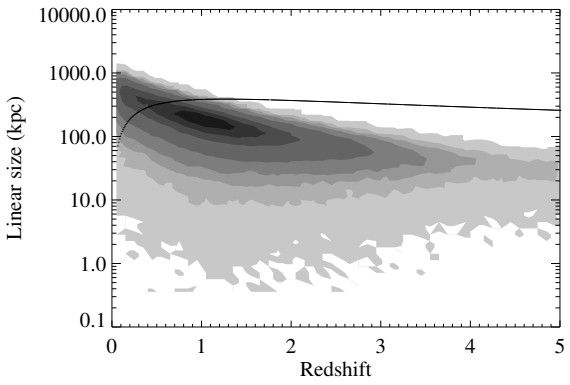

Figure 2.10 — The modeled physical size distribution of $S > 10$ mJy FRII radio galaxies in the NVSS catalogue. The source density in the linear size-redshift plane is indicated by contours to illustrate the underlying redshift distribution (darker greyscales indicate higher densities). Sources lying above the line can, in principle, be resolved given the angular resolution of the NVSS of $45''$(FWHM).

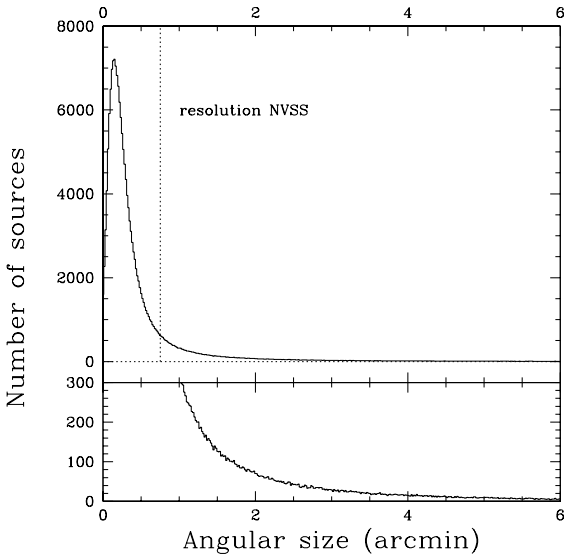

Figure 2.11 — The angular size distribution for FRII radio galaxies in the NVSS calculated from the modeled physical size distribution (assuming $\Omega_M = 1$). The number of input sources was chosen to match the predicted number of FRIIs in the $S > 10$ mJy subsample. The binsize is $1''$.

separations $DD_{mod}(\theta)$ in order to match the binning scheme of $DD_{dbl}(\theta)$. Fig. 2.12 shows the ratio of the observed doubles to the modeled doubles per distance interval. The errors in the observed counts are estimated from the 1σ-error in the amplitude of $w(\theta)$. The errors in the modeled pair counts are estimated by allowing a 10% error in the estimated fraction of FRIIs in the NVSS. We conclude that: *a model in which the small-scale ACF steepens due to resolving FRII radio galaxies into two distinct knots of radio emission is in good agreement with the measurements presented in Fig. 2.6.*

Several remarks that can be made are the following:
(i) The size distribution of radio sources at the mJy level is still largely unconstrained. Recently, however, Lara et al. (2001) presented a new sample of large radio galaxies (LRGs) selected from the NVSS. In the region $\delta \geq +60^\circ$ they found $\sim$80 radio galaxies with apparent angular sizes larger than $4'$ and total flux density greater than 100 mJy. If we roughly extrapolate our model to their sensitivity and correct for the area we successfully predict the number of FRIIs in the range $4' \lesssim \theta \lesssim 6'$. However, in this interval one third of the sample of Lara et al. (2001) consists of FRIs, while the model only uses FRIIs to estimate the number of surplus pairs expected. The model could be refined by decreasing the fraction of resolved FRIIs to also allow a contribution from large FRIs.
(ii) The model allows objects to be either single or double sources, although visual inspection of NVSS contour maps shows that sources are sometimes split into three or even more components. Therefore, we may expect an extra amount of spurious pair counts on top of the counts due to classical double radio sources. This may become increasingly important with increasing flux density limit.
(iii) The model predicts a fraction of resolved sources in NVSS of $\sim$0.07, in rough agreement with the value of $\sim$0.05 predicted by Condon et al. (1998).

The simple model allows us to explore the general relations between the physical size distribution of radio galaxies and $w(\theta)$ at small angular scales. Although our crude method is successful in reproducing the observations, it relies

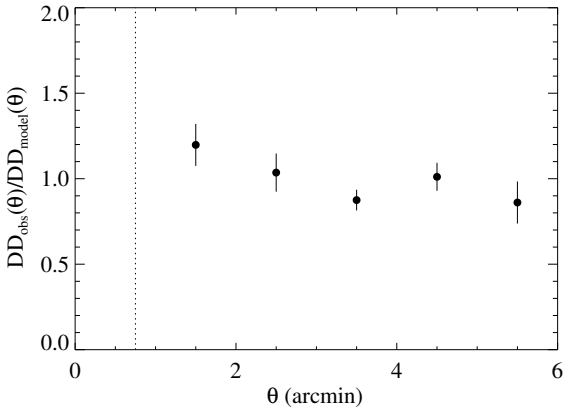

Figure 2.12 — The ratio of observed doubles to modeled doubles per distance interval. The angular resolution of the NVSS is indicated by the dotted line.

on a number of assumptions that are not easily verified from the data currently in literature. Radio sources come in a wide variety of sizes ranging from < 1 kpc for the class of gigahertz peaked spectrum sources (GPS), to 1–20 kpc for the compact steep spectrum sources (CSS), > 20 kpc for FRI- and FRII-type radio galaxies, and > 1 Mpc for giant radio galaxies (Fanti et al. 1990; O'Dea et al. 1991; Blundell et al. 1999; Schoenmakers et al. 2001). Evidently, the distribution of linear sizes of radio sources are very complex, and will remain an important subject for future studies. As we have shown, the ACF can be used to put constraints on the size distribution of large radio galaxies. However, perhaps more ideal would be to make a statistical redshift sample of *all* radio source pairs within some angular distance interval, and then take high resolution radio observations to constrain the numbers of intrinsic doubles in that sample.

2.5 The spatial clustering of NVSS sources

2.5.1 The redshift distribution

At the mJy level and higher it is standard practice to compute redshift distributions using the Dunlop & Peacock (1990) radio luminosity functions (RLFs). These authors have constructed a range of model luminosity functions using spectroscopically complete samples from several radio surveys at different frequencies. Using a free-form modelling approach they found a number of smooth functions that were consistent with the data. In addition, they attempted two models of a more physical nature by assuming pure luminosity evolution (PLE) and luminosity/density evolution (LDE) to describe the RLF. The total ensemble is expected to agree well at those luminosities and frequencies at which they are best constrained by the data, while uncertainties in the extrapolation of each of these models to those regions that are less constrained by the data may be reduced by taking the ensemble as a whole. We compute redshift distributions, $N(z)$, for each flux-limited subsample using the free-form models $1-4$ and the PLE/LDE models for the combined population of flat ($\alpha = 0$, $S_\nu \propto \nu^\alpha$) and steep ($\alpha = -0.8$) spectrum radio sources given by Dunlop & Peacock (1990,taking the MEAN-z data from their appendix C) from

$$\begin{aligned} \frac{dN(z)}{dz} &= \frac{dV(z)}{dz} \times \int_{P_{low}(z)}^{\infty} \Phi_i(P,z) dP, \qquad (2.6) \\ P_{low}(z) &= x(z)^2 \left(\frac{S}{(1+z)^{1-\alpha}} \right) \left(\frac{2.7\ GHz}{\nu} \right)^{\alpha}, \end{aligned}$$

where $V(z)$ is the comoving volume, $\Phi_i(P,z)$ is the model RLF, $x(z)$ the comoving distance, S the limiting flux density of the subsample, and ν the frequency of FIRST/NVSS. We note that $N(z)$ is independent of cosmology as long as the calculations are carried out in the cosmology used to construct the RLFs (i.e. $\Omega_M = 1.0$ and $H_0 = 50$ km s^{-1} Mpc^{-1}).

Figs. 2.13 and 2.14 show the redshift distributions for $S > 10$ mJy and $S > 100$ mJy, respectively. We calculate the average of the six different models (indicated by the solid curve), which will be our best estimate of $N(z)$ use in the analysis below (the same method was used for the $N(z)$ applied to the model of the angular size distribution described in Sect. 2.4.4). It is important to keep in mind that the functional form of $N(z)$ remains virtually unchanged from $3-200$ mJy. Over this range in flux densities

the RLFs represent a broad redshift distribution with a peak around $z \sim 1$, indicating the very large median redshift that is generally probed by radio surveys.

2.5.2 The spatial correlation function

Given the amplitudes of $w(\theta)$ determined in Sect. 2.4 we can use the cosmological Limber equation to estimate the spatial correlation length, r_0, by deprojecting $w(\theta)$ into the spatial correlation function, $\xi(r)$ using the redshift distribution and cosmology (e.g. Peebles 1980, §56). We consider two cosmological models: a flat, vacuum dominated, low-density Universe (ΛCDM; $\Omega_M = 0.3$, $\Omega_\Lambda = 0.7$), and an Einstein-de Sitter model Universe (τCDM; $\Omega_M = 1.0$, $\Omega_\Lambda = 0$). We use $H_0 = 100h$ km s^{-1} Mpc^{-1}.

We assume an epoch dependent power-law spatial correlation function of the form

$$\xi(r_p, z) = \left(\frac{r_p}{r_0}\right)^{-\gamma} (1+z)^{-(3+\epsilon)}, \qquad (2.7)$$

where r_p is the proper distance, r_0 is the spatial correlation length[3] at $z = 0$, and ϵ parameterizes the redshift evolution of the clustering. To express $\xi(r_p, z)$ in terms of comoving coordinates $r_c = r_p \times (1+z)$, we write:

$$\xi(r_c, z) = \left(\frac{r_c}{r_0}\right)^{-\gamma} (1+z)^{\gamma-(3+\epsilon)}, \qquad (2.8)$$

which can be written as

$$\xi(r_c, z) = \left(\frac{r_c}{r_0(z)}\right)^{-\gamma}, \; r_0(z) = r_0(1+z)^{1-\frac{3+\epsilon}{\gamma}}, \qquad (2.9)$$

where $r_0(z)$ is the (comoving) correlation length measured at z. In a flat model Universe, the cosmological Limber equation can be expressed as

[3]Note that the spatial correlation length is *not* a physical lengthscale in the space distribution of galaxies. It is just defined as that length at which $\xi(r)$ is unity (i.e. the chance of finding a galaxy at the distance r_0 from another galaxy is twice the Poissonian chance).

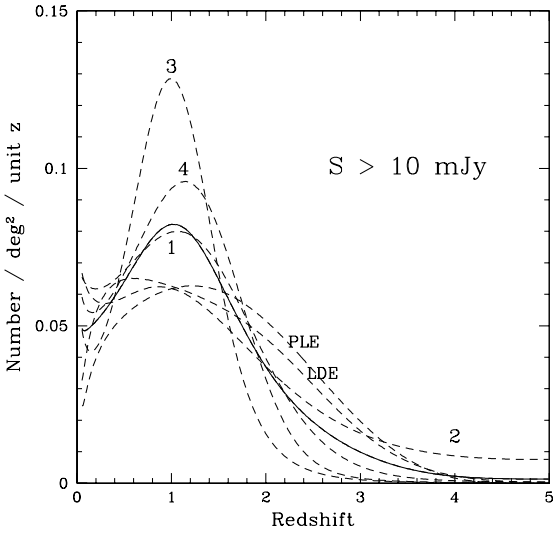

Figure 2.13 — Dashed lines show the redshift distributions for $S_{1.4} > 10$ mJy, computed from the free-form models $1-4$, the pure luminosity evolution model (*PLE*) and the luminosity/density evolution model (*LDE*) of Dunlop & Peacock (1990) (see text for details). The average of the six different models is indicated by the solid curve.

follows (see e.g. Peebles 1980):

$$\begin{aligned} w(\theta) &= A\theta^{1-\gamma} \qquad (2.10)\\ &= \sqrt{\Omega_M}\left(\frac{r_0 H_0}{c}\right)^{\gamma} \theta^{1-\gamma} H_\gamma \\ &\quad \times \frac{\int_0^\infty dz\, N(z)^2 (1+z)^{\gamma-3-\epsilon} x^{1-\gamma} Q(z)}{\left[\int_0^\infty dz\, N(z)\right]^2}, \end{aligned}$$

with

$$\begin{aligned} Q(z) &= \left[(1+z)^3 + \Omega_M^{-1} - 1\right]^{0.5}, \qquad (2.11)\\ x(z) &= \frac{1}{\sqrt{\Omega_M}} \int_0^z \frac{dz}{Q(z)}, \\ H_\gamma &= \Gamma\left(\frac{1}{2}\right)\Gamma\left(\frac{\gamma-1}{2}\right)\Gamma\left(\frac{\gamma}{2}\right)^{-1}, \end{aligned}$$

and using the approximation that angles are small ($\theta \ll 1$). We calculate $N(z)$ for each subsample.

The evolution parameter ϵ can represent a variety of clustering models. Three important cases are the following (see Phillipps et al. 1978; Kundić 1997). *(1) The stable clustering model* ($\epsilon =$

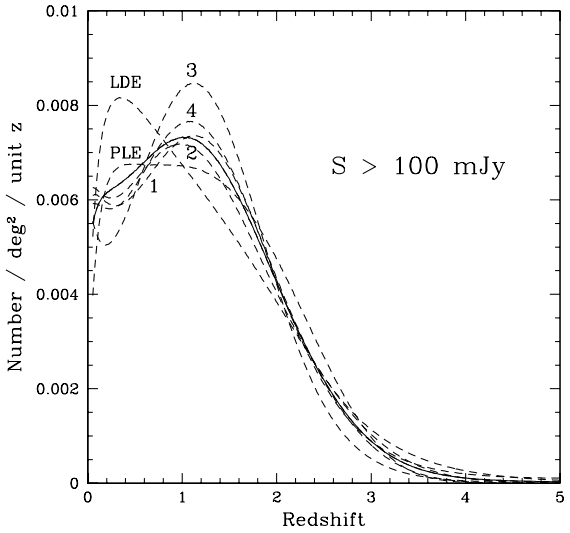

Figure 2.14 — The redshift distributions for $S_{1.4} > 100$ mJy. See the caption of Fig. 2.13 for details.

0): if galaxy clustering is gravitationally bound at small scales, then clusters have fixed physical sizes (i.e. they will neither contract nor expand) and will have a correlation function that decreases with redshift as $(1+z)^{-1.2}$. *(2) The comoving clustering model* ($\epsilon = \gamma - 3$): galaxies and clusters expand with the Universe, so their correlation function remains unchanged in comoving coordinates. This case applies well to a low density Universe where there is not enough gravitational pull to counterbalance expansion, and implies that structures have formed very early. *(3) The linear growth model* ($\epsilon = \gamma - 1$): clustering grows as expected under linear perturbation theory.

Studies of the spatial clustering properties of radio-quiet quasars indicate that the clustering history of active galaxies, unlike that of normal galaxies, is best characterized using a *negative* value for ϵ. Kundić (1997) measured the high-redshift quasar-quasar correlation function from the Palomar Transit Grism Survey, and found no evidence for a decrease in the correlation amplitude of quasars with redshift. Moreover, he found that $\xi_{qq}(z > 2)/\xi_{qq}(z < 2) \simeq 1.8$, suggesting an even higher amplitude at higher redshifts. Similarly, Croom et al. (2001) find almost no evolution in clustering strength for quasars taken from the 2dF QSO Redshift Survey out to $z \simeq 2.5$. Therefore, we opt for evolution model 2 (i.e. constant clustering in comoving coordinates), which implies $\epsilon = -1.2$ for $\gamma = 1.8$. In table 2.4 we list the results obtained using this model for the two different cosmological models. For comparison, we also indicate the results using the stable clustering model ($\epsilon = 0$). For $\epsilon = 0$ the present-day correlation length is ~ 1.4 times higher than for $\epsilon = -1.2$ in both cosmologies. However, given the strong peak in the redshift distribution at $z \sim 1$, we are effectively measuring clustering at $z \sim 1$. Calculating $r_0(z \sim 1)$ in the case of stable clustering using Eq. 2.9 yields a value that is only ~ 1.1 times lower than $r_0(z \sim 1) = r_0$ in the case of $\epsilon = -1.2$. Therefore, the value of $r_0(z \sim 1)$ is relatively independent of the exact value of ϵ. The results for the $\epsilon = -1.2$ (ΛCDM) case are presented in Fig. 2.15. We find an approximately constant spatial correlation length of $\simeq 6.0\ h^{-1}$ Mpc from 3–40 mJy, compared to $\simeq 14\ h^{-1}$ Mpc at 200 mJy.

As we have shown, the possibility that the observed flux-dependency of the clustering is just an effect of projection can be ruled out, since the shape of the redshift distribution is relatively constant with flux over several orders of magnitude (at least above ~ 1 mJy). This automatically implies that the average radio power of the subsamples increases with flux density (indicated by the top axis of Fig. 2.15). An alternative explanation was therefore suggested by Rengelink (1998) and Rengelink & Röttgering (1999) based on their measurements of the clustering of radio sources in the WENSS and GB6 surveys. They concluded that the clustering signal could change as a function of flux density if relatively low and high power radio galaxies represent different spatial structures at a similar epoch ($z \sim 1$). Taking the predicted population mix of radio sources from Wall & Jackson (1997), we find that for $S_{1.4} > 10$ mJy the fractions of FRIs and FRIIs are about equal. However, for $S_{1.4} > 100$ mJy the fraction of FRIIs is more than

Table 2.4 — Present-day spatial correlation lengths and 1σ errors derived from the galaxy ACF ($\gamma = 1.8$) of the NVSS as a function of flux density limit. Listed are the results found using two different cosmological models and two different values for the evolution parameter ϵ (see text for details).

	$\epsilon = -1.2$		$\epsilon = 0$	
S_{low}	τCDM	ΛCDM	τCDM	ΛCDM
	r_0 (h^{-1} Mpc)	r_0 (h^{-1} Mpc)	r_0 (h^{-1} Mpc)	r_0 (h^{-1} Mpc)
3 mJy	3.2 ± 0.2	4.5 ± 0.3	4.8 ± 0.3	6.3 ± 0.5
5 mJy	3.7 ± 0.2	5.2 ± 0.3	5.6 ± 0.3	7.5 ± 0.4
7 mJy	3.5 ± 0.5	4.9 ± 0.6	5.3 ± 0.7	7.2 ± 0.9
10 mJy	3.7 ± 0.4	5.3 ± 0.6	5.7 ± 0.7	7.8 ± 0.9
20 mJy	3.5 ± 0.4	5.0 ± 0.6	5.5 ± 0.7	7.5 ± 1.0
30 mJy	3.7 ± 0.4	5.3 ± 0.6	5.8 ± 0.7	7.9 ± 0.9
40 mJy	4.3 ± 1.0	6.1 ± 1.4	6.7 ± 1.6	9.1 ± 2.2
50 mJy	5.3 ± 1.4	7.5 ± 2.0	8.2 ± 2.2	11.2 ± 2.9
60 mJy	5.0 ± 0.7	7.0 ± 1.0	7.7 ± 1.1	10.4 ± 1.4
80 mJy	5.3 ± 1.2	7.4 ± 1.7	8.1 ± 1.8	10.9 ± 2.5
100 mJy	5.7 ± 1.1	8.0 ± 1.5	8.7 ± 1.7	11.6 ± 2.2
200 mJy	10.6 ± 1.8	14 ± 3.0	15.4 ± 2.6	19.8 ± 3.4

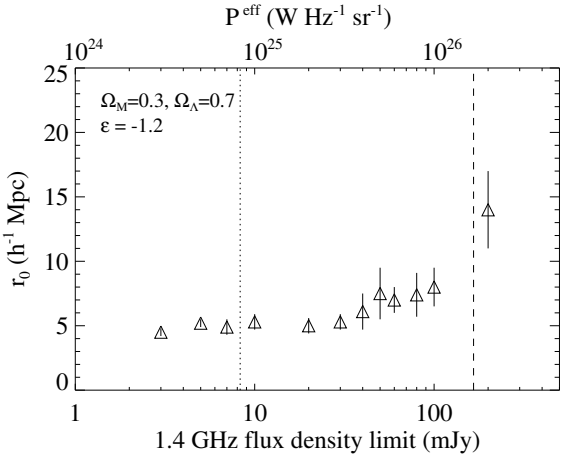

Figure 2.15 — Spatial correlation lengths and 1σ errors derived from the cosmological $w(\theta)$ of the NVSS, assuming an evolution parameter $\epsilon = -1.2$, and the ΛCDM model Universe. The dotted line indicates the flux density limit at which FRI- and FRII-type radio sources contribute roughly equally to 1.4 GHz radio source counts. The dashed line indicates the flux density limit above which the contribution of FRIIs is $\gtrsim 75\%$. The top axis indicates the effective radio luminosity as a function of flux density limit.

$\sim 75\%$. Given the fractional changes of the source populations with flux density limit, the clustering amplitudes measured are very well matched by a scenario in which *the clustering of powerful radio sources (mostly FRII) and average power radio sources (FRI/FRII) are intrinsically different, with FRIIs being more strongly clustered at $z \sim 1$ than the radio galaxy population on average.*

As pointed out by Rengelink (1998) and Rengelink & Röttgering (1999) the large difference in observing frequencies and sensitivities of WENSS and GB6 (the limiting 1.4 GHz flux densities probed by these surveys correspond to 10 mJy for WENSS and 70 mJy for Greenbank, respectively) only allowed them to make a comparison between the results, whereas the detection of the inferred flux-dependency of r_0 within a *single* survey would be highly desirable. Our analysis of the clustering in the single large-area, intermediate-frequency NVSS survey is in agreement with their conclusions.

2.6 Discussion

2.6.1 Clustering measurements from literature

We start this section by making a survey of other clustering measurements from literature.

However, readers may wish to skip directly to Sect. 2.6.2 for a discussion on these measurements and the results presented in this paper in their cosmological context.

In order to compare results from different studies, all values taken from literature were converted assuming a fixed slope $\gamma = 1.8$ by setting $r_{0,1.8} = (r_{0,\gamma})^{\gamma/1.8}$. All correlation lengths are expressed in comoving units, and we have transformed all values to a ΛCDM cosmology (see Magliocchetti et al. 2000). Please note that the list given below is not complete, and the reader is kindly invited to consult the individual papers and the references therein for further information.

2.6.1.1 *Clusters*

Estimates of the correlation length of rich Abell clusters are given by Bahcall & Soneira (1983) and Postman et al. (1992) who found $r_0 = 24 \pm 9$ h^{-1} Mpc. Lahav et al. (1989) found $r_0 = 21 \pm 7$ h^{-1} Mpc from an all-sky sample of the brightest X-ray clusters, and Dalton et al. (1994) and Croft et al. (1997) found $r_0 = 19 \pm 5\, h^{-1}$ Mpc and $r_0 = 16 \pm 4\, h^{-1}$ Mpc, respectively, for clusters selected from the APM Galaxy Survey. Recently, Gonzalez et al. (2002) measured the correlation length of distant clusters in the Las Campanas Distant Cluster Survey and found a correlation length of $24.8 \pm 4.5\, h^{-1}$ Mpc at $\bar{z} = 0.42$.

Different studies may have sampled clusters of different degrees of richness, which can account for most of the scatter in the reported values. In general, however, all results are consistent with clusters being the most strongly clustered objects known in the Universe.

2.6.1.2 *Optically-selected ordinary galaxies and IRAS galaxies*

Bright early-type galaxies are found to have a strongly clustered distribution in the local Universe. Willmer et al. (1998) find $r_0 = 6.8 \pm 0.4$ h^{-1} Mpc for local $L \gtrsim L_*$ ellipticals, and Guzzo et al. (1997) measure a considerably higher $r_0 = 11.4 \pm 1.3\, h^{-1}$ Mpc for a sample of similar galaxies. Although these results are only consistent with each other at the 3σ level, the latter sample contains a higher fraction of local clusters, presumably responsible for boosting the r_0. The dependence of galaxy clustering on luminosity and spectral type has been studied using the ongoing 2 degree Field Galaxy Redshift Survey (2dFGRS). Norberg et al. (2002) find $r_0 = 11.8 \pm 1.6$ h^{-1} Mpc for the brightest early-type galaxies in the 2dFGRS. Moreover, they find a strong dependence of clustering strength on luminosity, with the amplitude increasing by a factor of ~ 2.5 between L_* and $4L_*$. The ordinary population of galaxies has been found to be less strongly clustered than the population consisting of local (bright) ellipticals: Loveday et al. (1995) find $r_0 = 4.7 \pm 0.2$ h^{-1} Mpc from the APM survey. At higher redshifts, the clustering strength in a sample of faint K-selected galaxies with minimum rest-frame luminosities of $M_K = -23.5$, or about $0.5L_*$, is found to be fairly rapidly declining with redshift: Carlberg et al. (1997) find $r_0 = 3.3 \pm 0.1$ h^{-1} Mpc, $r_0 = 2.3 \pm 0.2$ h^{-1} Mpc, $r_0 = 1.6 \pm 0.2$ h^{-1} Mpc, and $r_0 = 1.2 \pm 0.2$ h^{-1} Mpc, at $\bar{z} = 0.34$, $\bar{z} = 0.62$, $\bar{z} = 0.97$, and $\bar{z} = 1.39$, respectively. Carlberg et al. (2000) present measurements on a sample of $L \sim L_*$ galaxies up to $z \approx 0.6$ and find a much milder decline from $r_0 = 5.1 \pm 0.1$ h^{-1} Mpc at $\bar{z} = 0.10$ to $r_0 = 4.2 \pm 0.4\, h^{-1}$ Mpc at $\bar{z} = 0.59$.

Clustering of the local population of IRAS-selected galaxies is best fit by $r_0 = 3.4 \pm 0.2\, h^{-1}$ Mpc (Fisher et al. 1994).

2.6.1.3 *Extremely red objects (EROs)*

Several recent studies indicate that the comoving correlation length of early-type galaxies undergoes little or no evolution from $0 \lesssim z \lesssim 1$. Evidence for this is provided by the clustering of extremely red objects, a population of galaxies having very red optical to infrared colors ($R - K_s > 5$). These red colors are consistent with them being either old, passively evolving elliptical galaxies, or strongly dust-enshrouded starburst galaxies at $z \sim 1 - 1.5$. Indeed, further observations have confirmed that both classes are present in the ERO population (e.g. Dunlop et al. 1996; Cimatti et al. 1998; Dey et al. 1999; Liu

et al. 2000). Daddi et al. (2001) have recently embarked on a study of the spatial clustering of a large sample of $L \gtrsim L_*$ EROs at $z \sim 1$, and found a large correlation length of $r_0 = 12 \pm 3\,h^{-1}$ Mpc. In Cimatti et al. (2002) the results are presented involving the EROs that were identified in a large flux limited redshift survey of ~ 500 galaxies with $K \leq 20$. The derived fraction of early-type EROs from that sample is $50 \pm 20\%$, while there is an increasing contribution of dusty star-forming EROs at faint magnitudes. Therefore, Daddi et al. (2002) have attempted to analyse separately the spatial clustering of EROs from both categories by studying the frequency of close pairs. They find that the comoving correlation length of the dust-enshrouded starbursts is constrained to be less than $r_0 = 2.5\,h^{-1}$ Mpc, while the old EROs are clustered with $5.5 \lesssim r_0 \lesssim 16\,h^{-1}$ Mpc. This is consistent with the value reported earlier in Daddi et al. (2001), which is still valid as a lower limit for the clustering of early-type EROs based on the argument that the much less clustered dusty star-forming EROs only dilute the clustering signal coming from the ellipticals in this sample (see also Roche et al. 2002). Furthermore, McCarthy et al. (2001) have identified a large sample of such faint red galaxies as being consistent with mildly evolved early-type galaxies at $z \sim 1.2$. They find a clustering strength of $r_0 = 9.5 \pm 1\,h^{-1}$ Mpc.

2.6.1.4 *Radio galaxies*

The results on the spatial clustering of radio sources at $z \sim 1$ presented in this paper indicate that r_0 depends on radio luminosity in such a way that very luminous (FRII) radio galaxies cluster more strongly than the total population of radio galaxies (both FRI and FRII) on average, reminiscent of a similar luminosity trend found for samples of optically-selected galaxies. We roughly construct two radio luminosity bins from our measurements by comparing the r_0 found for 3–40 mJy to the r_0 found for the 200 mJy subsample. We find $r_0 \simeq 6 \pm 1\ h^{-1}$ Mpc^{-1} for the relatively low power bin ($P_{1.4} \sim 10^{24-25}$ W Hz^{-1} sr^{-1}), and $r_0 \simeq 14 \pm 3\,h^{-1}$ Mpc^{-1} for the high power bin ($P > 10^{26}$ W Hz^{-1} sr^{-1}).

2.6.1.5 *Optically-selected quasars*

Croom et al. (2001) have determined the correlation length of quasars (QSOs) using 10,558 quasars taken from the 2dF QSO Redshift Survey. They find that QSO clustering appears to vary little with redshift, with $r_0 = 4.9 \pm 0.8$ h^{-1} Mpc at $\overline{z} = 0.69$, $r_0 = 2.9 \pm 0.8\ h^{-1}$ Mpc at $\overline{z} = 1.16$, $r_0 = 4.2 \pm 0.7\,h^{-1}$ Mpc at $\overline{z} = 1.53$, $r_0 = 5.3 \pm 0.9\,h^{-1}$ Mpc at $\overline{z} = 1.89$, and $r_0 = 5.8 \pm 1.2$ h^{-1} Mpc at $\overline{z} = 2.36$.

2.6.1.6 *Lyman-break galaxies*

Lyman-break galaxies (LBGs) are found to be associated with star-forming galaxies at $z \sim 3$, with comoving correlation lengths of $r_0 = 3.3 \pm 0.3\ h^{-1}$ Mpc (Adelberger 2000), and $r_0 = 3.6 \pm 1.2\,h^{-1}$ Mpc (Porciani & Giavalisco 2002). Ouchi et al. (2001) find $r_0 = 2.7 \pm 0.6\ h^{-1}$ Mpc for a sample of LBGs at $z \sim 4$.

2.6.2 Clustering evolution

2.6.2.1 *The clustering of massive ellipticals at $z \sim 1$*

In Fig. 2.16 we present an overview of the evolution of galaxy clustering, as it follows from the broad variety of observational results summarized above. The r_0 that we measure for the brightest radio sources at $z \sim 1$ is comparable to the r_0 measured for bright ellipticals locally, and $\sim 2\times$ higher than the r_0 measured for relatively faint radio sources and quasars, suggesting that they are considerably more biased and probably probe spatial structures associated with strongly clustered, massive objects. This does not come totally unexpectedly, as there is a range of observational evidence in support of this result. Best et al. (1998) found that powerful 3CR radio galaxies are mostly associated with massive galaxies at $z \sim 1$, and at high ($z \sim 1$) and very high ($z \gtrsim 2$) redshifts the most luminous (i.e. FRII-type) radio sources are found in very dense environments associated with forming clusters. This is based on for example the presence of large X-ray halos (Crawford & Fabian 1996), excesses of companion galaxies (McCarthy 1988; Röttgering et al. 1996;

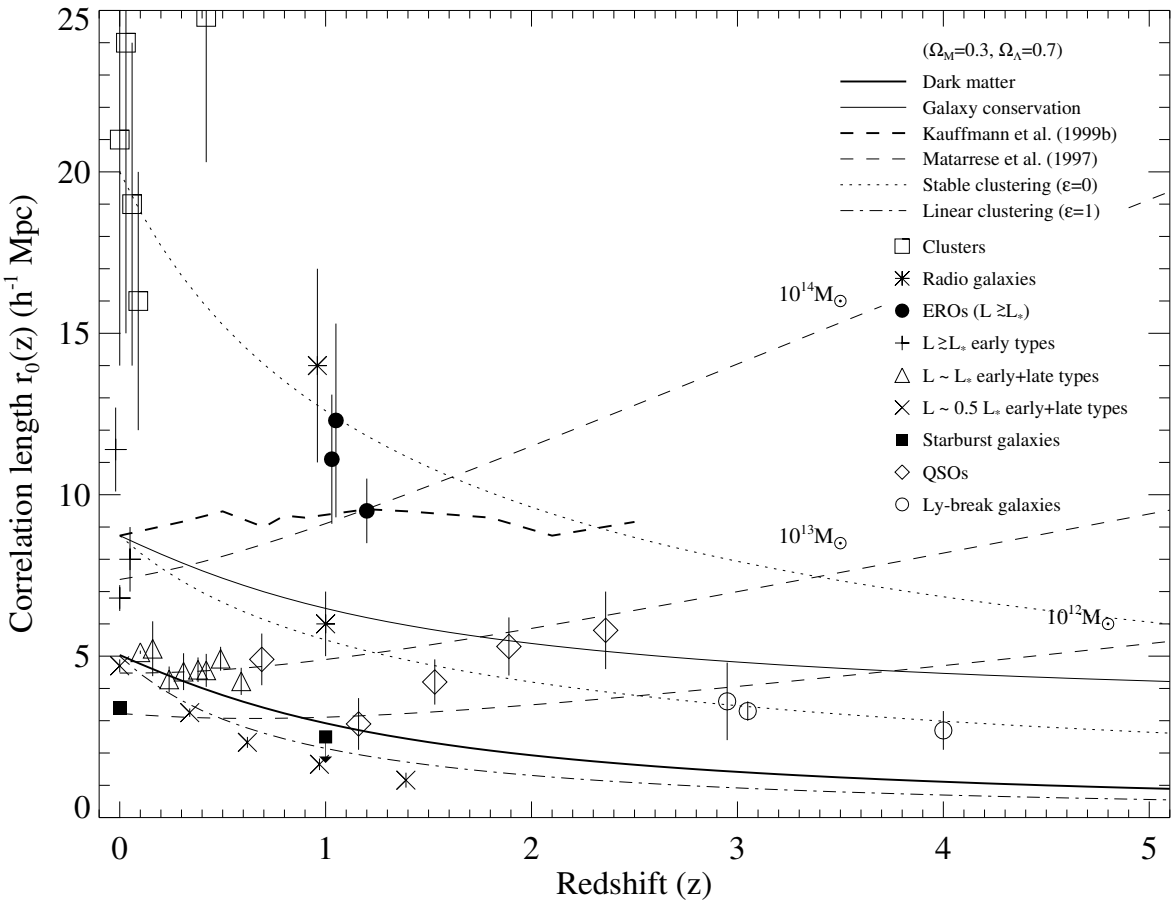

Figure 2.16 — The redshift evolution of galaxy clustering in a ΛCDM Universe. See the text for references to data taken from literature. Lines represent the following models: (i) stable clustering ($\epsilon = 0$) normalized to r_0 of local ellipticals and clusters (*dotted lines*), (ii) linear clustering ($\epsilon = 1$) normalized to $5\,h^{-1}$ Mpc (*dot-dashed line*), (iii) clustering of the dark matter (*thick solid line*, from Jenkins et al. (1998), see also Moustakas & Somerville (2002) for a useful parameterization), (iv) galaxy conservation model normalized to r_0 of local ellipticals (*thin solid line*, see Fry (1996)), (v) hierarchical model for clustering evolution of early-type galaxies normalized to r_0 of local ellipticals (*thick dashed line*, from Kauffmann et al. (1999b)), and (vi) clustering evolution as a function of dark matter halo masses with $\mathcal{M}_{min} = 10^{12-14} M_\odot$ (*thin dashed lines*, from Matarrese et al. (1997)). A nice representation of this figure showing actual images of the various objects rather than symbols can be found at our website: http://www.strw.leidenuniv.nl/~overzier/r0.html.

Nakata et al. 2001), and excesses of Lyα emitters around powerful radio sources (Kurk et al. 2000; Venemans et al. 2002). Furthermore, most very high redshift radio galaxies ($z > 2$) are surrounded by giant halos of emission line gas (e.g. Röttgering et al. 1999; De Breuck et al. 2000), and some have very clumpy morphologies suggestive of massive forming systems (e.g. Pentericci et al. 1999, 2000a). Using HST/NICMOS observations, Pentericci et al. (2001) have found a number of radio galaxies at $z \sim 2$ having morphologies that are represented well by a de Vaucouleurs profile, consistent with them being elliptical galaxies or proto-galaxy bulges.

As argued by Best et al. (1999), powerful radio sources must rely on (i) a plentiful supply of gas to fuel a supermassive blackhole that can drive the AGN activity, and (ii) a dense

surrounding medium able to contain the radio lobes. These environments are indeed expected to be found in the gas-rich galaxy clusters at high redshift, additionally supporting the conclusion that high redshift FRIIs are associated with strongly clustered, massive objects. One may argue that this conclusion somewhat contradicts the fact that low redshift FRIIs are primarily found to be situated in small, isolated galaxy groups, and not in the centers of large clusters (Butcher & Oemler 1978; Hill & Lilly 1991). This, however, can easily be explained by considering that the local analogs of the gas-rich cluster environments that are suitable for producing powerful FRIIs at high redshifts, are found in relatively small galaxy groups, and not in the gas-depleted centers of local rich clusters (Rengelink 1998).

Interestingly, we find that both EROs and powerful radio galaxies are strongly clustered with $r_0 \gtrsim 10\ h^{-1}$ Mpc at $z \sim 1$. Willott et al. (2001) suggested that high-redshift radio galaxies and EROs could be identical galaxies seen at different stages of their evolution, based on their findings of ERO-like host galaxies for a number of radio galaxies from the 7C Redshift Survey. This, of course, would be highly consistent with the belief that both radio galaxies and EROs may be the progenitors of local bright ellipticals. They conclude that the density of radio sources with minimum radio luminosities of $\log_{10} P_{151} = 24$ W Hz^{-1} sr^{-1} is consistent with a model in which all EROs go through a relatively short period of AGN activity, forming a radio galaxy somewhere between $z = 2$ and $z = 1$.

However, if *all* EROs are radio galaxies at some stage, their highly clustered spatial distribution should be reflected in the spatial distribution of the radio galaxies. Fig. 2.16 shows that the clustering of EROs and radio galaxies is consistent only for those galaxies with radio luminosities of $\log_{10} P_{1400} \gtrsim 26$ W Hz^{-1} sr^{-1}. The surface density of such radio sources in the redshift range $1 < z < 2$ in the NVSS is $\sim 2 \times 10^{-4}$ arcmin^{-2}, while the surface density of EROs having $K_s \leq 19$ and $R - K_s > 5$ is ~ 0.5 arcmin^{-2} (Daddi et al. 2001). If we take the fraction of old ellipticals among EROs to be $\sim 70\%$ (Cimatti et al. 2002), then only $\sim 0.06\%$ of these EROs are currently observed in their radio-loud phase. However, because the typically assumed AGN lifetimes are short compared to the cosmological time-scale from $z = 2$ and $z = 1$ ($t_{z=2-1} \simeq 3.5$ Gyr for $\Omega_M = 0.3$, $\Omega_\Lambda = 0.7$), the number of EROs that could undergo a radio-loud phase is $\sim 2 - 20\%$ (assuming $t_{AGN} \simeq 10^{7-8}$ yr.). These fractions can be increased significantly if, for example, we select EROs that are much redder: the density of EROs having $R - K_s > 6$ is a factor of ~ 10 lower compared to $R - K_s > 5$ (Daddi et al. 2001), giving $\sim 14 - 140\%$. It may be clear from the above that the unification of EROs and radio galaxies, although tempting, relies on a number of issues that have not yet been resolved. Further study of the luminosities, colors and morphologies of radio galaxy hosts, as well as the cluster environments of EROs may be expected to provide important clues for constraining this scenario.

2.6.2.2 Comparison with theoretical predictions

Linear ($\epsilon \sim 1$, dot-dashed line) or stable ($\epsilon = 0$, dotted line) clustering evolution models have been found to best fit the measurements of ordinary, optically-selected galaxies at $z \lesssim 1$ (e.g. Carlberg et al. 1997, 2000; McCracken et al. 2001,and references therein). However, as Fig. 2.16 shows, these models do not provide a good description for the evolution of massive early type galaxies as inferred from the measurements of local bright ellipticals and FRII radio galaxies and EROs at $z \sim 1$. Adjusting these models to the measurements would either require $z \sim 1$ massive ellipticals to have a correlation length around $6 - 7\ h^{-1}$ Mpc, or local bright ellipticals to have a correlation length of the order of that of local clusters, far greater than observed. For these galaxies, the current measurements require a model that predicts relatively constant clustering in comoving coordinates, i.e. a negative value of $\epsilon \approx -1$ in the simple ϵ-model.

Although the parameterization of clustering

evolution by means of the ϵ-model is useful for *characterizing* the measurements as a function of redshift, it does not provide good physical insight into evolution governed by the clustering of dark matter halos (see Giavalisco et al. 1998; McCracken et al. 2001). Galaxy clustering evolution can be described more precisely by

$$\xi_{gal}(z,r) = D^2(z)b^2(z)\xi_m(0,r), \tag{2.12}$$

where $D(z)$ is the linear cosmological growth rate (see Carroll et al. 1992), $b(z)$ the evolution of the bias, and $\xi_m(0,r)$ the correlation function of the underlying matter distribution at $z = 0$. Since $b(z)$ is related to the nature of the mechanism through which the galaxies were formed, measurements of $\xi_{gal}(z,r)$ can be used to constrain structure formation models.

In the galaxy conservation model, objects are formed by means of monolithic collapse at arbitrarily high redshift, and their clustering evolution is described solely by the cosmological growth of density perturbations (Fry 1996). In this model, bias evolves as

$$b(z) = 1 + (b_0 - 1)/D(z), \tag{2.13}$$

where $b_0 \equiv (\sigma_{8,gal}/\sigma_{8,m})$ and σ_8 is the rms fluctuation amplitude inside a sphere of 8 h^{-1} Mpc radius. Taking $r_{0,m}(0) = 5\,h^{-1}$ Mpc for the present-day correlation length of the dark matter from the GIF/VIRGO N-body simulations of Jenkins et al. (1998) (thick solid line in Fig. 2.16) and $\bar{r}_{0,gal}(0) = 8.7\ h^{-1}$ Mpc for ellipticals, we find $\sigma_{8,m} = 0.9$ and $\sigma_{8,gal} = 1.5$ corresponding to $b_0 \approx 1.65$. This model is indicated in Fig. 2.16 (thin solid line). Analogous to the above arguments against simple stable or linear clustering, extrapolating the clustering of local ellipticals to $z \sim 1$ in the galaxy conservation model does not fit the observed extreme clustering of EROs and powerful radio galaxies. On the other hand, this scenario shows good agreement with the $r_0 \sim 6$ h^{-1} Mpc measured for lower luminosity radio sources and QSOs at $z \sim 1$.

Crucial to the picture that is developing may be the recent results of Wilson (2003), who studied the clustering of $(V - I)$-selected L_* early-type galaxies in the redshift range $0.2 < z < 0.9$. This author found that these galaxies cluster slightly more strongly compared to the field, with a best-fitting ϵ-model of $\epsilon = 0$ and $r_0 = 5.25 \pm 0.28\ h^{-1}$ Mpc. This is in agreement with the correlation length of local L_* early-types in the 2dFGRS. Wilson (2003) remarks that this measurement is inconsistent with the large r_0 found for EROs, which are also believed to be $L \sim L_*$ early-type galaxies. The value of r_0 for EROs and radio galaxies could be spuriously high due to uncertainties in their redshift distributions which is not included in the quoted errors, although the selection functions of both EROs and powerful radio galaxies are considered to be understood relatively well (e.g. Dunlop & Peacock 1990; Daddi et al. 2001; McCarthy et al. 2001). Alternatively, EROs and radio galaxies at $z \sim 1$ may be much more strongly clustered because they correspond to a population of massive, bright cluster galaxies in the process of formation. If FRII radio galaxies and EROs are indeed the distant analogs of local $L \sim L_*$ early-types, they are becoming considerably more biased tracers of the underlying galaxy distribution with redshift, while this galaxy distribution itself probably traces the dark matter distribution with relatively constant bias. Interestingly, (semi-) analytic models and N-body simulations are able to explain this bias evolution and the large inferred r_0 at $z \sim 1$ of massive ellipticals, if the assumption that galaxies are conserved quantities (i.e. closed-box systems) is relaxed. These hierarchical merging models (e.g. Mo & White 1996; Matarrese et al. 1997; Moscardini et al. 1998; Kauffmann et al. 1999b; Moustakas & Somerville 2002; Mo & White 2002,and references therein) prescribe that for certain types of objects bias can grow stronger with redshift than the growth of perturbations, resulting in a r_0 that is constant or even increasing with redshift.

In the (transient) model of Matarrese et al. (1997) it is assumed that the mass of the dark matter halo also determines the physical parameters of the galaxy that it contains. Based on the work of Mo & White (1996) and the formalism of Press & Schechter (1974), Matarrese et al. (1997)

derive that the bias in such a model evolves as

$$b(z) = 1 - 1/\delta_c + [b_0 - (1 - 1/\delta_c)]/D(z)^{\beta}, \quad (2.14)$$

where $\delta_c = 1.686$ is the critical linear overdensity for spherical collapse (but see also Lilje 1992). The parameters b_0 and β depend on the minimum mass of the halo, and we have used the COBE-normalized (ΛCDM) values for $\mathcal{M}_{\rm min} = 10^{12-14} M_{\odot}$ given by Moscardini et al. (1998) to plot this model in Fig. 2.16 (thin dashed lines). We find that the $\mathcal{M}_{\rm min} = 10^{14} M_{\odot}$ model is able to fit the measurements at both $z \sim 1$ and $z = 0$. Likewise, the model with $\mathcal{M}_{\rm min} = 10^{13} M_{\odot}$ has been found to fit the spatial clustering of QSOs relatively well (Croom et al. 2001), although several serious caveats exist (see Rengelink 1998; Croom et al. 2001). Most importantly, the assumption that there always exists a simple relationship between the mass of the dark matter halo and the property by which a galaxy is selected may not be valid.

In Fig. 2.16 we have also indicated the predicted evolution of the clustering of early-type galaxies (thick dashed line) from the ΛCDM-models of Kauffmann et al. (1999a,b) (see also Somerville et al. 2001), normalised to r_0 found for local ellipticals. An important feature of the models presented in Kauffmann et al. (1999b) is that one naturally expects a dip in r_0 between $z = 0$ and $z \approx 1$, if structure is probed by galaxies of intermediate luminosities residing in haloes of masses $10^{11-12} M_{\odot}$ that have formed early and are unbiased tracers of the overall mass distribution. However, these simulations also show that this dip is very sensitive to sample selection criteria: massive early-type galaxies exhibit no dip in clustering between $z = 0$ and $z \approx 1$, because they occur in rare, very masssive haloes of $10^{13-14} M_{\odot}$ which are strongly biased locally, and which become even stronger biased with redshift. The agreement of this model with the results presented in this paper and the results of Daddi et al. (2001) and McCarthy et al. (2001) is striking. Although promising, some discrepancies between the model and the observations remain. For instance, Daddi et al. (2001, 2002) find strong disagreement between the model and the high observed space density of EROs, seemingly consistent with the purely passive evolution of local ellipticals. Furthermore, current merging models generally predict that these galaxies should have experienced recent star-formation activity, while this is not observed. It may become possible to still reconcile the observations with the ΛCDM merging models if, for example, the merging is accompanied by little star-formation (Daddi et al. 2001). Also, the EROs are found to have relatively old stellar populations of $\gtrsim 3$ Gyr that show no indications of recent formation processes. However, Moustakas & Somerville (2002) point out that the relatively old ages of their stellar populations do not automatically imply similar ages for the host galaxies.

Despite the success of current hierarchical models in predicting the evolution of bias for these massive galaxies, we would like to point out that galaxy conservation or linear/stable clustering evolution could still be able to explain the measurements if EROs and/or powerful radio galaxies are solely found in rich Abell-type clusters with (present-day) $r_0 \sim 15 - 25\, h^{-1}$ Mpc. As we have shown there is substantial evidence that this may be the case for, at least, the powerful radio galaxies, and future data may show whether this also holds for (a subset of) the population of EROs.

At the highest redshifts, clustering of LBGs at $3 \lesssim z \lesssim 4$ indicate that these objects can be connected to local ellipticals in a galaxy conservation scenario. However, it is now believed that LBGs probably occupy much less massive halos of $10^{11-12} M_{\odot}$ than those that contain local massive galaxies, suggesting that if these objects are to be the progenitors of local ellipticals, they must have accumulated a considerable amount of mass (Adelberger 2000; Moustakas & Somerville 2002).

2.6.2.3 *Clustering and the occurrence of AGN at high z*

Fig. 2.16 suggests that the clustering evolution of *active* galaxies in general is considerably different from that of ordinary galaxies. Albeit at

a lower amplitude, the clustering of QSOs also shows a trend of constant or slightly increasing amplitude with redshift, very similar to the trend that we derive for the clustering of the most massive ellipticals. According to the standard paradigm, AGN are powered by the accretion of matter onto a (super-)massive blackhole (e.g. Rees 1984). This fuelling mechanism may very well be associated with the injection and accretion of gas during major merging events, and thus, the occurrence of AGN seems to be logically linked to the hierarchical scenarios for structure formation. Recently, in a series of papers (Haehnelt et al. 1998; Haehnelt & Kauffmann 2000; Kauffmann & Haehnelt 2000, 2002) the simulations of Kauffmann et al. (1999b) were extended to a unified model for the evolution of both galaxies and quasars. In their model, elliptical galaxies, supermassive black holes and starbursts are formed during major merging events, in which a fraction of the available gas is used to trigger quasar activity by accretion for about 10^7 years, and the remaining gas is converted into stars in a single short burst. This model successfully reproduces the evolution of cold gas that is derived from observations of damped Lyα systems, the luminosity functions and clustering properties of QSOs from the 2dF QSO survey, and the relation between bulge velocity dispersion and black hole mass that has been found in demographic studies of black holes in nearby galaxies (e.g. Kormendy & Richstone 1995; Magorrian et al. 1998; Gebhardt et al. 2000).

Although it has yet remained unknown exactly what processes cause the physical differences between radio-quiet and radio-loud AGN, recent results indicate that the hosts of all powerful AGN (both radio-loud and radio-quiet) are almost exclusively $L \gtrsim L_*$ ellipticals (see Dunlop & McLure 2003,and references therein). However, the same studies also indicate that while radio-quiet AGN hosts can have black holes with masses of $10^{6-10} M_\odot$, the radio-loud sources are cleanly confined to black hole masses $M_{bh} \gtrsim 5 \times 10^8 M_\odot$. Furthermore, in the regime of extreme radio luminosities that lie well beyond the FRI/FRII luminosity-break, the power needed can only be achieved by black-holes with $M_{bh} > 10^9 M_\odot$, requiring host masses of $> 10^{12} M_\odot$ that imply $L > L_*$ luminosities (Dunlop & McLure 2003). This may explain why the most powerful NVSS sources are extremely clustered compared to the, on average, less massive hosts of QSOs. This is supported by the fact that the radio sources in our lower radio luminosity bin have a correlation length similar to that of QSOs at $z \sim 1$, while both populations are still clustered more strongly compared to the field at $z \sim 1$. We conclude that the masses of the haloes, host galaxies, and black holes that are probed by the most powerful radio sources are among the most massive objects in the Universe, possibly formed through massive mergers in hierarchical fashion.

2.7 Summary

The main conclusions that can be drawn from our analysis are the following:

• Below $\sim 6'$ $w(\theta)$ is dominated by the size distribution of multi-component radio sources. A simple model of the physical size distribution of FRII radio galaxies is able to explain the observed enhancement of the cosmological clustering signal.

• The amplitude of the ACF of radio sources increases with increasing radio flux, corresponding to a similar increase in r_0 with increasing average radio power of the samples. This suggests that powerful FRII radio galaxies are intrinsically more strongly clustered than the average population of radio galaxies at $z \sim 1$. This is consistent with the extremely rich environments in which high redshift FRIIs are generally found.

• The correlation lengths of powerful radio galaxies and EROs are of comparable magnitude and both are associated with massive ellipticals at $z \sim 1$. This suggests that we could be looking at identical objects at different stages of their evolution, implying that AGN activity is an important phase in the evolution of massive galaxies in general.

• The evolution that we infer for the clustering

of massive ellipticals between $z \sim 1$ and $z \sim 0$ is in agreement with predictions from hierarchical models for structure formation, because they can account for the observed lack of evolution in r_0. However, the large correlation length of powerful radio galaxies at $z \sim 1$ is also consistent with galaxy conservation models if they are primarily associated with rich, Abell-type clusters.

Acknowledgments

We would like to thank Chris Blake, Emanuele Daddi, Matt Jarvis, Melanie Johnston-Hollitt and Jaron Kurk for productive discussions and reading through the text. We also thank the referee for very helpful comments.

References

Adelberger, K. 2000, in ASP Conf. Ser. 200: Clustering at High Redshift, 13
Bahcall, N. A. & Soneira, R. M. 1983, ApJ, 270, 20
Barthel, P. D. & Miley, G. K. 1988, Nature, 333, 319
Becker, R. H., White, R. L., & Helfand, D. J. 1995, ApJ, 450, 559
Best, P. N., Longair, M., & Röttgering, H. J. A. 1999, in The Most Distant Radio Galaxies
Best, P. N., Longair, M. S., & Röttgering, H. J. A. 1998, MNRAS, 295, 549
Blake, C. & Wall, J. 2002a, MNRAS, 329, L37
—. 2002b, MNRAS, 337, 993
Blundell, K. M., Rawlings, S., & Willott, C. J. 1999, AJ, 117, 677
Butcher, H. & Oemler, A. 1978, ApJ, 219, 18
Carlberg, R. G., Cowie, L. L., Songaila, A., & Hu, E. M. 1997, ApJ, 484, 538
Carlberg, R. G., Yee, H. K. C., Morris, S. L., et al. 2000, ApJ, 542, 57
Carroll, S. M., Press, W. H., & Turner, E. L. 1992, ARA&A, 30, 499
Cimatti, A., Andreani, P., Röttgering, H., & Tilanus, R. 1998, Nature, 392, 895
Cimatti, A., Daddi, E., Mignoli, M., et al. 2002, A&A, 381, L68
Condon, J. J., Cotton, W. D., Greisen, E. W., et al. 1998, AJ, 115, 1693
Crawford, C. S. & Fabian, A. C. 1996, MNRAS, 282, 1483
Cress, C. M., Helfand, D. J., Becker, R. H., Gregg, M. D., & White, R. L. 1996, ApJ, 473, 7
Croft, R. A. C., Dalton, G. B., Efstathiou, G., Sutherland, W. J., & Maddox, S. J. 1997, MNRAS, 291, 305
Croom, S. M., Shanks, T., Boyle, B. J., et al. 2001, MNRAS, 325, 483
Daddi, E., Broadhurst, T., Zamorani, G., et al. 2001, A&A, 376, 825
Daddi, E., Cimatti, A., Broadhurst, T., et al. 2002, A&A, 384, L1
Dalton, G. B., Croft, R. A. C., Efstathiou, G., et al. 1994, MNRAS, 271, L47
Davis, M. & Peebles, P. J. E. 1983, ApJ, 267, 465
de Bernardis, P., Ade, P. A. R., Bock, J. J., et al. 2000, Nature, 404, 955
De Breuck, C., Röttgering, H., Miley, G., van Breugel, W., & Best, P. 2000, A&A, 362, 519
Dey, A., Graham, J. R., Ivison, R. J., et al. 1999, ApJ, 519, 610
Dunlop, J., Peacock, J., Spinrad, H., et al. 1996, Nature, 381, 581
Dunlop, J. S. & McLure, R. J. 2003, in The Mass of Galaxies at Low and High Redshift. Proceedings of the ESO Workshop held in Venice, Italy, 24-26 October 2001, p. 268., 268
Dunlop, J. S. & Peacock, J. A. 1990, MNRAS, 247, 19
Eggen, O. J., Lynden-Bell, D., & Sandage, A. R. 1962, ApJ, 136, 748
Fanaroff, B. L. & Riley, J. M. 1974, MNRAS, 167, 31
Fanti, R., Fanti, C., Schilizzi, R. T., et al. 1990, A&A, 231, 333
Firth, A. E., Somerville, R. S., McMahon, R. G., et al. 2002, MNRAS, 332, 617
Fisher, K. B., Davis, M., Strauss, M. A., Yahil, A., & Huchra, J. 1994, MNRAS, 266, 50
Fry, J. N. 1996, ApJ, 461, L65
Gebhardt, K., Bender, R., Bower, G., et al. 2000, ApJ, 539, L13
Giavalisco, M., Steidel, C. C., Adelberger, K. L., et al. 1998, ApJ, 503, 543
Gonzalez, A. H., Zaritsky, D., & Wechsler, R. H. 2002, ApJ, 571, 129
Griffith, M. R. 1993, Ph.D. Thesis
Guzzo, L., Strauss, M. A., Fisher, K. B., Giovanelli, R., & Haynes, M. P. 1997, ApJ, 489, 37
Haehnelt, M. G. & Kauffmann, G. 2000, MNRAS, 318, L35
Haehnelt, M. G., Natarajan, P., & Rees, M. J. 1998, MNRAS, 300, 817
Hamilton, A. J. S. 1993, ApJ, 417, 19
Hill, G. J. & Lilly, S. J. 1991, ApJ, 367, 1
Jenkins, A., Frenk, C., Pearce, F., et al. 1998, ApJ, 499, 20
Kapahi, V. K., Subrahmanya, C. R., & Kulkarni, V. K. 1987, Journal of Astrophysics and Astronomy, 8, 33
Kauffmann, G. & Charlot, S. 1998, MNRAS, 297, L23
Kauffmann, G., Colberg, J. . M., Diaferio, A., & White, S. D. M. 1999a, MNRAS, 307, 529
Kauffmann, G., Colberg, J. M., Diaferio, A., & White, S. D. M. 1999b, MNRAS, 303, 188
Kauffmann, G. & Haehnelt, M. 2000, MNRAS, 311, 576
Kauffmann, G. & Haehnelt, M. G. 2002, MNRAS, 332, 529
Kooiman, B. L., Burns, J. O., & Klypin, A. A. 1995, ApJ, 448, 500
Kormendy, J. & Richstone, D. 1995, ARA&A, 33, 581
Kundić, T. 1997, ApJ, 482, 631
Kurk, J. D., Röttgering, H. J. A., Pentericci, L., et al. 2000, A&A, 358, L1
Lahav, O., Fabian, A. C., Edge, A. C., & Putney, A. 1989,

MNRAS, 238, 881
Landy, S. D. & Szalay, A. S. 1993, ApJ, 412, 64
Lara, L., Cotton, W., Feretti, L., et al. 2001, A&A, 370, 409
Le Fèvre, O., Hudon, D., Lilly, S. J., et al. 1996, ApJ, 461, 534
Lilje, P. B. 1992, ApJ, 386, L33
Limber, D. N. 1953, ApJ, 117, 134
Ling, E. N., Barrow, J. D., & Frenk, C. S. 1986, MNRAS, 223, L21
Liu, M. C., Dey, A., Graham, J. R., et al. 2000, AJ, 119, 2556
Loan, A. J., Wall, J. V., & Lahav, O. 1997, MNRAS, 286, 994
Loveday, J., Maddox, S. J., Efstathiou, G., & Peterson, B. A. 1995, ApJ, 442, 457
Magliocchetti, M., Bagla, J. S., Maddox, S. J., & Lahav, O. 2000, MNRAS, 314, 546
Magliocchetti, M., Maddox, S. J., Lahav, O., & Wall, J. V. 1998, MNRAS, 300, 257
Magorrian, J., Tremaine, S., Richstone, D., et al. 1998, AJ, 115, 2285
Matarrese, S., Coles, P., Lucchin, F., & Moscardini, L. 1997, MNRAS, 286, 115
McCarthy, P. J. 1988, Ph.D. Thesis
McCarthy, P. J., Carlberg, R. G., Chen, H.-W., et al. 2001, ApJ, 560, L131
McCracken, H. J., Le Fèvre, O., Brodwin, M., et al. 2001, A&A, 376, 756
Mo, H. J. & White, S. D. M. 1996, MNRAS, 282, 347
—. 2002, MNRAS, 336, 112
Moscardini, L., Coles, P., Lucchin, F., & Matarrese, S. 1998, MNRAS, 299, 95
Moustakas, L. A. & Somerville, R. S. 2002, ApJ, 577, 1
Nakata, F., Kajisawa, M., Yamada, T., et al. 2001, PASJ, 53, 1139
Neeser, M. J., Eales, S. A., Law-Green, J. D., Leahy, J. P., & Rawlings, S. 1995, ApJ, 451, 76
Nilsson, K., Valtonen, M. J., Kotilainen, J., & Jaakkola, T. 1993, ApJ, 413, 453
Norberg, P., Baugh, C. M., Hawkins, E., et al. 2002, MNRAS, 332, 827
O'Dea, C. P., Baum, S. A., & Stanghellini, C. 1991, ApJ, 380, 66
Oort, M. J. A., Katgert, P., & Windhorst, R. A. 1987, Nature, 328, 500
Ouchi, M., Shimasaku, K., Okamura, S., et al. 2001, ApJ, 558, L83
Peebles, P. J. E. 1980, The large-scale structure of the universe (Princeton University Press)
Pentericci, L., Kurk, J. D., Röttgering, H. J. A., et al. 2000, A&A, 361, L25
Pentericci, L., McCarthy, P. J., Röttgering, H. J. A., et al. 2001, ApJ, 135, 63
Pentericci, L., Röttgering, H. J. A., Miley, G. K., et al. 1999, A&A, 341, 329
Phillipps, S., Fong, R., Fall, R. S. E. S. M., & MacGillivray, H. T. 1978, MNRAS, 182, 673
Porciani, C. & Giavalisco, M. 2002, ApJ, 565, 24
Postman, M., Huchra, J. P., & Geller, M. J. 1992, ApJ, 384, 404
Press, W. H. & Schechter, P. 1974, ApJ, 187, 425
Röttgering, H. J. A., Best, P. N., & Lehnert, M. D. 1999, in The Most Distant Radio Galaxies
Rees, M. J. 1984, ARA&A, 22, 471
—. 1990, Scientific American, 263, 56
Rengelink, R. B. 1998, Ph.D. Thesis
Rengelink, R. B. & Röttgering, H. J. A. 1999, in The Most Distant Radio Galaxies, 399
Roche, N. D., Almaini, O., Dunlop, J., Ivison, R. J., & Willott, C. J. 2002, MNRAS, 337, 1282
Röttgering, H. J. A., West, M. J., Miley, G. K., & Chambers, K. C. 1996, A&A, 307, 376
Rubin, V. C. 1954, Proceedings of the National Academy of Science, 40, 541
Schoenmakers, A. P., de Bruyn, A. G., Röttgering, H. J. A., & van der Laan, H. 2001, A&A, 374, 861
Singal, A. K. 1993, MNRAS, 263, 139
Somerville, R. S., Lemson, G., Sigad, Y., et al. 2001, MNRAS, 320, 289
Steidel, C. C., Pettini, M., & Hamilton, D. 1995, AJ, 110, 2519
Tegmark, M. & Peebles, P. J. E. 1998, ApJ, 500, L79
Venemans, B. P., Kurk, J. D., Miley, G. K., et al. 2002, ApJ, 569, L11
Wall, J. V. & Jackson, C. A. 1997, MNRAS, 290, L17
Webster, A. & Pearson, T. J. 1977, MNRAS, 179, 517
Willmer, C. N. A., da Costa, L. N., & Pellegrini, P. S. 1998, AJ, 115, 869
Willott, C. J., Rawlings, S., & Blundell, K. M. 2001, MNRAS, 324, 1
Wilman, R. J., Röttgering, H. J. A., Overzier, R. A., & Jarvis, M. J. 2003, MNRAS, 339, 695
Wilson, G. 2003, ApJ, 585, 191

Chapter 3

On the X-ray emission of $z \sim 2$ radio galaxies: IC scattering of the CMB & no evidence for fully-formed potential wells

Abstract. We present the results of 20 ks *Chandra* observations for each of 5 radio galaxies in the redshift range $2.0 < z < 2.6$. The goals were to (i) study the nature of their non-thermal X-ray emission, (ii) investigate the presence and amount of hot gas, and (iii) look for active galactic nuclei (AGN) overdensities in fields around high redshift radio galaxies. For 4 of the 5 targets we detect unresolved X-ray components coincident with the radio nuclei. From spectral analysis of one of the cores and comparison to the empirical radio to X-ray luminosity ratio (L_R/L_X) correlation for AGN, we find that the cores are underluminous in the X-rays indicating that obscuring material (n(H I) $\sim 10^{22}$ cm^{-2}) may be surrounding the nuclei. We detect X-ray emission coincident with the radio hotspots or lobes in 4 of the 5 targets. This extended emission can be explained by the Inverse Compton (IC) scattering of photons that make up the cosmic microwave background (CMB). The magnetic field strengths of $\sim 100 - 200$ μG that we derive agree with the equipartition magnetic field strengths. The relative ease with which the lobe X-ray emission is detected is a consequence of the $(1+z)^4$ increase in the energy density of the CMB. For one of the lobes, the X-ray emission could also be produced by a reservoir of hot, shocked gas. An HST image of the region around this radio component shows bright optical emission reminiscent of a bow-shock. By co-adding the 5 fields we created a deep, 100 ks exposure to search for diffuse X-ray emission from thermal intra-cluster gas. We detect no diffuse emission and derive upper limits of $\sim 10^{44}$ erg s^{-1}, thereby ruling out a virialized structure of cluster-size scale at $z \sim 2$. The average number of soft X-ray sources in the field surrounding the radio sources is consistent with the number density of AGN in the *Chandra* Deep Fields, with only one of the fields showing a marginally statistically significant factor 2 excess of sources with $f_{0.5-2keV} > 3 \times 10^{-15}$ erg s^{-1} cm^{-2}. Analysis of the angular distribution of the field sources shows no evidence for large-scale structure associated with the radio galaxies, as was observed in the case of PKS 1138–262 by Pentericci et al. (2002).

R. A. Overzier, D. E. Harris, C. L. Carilli, L. Pentericci, H. J. A. Röttgering & G. K. Miley
Astronomy & Astrophysics, **433**, 87 (2005)

3.1 Introduction

Radio galaxies can be used to trace the formation and evolution of the most massive galaxies known at high redshift. They usually have continuum morphologies suggestive of the merging of L_* systems (e.g. Pentericci et al. 1999, 2001), and are surrounded by large reservoirs of line emitting gas (e.g. van Ojik et al. 1997) that are comparable in size to cD galaxy envelopes. High redshift radio galaxy (HzRG) fields targeted by broad and narrow band imaging and spectroscopy have been found to locate 'protoclusters'. They have large excesses of Lyα and/or Hα emitters, Lyman break galaxies and extremely red objects (e.g. Pentericci et al. 2000a; Kurk et al. 2000; Kurk et al. 2003; Venemans et al. 2002; Miley et al. 2004). Thus, HzRGs act as beacons to the progenitors of present-day galaxy clusters (see also e.g. Windhorst et al. 1998; Ivison et al. 2000; Brand et al. 2003; Smail et al. 2003; Stevens et al. 2003). Finding these distant (i.e. $z \gtrsim 2$) protoclusters is important for constraining models of structure formation and cosmology.

Radio continuum polarimetric observations of HzRGs have revealed large rotation measures (*RM*) and large *RM* gradients. At $z \gtrsim 2$ the typical *RM* observed is several hundreds rad m^{-2}, but extreme values of > 1000 rad m^{-2} are not uncommon (Carilli et al. 1997; Athreya et al. 1998; Pentericci et al. 2000). It is believed that *RM* arises from 'Faraday screens' in our galaxy (i.e. the interstellar medium, ISM), in intervening galaxies and clusters, or near the source itself. At low redshifts, most radio galaxies have relatively small *RM* values that can be attributed to the local ISM (Simard-Normandin & Kronberg 1980; Leahy 1987, and references therein). However, *RM* values observed towards HzRGs are significantly larger, and are believed to be due to Faraday screening of extra-galactic origin somewhere along the line of sight. Athreya et al. (1998) show that the chance superpositions of distant radio sources and intervening systems such as foreground Abell clusters and damped Lyα absorbers are too small to explain the fraction of high *RM*s observed. Likewise, the expected *RM*s from such intervening systems are too small to account for the high values seen towards distant radio sources. Hence, the large *RM* values may occur in a medium close to the source, although it is unclear whether they are caused by extended cluster-sized media or smaller gas distributions on scales comparable to the radio sources (e.g. Carilli et al. 2002). Some radio galaxies at low redshift have extremely large values of *RM* that are caused by Faraday rotation in so-called 'cooling flow' cluster atmospheres (e.g. 3C 295; Perley & Taylor 1991, see Carilli & Taylor (2002) for a review on cluster magnetic fields). There is evidence that the strength of cooling flows is correlated with *RM*, indicating that *RM* is an indicator of the fields in the intracluster medium rather than the radio cocoon (Taylor et al. 1994; Eilek & Owen 2002; Ensslin et al. 2003, but see Rudnick & Blundell (2003)).

X-ray observations are also a powerful tool to find deep, gravitational potential wells in the early Universe. Diffuse X-ray emission caused by thermal bremsstrahlung from a hot ICM, is evidence for a bound system in which the gas is in dynamical equilibrium with the galaxies and the cold dark matter. Deep X-ray surveys have uncovered significant numbers of rich galaxy clusters out to $z \sim 1.2$ (e.g. Rosati et al. 1999; Stanford et al. 2001; Rosati et al. 2004). Remarkably, the diffuse ICM in these distant objects traces the galaxy distribution, and their surface brightness and temperature profiles are similar to those of lower redshift clusters, indicating that clusters formed very early in the history of the Universe. The study of thermal emission from HzRGs is important because of their suggested linkage to cluster formation. However, if an ICM is present in such structures at $z > 1.5$, the extreme cosmological surface brightness dimming makes their detection very difficult.

So far only a handful of distant radio sources has been studied with *Chandra*. Fabian et al. (2003) performed a very deep (200 ks) study of the radio galaxy 3C 294 at $z = 1.79$. They observed a 100 kpc region of diffuse emission bounded by sharp edges. Although some ther-

mal component from the ICM could not be ruled out, most of the emission was ascribed to Inverse Compton (IC) scattering of the cosmic microwave background (CMB) by an older population of electrons tracing out an hourglass-shaped region around the radio source. Belsole et al. (2004) found weak cluster luminosities and IC scattering among a sample of three bright HzRGs. Carilli et al. (2002) found diffuse X-ray emission around the radio galaxy PKS 1138–262 at $z = 2.16$, which is believed to be the forming, massive galaxy at the center of a protocluster (Pentericci et al. 2000a; Kurk et al. 2000; Kurk et al. 2003). However, the extended emission is seen only along the radio axis, and is therefore believed to be associated with shocked material inside the radio source. The upper limit that Carilli et al. (2002) derive for the X-ray luminosity of the ICM ($\sim$ 40% of the luminosity of the Cygnus A cluster, see e.g. Smith et al. (2002)) is not unexpectedly low because there has not been enough time since the big bang for these structures at $z \sim 2$ to form a sufficiently deep potential well. Scharf et al. (2003) detected extended X-ray emission around 4C 41.17 at $z = 3.8$ roughly following the radio morphology. They conclude that the X-ray emission arises from 'Inverse Compton scattering of far-infrared photons from a relativistic electron population probably associated with past and current activity from the central object', in addition to a lesser contribution from the upscattering of CMB photons.

It is clear that the nature of the X-ray emission mechanisms operating in radio galaxies is diverse. Better sample statistics are required to enlarge our current understanding of e.g. the dominant X-ray emission mechanisms, the role of magnetic fields on galaxy and cluster-size scales, the origin of the hot gas observed in X-ray luminous clusters, and large-scale structure associated with HzRGs. Here we present observations with the *Chandra* X-ray observatory of five additional radio galaxies at $z \sim 2$. The sources were selected from a compendium of $z > 2$ HzRGs, focusing on the lower end of the redshift distribution in order to minimize surface brightness dimming effects, while still being at high enough redshift to allow for cosmological evolution effects in source properties. Sources were further selected on the presence of one or more of the various characteristics: distorted radio morphology, large rotation measure ($\geq$ 1000 rad m^{-2}), evidence for interaction between Lyα and radio structure, and extended Lyα absorption features.

Throughout this paper we assume $H_0 = 70$ km s^{-1}, $\Omega_M = 0.3$, and $\Omega_\Lambda = 0.7$. The resulting scale factors range from 8.0 to 8.4 kpc arcsec^{-1} from $z = 2.6$ to $z = 2$. We will use power-law spectra defined as $S_\nu \propto \nu^{-\alpha}$, where α is the spectral index.

3.2 Observations

3.2.1 Observations and data reduction

Each of the 5 sources was observed for 20 ks with the back-illuminated ACIS-S3 chip on *Chandra*, using the standard 3.2 s readout timed exposure mode and the faint telemetry format. Sources were positioned at approximately 20″ away from the aimpoint. The data were processed and analysed in June 2003 using the *Chandra* data analysis package CIAO 2.3[1] together with CALDB 2.22. We applied the 'ACIS-ABS' script that corrects the *Chandra* auxiliary response files for a continuous degradation in the ACIS quantum efficiency. We did not apply the 'tgain' correction that has become standard practice only in the most recent release of CIAO to correct for the drift in the effective detector gain due to an increase in the charge transfer inefficiency over time. However, for ACIS–S3 the resulting effect on the measured photon energies was of the order of only $\sim$ 0.3% near the end of 2002 when the data were taken.

A log of the observations is given in Table 1. 0156–252 was observed on 2 separate dates, because the initial observation was interrupted after 11.5 ks by a high radiation shutdown of the system due to an excess of solar wind particles. To ease the analysis of these observations, the two exposures were merged into a

[1] http://cxc.harvard.edu/ciao/

Table 3.1 — Log of observations. The last column lists the average galactic HI column density in the direction of each source as given by Dickey & Lockman (1990).

Source	R.A. (J2000)	Decl. (J2000)	z	Dates of observation	Exposure time (s)	n(H I) ($\times 10^{20}$ cm^{-2})
0156–252	$01^h58^m33.5^s$	$-24°59'32.26''$	2.09	2002-11-09	11477	1.34
				2002-12-20	8401	
0406–244	$04^h08^m51.5^s$	$-24°18'16.8''$	2.44	2002-12-07	20179	3.30
0828+193	$08^h30^m53.4^s$	$+19°13'15.7''$	2.57	2002-11-05	19212	3.72
2036–254	$20^h39^m24.5^s$	$-25°14'30.4''$	2.00	2002-09-01	19660	4.92
2048–272	$20^h51^m03.6^s$	$-27°03'02.1''$	2.06	2002-11-11	19555	6.29

single event file by 'reprojecting' the events. A lightcurve analysis of the other sources indicates no further periods of significant fluctuations in the count rates of source and large, source-free background regions.

Radio images at 5 and 8 GHz where obtained by Carilli et al. (1997) and Pentericci et al. (2000a) using the VLA in A configuration. The noise is 50 μJy/beam at 5 Ghz and 25 μJy/beam at 8 GHz. The resolution of the observations is $0\farcs43$ for the 5 GHz maps and $0\farcs23$ for the 8 GHz maps. Analysis of the radio data was performed using the Astronomical Image Processing System (AIPS) and the Multichannel Image Reconstruction, Image Analysis and Display (MIRIAD) software.

We will also make use of observations obtained with the Wide-Field Planetary Camera 2 (WFPC2) on *HST*. 0156–252 and 2048–272 were observed as part of Program 8183 (PI: Miley), and an image of 0406–244 was retrieved from the HST archive (program 8338, PI: Lehnert). 0156–252 was observed for 4800 s and 2048–272 for 7200 s, both through filter *F*555*W*. This filter has a central wavelength of 5443 Å. 0406–244 was observed for 2000 s through filter *F*675*W* which has a central wavelength of 6718 Å. Measurements from these images were made using the conversion from counts to flux density as given in the PHOTFLAM header keyword of each image. To get to the flux density S_ν (erg s^{-1} cm^{-2} Hz^{-1}) we calculate $S_\nu = (\lambda^2/c) \times (\text{counts}/t_{exp}) \times \text{PHOTFLAM}$ (see Pentericci et al. 1999, for a description of procedures).

3.2.2 Image registration

To recover the inherent resolution of the *Chandra* mirror/detector system, we removed the pixel randomization added in the pipeline processing and regridded our maps to 1/10 native ACIS pixel size. After applying a suitable smoothing function, we were able to find the position of the X-ray core to an accuracy of better than $0\farcs1$ provided the core had sufficient signal to noise (S/N). We then shifted the images to align the X-ray core with the radio core. The typical shift needed was one half of an original *Chandra* pixel in right ascension and/or declination, consistent with the known astrometric accuracy. In the case of 2048–272 no shift was applied, because the nucleus was not detected in either the radio or the X-rays.

3.2.3 Analysis

The *Chandra* images are shown in Fig. 3.1, where yellow contours indicate the 4.7 GHz radio maps from Carilli et al. (1997) and Pentericci et al. (2000). We measured the X-ray counts from the distinct radio components (e.g. cores and lobes) using boxed or circular extraction regions. The counts are background-subtracted by using a large, point source free, annular region centered on the radio source. We restrict our measurements to counts in the energy range of 0.2–6 keV for which the contribution of the background is minimal. We calculate the total net (i.e. background subtracted) counts $N =$

$S - B$, where S and B are the counts in the source region A_S and the background region A_B, respectively. We consider a radio component detected in the X-rays when N is greater than its formal error, $\sigma_N = [(\sigma_S)^2 + (\sigma_B)^2]^{1/2}$, where $\sigma_S = 1 + (S + 0.75)^{1/2}$ and $\sigma_B = [1 + (B + 0.75)^{1/2}](A_S/A_B)$ from Gehrels (1986). For undetected components we calculate 2σ upper limits in the 0.2–6 keV band using the above expression for σ_N. The upper limit on flux is estimated by assuming a power-law spectrum with a spectral index of 0.8 using the online tool PIMMS[2].

The procedure to convert counts into fluxes is as follows: we create exposure maps for the soft (0.5–2 keV) and hard (2–6 keV) band at nominal energies, and divide the images in each band by the corresponding exposure map to obtain fluxed images. When extracting the flux for a given region, we calculate weight factors defined by the ratio of the average energy of counts in that region to the nominal energy of each exposure map. The total flux in a region is then calculated by summing the weighted fluxes in the two bands. We remark that our method is slightly different compared to the usual procedure of calculating fluxes from exposure maps using a conversion factor that is based on the spectral response within the given band as well as an assumed spectral energy distribution. Our method is preferred because it allows us to measure fluxes, without having to assume a specific spectral shape.

The measurements are given in Table 3.3. Where indicated, fluxes are corrected for galactic absorption using PIMMS, assuming a power-law spectrum with a spectral index of 0.8 and taking the HI column density in the direction of each source from Dickey & Lockman (1990) indicated in Table 3.1. All energy ranges are in the observed frame, unless stated otherwise.

3.3 Results

3.3.1 Source description

We will briefly summarize some of the main characteristics of each source. Details on radio observations, ground-based imaging and spectroscopy, and *Hubble Space Telescope* (*HST*) observations can be found in McCarthy et al. (1996), Carilli et al. (1997), Pentericci et al. (1999), Pentericci et al. (2001), Iwamuro et al. (2003) and references therein. Table 3.2 summarizes the intrinsic rotation measures, $RM_{int} = RM_{obs} \times (1 + z)^2$.

[2] http://heasarc.gsfc.nasa.gov/Tools/w3pimms.html

Table 3.2 — Rotation measures, $RM_{int} = RM_{obs} \times (1 + z)^2$, for the Northern (N.) and Southern (S.) lobes of each source taken from the literature.

Source	RM_{int} (rad m^{-2})		Refs.[†]
	N. lobe	S. lobe	
0156–252	1528 ± 296	–	1
0406–244	880 ± 19	-705 ± 30	1
0828+193	–	–	2
2036–254	3 ± 227	-3321 ± 429	1
2048–272	590	–	3

[†] References: (1) Athreya et al. (1998), (2) Carilli et al. (1997), (3) Pentericci et al. (2000).

• 0156–252 at $z = 2.09$ has several characteristics reminiscent of the well-studied radio galaxy PKS 1138–262 (Carilli et al. 2002; Pentericci et al. 2000a). Near-infrared continuum shows a host galaxy extended over $\sim 2''$ parallel to the radio axis, and narrow-band Lyα shows emission line gas extended over the entire region encompassed by the northern and southern radio hot spots. The Lyα brightness is at a minimum at the position of the host galaxy and peaks at the location where there is a sharp bend in the (northern) radio jet, probably due to shock-induced ionization of the gas where the radio jet is deflected by denser material. The northern hot spot has an intrinsic RM of ~ 1000 rad m^{-2}.
• 0406–244 at $z = 2.44$ consists of two main optical/infrared continuum features aligned with the radio axis (see Rush et al. (1997) for a detailed study). The continuum components lie embedded in a large Lyα halo with a spatial extent of $\sim 8''$ along the radio axis. Both radio lobes have an intrinsic RM of ~ 1000 rad m^{-2} with opposite signs.
• 0828+193 at $z = 2.57$ is the largest radio source

in our sample ($\sim$ 100 kpc). It has a jet-like feature north of the radio core. The northern lobe contains several hot spots with a peculiar 90 degree bend. The southern radio hotspot is unresolved. Pentericci et al. (1999) have identified the radio core with the brightest optical component of several clumps in a $\sim 2''$ region seen by *HST*.

No *RM* is given for this source in Table 3.2, since the fractional polarization at 8.2 GHz for both lobes was below the 4σ sensitivity limit of the observations (Carilli et al. 1997).

• 2036–254 at $z = 2.00$ is the only source in our sample for which no optical/near-infrared data are available. The radio core is most likely the faint, compact component close to the southern lobe. There is a pair of hot spots parallel to the radio axis in the north. The southern lobe has a RM_{int} of $\sim$ 3500 rad m^{-2}.

• 2048–272 at $z = 2.06$ is among the $\sim$ 30% of sources in the sample of Carilli et al. (1997) for which the core is undetected. However, a bright near-infrared object seen in between the lobes is presumed to be the galaxy hosting the radio source. The northern hot spot has a RM_{int} of $\sim$ 590 rad m^{-2}.

3.3.2 X-ray Cores

We have detected X-ray cores in 4 of the 5 targets. No core was detected in the case of 2048–272, and we note that the core was also not detected in the radio maps indicating that nuclear activity may have ceased. The core X-ray luminosities are in the range $L_{X[0.5-6keV]} = 1.3 \times 10^{44} - 2.3 \times 10^{45}$ erg s^{-1}. 0156–252 has $> 4\times$ the luminosity of the other cores. We place an upper limit on the core luminosity of 2048–272 of 7×10^{43} erg s^{-1}. Hardcastle & Worrall (1999) and Brinkmann et al. (2000) presented a correlation between the X-ray and radio luminosity of radio-loud quasars from the cross-correlation of ROSAT and radio sources. It has been suggested that this correlation implies a physical relationship between X-ray and radio cores, which can be explained by models in which e.g. the X-ray emission originates from the base of the jet (Hardcastle & Worrall 1999). In Fig. 3.2 we show objects from the Brinkmann et al. (2000) sample classified as narrow-line AGN, as well as the best-fit correlation for their subsample of radio-loud quasars, $\log L_X = 11.22 + 0.483 \times \log L_r$. We have also indicated several other $z > 2$ radio galaxies (1138–262 at $z = 2.16$, B0902+343 at $z = 3.395$, 4C41.17 at $z = 3.798$) and the local source Cygnus A for comparison (see Carilli et al. 2002; Scharf et al. 2003; Fabian et al. 2002, and references therein).

As shown in Fig. 3.2, three out of four sources in our sample agree with the L_r/L_X relation if we use the observed 2–6 keV (rest-frame 6–18 keV) flux with a power-law spectrum ($\alpha = 0.8$) to calculate the luminosity at rest-frame 2 keV (observed 0.7 keV). This result is virtually independent of the amount of intrinsic absorption, since it is of negligible effect at rest-frame 6–18 keV. Calculating the 2 keV luminosity from the 0.5–2 keV observed flux (rest-frame 1.5–6 keV) yields values that are significantly lower, but for 0156–252, 0828+193 and 2036–254 this can be explained by an intrinsic absorption column density of $n(\mathrm{H\,I}) \sim 10^{23}$ cm^{-2}. Interestingly, the core of 0406–244 seems highly underluminous in Fig. 3.2, a discrepancy that cannot be explained away by invoking a large amount of absorption. However, this may be a S/N issue: we have detected only 2 photons in the hard 2–6 keV band, compared to 62, 10 and 15 for the other 3 sources. If we instead calculate the 2 keV luminosity from the 0.5–2 keV observed flux (8 photons detected) with $n(\mathrm{H\,I}) = 10^{23}$ cm^{-2} we find $\log(L_{2keV}) \approx 26.4$ compared to ~ 25.9 for the earlier method, and note that its deviation from the L_r/L_X relation is now comparable to that of 4C41.17.

0156–252 is the only source in our sample for which the core is detected with sufficient S/N to carry out a (crude) spectral analysis. The X-ray spectrum is shown in Fig. 3.3. Assuming a power-law spectrum with absorption at the redshift of the source, we find $\alpha_X = 0.8 \pm 0.2$ and $n(\mathrm{H\,I}) = (1.6 \pm 0.7) \times 10^{22}$ cm^{-2}. The fit has a reduced χ^2 of 0.34, and is indicated in Fig. 3.3. The error bars for the fit parameters correspond

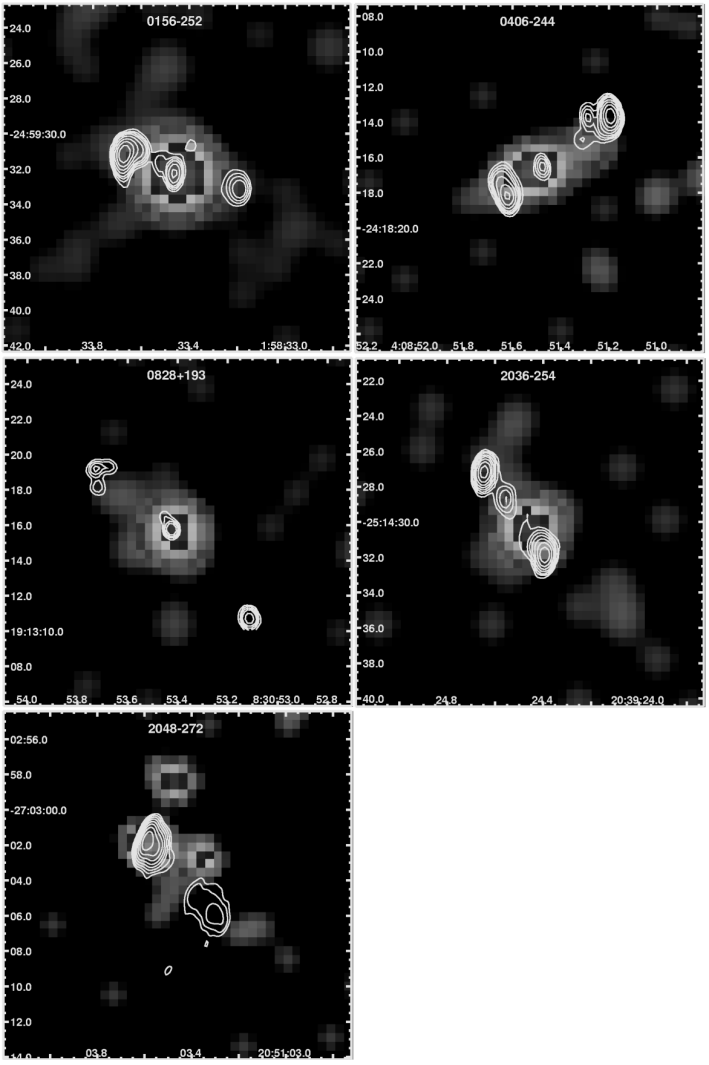

Figure 3.1 — *Chandra* images of 0156–252, 0406–244, 0828+193, 2036–254 and 2048–272, showing the 0.2–6 keV X-ray images in colorscales, and the 4.7 GHz VLA radio contours in yellow (from Carilli et al. 1997; Pentericci et al. 2000a). The $20'' \times 20''$ *Chandra* images have been smoothed using a Gaussian kernel of width $2''$ (FWHM). Radio contours are $1.0 \times (0.2, 0.4, 0.8, 1.6, \ldots)$ mJy beam^{-1}.

to a change of 1 in the reduced χ^2. Repeating the fit using using the *Cash* statistic valid for the low counts regime we find $n(\mathrm{H\,I}) = (1.5 \pm 0.8) \times 10^{22}$ cm^{-2} with α unchanged. The galactic H I column density towards this source is 1.34×10^{20} cm^{-2} (see Table 1). For completeness, we note that the spectrum can be fitted by a Mewe-Kaastra-Liedahl (Mekal) thermal plasma model with $kT = 23 \pm 8$ keV (reduced χ^2 of 0.50).

The signal-to-noise of the 3 other cores is insufficient to make spectra. However, if we assume that they are a generic class we might estimate the amount of intrinsic absorption by stacking the data. The hardness ratio $HR \equiv (H - S)/(H + S)$ (where H and S are the number counts observed in the hard and soft bands) is

Table 3.3 — X-ray measurements.

Source	θ^e ($''$)	Counts[a] (0.2–6 keV)	Soft[b] (0.5–2 keV)	Hard[b] (2–6 keV)	$f^c_{0.5-2keV}$ erg s^{-1} cm^{-2}	f^c_{2-6keV} erg s^{-1} cm^{-2}	$\log(L_{0.5-6keV})$ erg s^{-1}
0156–252							
Total	4.2	275 ± 18	200 ± 14.2	69 ± 8.3	(310 ± 20)	(490 ± 60)	45.42
Core	1.1	249 ± 17	181 ± 13.5	62 ± 7.9	(280 ± 20)	(440 ± 60)	45.37
NE	1.6	7 ± 4	4.9 ± 2.2	1.0 ± 1.0	(7.4 ± 3.4)	(3.9 ± 4.7)	43.56
SW	1.2	4 ± 3	1.9 ± 1.4	1.9 ± 1.4	(4.6 ± 3.4)	(16 ± 12)	43.82
0406–244							
Total	4.8	21 ± 6	18 ± 4.4	0.5 ± 1.4	(29 ± 7)	(3.6 ± 9.3)	44.19
Core	0.9	10 ± 4	8.0 ± 2.8	2.0 ± 1.4	(14 ± 5)	(13 ± 9)	44.11
SE	1.8	9 ± 4	6.9 ± 2.6	1.0 ± 1.0	(10 ± 4)	(5.2 ± 6.5)	43.88
NW	2.0	...[d]	...		< 24		< 44.05
0828+193							
Total	7.0	32 ± 7	17 ± 4.4	13.3 ± 4.0	(32 ± 8)	(120 ± 40)	44.91
Core	1.0	23 ± 6	12 ± 3.5	9.9 ± 3.2	(21 ± 6)	(87 ± 28)	44.78
NE	1.4	...[d]	...		< 19		< 44.00
SW	1.0	...[d]	...		< 16		< 43.93
2036–254							
Total	4.1	35 ± 7	14 ± 3.9	18.5 ± 4.4	(26 ± 7)	(120 ± 30)	44.65
Core	0.6	22 ± 6	7.0 ± 2.6	15.0 ± 3.9	(14 ± 5)	(96 ± 25)	44.51
NE	1.3	...[d]	...		< 20		< 43.76
SW	1.4	6 ± 4	5.9 ± 2.5	0.0 ± 0.0	(10 ± 4)	...	43.47
2048–272							
Total	4.3	8 ± 4	4.1 ± 2.2	4.0 ± 2.2	(6.0 ± 3.3)	(29 ± 16)	44.05
Core	0.8	...[d]	...		< 21		< 43.82
NE	1.7	6 ± 4	2.8 ± 1.7	1.8 ± 1.4	(4.5 ± 2.8)	(12 ± 10)	43.73
SW	1.5	...[d]	...		< 17		< 43.72

[a] Errors are calculated using Gehrels (1986) in the low-count regime.
[b] Errors are $\sqrt{counts}$.
[c] Observed fluxes in units of 10^{-16} erg s^{-1} cm^{-2} (not corrected for galactic absorption).
[d] Undetected. We give a 2σ upper limit for the total flux at 0.2–6 keV.
[e] Circular extraction radius.

0.0 ± 0.2, consistent with a Type II AGN at $z \sim 2$ with an obscured (n(H I) $\approx 10^{23}$ cm^{-2}) power-law spectrum with a photon index of $\Gamma = 1.8$ (Tozzi et al. 2001).

3.3.3 X-ray emission from lobes/hotspots

We obtained positive detections of X-ray components coincident with the northeastern (NE) and southwestern (SW) radio lobes of 0156–252, the southeastern (SE) lobe of 0406–244, the SW lobe of 2036–254, and the NE lobe of 2048–272. Below we will evaluate the likely mechanisms for these detections. Given the generally low signal to noise of all features we detected, we will focus on the X-ray emission that is identified with the radio lobes[3].

• Synchrotron radiation
In Fig. 3.4 we plot spectra for the lobes that have a detection in the X-ray. The spectra were constructed by (i) extrapolating the radio flux densities to X-ray frequencies using the radio spec-

[3]Our radio data are inadequate to confidently identify radio features as *lobes* or *hotspots*. We adopt the term *lobes* to mean any radio emission not associated with the core.

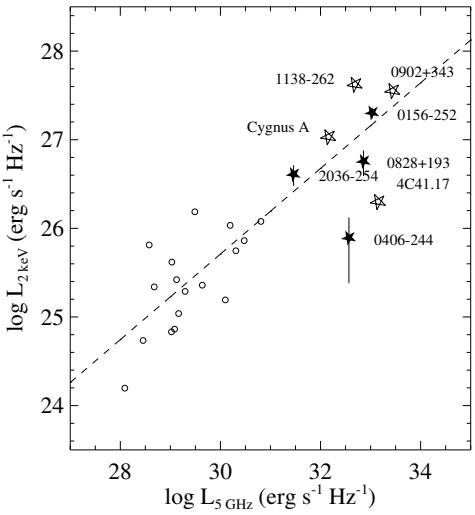

Figure 3.2 — Monochromatic X-ray luminosity versus radio luminosity. The four detected cores from our sample are indicated by filled stars. Their X-ray luminosities were corrected for galactic absorption only. Narrow line AGN from the FIRST/ROSAT sample of Brinkmann et al. (2000) are indicated by circles. The dashed line indicates the correlation for radio-loud quasars of Brinkmann et al. (2000). Open stars indicate several low (Cygnus A at $z = 0.06$) and high redshift (1138–262 at $z = 2.16$, B0902+343 at $z = 3.395$, 4C41.17 at $z = 3.798$) radio galaxies from the literature (see Carilli et al. 2002; Scharf et al. 2003; Fabian et al. 2002, and references therein). The X-ray luminosities of these sources were all corrected for intrinsic absorption.

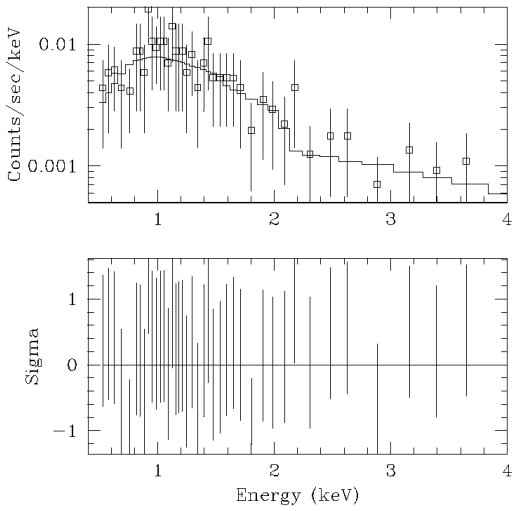

Figure 3.3 — Spectrum of the core of 0156–252, fitted with a power-law spectrum modified by absorption at the source.

tral index $\alpha_{4.7}^{8.2}$, and (ii) using the 4.7 GHz to X-ray spectral index, $\alpha_{4.7}^{X}$. The results of our analysis are indicated in Table 3.4. In the first method (indicated by dotted lines in Fig. 3.4), we can directly compare the observed X-ray flux density to the predicted synchrotron flux density based on the radio spectrum. Except for the NE lobe of 0156–252, the predicted flux densities are several orders of magnitude lower than that observed. This seems to rule out a synchrotron origin for the X-ray emission from these lobes. However, S_ν is a strong function of the spectral index, since we are extrapolating over $\sim 10^8$ decades of frequency. Only a small offset in $\alpha_{4.7}^{8.2}$ can lead to a significant under- or overprediction of the X-ray flux density. The radio spectral indices used were measured over a relatively narrow frequency range, and may be subject to errors. We estimate that the typical error in $\alpha_{4.7}^{8.2}$ is ~ 0.2, based on the comparison with a spectral index $\alpha_{1.4}^{8.2}$ determined by combining our data with data (not shown here) from the publicly available NRAO VLA Sky Survey (NVSS)[4], albeit at much lower resolution. Therefore, we attempt the second method (indicated by solid lines in Fig. 3.4). We slightly modify the above procedure and now estimate the radio flux density expected at 8.2 GHz, assuming *a priori* that the spectrum is synchrotron with a radio to X-ray spectral index $\alpha_{4.7}^{X}$. The ratio of predicted to observed 8.2 GHz flux densities is 1.0 for the NE lobe of 0156–252 and ranges from 1.2 to 1.5 for the other lobes. This indicates that the observed X-ray flux densities are consistent with synchrotron radiation, provided that the error in the integrated flux densities at 8.2 GHz are $\gtrsim 20\%$. Typically, errors in the integrated radio flux densities are of the order of $\sim 5\%$. Furthermore, the extrapolation from the radio to the X-ray using the radio spectral index *under*-predicted the observed X-ray emission in all

[4] http://www.cv.nrao.edu/nvss/

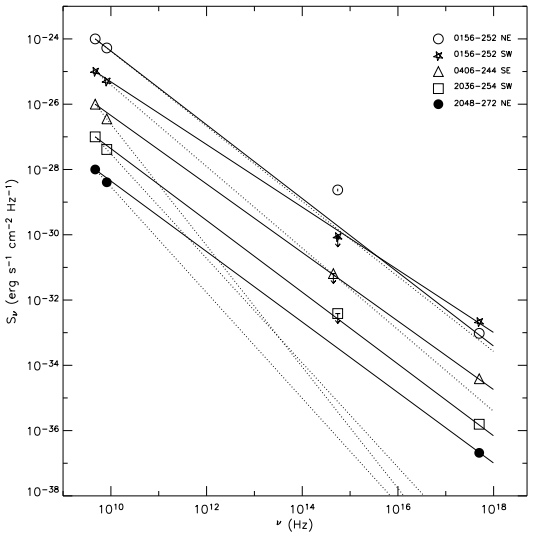

Figure 3.4 — Synchrotron model predictions. We indicate the observed radio, optical and X-ray flux densities for all components that have a positive X-ray detection. Solid lines represent synchrotron spectra constructed using the 4.7 GHz radio to X-ray spectral index, $\alpha_{4.7}^{X}$. Dotted lines indicate spectra constructed using a radio spectral index, $\alpha_{4.7}^{8.2}$. For each component, the data and models were offset for clearer visibility of the results. The multiplicative factors for 0156–252 NE, 0156–252 SW, 0406–244 SE, 2036–254 SE and 2048–272 NE were 1.1, 1.4, 0.03, 0.001, 0.0003, respectively.

cases. If there were to be a large, random error in the integrated radio flux densities, we might have expected to see some of the spectra *over*-predict the X-ray flux as well. The fact that this is not observed may indicate that the typical error in the radio flux densities is indeed only a few percent.

To further test our synchrotron models, we have extracted flux densities in the optical ($\sim$ 6000Å) using the *HST* WFPC2 observations of 0156–252, 0406–244, and 2048–272 (see Sect. 3.2). In Fig. 3.4 we have indicated 1σ upper limits on the optical emission of the SW lobe of 0156–252, the SE lobe of 0406–244 and the NE lobe of 2048–272. Although the flux densities in the optical are consistent with the synchrotron models, they are unfortunately not deep enough to rule them out.

Interestingly, the optical flux density of the NE lobe of 0156–252 is about 1 order of magnitude higher than predicted. We suspect that the optical emission in this lobe is most likely not continuum emission, but line emission. The NE lobe coincides with the peak of the Lyα intensity, and several strong emission lines common to HzRG spectra fall within the filter. Moreover, the *HST* WFPC2 image (Fig. 3.5) shows a bright component roughly following the morphology of the radio lobe, reminiscent of a shell of shocked gas. We will treat this feature in a separate discussion below.

• Synchrotron self-Compton (SSC) emission
SSC emission arises due to IC scattering of local synchrotron photons. This process dominates over other IC mechanisms when the local synchrotron photon energy density is higher than that of the external (e.g. CMB) photon field, and has been found to explain the *Chandra* hot spots of radio sources such as 3C 295 (Harris et al. 2000) and Cygnus A (Wilson et al. 2000). We calculate the energy density of the local synchrotron photon field, u_s, by integrating the radio flux density over 1 decade of frequency (1–10 GHz) and assuming a cylindrical geometry for the radio lobes. The results are listed in Table 3.5.

A detailed calculation of SSC (see e.g. Band & Grindlay (1985) for the theoretical framework) would require knowledge of the full radio spectrum and the geometry of lobes and hot spots. However, we can roughly estimate the SSC flux density in the X-ray from the ratio of the energy losses in the IC and synchrotron channels R=$u_s/u_B \approx L_{IC}/L_S$, where u_B is the energy density of the magnetic field B, and L_{IC} and L_S are the IC and synchrotron luminosities (see Harris et al. 2000; Donahue et al. 2003). We calculate u_B from the magnetic field strength B_{eq} that will make the energy densities of fields and particles approximately equal. We use the formula given by Miley (1980):

$$B_{eq} = 5.69 \times 10^{-5} \times \left[\frac{(1+k)}{\eta} \frac{(1+z)^{3+\alpha_r} S_r \nu_r^{\alpha_r}}{\theta^2 \, s \, \sin^{\frac{3}{2}} \phi} \frac{\nu_2^{\frac{1}{2}-\alpha_r} - \nu_1^{\frac{1}{2}-\alpha_r}}{\frac{1}{2}-\alpha_r} \right]^{\frac{2}{7}}, \quad (3.1)$$

where B_{eq} is in Gauss, k is the ratio of energy in

Table 3.4 — Synchrotron models.

ID	$S^{a}_{4.7GHz}$ (mJy)	$S^{a}_{8.2GHz}$ (mJy)	$\alpha^{8.2b}_{4.7}$	$S^{c}_{X,model}$ (Jy)	$S^{d}_{X,obs}$ (Jy)	$\alpha^{X\ e}_{4.7}$	$S^{f}_{8.2GHz,model}$ (mJy)	$S^{g}_{5000\mathring{A},model}$ (Jy)
0156–252								
NE	89	47	1.15	5.0×10^{-11}	0.9	1.13	48	16
SW	7	3.5	1.25	6.4×10^{-13}	1.5	0.96	4.1	9.2
0406–244								
SE	31	11	1.86	4.8×10^{-17}	1.2	1.05	17	14
NW	72	32	1.46	1.5×10^{-13}	<1.8	>1.07	<40	<24
0828+193								
NE	7	2.0	2.25	1.0×10^{-20}	<1.4	>0.96	<4.1	<8.7
SW	9	3.6	1.65	6.0×10^{-16}	<1.2	>0.98	<5.2	<8.6
2036–254								
NE	51	29	1.01	3.7×10^{-10}	<1.5	>1.06	<28	<19
SW	37	15	1.62	4.2×10^{-15}	0.8	1.08	20	11
2048–272								
NE	83	34	1.60	1.4×10^{-14}	1.3	1.10	45	20
SW	6	1.1	3.05 (2.2)	2.1×10^{-20}	<1.3	>0.96	<3.5	<7.7

[a] Integrated radio flux density at 4.7 and 8.2 GHz. The typical error is assumed to be $\sim 5\%$.
[b] Radio spectral index. The typical error is assumed to be ~ 0.2.
[c] Predicted flux density at 2 keV for a radio synchrotron model.
[d] Observed flux density at 2 keV in units of 10^{-10} Jy.
[e] X-ray to (4.7 GHz) radio spectral index.
[f] Predicted flux density at 8.2 GHz.
[g] Predicted flux density at 5000Å in units of 10^{-8} Jy.

heavy particles to that in electrons, η the filling factor, θ^2 (arcsec^2) the area taken up by the radio lobe (assumed to be a cylinder viewed broadside), s the pathlength through the lobe (kpc), and ν_1 and ν_2 (GHz) are the lower and upper cut-off frequencies of the synchrotron spectrum. We take $\phi = \pi/2$, $k = 0$ and filling factor unity so as to obtain a real minimum, and note that the results are only weakly dependent on these parameters given the 2/7 power. R, B_{eq} and $S_{X,SSC}$ are given in Table 3.5, where $B_{eq} \sim 100 - 200\ \mu$G. In all cases, the ratio of predicted X-ray SSC flux to observed X-ray flux is less than 0.4.

• Inverse-Compton (IC) scattering of the CMB
Another possibility is the up-scattering of CMB photons by relativistic electrons in the radio source. This effect is expected to become significantly more dominant at higher redshifts due to the $(1+z)^4$ increase in the energy density of the CMB ($u_{CMB} \sim 3.4 \times 10^{-11}$ erg cm^{-3} at $z \sim 2$).

The scattering electrons are assumed to belong to the same power law distribution of electrons which is responsible for the radio synchrotron emission. Therefore, the X-ray flux may be used to constrain the magnetic field strength: since the energy density of the CMB is fixed at any given z, less observed X-ray flux implies fewer electrons, so the magnetic field producing the observed radio synchrotron emission must be stronger. Using the formalism of Harris & Grindlay (1979) we calculate the magnetic field strength, B_{IC}:

Table 3.5 — Predictions for SSC and IC/CMB emission, and the equipartition and IC/CMB magnetic field strengths.

ID	area[a]	u_s^b	u_s/u_{CMB}^c	R^d	$f^e_{0.5-6keV,SSC}$	$\frac{f_{0.5-6keV,SSC}}{f_{0.5-6keV,obs}}$ [f]	B^g_{eq}	$B^h_{IC/CMB}$
0156–252								
NE	$r = 0\farcs35, l = 1\farcs0$	2.8	0.7	0.04	4.4	0.4	129	104
SW	$r = 0\farcs4, l = 0\farcs7$	0.3	0.1	0.02	0.2	0.01	67	30
0406–244								
SE	$r = 0\farcs3, l = 1\farcs2$	5.6	0.9	0.05	2.7	0.2	169	179
NW	$r = 0\farcs3, l = 1\farcs2$	6.0	1.0	0.05	5.1	> 0.2	170	> 130
0828+193								
NE	$r = 0\farcs2, l = 0\farcs7$	7.9	1.2	0.04	0.7	> 0.04	213	> 152
SW	$r = 0\farcs2, l = 0\farcs7$	3.3	0.5	0.03	0.4	> 0.03	162	> 93
2036–254								
NE	$r = 0\farcs3$	2.9	0.9	0.04	2.1	> 0.1	139	> 44
SW	$r = 0\farcs3, l = 1\farcs0$	2.7	0.8	0.04	2.0	0.2	135	135
2048–272								
NE	$r = 0\farcs5, l = 1\farcs1$	3.4	0.9	0.04	6.7	0.4	126	154
SW	$r = 0\farcs6, l = 2\farcs4$	0.3	0.1	0.02	0.3	> 0.02	61	> 117

[a] Cylinder of length l and radius r (r along the line of sight), or a sphere of radius r.
[b] Synchrotron energy density, u_S, in units of 10^{-11} erg cm^{-3}.
[c] Ratio of the synchrotron to cosmic microwave background energy densities.
[d] Ratio of the synchrotron to equipartition magnetic field energy densities, $R = u_S/u_B$.
[e] Predicted synchrotron self-Compton (SSC) flux in the 0.5–6 keV band in units of 10^{-16} erg s^{-1} cm^{-2}.
[f] Ratio of predicted SSC flux to observed X-ray flux.
[g] Equipartition magnetic field strength in μG.
[h] IC/CMB magnetic field strength in μG.

$$B_{IC}^{1+\alpha_r} = \left[\frac{(5.05 \times 10^4)^{\alpha_r} C(\alpha_r) G(\alpha_r) (1+z)^{3+\alpha_r} S_r \nu_r^{\alpha_r}}{10^{47} S_X \nu_X^{\alpha_r}} \right],$$

where B_{IC} is in Gauss, α_r is the radio spectral index, S_r and S_X are the radio and X-ray flux densities (erg s^{-1} cm^{-2} Hz^{-1}) at ν_r and ν_X (both in Hz), respectively. $C(\alpha_r)$, which is well approximated by the value 1.15×10^{31}, and $G(\alpha_r)$, which is a function that is slowly varying with α_r, can be found in Harris & Grindlay (1979). From the radio and X-ray flux densities listed in Table 3.4 we derive field strengths of $\sim 30 - 180$ μG for the components that are detected in the X-ray. The results are listed in Table 3.5, where we also give lower limits on B_{IC} for the undetected lobes.

We can compare B_{IC} to B_{eq}, which is an estimate of the magnetic field that is solely based on the observed radio synchrotron flux (see expression above). The B_{eq} field strengths are typically $\sim 100 - 200$ μG, remarkably close to the field strengths derived for the IC/CMB mechanism. The general agreement that we find between the magnetic field strengths using the two independent field estimators is consistent with the X-ray flux being produced by the IC/CMB process.

The (observed) 1–10 GHZ synchrotron flux in HzRGs is produced by relativistic electrons that have $\gamma \sim 10^{3.4-3.9}$ for $B \sim 100$ μG ($\nu_{syn} = 4.2(B/1\mu G)\gamma^2$ Hz, see Bagchi et al. 1998). The number density of relativistic electrons with energies between γ and $\gamma + d\gamma$ can be expressed as a power-law, $N(\gamma)d\gamma = N\gamma^{-s}d\gamma$ with $s = 2\alpha + 1$.

The up-scattering of CMB photons to X-ray frequencies is provided by electrons with a Lorentz factor $\gamma \sim 10^3$, since $\nu_{out} \approx \gamma^2 \nu_{in}$, and the frequency for which the energy density of the CMB peaks is $\sim 1.6 \times 10^{11} \times (1+z)$ Hz. Electrons having such Lorentz factors are highly abundant, given the extrapolation of $N(\gamma)$ to $\gamma \sim 10^3$. Note that in the SSC process described above, the X-ray emission must be produced by the up-scattering of synchrotron photons off a population of relativistic electrons having $\gamma \sim 10^{4-4.5}$. Since $N(\gamma)$ decreases strongly with increasing γ and $\alpha > 1$ for all our sources, $N(10^{4.5})$ will be several orders of magnitude lower than $N(10^3)$. Together with the fact that u_s/u_{CMB}, is around unity (see Table 3.5) this implies that the IC/CMB process will be a far more efficient process for producing X-rays at these redshifts. While the contribution of SSC to the observed X-ray flux might still be in the range of $\sim 1 - 40\%$ as detailed above, the SSC output is expected to peak around 10^{15} Hz, or in the UV part of the spectrum.

• Other mechanisms
The ambient medium in which a radio source expands is expected to be very different for HzRGs compared to radio sources at low redshift. Low redshift sources often lie in a smooth, virialised ($T \sim 10^8$ K) atmosphere. For HzRGs such a smooth medium does probably not exist because the necessary potential well has not yet formed. Instead they lie in a multiphase medium, consisting of cold (10^4 K), high density clouds embedded in low density regions approaching virial temperatures (10^{6-7}). The passage of a radio jet through the multiphase can lead to interesting phenomena, such as jet-induced star formation in the high density clouds and shock heating of lower density regions. When intermediate density regions are shocked they may cool off, emitting strong emission lines such as Lyα. The lower density gas with high filling factor will be shock heated to temperatures where the gas starts producing X-rays. Can the X-ray emission coincident with the NE lobe of 0156–252 be produced by shocks in this thermal gas? Interestingly, the NE radio lobe of 0156–252 coincides with the peak of the Lyα emission, and the *HST* WFPC2 image (see Fig. 3.5) shows evidence for a shell of shocked (emission-line) gas that follows the bend of the radio lobe.

For 1138–262, Carilli et al. (2002) propose that much of the extended X-ray emission comes from ambient gas that is shock heated by the expanding radio source. For this gas they estimate a density of 0.05 cm^{-3} and a pressure of 10^{-9} dyn cm^{-2}. This pressure is comparable to the optical line emitting gas and to minimum pressures in the radio source, with a total gas mass of about 2.5×10^{12} M$_\odot$. Carilli et al. hypothesize that the high filling factor X-ray emitting gas may confine both the radio source and the line emitting clouds. The extended X-ray luminosity associated with the NE lobe of 0156–252 is a factor 5 or so less than in 1138–262, implying a factor 5 lower total gas mass (for a fixed density) if the X-rays represent shocked gas.

So far, the discussion has been limited to the X-ray emission directly coincident with the radio lobes and hotspots. Brunetti (2000) describes a mechanism in which IC scattering of (mostly infrared) AGN photons by relativistic electrons can also produce X-ray bright emission. Such a mechanism, if it exists, may contribute significantly to the radio/X-ray alignment effect. Under the Brunetti mechanism the X-ray luminosity is expected to decrease with increasing distance from the source (i.e. the hidden quasar) producing the photons. This will result in opposite gradients in the X-ray and radio luminosities, and entails (in our case) the presence of an inner, undetected part of the radio lobe. Brunetti (2000) predicts that the receding radio lobe will produce brighter X-ray emission than the approaching lobe, because time delay makes it closer to the nucleus and because backward scattering is more effective than forward scattering. In 0406–244 (and possibly in one or several of the other sources as well) there is X-ray emission in between the core and the SE lobe. The nature of this emission could be similar to the aligned emission seen in several other high-redshift quasars and radio galaxies (e.g.

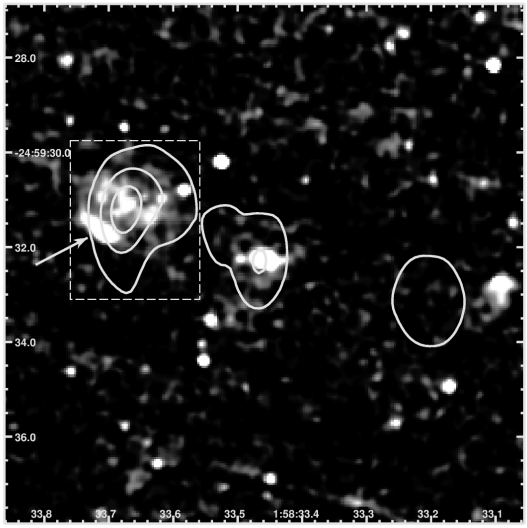

Figure 3.5 — *HST* WFPC2 F555W image of 0156–252 with 4.7 GHz VLA radio contours superimposed. We have detected extended UV line emission (most likely C III]) at the position of the NE lobe (box region). An elongated feature in the extended emission resembles a bow-shock that follows the radio lobe (arrow).

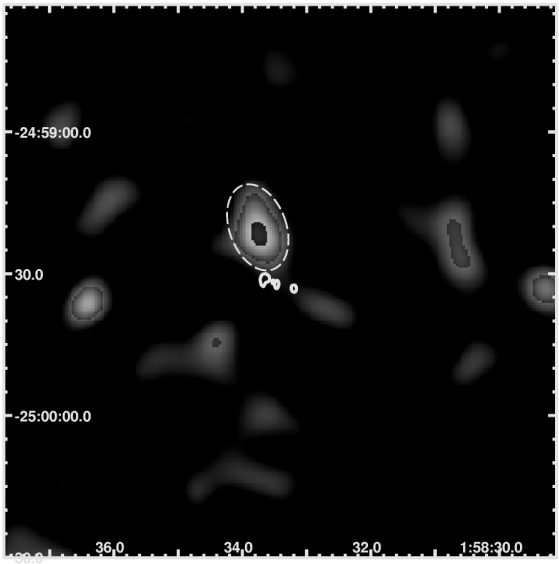

Figure 3.6 — X-ray image of the field around 0156–252 . The image was smoothed by a Gaussian (10″ FWHM), after replacing the X-ray counts due to the radio source and point sources in the field by a Poissonian background. A large region of diffuse emission (indicated by the dashed ellipse) is found just northeast to the radio galaxy (indicated by its radio contours).

Yuan et al. 2003; Fabian et al. 2003; Scharf et al. 2003) for which the Brunetti model is among the possible scenarios. However, the proposed mechanism relies on a (suggested) supply of electrons with $\gamma \lesssim 100$. Given the highly speculative amplitudes at these low energies, we will not pursue this mechanism quantitatively.

3.3.4 Thermal emission from hot (cluster) gas

An important driver for observing powerful HzRGs in the X-ray is to search for traces of thermal emission from an ICM. To test whether our data show any evidence for the presence of extended, diffuse X-ray emission we will attempt two methods:

• Smoothed fields

To obtain upper limits on the luminosity of extended regions in each field, we place 10 circles of 12″ diameter (corresponding to ~ 100 kpc at $z \sim 2$) around each radio source in regions without visible point sources. We calculate the average background count in these regions and the 1σ deviation from the mean. We use the resulting 5σ countrates to calculate 5σ upper limits on the X-ray flux of typical 100 kpc-sized areas. We assumed a Raymond-Smith thermal spectrum with $kT = 1$ keV, and used the galactic n_{HI} for each source to produce the unabsorbed flux at 0.2–6 keV. We derive an upper limit on the flux of (4–9)$\times 10^{-15}$ erg cm^{-2} s^{-1}, corresponding to luminosities of (1.5–4)$\times 10^{44}$ erg s^{-1} (for a uniform sphere).

A 5σ deviation from the background countrate over a 12″ region would easily stand out from the X-ray maps after smoothing with a large kernel. Therefore, we create smoothed images of diffuse emission. First, we remove counts that are associated with the radio galaxy by replacing all counts in a circular region encompassing the entire radio structure by the background using the task DMFILTH that maintains the Poissonian nature of the background.

The background was estimated from a large annular region around the radio source. We then run the WAVDETECT algorithm (Freeman et al. 2002) within CIAO to identify the remaining point sources and replace them by the background. The images were smoothed by a $10''$ (FWHM) Gaussian. The images were then visually inspected to look for regions of diffuse emission. We found a single detection of an extended X-ray component in the smoothed map of 0156–252 shown in Fig. 3.6. In an ovally shaped region that can be approximated by an ellipse of $10'' \times 17''$ (83×142 kpc if it were to be located at the same distance as the radio galaxy), we find 14.4 ± 5 net counts (3σ) in the energy range (0.2–6) keV with an average energy of 1.2 keV. The centroid of the region is situated approximately $12''$ to the northeast of the core of the radio source. The (observed-frame) 0.5–2 keV unabsorbed flux is 2.3×10^{-15} erg cm^{-2} s^{-1}. If this emission were to come from a sphere of thermal gas at the redshift of the radio source, it would correspond to a luminosity of 7.4×10^{43} erg s^{-1} and a mass of 10^{11} $M_\odot$ (assuming a uniform sphere). We could not identify this X-ray region with objects in any of our optical and near-infrared imaging data. Therefore, in this particular case the true nature of the emission remains highly obscure, and we cannot rule out it being due to noise. However, it illustrates the kind of emission that might be detectable in the search for high redshift cluster gas, provided a proper identification can be made.

• Stacked fields
To further search for emission from thermal gas in an annular region surrounding the radio sources, we stacked the five 20 ks exposures to obtain a single 100 ks exposure of a typical HzRG field. Each field was cleared of point sources before stacking them. In the stacked image, we then replaced the entire region inside a circle encompassing the largest of the radio sources by the background to ensure that we are not measuring extended X-ray emission associated with the radio structures. The stacked image was smoothed by a $10''$ (FWHM) Gaussian. The stacked image and the smoothed image are shown in Fig. 3.7. The region used for the background determination is indicated by the large, dashed annulus. The small circle in the center of the field indicates the size of the largest radio source. From the smoothed image, where the scales run from 2σ below the mean to 2σ above the mean, we see no evidence for diffuse, extended emission in the vicinity of the radio source(s). We obtained a radial profile of surface brightness from the stacked image using the annuli as indicated in Fig. 3.7. The radial profile out to $1'$ is consistent with zero contribution from diffuse, extended X-ray emission, as shown in Fig. 3.8. Out to a radius of $\sim 75''$ (~ 625 kpc) we measure 25 ± 85 counts. Assuming a 1 keV thermal spectrum and correcting for galactic absorption, the 3σ upper limit on the (observed) 0.2–6 keV flux inside this radius is 1.2×10^{-14} erg cm^{-2} s^{-1}, corresponding to a luminosity of $< 4 \times 10^{44}$ erg s^{-1}. We derive a central electron density of $< 7 \times 10^{-3}$ cm^{-3} and a total enclosed gas mass of $< 4 \times 10^{13} M_\odot$, assuming an isothermal sphere with a cluster β-model surface brightness profile with $\beta = 0.67$ and a core radius of 200 kpc.

3.3.5 Serendipitous X-ray sources

Pentericci et al. (2002) found evidence of an excess of *Chandra* detected X-ray sources in the vicinity of radio galaxy PKS 1138–262 at $z = 2.16$. They found 16 sources in the soft band (0.5–2 keV) with a minimum flux of 1×10^{-15} erg cm^{-2} s^{-1}, compared to 10.3 (11) calculated from the *Chandra* Deep Field South (North) for a similarly sized region, and 8 sources with fluxes $\geq 3 \times 10^{-15}$ erg cm^{-2} s^{-1} compared to 4 (5.1) for the *Chandra* Deep Fields. Although this may not be considered a substantial overdensity in angular space (an excess of $\sim 50\%$ compared to a typical cosmic variance of $20 - 30\%$), it is very significant in redshift space given that six of the serendipitous X-ray sources could be identified with previously discovered Lyα or Hα emitting galaxies in the protocluster surrounding PKS 1138–262 (Pentericci et al. 2002). Therefore, observing overdensities of X-ray sources may provide evidence for the existence of galaxy over-

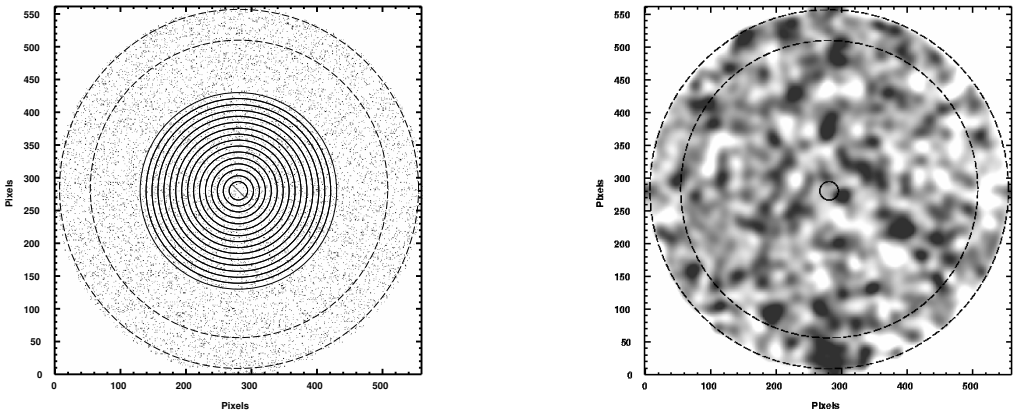

Figure 3.7 — Left: Stacked image of the five HzRG fields, after subtraction of point sources. Indicated are the annuli from which a radial surface brightness profile was extracted. The innermost circle encompasses the total extent of the largest radio source in the sample. Counts inside this region due to the radio sources have been replaced by the background, estimated from the large, dashed annular region. Right: Stacked image smoothed by a 10″(FWHM) Gaussian. Scales run from 2σ below (white) to 2σ above (black) the mean. The background region and the maximum size of the radio sources are indicated. The distinct peaks in this summed image are not traced back to significant features in any of the individual images.

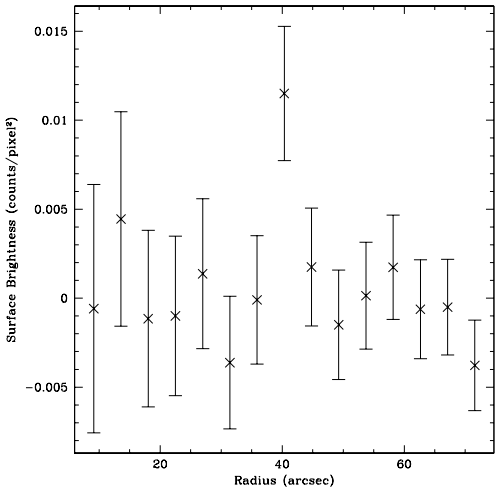

Figure 3.8 — Radial surface brightness profile extracted from the stacked image shown in Fig. 3.7.

densities associated with radio sources (see also Cappi et al. 2001).

Following Pentericci et al. (2002), we use WAVDETECT to investigate the presence of serendipitous sources in our 5 fields. Because the 2 separate observations of 0156–252 were taken at different roll angles, the corners of the ACIS-S3 chip only have half of the total 20 ks exposure time. We specify a circular region covering the maximum area having the full 20 ks depth. The circle has a radius of 3.852′, thereby covering an area of 46.62 arcmin^2. For consistency we use this region in all the fields. We limit the energy range for source detection to a maximum of 2 keV (cf. Pentericci et al. 2002) to improve the S/N (the background is lower at lower energies). For each field, we exclude the radio source, and we only consider sources that are detected with $S/N > 3$, where we define S/N as the number of background-subtracted counts divided by the root of the total counts. The net count rates of the detected sources were converted into fluxes assuming a power-law spectrum with Galactic absorption along the line of sight, and a photon index of $\Gamma = 2.0$ for the soft band. Table 3.6 lists the number of sources in each field that have soft (0.5–2 keV) fluxes of > 1.5 and $> 3 \times 10^{-15}$ erg cm^{-2} s^{-1}. Besides the number of sources found

Table 3.6 — The number of X-ray sources detected in the fields of $z \sim 2$ radio galaxies, and comparison with the field population expected based on the *Chandra* deep fields.

Field	Number of sources[a]	
	$f^b_{0.5-2keV} > 1.5$	$f^b_{0.5-2keV} > 3.0$
$0156-252$	7 (541)	5 (386)
$0406-244$	7 (541)	7 (541)
$0828+193$	5 (386)	4 (309)
$2036-254$	7 (541)	5 (386)
$2048-272$	2 (154)	1 (77)
average of fields	6 (463)	4 (309)
$1138-262$[c]	7 (541)	6 (463)
$1138-262$[d]	11 (715)	7 (541)
CDFs[e]	6/7 (470/540)	3/4 (260/330)

[a] Number of X-ray sources sources found in the field (per deg^2)
[b] Minimum source flux in units of 10^{-15} erg s^{-1} cm^{-2}
[c] Comparison 1: A 20 ks subsample of the full 40 ks observation of 1138–262
[d] Comparison 2: The full 40 ks exposure of 1138–262 (Pentericci et al. 2002)
[e] Comparison 3: The *Chandra* Deep Field South/North (Mushotzky et al. 2000; Giacconi et al. 2001)

in each 46.62 $arcmin^2$ area we give the number density per square degree between parentheses. We also list the number of sources in each bin averaged over the 5 fields. For comparison, we have run the same detection procedure on the observations of PKS 1138–262 using (i) the full 40 ks exposure, and (ii) a 20 ks subsample. We have also indicated the number of sources found in the *Chandra* Deep Fields (Mushotzky et al. 2000; Giacconi et al. 2001).

The number of bright sources in the field of 0406–244 is twice as high compared to the *Chandra* Deep Fields, and similarly high as PKS 1138–262. The number of sources in the field of 2048–272 is less than half of the number of sources in the CDFs in both flux bins. On average we find 6 and 4 sources in the > 1.5 and $> 3 \times 10^{-15}$ erg cm^{-2} s^{-1} flux bins, respectively, in good agreement with the CDFs. Based on these number counts of serendipitous sources, we find no evidence that the radio sources lie in the same cluster environments as is observed in the case of PKS 1138–262 by Pentericci et al. (2002). However, as indicated in Table 3.6 the factor ~ 2 excess of faint, $> 3\sigma$ sources in the field of PKS 1138–262 only becomes apparent in the full 40ks exposure, which may indicate that our exposures are not deep enough to make a good comparison.

To further study whether there is a preference for field sources to lie in the vicinity of high-redshift radio sources, we register the five fields using the radio source positions as centroids, and we rotate the fields around their original center so that the area of overlap is maximized. This is shown in Fig. 3.9. The number density of sources found within 1 Mpc (at $z \sim 2$) from the radio sources is 0.77 $arcmin^{-2}$, compared to 0.4 $arcmin^{-2}$ for the density of sources outside this region and 0.6 $arcmin^{-2}$ for the average density of the entire field. However, the cosmic variance of field X-ray sources is significant (25%, e.g. Cappi et al. 2001), making it impossible to conclude if serendipitous sources cluster around radio sources on the basis of the current data. Spectroscopy may confirm whether some of these sources are associated with the radio galaxies.

3.4 Summary and conclusions

We have studied X-ray observations of five radio galaxies at $2 < z < 2.6$, thereby significantly increasing the number of *Chandra* studies on high redshift radio galaxies. The main conclusions from our analysis are the following.

The X-ray emission that we detect from the nuclei are consistent with obscured power-law spectra as observed for powerful radio galaxies over a wide redshift range (e.g. Harris et al. 2000; Carilli et al. 2002; Young et al. 2002; Hardcastle et al. 2002; Scharf et al. 2003), and can be explained by the unified model in which the broad-line region of radio galaxies is obscured by a dusty torus surrounding the nucleus. For 0156–252, this conclusion is confirmed by the fact that the best-fit core spectrum is an absorbed power-law with $n(\mathrm{H\,I}) \sim 2 \times 10^{22}$ cm^{-2}.

Extended X-ray emission coincident with the radio lobes was detected for several of the

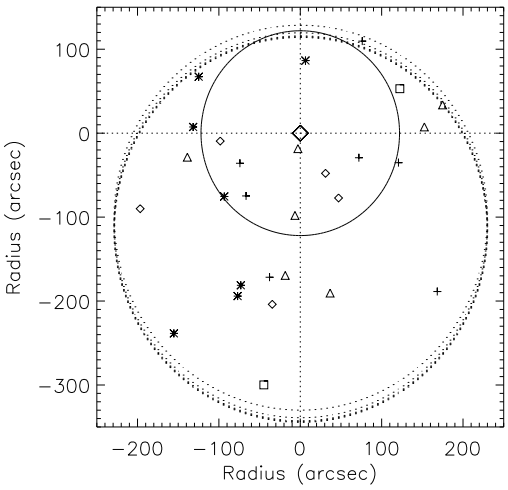

Figure 3.9 — The positions of serendipitous X-ray sources with flux $> 1.5 \times 10^{-15}$ erg cm^{-2} s^{-1} in the five HzRG fields combined. Different symbols indicate the sources in the 5 individual fields. The five images are aligned so that the radio sources (indicated by large diamond) all coincide with the position of 0156-252, and rotated to maximize the overlapping areas of the different pointings (indicated by dotted circles). The full circle indicates an area of 1 Mpc in radius around the radio source.

sources, albeit at low S/N. For all but one source, the straight extrapolation from the radio to the X-ray using the radio spectral index rules out a synchrotron origin of the emission, unless there are large errors in the radio spectral indices measured between 5 and 8 Ghz. Although the predicted X-ray synchrotron flux in source 0156–252 is close to the observed value, we have found evidence for the X-ray emission being likely associated with shocked, line emitting gas. Our observations confirm that the radio lobes of these high redshift sources may interact with the surrounding (forming) IGM.

We interpret the X-ray emission of the remaining sources as being due to the IC scattering of CMB photons off radio synchrotron electrons. This conclusion is supported by the fact that our estimates of the IC/CMB and equipartition magnetic field strengths are in good agreement. Although IC/CMB is usually dominated by other processes (e.g. SSC) at low redshift, the relative ease with which it is detected in these HzRGs may be ascribed to the $(1+z)^4$ increase in the energy density of the CMB.

This research was partly motivated by the large *RM* observed for a significant fraction of HzRGs. Can the large *RM* be caused by cluster-sized atmospheres surrounding the radio sources? Taking reasonable estimates for the pathlength (~ 100 kpc) and the cluster magnetic field strength ($\sim 10\mu$G), an intrinsic *RM* of ~ 1000 rad m^{-2} would require an ICM electron density of $\sim 1 \times 10^{-3}$ cm^{-3}. The existence of cores much denser than this is unlikely, since they would have an X-ray luminosity of $\gtrsim 10^{44}$ erg s^{-1} which has not been observed in any of the HzRGs observed to this date. Although higher density material ($n_e \sim 200$ cm^{-3}) is present in many HzRGs in the form of 10^4 K emission line clouds, the filling factor of this gas ($f_e \sim 10^{-6}$) usually implied makes it hard to reproduce the high values of *RM* (e.g. Pentericci 1999). Alternatively, the large *RM* can arise from the radio emission passing through a sheath of shocked gas surrounding the radio lobes (e.g. Athreya et al. 1998; Carilli et al. 2002,and references therein). The increased gas density implied can then explain the large *RM* if the magnetic field is ordered on scales of only a few kpc. If the X-ray emission from the NE lobe of 0156–252 is from shocked gas (as suggested by the bow shock feature seen in the *HST* WFPC2 image, see Fig. 3.5), then $B \sim 13\mu$G given the *RM* from Table 3.2 and the derived density of 0.05 cm^{-3}.

The existence of protoclusters around several HzRGs at $z \sim 2$ and higher has been established, mainly through narrow-band, Lyα imaging observations and spectroscopy. However, such studies have not yet been carried out for the sources presented in this paper. An overdensity of X-ray sources associated with the well-known galaxy protocluster around the radio source 1138–262 at $z = 2.2$ was found by Pentericci et al. (2002). We have analysed the number density of X-ray sources in each of the five *Chandra* fields. None of the fields showed evidence of large-scale structure associated with

the radio sources. This may suggest that these HzRGs are not found in the same, overdense environments as 1138–262. Similarly, employing several different methods we found no evidence for virialised gas, although the upper limits that we derive on thermal gas are not inconsistent with a direct, no-evolution extrapolation of local X-ray luminous clusters out to $z \sim 2$. Based on the X-ray observations presented in this paper alone, the current standing is that these five HzRGs are not in galaxy overdensities. However, we remark that X-ray observations are not the most effective way to search for galaxy overdensities given the relatively small number fraction of AGN expected at each particular epoch.

Recent observations of some of the most distant, X-ray luminous clusters made with the *Advanced Camera for Surveys* aboard *HST*, show a color-magnitude relation comparable to that of local clusters, indicating that early-type galaxies were already well-established by $z \sim 1$ (Blakeslee et al. 2003). Thus, the epoch in which the global relations that exist in clusters today are shaped must probably be sought at significantly higher redshifts than currently probed (i.e. $z \gtrsim 1.3$). About a dozen high redshift galaxy overdensities or protoclusters have now been found at $z \gtrsim 2$, either around HzRGs and quasars or in wide-field surveys. In the near future we may expect several candidates suitable for a detailed study with *Chandra* that could determine exactly at what redshift the virialised gas was established. However, the sensitivity required may be of the order of that of the *Chandra* deep fields, due to the extreme cosmological surface brightness dimming. While HzRGs have so far presented the best evidence of being associated with massive, forming clusters, they usually come with a plethora of non-thermal X-ray mechanisms. Especially if the radio sources lie at the bottom of the potential well that coincides with the peak of the bremsstrahlung luminosity, they may not be ideal targets for trying to detect this extremely low surface brightness emission from the ICM.

References

Athreya, R. M., Kapahi, V. K., McCarthy, P. J., & van Breugel, W. 1998, A&A, 329, 809

Bagchi, J., Pislar, V., & Lima Neto, G. B. 1998, MNRAS, 296, L23

Band, D. L. & Grindlay, J. E. 1985, ApJ, 298, 128

Belsole, E., Worrall, D. M., Hardcastle, M. J., Birkinshaw, M., & Lawrence, C. R. 2004, MNRAS, 352, 924

Blakeslee, J. P., Franx, M., Postman, M., et al. 2003, ApJ, 596, L143

Brand, K., Rawlings, S., Hill, G. J., et al. 2003, MNRAS, 344, 283

Brinkmann, W., Laurent-Muehleisen, S. A., Voges, W., et al. 2000, A&A, 356, 445

Brunetti, G. 2000, Astroparticle Physics, 13, 107

Cappi, M., Mazzotta, P., Elvis, M., et al. 2001, ApJ, 548, 624

Carilli, C. L., Harris, D. E., Pentericci, L., et al. 2002, ApJ, 567, 781

Carilli, C. L., Röttgering, H. J. A., van Ojik, R., Miley, G. K., & van Breugel, W. J. M. 1997, ApJ, 109, 1

Carilli, C. L. & Taylor, G. B. 2002, ARA&A, 40, 319

Dickey, J. M. & Lockman, F. J. 1990, ARA&A, 28, 215

Donahue, M., Daly, R. A., & Horner, D. J. 2003, ApJ, 584, 643

Eilek, J. A. & Owen, F. N. 2002, ApJ, 567, 202

Ensslin, T. A., Vogt, C., Clarke, T. E., & Taylor, G. B. 2003, ApJ, 597, 870

Fabian, A. C., Crawford, C. S., & Iwasawa, K. 2002, MNRAS, 331, L57

Fabian, A. C., Sanders, J. S., Crawford, C. S., & Ettori, S. 2003, MNRAS, 341, 729

Gehrels, N. 1986, ApJ, 303, 336

Giacconi, R., Rosati, P., Tozzi, P., et al. 2001, ApJ, 551, 624

Hardcastle, M. J., Birkinshaw, M., Cameron, R. A., et al. 2002, ApJ, 581, 948

Hardcastle, M. J. & Worrall, D. M. 1999, MNRAS, 309, 969

Harris, D. E. & Grindlay, J. E. 1979, MNRAS, 188, 25

Harris, D. E., Nulsen, P. E. J., Ponman, T. J., et al. 2000, ApJ, 530, L81

Ivison, R. J., Dunlop, J. S., Smail, I., et al. 2000, ApJ, 542, 27

Iwamuro, F., Motohara, K., Maihara, T., et al. 2003, ApJ, 598, 178

Kurk, J. 2003, Ph.D. Thesis, Universiteit Leiden

Kurk, J. D., Röttgering, H. J. A., Pentericci, L., et al. 2000, A&A, 358, L1

Leahy, J. P. 1987, MNRAS, 226, 433

McCarthy, P. J., Baum, S. A., & Spinrad, H. 1996, ApJ, 106, 281

Miley, G. 1980, ARA&A, 18, 165

Miley, G. K., Overzier, R. A., Tsvetanov, Z. I., et al. 2004, Nature, 427, 47

Mushotzky, R. F., Cowie, L. L., Barger, A. J., & Arnaud, K. A. 2000, Nature, 404, 459

Pentericci, L. 1999, Ph.D. Thesis

Pentericci, L., Kurk, J. D., Carilli, C. L., et al. 2002, A&A, 396, 109

Pentericci, L., Kurk, J. D., Röttgering, H. J. A., et al. 2000a, A&A, 361, L25

Pentericci, L., McCarthy, P. J., Röttgering, H. J. A., et al. 2001, ApJ, 135, 63

Pentericci, L., Röttgering, H. J. A., Miley, G. K., et al. 1999, A&A, 341, 329
Pentericci, L., Van Reeven, W., Carilli, C. L., Röttgering, H. J. A., & Miley, G. K. 2000b, A&AS, 145, 121
Perley, R. A. & Taylor, G. B. 1991, AJ, 101, 1623
Rosati, P., Stanford, S. A., Eisenhardt, P. R., et al. 1999, AJ, 118, 76
Rosati, P., Tozzi, P., Ettori, S., et al. 2004, AJ, 127, 230
Rudnick, L. & Blundell, K. M. 2003, ApJ, 588, 143
Rush, B., McCarthy, P. J., Athreya, R. M., & Persson, S. E. 1997, ApJ, 484, 163
Scharf, C., Smail, I., Ivison, R., et al. 2003, ApJ, 596, 105
Simard-Normandin, M. & Kronberg, P. P. 1980, ApJ, 242, 74
Smail, I., Scharf, C. A., Ivison, R. J., et al. 2003, ApJ, 599, 86
Smith, D. A., Wilson, A. S., Arnaud, K. A., Terashima, Y., & Young, A. J. 2002, ApJ, 565, 195
Stanford, S. A., Holden, B., Rosati, P., et al. 2001, ApJ, 552, 504
Stevens, J. A., Ivison, R. J., Dunlop, J. S., et al. 2003, Nature, 425, 264
Taylor, G. B., Barton, E. J., & Ge, J. 1994, AJ, 107, 1942
Tozzi, P., Rosati, P., Nonino, M., et al. 2001, ApJ, 562, 42
van Ojik, R., Röttgering, H. J. A., Miley, G. K., & Hunstead, R. W. 1997, A&A, 317, 358
Venemans, B. P., Kurk, J. D., Miley, G. K., et al. 2002, ApJ, 569, L11
Wilson, A. S., Young, A. J., & Shopbell, P. L. 2000, ApJ, 544, L27
Windhorst, R. A., Keel, W. C., & Pascarelle, S. M. 1998, ApJ, 494, L27
Young, A. J., Wilson, A. S., Terashima, Y., Arnaud, K. A., & Smith, D. A. 2002, ApJ, 564, 176
Yuan, W., Fabian, A. C., Celotti, A., & Jonker, P. G. 2003, MNRAS, 346, L7

Chapter 4

A large population of 'Lyman-break' galaxies in a protocluster at redshift $z \approx 4.1$

Abstract. The most massive galaxies and the richest clusters are believed to have emerged from regions with the largest enhancements of mass density[1–4] relative to the surrounding space. Distant radio galaxies may pinpoint the locations of the ancestors of rich clusters, because they are massive systems associated with 'overdensities' of galaxies that are bright in the Lyman-α line of hydrogen[5–7]. A powerful technique for detecting high-redshift galaxies is to search for the characteristic 'Lyman break' feature in the galaxy colour, at wavelengths just shortwards of Lyα, which is due to absorption of radiation from the galaxy by the intervening galactic medium. Here we report multicolour imaging of the most distant candidate[7–9] protocluster, TN J1338-1942 at a redshift $z \approx 4.1$. We find a large number of objects with the characteristic colours of galaxies at that redshift, and we show that this excess is concentrated around the targeted dominant radio galaxy. Our data therefore indicate that TN J1338-1942 is indeed the most distant cluster progenitor of a rich local cluster, and that galaxy clusters began forming when the Universe was only ten per cent of its present age.

G. K. Miley, R. A. Overzier, Z. I. Tsvetanov, R. J. Bouwens, N. Benítez, J. P. Blakeslee, H. C. Ford, G. D. Illingworth, M. Postman, P. Rosati, M. Clampin, G. F. Hartig, A. W. Zirm, H. J. A. Röttgering, B. P. Venemans, D. R. Ardila, F. Bartko, T. J. Broadhurst, R. A. Brown, C. J. Burrows, E. S. Cheng, N. J. G. Cross, C. De Breuck, P. D. Feldman, M. Franx, D. A. Golimowski, C. Gronwall, L. Infante, A. R. Martel, F. Menanteau, G. R. Meurer, M. Sirianni, R. A. Kimble, J. E. Krist, W. B. Sparks, H. D. Tran, R. L. White & W. Zheng

Nature, **427**, 47 (2004)

There is increasing evidence that structures of galaxies existed in the early Universe, but the detection of protoclusters at redshifts $z > 1$ using conventional optical and X-ray techniques is difficult[10–12]. Some of us have developed an efficient method for pinpointing distant protoclusters. The technique is based on the hypothesis that the most powerful known high-redshift radio galaxies are frequently associated with massive forming galaxies[13–16] in protoclusters[5]. As a first step towards testing this hypothesis, we recently conducted a large programme with the Very Large Telescope (VLT) of the European Southern Observatory to search for galaxy overdensities associated with protoclusters around luminous high-redshift radio galaxies. Deep narrow- and broad-band imaging was used to locate candidate galaxies having bright Lyα emission, and follow-up spectra have confirmed that most of these candidates have similar redshifts to the high-redshift radio galaxies. All five targets studied with the VLT to sufficient depth have > 20 spectroscopically confirmed Lyα and/or Hα companion galaxies, associated with galaxy overdensities[6,7]. Their formal velocity dispersions are a few hundred km s^{-1}, but there was not enough time since the Big Bang for them to have become virialized. The scale sizes of the structures inferred from their spatial boundaries are $\sim 3 - 5$ Mpc. Assuming that the overdensities are due to a single structure, the masses derived from the observed structure sizes and overdensities are comparable to those of clusters of galaxies in the local Universe[7]. These observations led us to hypothesize that the overdensities of Lyα galaxies around radio sources are due to the fact that they are in protoclusters.

Galaxies that emit strong Lyα comprise only a small fraction of distant galaxies, and are biased towards non-dusty objects and galaxies that are undergoing the most vigorous star formation. Only about 25% of $z \approx 3$ galaxies have Lyα equivalent widths detectable by our VLT narrow-band imaging searches[17,18]. If the overdensities of Lyα galaxies are located in protoclusters, additional galaxy populations should be present and detectable on the basis of characteristic continuum features in the galaxy spectra. The most important of these features is the sharp 'Lyman break' blueward of Lyα, caused by the absorption of the galaxy continuum radiation by neutral hydrogen clouds along the line of sight. Searching for Lyman-break galaxies is a powerful technique for finding high-redshift galaxies[11,19,20].

Because of its high spatial resolution, large field of view and excellent sensitivity, the Advanced Camera for Surveys[21] (ACS) on the Hubble Space Telescope is uniquely suited for studying the morphologies of galaxies in the protoclusters and for finding additional galaxies on the basis of the Lyman-break features in their spectra. We therefore used the ACS to observe the most distant of our VLT protoclusters, TN J1338-1942 (ref. 7) at $z = 4.1$. This is a structure with 21 spectroscopically confirmed Lyα emitters and a rest-frame velocity dispersion of 325 km s^{-1}. Images were taken through three 'Sloan' filters–g band centred at 4,750 Å, r band centred near 6,250 Å and i band centred near 7,750 Å. These filters were chosen so that their wavelength responses bracketed redshifted Lyα at 6,214 Å and were sensitive to the Lyman-break feature blueward of Lyα.

A $3.4' \times 3.4'$ field was observed, with the radio galaxy located $\sim 1'$ from the image centre. Besides the radio galaxy, this field covered 12 of the 21 known Lyα emitting galaxies in the candidate protocluster. All 12 objects were detected in both r band and i band, with i-band magnitudes ranging from 25 to 28, compared with 23.3 ± 0.03 for the radio galaxy. As illustrated in Fig. 1, these objects were either absent or substantially attenuated in the g band, and their $g - r$ colours are generally consistent with predicted values of Lyman breaks[22]. Half of the objects are extended in i_{775}, and three of these are resolved into two distinct knots of continuum emission, suggestive of merging.

We next used the Lyman-break technique to search for a population of Lyman-break galaxies in the protocluster that do not emit strong Lyα and would therefore have been undetectable in

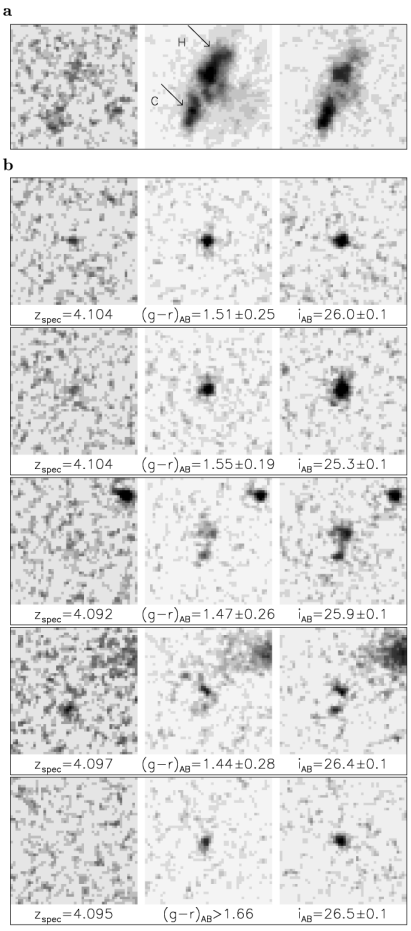

Figure 4.1 — Deep images of Lyα-emitting protocluster galaxies. Images show galaxy morphologies observed through three filters: g band (left), r band (middle) and i band (right). Each $2.5'' \times 2.5''$ image has been smoothed by a gaussian function with a fullwidth at half-maximum of 1.5 pixels ($0.074''$). The observations were carried out between 8 and 12 July 2002 with the Wide Field Channel of the ACS[21]. The total observing time of 13 orbits was split over the broad-band filters F475W (g band, four orbits), F625W (r band, four orbits) and F775W (i band, five orbits), thereby bracketing redshifted Lyα at 6,214 Å. During each orbit, two 1,200-s exposures were made, to facilitate the removal of cosmic rays. The observations were processed through the ACS GTO pipeline[26] to produce registered, cosmic-ray-rejected images. The limiting 2σ magnitudes in a 0.2-arcsec^2 aperture were 28.71 (F475W), 28.44 (F625W) and 28.26 (F775W). Object detection and photometry were then obtained using SExtractor[27]. **a**, The clumpy radio galaxy TN J1338-1942 at $z = 4.1$. This is the brightest galaxy in the protocluster and inferred to be the dominant cluster galaxy in the process of formation. Because the equivalent width of Lyα is large (~ 500 Å), the r band is dominated by Lyα. Arrows indicate the positions[8] of the radio core (C) and the northern hotspot (H). The Lyα emission is elongated in the direction of the radio emission and the large-scale Lyα halo[7] with a projected linear size of ~ 15 kpc (assuming $H_0 = 65$ km s^{-1} Mpc^{-1}, $\Omega_M = 0.3$, $\Omega_\Lambda = 0.7$). **b**, Images of five spectroscopically confirmed Lyα emitters in the protocluster. Listed below each galaxy are its spectroscopic redshift[7], the magnitude of the observed Lyman break, and the i-band magnitude. Two of the Lyα emitters are clumpy, as expected from young galaxies.

our VLT observations. Evidence for the existence of such a population was sought by analysing the number and spatial distribution of 'g-band dropout' objects–that is, objects whose colours are consistent with Lyman breaks in their spectra at the redshift of the protocluster. To investigate whether there is a statistically significant excess of such g-band dropout objects, we estimated the surface density and cosmic variance of g-band dropouts in a typical ACS field observed with the same filters and to the same depth as TN J1338-1942. We did this by cloning[23] B_{435}-band dropouts in 15 different pointings from the southern field of the Great Observatories Origins Deep Survey (GOODS)[24]. Results indicate that the number of g-band dropouts in our field is a factor of 2.5 times higher than the average number found in a random GOODS field. Taking account of the typical cosmic variance[25] in the distribution of $z \approx 4$ Lyman-break galaxies, this is a 3σ excess on the assumption that the distribution function is gaussian. Further evidence that a substantial fraction of these g-dropout objects are Lyman-break galaxies associated with the protocluster is provided by the strong concentration of the g-band dropouts in a cluster-sized region around the radio galaxy. This is illustrated in Fig. 2. More than half of the g-band dropouts are located in a region of $\sim 1'$ in radius (corresponding to a diameter of ~ 1 Mpc at $z = 4.1$). The number of g-band dropouts in this region

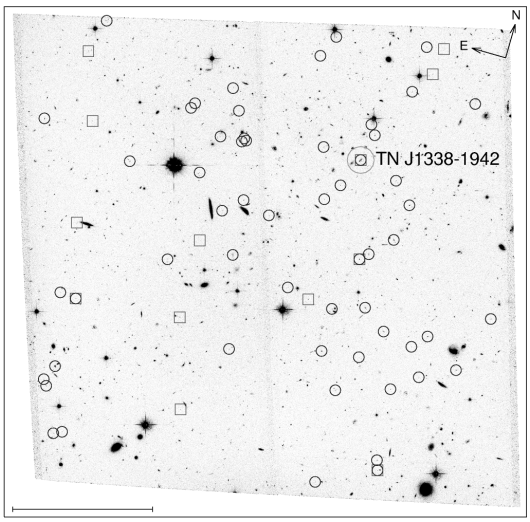

Figure 4.2 — The spatial distribution of g-band dropout objects. Superimposed on the combined $3.4' \times 3.4'$ ACS greyscale image are the locations of g-band dropout objects (blue circles), selected to have colours and magnitudes of $(g-r) \geq 1.5$, $(g-r) \geq (r-i)+1.1$, $(r-i) \leq 1$ and $i < 27$. In addition, objects were required to have a SExtractor[27] stellarity parameter of less than 0.85 to ensure that the sample was not contaminated by stars. These criteria filter galaxies having Lyman breaks at $z \approx 4$, thereby providing a sample of protocluster Lyman-break galaxy candidates. We detected 30 g-dropout objects in the field around TN J1338-1942 with $i_{775} < 26$, and 56 with $i_{775} < 27$. The number of g-band dropout objects is anomalously large, and their distribution is concentrated within a circular region of $\sim 1'$ in radius that includes the radio galaxy TN J1338-1942 (large green circle). Also shown are the positions of the spectroscopically confirmed Lyα emitters (red squares). Because the selection criteria were optimized to detect Lyman-break galaxies, some of the Lyα emitters did not fall into the formal sample of Lyman-break galaxies. The measured excess and its spatial clustering are evidence that a substantial fraction of the g-band dropout objects are Lyman-break galaxies associated with the protocluster. (See Fig. 1 legend for further details about the observations and the subsequent analysis.) Scale bar, $1'$.

is a factor of 5 times the average number encountered in similarly sized regions that are randomly drawn from the GOODS survey. This is a 5σ excess, indicating that the number of g-band dropouts in our field is anomalously high at greater than the 99% confidence level. The spatial non-uniformity of g-band dropout objects in our field becomes even more pronounced when fainter objects down to a magnitude of $i = 27$ are included (Fig. 2).

Are there alternative explanations for the observed excess of g-band dropout objects other than a population of Lyman-break galaxies at $z \approx 4.1$? An object with a Balmer break at $z \approx 0.5$ could also be observed as a g-band dropout object. However, a population of such $z \approx 0.5$ objects would also be present in the GOODS comparison sample. Although the existence of an intervening structure of Balmer-break galaxies at $z \approx 0.5$ cannot be completely ruled out, its coincidence in location with the $z \approx 4.1$ structure of Lyα galaxies and the faintness and small sizes of the observed objects make this possibility highly unlikely.

The spatial coincidence of the excess in g-band dropout objects with the previously detected overdensity of Lyα emitters around a forming massive galaxy is strong evidence that we are observing a new population of Lyman-break galaxies in a protocluster. This would mean that TN J1338-1942, at $z \approx 4.1$, is indeed the most distant known protocluster, and that distant luminous radio galaxies pinpoint the progenitors of nearby rich clusters. Such protoclusters provide an opportunity to study the development of galaxies and clusters in the early Universe. They provide samples of different galaxy populations at the same distance, whose morphologies and spectral energy distributions could be used to disentangle the evolution and star formation history of different types of galaxies. The topological information that could be derived by mapping the shapes and sizes of such protoclusters over larger areas could answer the question of whether the first protoclusters in the early Universe formed in sheets or filaments.

References

1. Kaiser, N. On the spatial correlation function of Abell clusters. Astrophys. J. 284, L9-L12 (1984).
2. White, S. D. M. & Rees, M. J. Core condensation in heavy halos–A two-stage theory for galaxy formation and clustering. Mon. Not. R. Astron. Soc. 183, 341-358 (1978).
3. Baugh, C. M., Cole, S., Frenk, C. S. & Lacey, C. G. The epoch of galaxy formation. Astrophys. J. 498, 504-521 (1998).
4. Bahcall, N. A. & Fan, X. The most massive distant clusters: Determining Ω and σ_8. Astrophys. J. 504, 16 (1998).
5. Miley, G. in Extrasolar Planets to Cosmology: The VLT Opening Symposium (eds Bergeron, J. & Renzini, A.) 32-42 (Springer, Berlin, 2000).
6. Pentericci, L. et al. A search for clusters at high redshift. II. A proto cluster around a radio galaxy at $z = 2.16$. Astron. Astrophys. 361, L25-L28 (2000).
7. Venemans, B. P. et al. The most distant structure of galaxies known: A protocluster at $z = 4.1$. Astrophys. J. 569, L11-L14 (2002).
8. De Breuck, C. et al. VLT spectroscopy of the $z = 4.11$ radio galaxy TN J1338-1942. Astron. Astrophys. 352, L51-L56 (1999).
9. De Breuck, C., van Breugel, W., Rottgering, H. J. A. & Miley, G. A sample of 669 ultra steep spectrum radio sources to find high redshift radio galaxies. Astron. Astrophys. Suppl. 143, 303-333 (2000).
10. Rosati, P. et al. An X-ray-selected galaxy cluster at $z = 1.26$. Astron. J. 118, 76-85 (1999).
11. Steidel, C. C. et al. A large structure of galaxies at redshift $z \sim 3$ and its cosmological implications. Astrophys. J. 492, 428-438 (1998).
12. Shimasaku, K. et al. Subaru deep survey IV: Discovery of a large-scale structure at redshift $\simeq 5$. Astrophys. J. 586, L111-L114 (2003).
13. De Breuck, C. et al. Optical and near-infrared imaging of ultra-steep-spectrum radio sources: The K-z diagram of radio-selected and optically selected galaxies. Astron. J. 123, 637-677 (2002).
14. Dey, A., van Breugel, W., Vacca, W. D. & Antonucci, R. Triggered star formation in a massive galaxy at $z = 3.8$: 4C 41.17. Astrophys. J. 490, 698-709 (1997).
15. Pentericci, L. et al. HST images and properties of the most distant radio galaxies. Astrophys. J. 504, 139-146 (1999).
16. van Ojik, R. *Gas in Distant Radio Galaxies: Probing the Early Universe*. Thesis, Leiden Univ. (1995).
17. Steidel, C. C. et al. Lya imaging of a proto-cluster region at $\langle z \rangle = 3.09$. Astrophys. J. 532, 170-182 (2000).
18. Shapley, A. E., Steidel, C. C., Pettini, M. & Adelberger, K. Rest-frame ultraviolet spectra of $z \sim 3$ Lyman break galaxies. Astrophys. J. 588, 65-89 (2003).
19. Steidel, C. C., Giavalisco, M., Pettini, M., Dickinson, M. & Adelberger, K. Spectroscopic confirmation of a population of normal star-forming galaxies at redshifts $z > 3$. Astrophys. J. 462, L1-L7 (1999).
20. Steidel, C. C., Adelberger, K., Giavalisco, M., Dickinson, M. & Pettini, M. Lyman-break galaxies at $z > 4$ and the evolution of the ultraviolet luminosity density at high redshift. Astrophys. J. 519, 1-17 (1999).
21. Ford, H. C. et al. Advanced camera for the Hubble Space Telescope. Proc. SPIE 3356, 234-248 (1998).
22. Madau, P. Radiative transfer in a clumpy universe: The colors of high-redshift galaxies. Astrophys. J. 441, 18-27 (1995).
23. Bouwens, R. J., Broadhurst, T. & Illingworth, G. Cloning dropouts: Implications for galaxy evolution at high redshift. Astrophys. J. 593, 640–660 (2003).
24. Giavalisco, M. et al. The Great Observatories Origins Deep Survey. Astrophys. J. Lett. 600, L93 (2004).
25. Somerville, R. S. et al. Cosmic variance in the Great Observatories Origins Deep Survey. Astrophys. J. Lett. 600, L171 (2004).
26. Blakeslee, J. P., Anderson, K. R., Meurer, G. R., Benítez, N. & Magee, D. An automatic image reduction pipeline for the Advanced Camera for Surveys. ASP Conf. Ser. 295, 257–260 (2003). 27. Bertin, E. & Arnouts, S. SExtractor: Software for source extraction. Astron. Astrophys. 117, 393-404 (1996).

Chapter 5

Star formation, morphologies and clustering of galaxies in a radio galaxy protocluster at $z = 4.1$

Abstract. We present deep $g_{475}r_{625}i_{775}z_{850}K_S$ observations towards the radio galaxy TN J1338–1942 at $z = 4.1$. The radio galaxy is a $\sim 6L^*_{z=4}$ galaxy. The data allow us to study in detail 12 spectroscopically confirmed companions previously found through their excess Lyα emission by Venemans et al. (2002). We conclude that the Lyα emitters (LAEs) are young (a few $\times 10^7$ yr), dust-free galaxies based on small sizes, steep UV slopes ($\beta \approx -2$) and blue UV-optical colors with star formation rates (SFRs) of $< 14\ M_\odot\ \mathrm{yr}^{-1}$. When stacking the K_S-band fluxes, the LAEs seem to be less massive (masses of a few $\times 10^8$ M$_\odot$) than UV-selected Lyman break galaxies (LBGs) while having comparable UV SFRs. We estimate the LAE AGN fraction to be minimal.

The field further contains 66 g_{475}-dropouts to z_{850}= 27 (5σ), 6 of which are in the LAE sample. Their SFRs, sizes, morphological parameters, UV slope-magnitude and (i_{775}–K_S) vs. K_S color-magnitude relations are all similar to those found for LBGs in the 'field'. We quantify the number density and cosmic variance of $z \sim 4$ g_{475}-dropouts extracted from a pixel-by-pixel transformation of the $B_{435}V_{606}i_{775}z_{850}$ GOODS survey to $g_{475}r_{625}i_{775}z_{850}$, and show that the field of TN J1338–1942 is richer than the average field at $\sim 3-5\sigma$ significance. The angular distribution is highly filamentary, with about half of the objects clustered in a 4.4 arcmin^2 region that includes the radio galaxy and the brightest LBGs. A second, but much less pronounced concentration of objects is seen around another $\sim 6L^*$ LBG located within the same field, for which we obtained a spectroscopic redshift of $z = 3.8$. The generally fainter LAEs appear to favour regions that are devoid of LBGs, while LBGs detected in the rest-frame optical (K_S) tend to lie in the richest region, suggesting a forming age- or mass-density relation. We compare the angular two-point correlation function, $w(\theta)$, to the signal measured in similarly sized mock samples with a built-in two-point clustering as measured for field LBGs at $z \sim 4$. We find an excess signal (2σ) at separations of $\theta \lesssim 20''$, corresponding to the typical halo size of dark matter halos hosting bright LBGs. The large galaxy overdensity, its corresponding mass overdensity and the sub-clustering at the approximate redshift of TN J1338–1942 suggest the assemblage of a $> 10^{14}$ M$_\odot$ structure, possibly a 'protocluster'.

R. A. Overzier, R. J. Bouwens, N. J. G. Cross, B. Venemans, G. K. Miley, A. W. Zirm, N. Benítez, J. P. Blakeslee,
D. Coe, R. Demarco, H. C. Ford, N. Homeier, G. D. Illingworth, J.D. Kurk,
A. R. Martel, S. Mei, H.J.A. Röttgering, Z. Tsvetanov & W. Zheng
Submitted to *The Astrophysical Journal*

5.1 Introduction

The complexity of the present-day large-scale structure originates from small seed density fluctuations, as evidenced by the discovery of the minute cosmic microwave background (CMB) anisotropies. The power spectra of the CMB and galaxy redshift surveys have given important clues to the cosmic matter budget, the density field at recombination ($z \approx 1000$) and the development of galaxies and galaxy bias. The emerging picture is that of bound objects, forming on increasingly larger spatial scales due to gravitational instabilities of the cold dark matter (CDM) in a flat, Λ-dominated universe. It is currently believed that the universe became (re-)ionized by the first light of stars and/or quasars at $z \sim 7 - 25$ (Kogut et al. 2003).

Large samples of UV-selected Lyman break galaxies (LBGs; masses of a few $\times 10^{10}$ $M_{\odot}$ (Papovich et al. 2001; Barmby et al. 2004)) at $3 < z < 5$ have been used to determine the cosmic star formation rate density well beyond $z \sim 2$ (e.g. Madau et al. 1996; Steidel et al. 1996, 1999; Ouchi et al. 2004). LBGs, as well as the partially overlapping population of Lyα emitters (LAEs), are strongly clustered at $z = 3 - 5$, and are highly biased relative to predictions for the dark matter distribution (Giavalisco et al. 1998; Adelberger et al. 1998; Ouchi et al. 2004; Lee et al. 2005; Kashikawa et al. 2005). The biasing becomes stronger for galaxies with higher rest-frame UV luminosity (Giavalisco & Dickinson 2001). In an all-encompassing census of the clustering properties of LBGs, Ouchi et al. (2004) found that the bias may also increase with redshift and dust extinction. They suggest that the reddest LBGs could be connected with the similarly strong clustered sub-mm sources (but see Webb et al. 2003) or the extremely red objects (EROs, Elston et al. 1988; McCarthy et al. 2001; Daddi et al. 2002). By comparing the number densities of LBGs to that of dark halos predicted by Sheth & Tormen (1999), they concluded that $z = 4$ LBGs are hosted by halos of $1 \times 10^{11} - 5 \times 10^{12}$ $M_{\odot}$, and that the descendants of those halos at $z = 0$ have masses that are comparable to the masses of groups and clusters. The derived halo occupation numbers of LBGs increase with luminosity from a few tenths to roughly unity, implying that there is only one-to-one correspondence between halos and LBGs at the highest masses. On the other hand, the halo occupation numbers of SCUBA sources and distant red galaxies (Franx et al. 2003) are significantly above unity, implying that for a given massive halo only 10% of the galaxies would be identified as an LBG.

The evolution of the earliest objects into present-day galaxies can currently be probed to $z \sim 7$, predominantly using the superb resolution and sensitivity of the *Advanced Camera for Surveys* on the *Hubble Space Telescope* (*HST* ACS, Ford et al. 1998). The deepest samples of high redshift galaxies currently available come from the Hubble Deep Field North and South (HDFs), the Great Observatories Origins Deep Fields (GOODS) CDF-S and HDF-N, the Hubble Ultra Deep Field (UDF) and the two UDF-Parallel Fields (UDF-Ps). Highlights from these deep studies include the discovery of significant samples of UV-bright i_{775}-dropouts – galaxies with red enough i_{775}–z_{850} to lie at $z \sim 6$ (Bouwens et al. 2003b, 2004b, 2006; Stanway et al. 2003; Yan & Windhorst 2004; Dickinson et al. 2004), allowing the determination of the cosmic star formation rate (SFR) from $z = 6$ to $z = 0$. There is a significant but modest decrease in the SFR from $z \sim 2$ out to $z \sim 6$ (Giavalisco et al. 2004a; Bouwens et al. 2005b). Studies of galaxy sizes indicate that high-redshift galaxies are compact in size ($\sim$0.″1–0.″3), while large ($\gtrsim$0.″4) low surface brightness galaxies are rare (Bouwens et al. 2004a). Furthermore, there is a clear decrease in size with redshift for objects of fixed luminosity, with a preferred redshift size scaling $(1+z)^{-1.05\pm0.21}$ (Bouwens et al. 2004a,see also Ferguson et al. (2004)). Morphological analysis of LBGs indicates that they often possess brighter nuclei and more disturbed profiles than local Hubble types degraded to the same image quality (e.g. Lotz et al. 2004). NICMOS imaging of the UDF in J_{110} and H_{160} suggest that luminous galaxies at $z \sim 7 - 8$ exist with a total UV luminosity density that is still significant compared to $z \sim 6$ (Bouwens et al. 2004c). This sug-

gests that cosmic star formation is a continuous process with only gradual changes in the UV luminosity density since $z \sim 6 - 7$.

Despite these advances in the study of the evolution of the highest redshift galaxies, *galaxy clusters* have been studied out to only $z = 1.4$ (Mullis et al. 2005). High redshift clusters are X-ray luminous due to virialized gas and galaxies moving within the cluster gravitational potential. These clusters contain populations of old and relatively massive galaxies, as well as younger star-forming galaxies (e.g. Dressler et al. 1999; van Dokkum et al. 2000; Goto et al. 2005). The scatter in the color-magnitude relation for cluster ellipticals at $z \sim 1$ is virtually indistinguishable from that at low redshift, suggesting that some of the galaxy populations in these clusters are already remarkably old (e.g. Stanford et al. 1998; Blakeslee et al. 2003a; Wuyts et al. 2004; Holden et al. 2005). Postman et al. (2005) measured the morphology-density relation (MDR) in seven $z \sim 1$ clusters that have been observed with the ACS. Evolution in the MDR appears to be primarily due to a deficit of S0 galaxies and an excess of Spiral/Irr galaxies relative to the local galaxy population, while the MDR for ellipticals exhibits no such significant evolution between $z \sim 1$ and $z = 0$.

It has become clear that the rich clusters began forming at earlier epochs than hitherto believed, and their progenitors may be found at much earlier epochs. Finding and studying these progenitors may yield powerful tests for (semi-)analytical models and *N*-body simulations of structure formation. Although these models are relatively successful in reproducing large-scale galaxy clustering and galaxy luminosity functions, they still remain relatively untested on cluster-sized scales because of the absence of observed cluster progenitors beyond $z \sim 1$.

Several good candidates for galaxy overdensities, possibly 'protoclusters[1]', have been discovered at very high redshift (e.g. Pascarelle et al. (1996); Keel et al. (1999); Francis et al. (2001); Möller & Fynbo (2001); Steidel et al. (1998, 2005); Shimasaku et al. (2003); Ouchi et al. (2005)). These structures have been found often as by-products of wide field surveys using broad or narrow band imaging. Overdensities have been found as by-products of wide field surveys with broad or narrow band imaging, but also through an established technique that is based on the hypothesis that luminous radio sources are amongst the most massive forming galaxies at high redshift (e.g. De Breuck et al. 2002; Dey et al. 1997; Pentericci et al. 2001; Villar-Martín et al. 2005) that may pinpoint the location of overdense regions. The association of distant, powerful radio galaxies with massive galaxy and cluster formation is mainly based on two observational clues. First, radio galaxies form a bright envelope in the *K*-band Hubble redshift diagram (De Breuck et al. 2002), suggesting that their host galaxies are the prime candidates for later brightest cluster galaxies (BCGs) that dominate the deep potential wells of clusters. Second, high redshift radio galaxies have companion galaxies, ranging from the red galaxy overdensities at $1.5 < z < 2$ (e.g. Sánchez & González-Serrano 1999, 2002; Thompson et al. 2000; Hall et al. 2001; Best et al. 2003; Wold et al. 2003) to the large excesses of LAEs discovered through deep narrow-band imaging and spectroscopic follow-up with the Very Large Telescope (VLT) of the European Southern Observatory (e.g. Pentericci et al. 2000; Kurk et al. 2003; Venemans et al. 2002, 2004; Venemans et al. 2005).

Building on the excesses of LAEs discovered in the vicinity of distant radio sources, we are performing a survey of candidate LBGs in such radio-selected protoclusters with ACS. In Miley et al. (2004) and Overzier et al. (2006) we reported on the detection of a significant population of LBGs around radio galaxies at $z = 4.1$ (TN J1338–1942) and $z = 5.2$ (TN J0924–2201). Here, we will present a detailed analysis of the ACS observations of protocluster TN

[1]The term *protocluster* is commonly used to describe galaxy overdensities at high redshift ($z \gtrsim 2$) with mass estimates that are comparable to those of the virialized galaxy clusters, but without any evidence for a virialized intracluster medium.

J1338–1942 at $z = 4.1$, augmented by ground-based observations with the VLT. This structure is amongst the handful of overdense regions so far discovered at $z > 4$, as evidenced by 37 LAEs that represent a surface overdensity of ~ 5 compared to other fields (Rhoads et al. 2000; Dawson et al. 2004; Shimasaku et al. 2003). The FWHM of the distribution is 625 km s^{-1}, $\sim 4\times$ narrower than the narrowband filter used. The mass overdensity as well as the velocity structure is consistent with the global properties of $z \sim 4$ protoclusters derived from N-body simulations combined with semi-analytical modeling (De Lucia et al. 2004; Venemans 2005, but see Monaco et al. (2005)). The protocluster may possibly harbor several sub-mm sources as well (De Breuck et al. 2004). The radio galaxy itself is extremely bright in the rest-frame UV/optical and the sub-mm, suggesting the formation of a massive galaxy. It has a complex morphology which we have interpreted as arising from AGN feedback on the forming ISM and a massive starburst-driven wind (Zirm et al. 2005).

The main issues that we will attemt to address include the following. What can the observational properties tell us about the star formation histories and physical sizes of LAEs and LBGs? In particular we wish to study these properties in relation to the overdense environment that the TN1338 field is believed to be associated with, analogous to galaxy environmental dependencies that have been observed at lower redshifts and are predicted by models (e.g. Kauffmann et al. 2004; Postman et al. 2005; De Lucia et al. 2006). How do the clustering and mass overdensity of the TN1338 structure compare to the 'field', and what is the relation to lower redshift galaxy clusters? In Sect. 2 we will describe the observations, data reduction and methods. We present our sample of LBGs in Sect. 3, and describe the rest-frame UV and optical properties of LBGs and LAEs. In Sect. 4 we present the results of a nonparametric morphological analysis. In Sect. 5 we will present the evidence for a galaxy overdensity associated with TN J1338–1942 and investigate its clustering properties. We conclude with a summary of the main results and a discussion in Sect. 6. We use a cosmology in which $H_0 = 72$ km s^{-1} Mpc^{-1}, $\Omega_M = 0.27$, and $\Omega_\Lambda = 0.73$ (Spergel et al. 2003). In this Universe, the luminosity distance is 37.1 Gpc and the angular scale size is 6.9 kpc arcsec^{-1} at $z = 4.1$. The lookback time is 11.9 Gyr, corresponding to an epoch when the Universe was approximately 11% of its current age. All colors and magnitudes quoted in this paper are expressed in the AB system (Oke 1971).

5.2 Observations and data reduction

5.2.1 ACS imaging

We observed one field with the ACS around the radio galaxy TN J1338–1942 (henceforward 'TN1338'). These observations were part of the ACS Guaranteed Time Observing high redshift cluster program. To search for candidate cluster members on the basis of a Lyman-break at the approximate wavelength of Lyα redshifted to $z = 4.1$, we used the Wide Field Channel to obtain imaging through the broadband filters[2] g_{475}, r_{625}, i_{775}, and z_{850}. The total observing time of 18 orbits was split into 9400 s in each of g_{475} and r_{625}, and 11700 s in each of i_{775} and z_{850}. The filter transmission curves are indicated in Fig. 7.1. The r_{625}-band may include Lyα if present.

Each orbit of observation time was split into two 1200 s exposures to facilitate the removal of cosmic rays. The data were reduced using the ACS pipeline science investigation software (*Apsis*; Blakeslee et al. 2003). After initial processing of the raw data through CALACS at STScI (bias/dark subtraction and flat-fielding), the following processing was performed by *Apsis*: empirical determination of image offsets and rotations using a triangle matching algorithm, background subtraction, the rejection of cosmic rays and the geometric correction and combining of exposures through drizzling using the STSDAS Dither package. The final science images have a scale of $0\farcs05$ pixel^{-1}. The total field of view is 11.7 arcmin^2. The radio

[2] We use g_{475}, r_{625}, i_{775} and z_{850} to denote magnitudes in the *HST* ACS passbands F475W, F625W, F775W and F850LP, respectively, or to denote the passbands themselves.

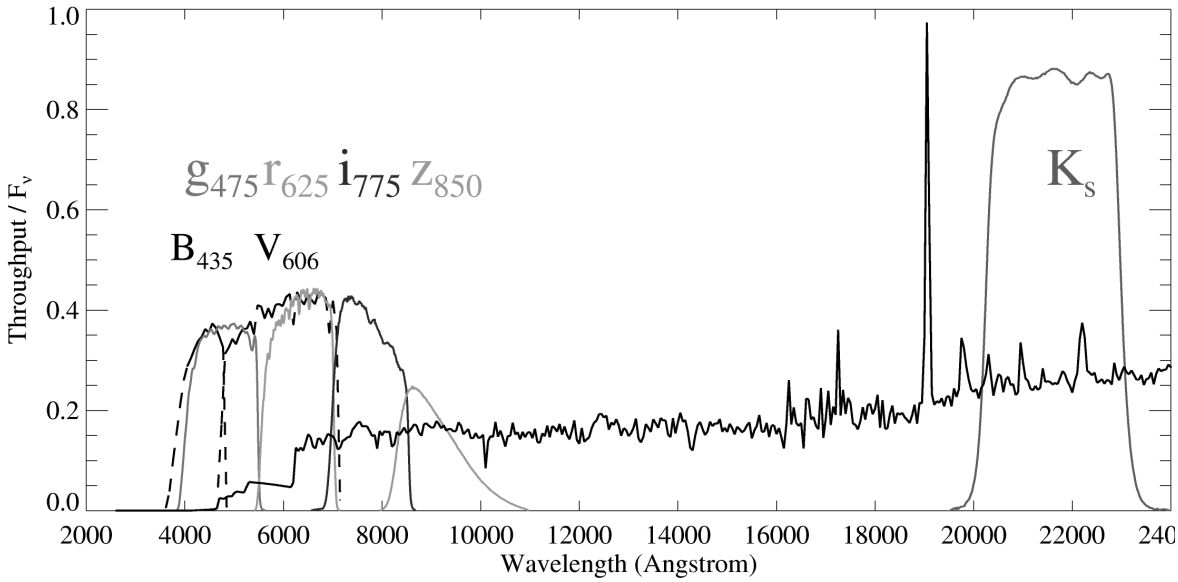

Figure 5.1 — Total effective throughput of the *HST* ACS $g_{475}r_{625}i_{775}z_{850}$ and VLT/ISAAC K_S filters. The SED template shown is the $SB2$ template from Benítez (2000) redshifted to $z = 4.1$ following the attenuation prescription of Madau et al. (1996). The GOODS $B_{435}V_{606}$ filters are indicated by dashed lines.

galaxy ($\alpha_{J2000} = 13^h38^m30^s$, $\delta_{J2000} = -19°42'30''$) is located about 1′ away from the image centre. The field further includes 12 of the 37 spectroscopically confirmed LAEs (Venemans et al. 2002; Venemans et al. 2006). The resultant color image of the field is shown in Fig. 7.2, with g_{475} in blue, r_{625} in green, and z_{850} in red. The radio galaxy clearly stands out as the sole 'green' object in the entire field, due to its prominent halo of Lyα emission observed in r_{625}(see Zirm et al. 2005).

We used the latest ACS zeropoints from Sirianni et al. (2005), and an extinction value of $E(B - V) = 0.096$ from Schlegel et al. (1998). We measured the limiting magnitudes from the RMS of noise fluctuations in 10000 square apertures of varying size that were distributed over the images in regions free of objects. A summary of the observations and the limiting magnitudes are listed in Table 5.1.

5.2.2 VLT optical spectroscopy and NIR imaging

We obtained 10 hours of VLT/FORS2 spectroscopy in service mode[3]. The instrumental setup, the seeing conditions, and the method of processing of the data were similar as described in Venemans et al. (2002); Venemans et al. (2005).

Near-infrared data in the K_S-band were obtained with VLT/ISAAC[4]. We observed a 2.′4 × 2.′4 field for 2.1 hours in March 2002, and for 5.4 hours in a partly overlapping field in 2004. After dark subtraction, flat fielding and rejection of science frames of poor quality, the data for each night was individually processed into a combined image using the XDIMSUM package in IRAF. Since only the data taken on the night of March 26 2002 was considered photometric, the combined images of the other nights were scaled to match that particular night using several unsaturated stars for reference. We derived the zeropoint based on observations of the near-

[3]Program ID: 071.A-0495(A)
[4]Program ID: 073.A-0286(A)

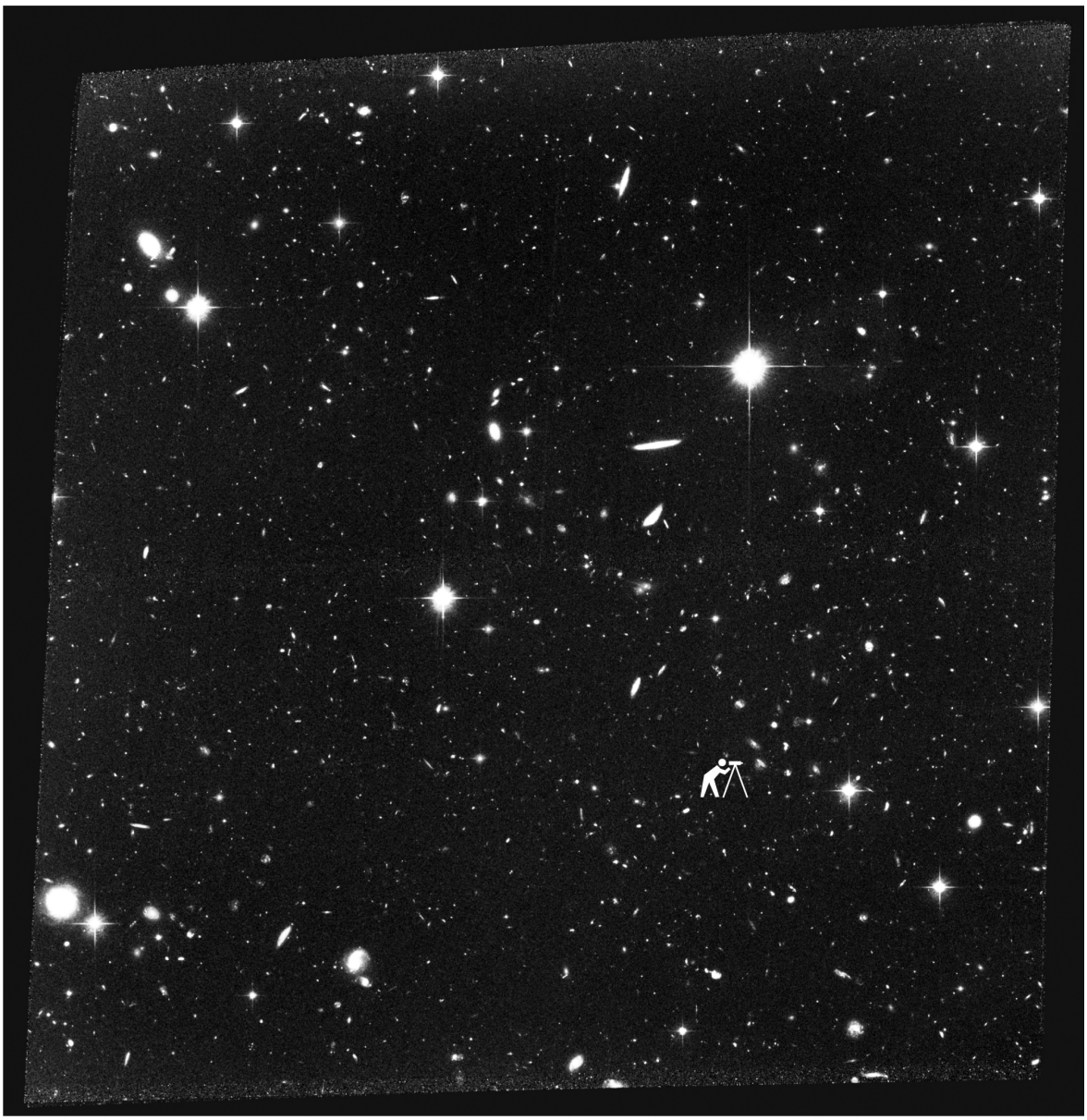

Figure 5.2 — ACS color image showing g_{475} in blue, r_{625} in green and z_{850} in red. The field measures 11.7 arcmin^2. The observer is observing the radio galaxy TN J1338–1942.

IR photometric standard FS 142. However, we had to adjust the zeropoint by 0.2 magnitudes to match the magnitudes of several 2MASS stars in the field. The seeing was $\sim$0.″5 (FWHM), and the galactic extinction in K_S was 0.036 mag.

Next, each of the combined images with the native ISAAC scale of 0.″148 pixel^{-1} was projected onto the 0.″05^{-1} pixel ACS i_{775} image using the tasks `GEOMAP`/`GEOTRAN` in `IRAF`. Using $\sim$ 25 stars in common between the ACS image

and the ISAAC images, the projection had a typical accuracy of 1.5 ACS pixels (RMS). Where available, reference stars close to the corners and edges of the images were selected so as to take out the effect of the geometric distortion on the ISAAC frames. The registered images were combined using a weighting based on the variance measured in a source-free region of each image. The limiting 2σ depth in the AB[5] system was 25.2 magnitudes for a circular aperture of 1.″4 diameter. Areas that are only covered by either the 2002 or the 2004 data are shallower by 0.5 and 0.3 magnitudes, respectively. The K_S-band data cover 81% of the ACS field, and contain the radio galaxy and 11 LAEs.

5.2.3 Object detection and photometry

Object detection and photometry was done using the `SExtractor` software package of Bertin & Arnouts (1996). We used SExtractor in double-image mode, where object detection and aperture determination are carried out on the so-called "detection image", and the photometry is carried out on the individual filter images. For the detection image we used an inverse variance weighted average of the r_{625}, i_{775} and z_{850} images, and a map of the total exposure time per pixel was used as the detection weight map. Photometric errors were calculated using the root mean square (RMS) images from *Apsis*. These images contain the absolute error per pixel for each output science image. We detected objects by requiring a minimum of 5 connected pixels at a threshold of 1.5 times the local background (S/N of > 3.35). The values for SExtractor's deblending parameters (`DEBLEND_MINCONT` $= 0.1$, `DEBLEND_NTHRESH` $= 8$) were chosen to limit the extent to which our often clumpy $z \sim 4$ g_{475}-dropouts were split into multiple objects. Our 'raw' detection catalog contained 3994 objects. We rejected all objects which had S/N less than 5 in z_{850}, where we define S/N as the ratio of counts in the isophotal aperture to the errors on the counts. The remaining 2022 objects were considered real objects, although they still contain a small fraction of artefacts.

We use SExtractor's `MAG_AUTO` to estimate total object magnitudes within an aperture radius of $2.5 \times r_{\rm Kron}$ (Kron 1980). However, when accurate color estimation is more important than estimating a galaxy's total flux, for example in the case of color-selection or when determining photometric redshifts, isophotal magnitudes are preferred because of the higher S/N and the smaller contribution of neighboring sources. Therefore we calculate *galaxy colors* from isophotal magnitudes. These procedures are optimal for (faint) object detection and aperture photometry with ACS (Benítez et al. 2004).

Optical-NIR (observed-frame) colors were derived from combining the ACS data with lower-resolution groundbased K_S data in the following way. We used PSFMATCH in IRAF to determine the 2D kernel that will match the point spread function in the ACS images to that obtained in the K_S-band, and convolved the ACS images with this kernel. The photometry was done using SExtractor in double image mode, using the K_S-band image for object detection. Colors involving the NIR data were determined in circular apertures with a diameter of 1.″4. For the radio galaxy TN J1338–1942 a circular aperture of 3.″0 diameter was used, due to its significantly larger size.

5.2.4 Aperture and completeness corrections

The photometric properties of galaxies are usually measured using source extraction algorithms such as SExtractor. We can conveniently use this software to determine aperture corrections and completeness limits as a function of e.g., the 'intrinsic' or real apparent magnitude, half-light radius (r_{hl}) or the shape of the galaxy surface brightness profile (see also Benítez et al. 2004; Giavalisco et al. 2004). To this end we populated the ACS z_{850} image with artificial galaxies consisting of a 50/50 mix of exponential and de Vaucouleurs profiles. We simulated $\sim 10,000$ galaxies with ~ 200 per simulated image to avoid over-crowding. We took uniformly distributed half-light radii in the range 0.″1–1.″0,

[5] $K_{s,AB} = K_{s,Vega} + 1.86$

Table 5.1 — Summary of observations.

Filter	Date	T_{exp}	A	Depth	
g_{475} (F475W)	July 11–12 2002	9400	0.359	28.46[a]	27.47[a]
r_{625} (F625W)	July 8–9 2002	9400	0.256	28.23[a]	27.23[a]
i_{775} (F775W)	July 8–9 2002	11700	0.193	28.07[a]	27.08[a]
z_{850} (F850LP)	July 11–12 2003	11800	0.141	27.73[a]	26.73[a]
K_S	2002,2004	27000	0.036	25.15[b]	24.16[b]

[a] Measured in 0.″45 diameter square apertures.
[b] Measured in 1.″4 diameter circular apertures.

and uniformly distributed axial ratios in the range 0.1–1.0. Galaxies were placed on the images with random position angles on the sky. Using the zeropoint we scale the counts of each galaxy to uniformly populate the range z_{850}=20–28 magnitudes. We added Poisson noise to the simulated profiles, and convolved with the z_{850} point spread function (PSF). Next, SExtractor was used to recover the model galaxies as described in Sect. 5.2.3.

Approximately 75% of the artificial galaxies were detected. In Fig. 5.3 (top left) we show the measured r_{hl} versus the input 'intrinsic' r_{hl}. Radii are increasingly underestimated as the input radii become larger, because the surface brightness gets fainter as r_{hl}^2. On average, the radius is underestimated by about 50% for a $z_{850}\sim$ 26 magnitude object with an intrinsic half-light radius of 0.″4. The discrepancy between input and output radius is generally smaller for an exponential than for a de Vaucouleurs profile.

In Fig. 5.3 (top right) we show the aperture corrections defined by the difference between the Sextractor MAG_AUTO magnitude and the total magnitude of the simulated profile. The amount of flux missed rises significantly towards fainter magnitudes, with a 0.5–1.0 magnitude correction for objects with output magnitudes of $z_{850}= 25-27$. For future reference, we also show the modeled versus the recovered ellipticities, b/a, in Fig. 5.3 (bottom left). The correspondence becomes poorer towards fainter and smaller objects, as well as more elongated ones. This is because the PSF causes small objects to appear generally rounder, and because the structural parameters are measured by SExtractor *after* convolving the image with a (Gaussian) detection kernel. Finally, in Fig. 5.3 (bottom right) we show the z_{850} completeness limits as a function of z_{850} and r_{hl}. About 50% completeness is reached at $z_{850}= 26-26.5$ for unresolved or slightly resolved sources. Note that the 50% completeness limit will lie at measured MAG_AUTO magnitudes that are fainter by 0.5–1.0 magnitude, given the significant aperture corrections presented in Fig. 5.3 (top right).

In the analysis that follows we will apply approximate corrections to the physical quantities derived from measured r_{hl} and magnitudes (e.g. physical sizes, luminosities, and SFRs) based on the above results for exponential profiles. The quoted angular sizes and magnitudes are always as measured.

5.2.5 Photometric redshift technique

We will use the Bayesian Photometric Redshift code (BPZ) of Benítez (2000) to estimate galaxy redshifts, z_B. For a complete description of BPZ and the robustness of its results, we refer the reader to Benítez (2000) and Benítez et al. (2004). Our library of galaxy spectra is based on the elliptical, intermediate (*Sbc*) and late type spiral (*Scd*), and irregular templates of Coleman et al. (1980), augmented by two starburst galaxy templates with $E(B-V)\sim 0.3$ ($SB2$) and $E(B-V)\sim 0.45$ ($SB3$) from Kinney et al. (1996), and two simple stellar population (SSP) models with ages of 5 Myr and 25 Myr from Bruzual &

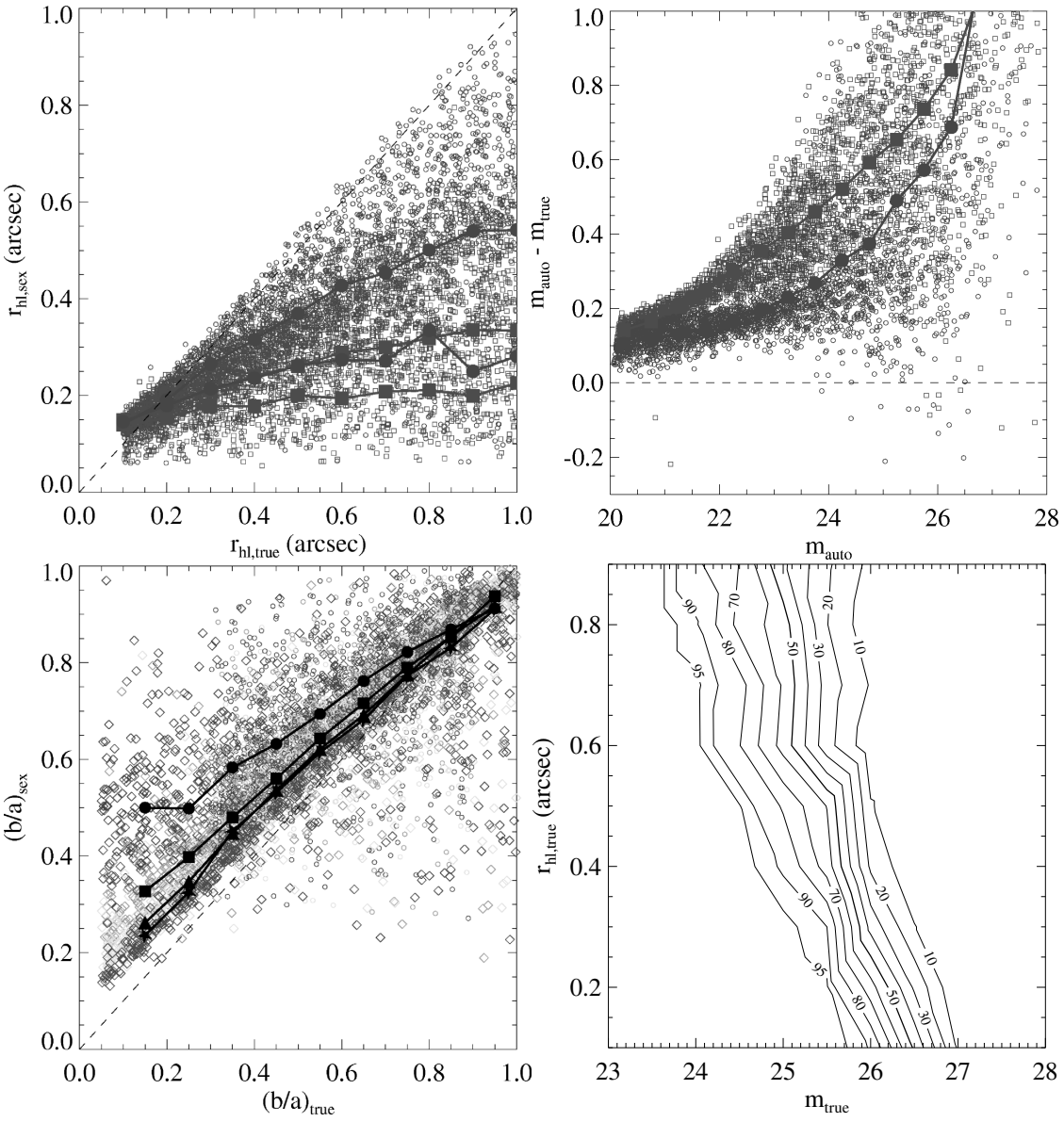

Figure 5.3 — *Top left:* Intrinsic $r_{hl,z}$ versus $r_{hl,z}$ measured by SExtractor for de Vaucouleurs profiles (squares) and exponentials (circles). The difference between intrinsic and measured radius is smaller for exponentials. The intrinsic sizes are increasingly underestimated when going to fainter magnitudes, e.g. from $z_{850}\sim$ 24 (upper lines) to $z_{850}\sim$ 26 (lower lines). – *Top right:* The difference between z_{850} MAG_AUTO and total 'intrinsic' magnitudes for de Vaucouleurs profiles (squares) and exponentials (circles). – *Bottom left:* Input vs. recovered ellipticity (b/a) for sources with $0\farcs1 < r_{hl} < 0\farcs3$ (blue), $0\farcs3 < r_{hl} < 0\farcs5$ (green), $0\farcs5 < r_{hl} < 0\farcs7$ (yellow), and $0\farcs7 < r_{hl} < 0\farcs9$ (red). – *Bottom right:* Completeness limits in z_{850} as a function of total 'intrinsic' magnitudes and r_{hl}, where completeness is defined as the ratio of the number of objects detected to the number of artificial objects added to the image (50% exponential; 50% de Vaucouleurs). The 50% completeness limit lies at an intrinsic magnitude of $\approx$ 26.5 for small sources. When expressed in terms of the measured MAG_AUTO magnitudes, the completeness limits shown here should be some $\sim$0.5–1.0 fainter, due to an underestimate of the 'total' fluxes for faint galaxies in our sample.

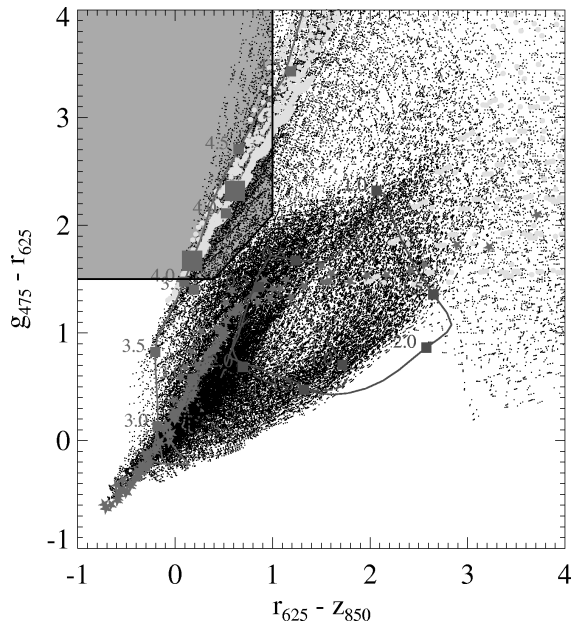

Figure 5.4 — g_{475}–r_{625} versus r_{625}–z_{850} for model SEDs (points) simulated using the Bruzual & Charlot (2003) libraries. The model parameter grid is given in Table 5.2. Galaxies at $z = 4.1$ are shown as (yellow) large solid circles. The shaded area is defined by g_{475}–$r_{625} \geq 1.5$, g_{475}–$r_{625} \geq r_{625}$–z_{850}+1.1, r_{625}–$z_{850} \leq 1.0$. The spectral tracks are an elliptical (red solid line), an Sbc (red dashed line), an Scd (red dotted line), and a 100 Myr constant star formation model with $E(B-V) = 0.0$ (blue solid line) and $E(B-V) = 0.2$ (blue dotted line). Redshifts are indicated along the tracks. The redshift of the overdensity of Venemans et al. (2002) is marked by blue squares ($z \approx 4.1$). Green stars mark the stellar locus based on the stellar SED library of Pickles (1998).

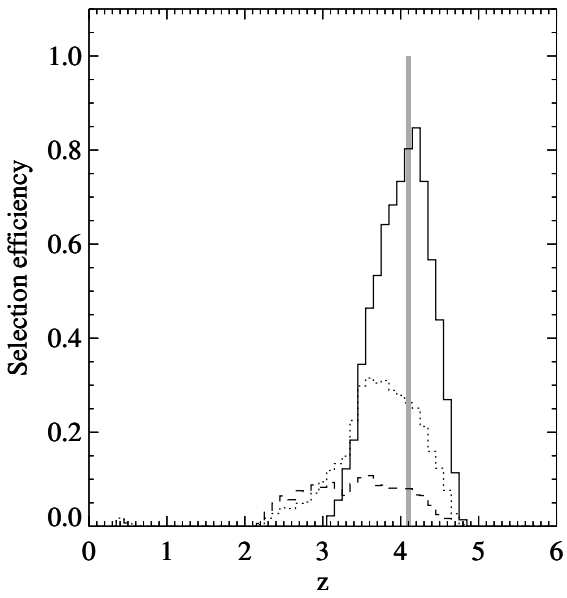

Figure 5.5 — Selection efficiency for $z \sim 4$ LBGs. The solid histogram shows the fraction of model galaxies that meet the selection criteria in each redshift bin. The dotted histogram shows the selection efficiency for model galaxies with ages less than 100 Myr and $0 < E(B-V) < 0.3$. The dashed histogram shows the fraction of models with ages greater than 0.5 Gyr selected, illustrating possible contamination of our $z \sim 4.1$ sample by relatively old galaxies at $z \sim 2.5$. Another source of contamination is the inclusion of Balmer-break objects at $z \sim 0.5$. The shaded region indicates the redshift interval ($z = 4.07 - 4.13$) of the protocluster of LAEs.

Charlot (2003). The latter two templates have been found to improve the accuracy of BPZ for very blue, young high redshift galaxies in the UDF (Coe et al. 2005). BPZ makes use of a parameter 'ODDS' defined as $P(|z - z_B| < \Delta z)$ that gives the total probability that the true redshift is within an uncertainty Δz. For the uncertainty we can take the empirical accuracy of BPZ for the HDF-N which has $\sigma = 0.06(1 + z_B)$. For a Gaussian probability distribution a 2σ confidence interval centered on z_B would get an ODDS of > 0.95. The empirical accuracy of BPZ is $\sigma \approx 0.1(1 + z_B)$ for objects with $I_{814} \lesssim 24$ and $z \lesssim 4$ observed in the $B_{435}V_{606}I_{814}$-bands with ACS to a depth comparable to our observations (Benítez et al. 2004). Note that we will be applying BPZ to generally fainter objects at $z \sim 4$ observed in $g_{475}r_{625}i_{775}z_{850}$. The true accuracy for such a sample has yet to be determined empirically. The accuracy of BPZ may be improved by using certain *priors*. We apply the commonly used magnitude prior that is based on the magnitude distribution of galaxies in real observations (e.g. the HDF).

5.2.6 Template-based color-color selection of protocluster LBG candidates

We extracted LBGs from our catalogs using color criteria that are optimized for detecting star-forming galaxies at $z \sim 4$ (Steidel et al.

1999; Ouchi et al. 2004a; Giavalisco et al. 2004a). To define the optimal selection for our filters we followed the approach employed by Madau et al. (1996). We used the evolutionary stellar population synthesis model code GALAXEV (Bruzual & Charlot 2003) to simulate a large variety of galaxy spectral energy distributions (SEDs) using: (i) the Padova 1994 simple stellar population model with a Salpeter (1955) IMF with lower and upper mass cutoffs $m_L = 0.1\ M_\odot$ and $m_U = 100\ M_\odot$ of three metallicities $(0.2Z_\odot, 0.4Z_\odot, Z_\odot)$, and (ii) the predefined star formation histories for instantaneous burst, exponentially declining ($\tau = 0.01$ Gyr) and constant ($t = 0.1, 1.0$ Gyr) star formation. We extracted spectra with ages between 1 Myr and 13 Gyr, applied the reddening law of Calzetti et al. (2000) with $E(B-V)$ of 0.0–0.5, and redshifted each spectrum to redshifts between 0.001 and 6.0, including the effects of attenuation by the IGM using the Madau et al. (1996) recipe. Galaxies were required to be younger than the age of the universe at their redshift, but other parameters were not tied to redshift. The full parameter grid is summarized in Table 5.2. While this approach is rather simplistic due to the fact that the model spectra are not directly tied to real observed spectra and luminosity functions, it is reasonable to expect that they at least span the range of allowed physical spectra. The resulting library can then be used to define a robust set of color criteria for selecting star-forming galaxies at the appropriate redshift, and estimating color-completeness and contamination (Madau et al. 1996)[6].

We extracted the model colors by folding each spectrum through the corresponding ACS filter transmission curves. No photometric scatter was applied to the models. The g_{475}–r_{625} and r_{625}–z_{850} color-color diagram is shown in Fig. 5.4. LBGs at $z \sim 4$ can be isolated from lower redshift objects by a selection that is based on the g_{475}–r_{625} and r_{625}–z_{850} colors. For comparison, we have overplotted the color-color tracks of the standard spectral types from Benítez (2000). We elected to use the r_{625}–z_{850} color in defining our selection region (instead of the r_{625}–i_{775} color used in Miley et al. (2004)) due to the greater leverage in wavelength.

The color-color region that we use to select $z \sim 4.1$ LBGs is defined as:

$$\begin{aligned} & g_{475} - r_{625} \geq 1.5, \\ & g_{475} - r_{625} \geq r_{625} - z_{850} + 1.1, \\ & r_{625} - z_{850} \leq 1.0. \end{aligned} \tag{5.1}$$

Fig. 5.5 shows the color selection efficiency as a function of redshift, defined as the number of galaxies selected in a redshift bin, divided by the total number of model galaxies in that redshift bin. The solid histogram indicates the fraction of model galaxies meeting the selection criteria. The resulting redshift distribution has an approximately constant maximum efficiency of $\sim 45\%$ for $3.5 < z < 4.5$. If we limit the model galaxies to ages less than 100 Myr and $0 < E(B-V) < 0.3$ (consistent with the average LBG population at $z \sim 3-4$ (Papovich et al. 2001; Steidel et al. 1999)), the color completeness (dotted histogram) becomes $\sim 90\%$ for models at $z \sim 4.1$. The dashed histogram shows the fraction of models with ages greater than 0.5 Gyr selected, illustrating the main sources of contamination in our $z \sim 4.1$ sample, namely from relatively old galaxies at $z \sim 2.5$ and the possible inclusion of Balmer-break objects at $z \sim 0.5$.

5.2.7 GOODS simulated images

To determine whether TN1338 is also host to an overdensity of LBGs at $z \sim 4.1$, we will want to compare the number of g_{475}-dropouts found in our ACS field with that found in a random field on the sky. Unfortunately, at present, there are not many ACS fields available, with comparable depths in g_{475}, r_{625}, and z_{850} to carry out such comparison. We therefore avail ourselves of the four-band GOODS field for our

[6] Alternatively, these quantities can be estimated with more accuracy by carrying out extensive Monte Carlo simulations of model galaxies that follow the observed size and color distributions of dropout galaxies when observed with the typical photometric quality of the data (e.g. Steidel et al. 1999; Giavalisco et al. 2004a; Bouwens et al. 2005b). However, this requires samples that are significantly larger than our current sample for TN1338.

Table 5.2 — Parameter grid of synthetic spectra.

SED Parameter	Values
Instantaneous burst	–
Exponential star formation timescales	0.01 Gyr
Constant star formation durations	0.1 1.0 Gyr
Ages	0.001 0.005 0.01 0.03 0.07 0.1 0.2
	0.3 0.4 0.5 0.6 0.7 0.8 0.9 1.0 1.1
	1.2 1.3 1.4 2.0 3.0 5.0 7.0 13.0 Gyr
Metallicities	$0.2Z_\odot$ $0.4Z_\odot$ $1.0Z_\odot$
$E(B-V)$	0.0 0.1 0.2 0.3 0.4 0.5
Redshifts	0.001 0.01 0.05 0.1 0.15 0.2 0.25 0.3 0.35
	0.4 0.45 0.5 0.55 0.6 0.65 0.7 0.75 0.8
	0.85 0.9 0.95 1.0 1.1 1.2 1.3 1.4 1.5
	1.6 1.7 1.8 1.9 2.0 2.1 2.2 2.3 2.4
	2.5 2.6 2.7 2.8 2.9 3.0 3.1 3.2 3.3
	3.4 3.5 3.6 3.7 3.8 3.9 4.0 4.1 4.2
	4.3 4.4 4.5 4.6 4.7 4.8 4.9 5.0 5.1
	5.2 5.3 5.4 5.5 5.6 5.7 5.8 5.9 6.0

control. The 3 orbit B_{435}, 2.5 orbit V_{606}, 2.5 orbit i_{775}, and 5 orbit z_{850} coverage is strikingly similar in depth and much larger in coverage, to the $g_{475}r_{625}i_{775}z_{850}$ imaging we have on TN1338, suggesting that with simple wavelength interpolation, we should be able to mirror our TN1338 selection.

Though there are many ways to have performed this interpolation, we chose to perform the interpolation directly on the ACS data itself, changing it from the observed $B_{435}V_{606}i_{775}z_{850}$ filter set to the $g_{475}r_{625}i_{775}z_{850}$ filter set. This transformation was performed on a pixel-by-pixel basis, using the formula:

$$f^Y_{i,j} = I_{i,j}\,\mathrm{g}(SED, Y, i_{775}, z) + \Sigma^{X_H}_{X=X_L}\left(\frac{|\lambda(Y)-\lambda(X)|}{\lambda(X_H)-\lambda(X_L)}\right) \times \mathrm{g}(SED, Y, X, z)\Delta f^X_{i,j}, \quad (5.2)$$

(5.3)

where $f^Y_{i,j}$ is the flux at pixel (i, j) in some band Y, $I_{i,j}$ is the best-fit fluxes in each pixel (expressed as an i_{775}-band flux), $\mathrm{g}(SED, Y, X, z)$ is a generalized k-correction from some band X to another band Y for some SED and redshift z, $\lambda(X)$ is the mean wavelength for some band X, the summation $\Sigma^{X_H}_{X=X_L}$ runs over those bands which immediately straddle the Y band, and the $\Delta f^X_{i,j}$ terms which account for the error in the fits to individual pixels. The best-fit fluxes $I_{i,j}$ were determined by minimizing

$$\chi^2 = \Sigma_X\left[\frac{I_{i,j}\mathrm{g}(SED, X, i_{775}, z) - f^X_{i,j}}{\sigma^X_{i,j}}\right], \quad (5.4)$$

where $f^X_{i,j}$ and $\sigma^X_{i,j}$ are the flux and its uncertainty, respectively, in the X band at pixel position (i, j). The error terms $\Delta f^X_{i,j}$ are equal to $f_{i,j} - \mathrm{g}(SED, X, i_{775}, z)$. The first term in Eq. 5.3 is a generalized k-correction applied to the best-fit model SEDs, while the second is an interpolation applied to the flux residuals from the fit. This is nearly identical to expressions from Appendix B1 of Bouwens et al. (2003) and represents a slight update to that procedure.

The redshifts z and SEDs SED we use for individual pixels are based upon an initial object catalog we made of each field before doing the transformation. Objects are detected off a χ^2 image (Szalay et al. 1999) constructed from the $V_{606}i_{775}z_{850}$-band using a fairly aggressive 3σ threshold and splitting parameter (SEx-

tractor DEBLEND_MINCONT=0.005). Best-fit redshifts and SEDs are then estimated for each object from the photometry. These model parameters, in turn, are assigned to all the pixels which make up these objects (according to the SExtractor deblending maps), and thus used in the transformation given by Eq. 5.3. Only pixels belonging to objects with colors $(B_{435} - V_{606}) > 0.8$, $(B_{435} - V_{606}) > 0.6(V_{606} - z_{850}) + 0.5$, $(B_{435} - V_{606}) > 3.375(V_{606} - z_{850}) - 4.575$ were transformed.

Since our ACS reduction of the TN1338 field had a different pixel scale (i.e., 0.″05) than that of the GOODS v1.0 reduction (0.″03: Giavalisco et al. 2004), we did not use that reduction as the basis for our simulation of the CDF-S GOODS field. Instead, we made use of an independent reduction we had made of the GOODS field with *Apsis*. That reduction was performed on a 0.″05 grid, using a procedure nearly identical to that described in Bouwens et al. (2005b), but using a 'Lanzcos3' kernel (which matches the TN1338 ACS reduction).

5.3 Properties of LBGs and LAEs in TN1338

We will apply the color-color section defined in the previous section to the TN1338 field to select a sample of candidate $z \sim 4.1$ LBGs (g_{475}-dropouts) and study their properties in Sect. 5.3.1. In Sect. 5.3.2 we will study the same properties for the sample of $z = 4.1$ LAEs within the ACS field.

5.3.1 The g_{475}-dropout sample

Using the selection criteria defined in Eq. 5.1 we extracted a sample of LBGs from the TN1338 field. In total there are 66 such objects in TN1338 with z_{850}<27.0, 51 of which have z_{850}<26.5, and 32 of which have z_{850}<26.0. The color-color diagram is shown in Fig. 7.7. Although the stellar locus (based on Pickles (1998)) lies outside the region defined by our selection criteria, we required objects to have a SExtractor stellarity index of < 0.85 (non-stellar objects with high confidence). This should exclude essentially all star-like objects from our sample.

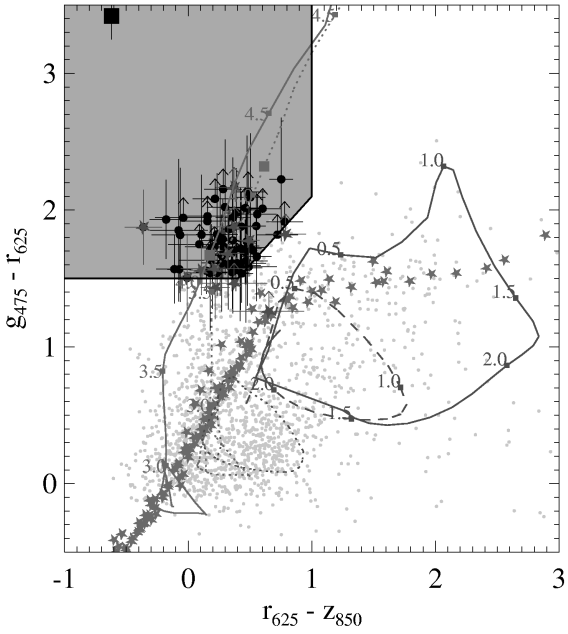

Figure 5.6 — Color-color diagram of g_{475}-dropouts in TN1338 (circles) and the detection catalog (points). The shaded region shows our selection window (Eq. 1). Confirmed LAEs from Venemans et al. (2002) are marked by red stars, and the radio galaxy by the square. See the caption of Fig. 5.4 for further details.

5.3.1.1 *Star formation rates*

The characteristic luminosity, $L^*_{z=4}$, of the LBG luminosity function at $z \sim 4$ corresponds to $z_{850} \sim 25.0$ (Steidel et al. 1999). The sample contains two objects, one of which is the radio galaxy, with a luminosity of $\sim 6L^*$ ($i_{775} \approx 23$). The remainder of the sample spans luminosities in the range $\sim 0.4 - 2L^*$, where we have applied aperture corrections of up to ~ 1 magnitude based on the exponential profiles in Fig. 5.3.

We calculated SFRs from the emission-line free UV flux at 1500 Å (i_{775}) using the conversion between luminosity and SFR for a Salpeter initial mass function (IMF) given in Madau et al. (1998): SFR ($M_\odot$ yr^{-1}) = $L_{1500Å}$ (erg s^{-1} Hz^{-1})/8×10^{27}. For ages that are larger than the average time that late-O/early-B stars spend on

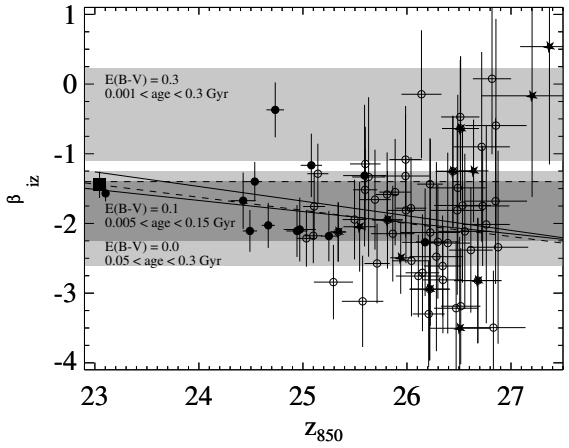

Figure 5.7 — z_{850} versus β_{iz} for g_{475}-dropouts detected/undetected in K_S (filled/open circles), LAEs (stars), and the radio galaxy (square). The best-fit linear relations are indicated (thick lines, see text for details). The thin solid line is the relation for B_{435}-dropouts (Bouwens et al. 2005b). The best-fit SED from Papovich et al. (2001) redshifted to $z = 4$ has $\beta_{iz} \approx -1.4$ (thin dashed line). Shaded regions are for $E(B-V) = 0.0$ with ages between 0.05 and 0.3 Gyr (bottom light shaded region), $E(B-V) = 0.1$ with ages between 0.005 and 0.15 Gyr (dark shaded region), and $E(B-V) = 0.3$ with ages between 0.001 and 0.3 Gyr (top light shaded region), assuming an exponential star formation history ($\tau =$ 10 Myr) with $0.2Z_\odot$ metallicity and a Salpeter IMF.

the main sequence, the UV luminosity is proportional to the SFR, relatively independent of the prior star formation history. The SFRs are listed in Table 7.3. The radio galaxy and object #367 each have a SFR of $\sim 95\ M_\odot\ \mathrm{yr}^{-1}$. The median SFR of the entire sample is $\sim 8\ M_\odot\ \mathrm{yr}^{-1}$. Although we assumed here that the LBGs are dust-free, one could multiply the SFRs by a factor of 2.5 to correct for an average LBG extinction of $E(B-V) \approx 0.1$ (see next section) giving a median SFR of $\sim 20\ M_\odot\ \mathrm{yr}^{-1}$.

5.3.1.2 UV Continuum colors

We calculate the UV continuum slopes from the i_{775}–z_{850} color. This color spans the rest-frame wavelength range from ~ 1400 Å to ~ 2000 Å. We assume a standard power-law spectrum with slope β ($f_\lambda \propto \lambda^\beta$, so that a spectrum that is flat in f_ν has $\beta = -2$). We calculate

$$\beta_{iz} = \frac{\mathtt{log}_{10}\frac{Q_{850}}{Q_{775}} - 0.4(i_{775} - z_{850})}{\mathtt{log}_{10}\frac{\lambda_{775}}{\lambda_{850}}} - 2\ , \quad (5.5)$$

where λ_{775} and λ_{850} are the effective bandpass wavelengths, and Q_{775} and Q_{850} are the fractions of the continuum fluxes remaining after applying the recipe for foreground neutral hydrogen absorption of Madau (1995). The break at rest-frame 1216 Å only starts to enter the i_{775}-band for galaxies at $z \gtrsim 4.7$. Thus Q_{775} and Q_{850} are unity and β will be relatively independent of redshift for $3.5 \lesssim z \lesssim 4.5$. The uncertainties on β_{iz} were obtained by propagating the individual errors on the measured magnitudes. The measured slopes are plotted in Fig. 5.7. Excluding the two brightest sources, we find $\langle \beta_{iz} \rangle = -1.95$. This is significantly bluer than that found by Papovich et al. (2001), although it is consistent at the bright magnitude end where the comparison with L^* galaxies is appropriate (thin dashed line).

We have modeled the dependencies of the slope on age and dust using an exponential star formation history ($\tau = 10$ Myr) with $0.2Z_\odot$ metallicity and a Salpeter IMF. For a constant $E(B-V) \approx 0.0$ the range of slopes favours ages in the range 50–300 Myr. A high dust content ($E(B-V) \approx 0.3$) is incompatible with the majority of the slopes observed. A linear fit to the data gave a slope-magnitude relation of $\beta_{iz} = (-0.16 \pm 0.05)(z_{850} - 25) - 1.84$ (thick solid line), which remains virtually unchanged when we excluded the two brightest objects (thick dashed line). There could be a possible higher incompleteness towards faint, relatively red objects (e.g. Ouchi et al. 2004a). However, the effect is likely to be much smaller than the observed correlation as shown by simulations incorporating B_{435}-dropout selection in GOODS (Bouwens et al. 2005b). Our relation is in good agreement with that of B_{435}-dropouts in GOODS of $-0.21 \pm 0.03\ \mathrm{mag}^{-1}$ found by Bouwens et al. (2005b). The best-fit relation spans ages in the range 5–150 Myr for a constant $E(B-V) \approx 0.1$. A similar slope-magnitude relation is also observed in other works (Meurer et al. 1999; Ouchi

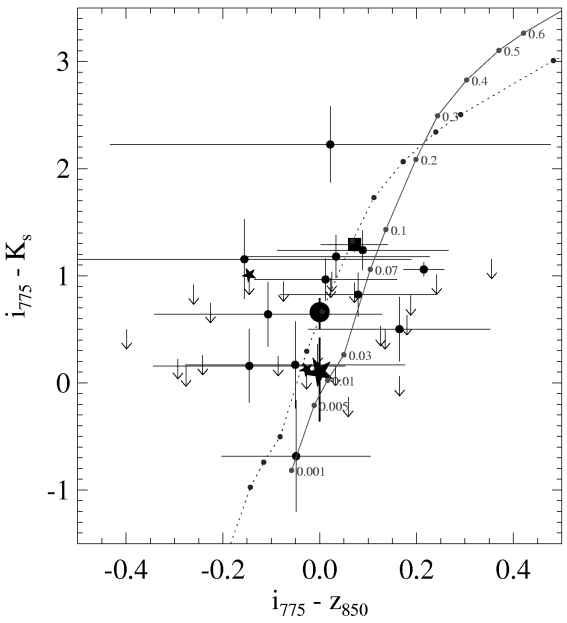

Figure 5.8 — Rest-frame UV-optical colors of the g_{475}-dropouts (circles), the LAEs L9 and L25 (stars), and the radio galaxy (square). Arrows indicate 2σ limits for non-detections in K_S (errors omitted for clarity). Lines indicate the colors of a $\tau = 10$ Myr SED ($0.2Z_{\odot}$) with ages in Gyr along the track for $E(B-V) = 0.0$ (dotted) and $E(B-V) = 0.15$ (solid). The large circle was obtained from a K_S-band stack of 12 g_{475}-dropouts having $25.3 < i_{775} < 26.4$. The large star was obtained from a K_S-band stack of 5 LAEs within a similar magnitude range. Their i_{775}–K_S colors differ by ~ 0.7 magnitude.

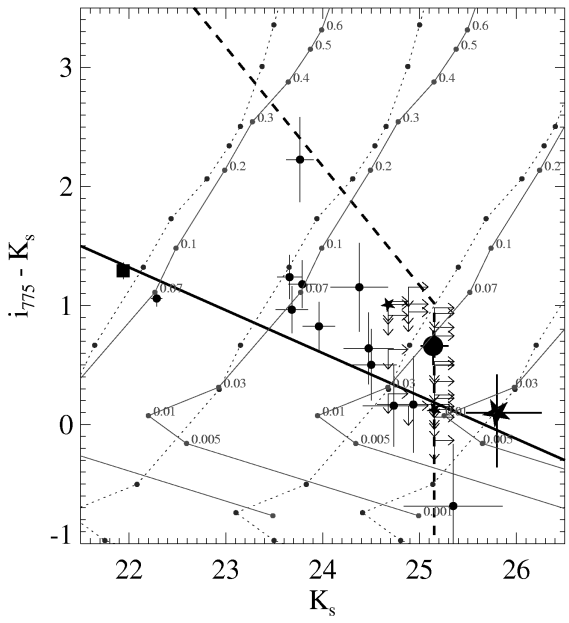

Figure 5.9 — Color magnitude diagram of the g_{475}-dropouts (circles). The dashed line indicates the approximate 2σ detection limits. The tracks are for $\tau = 10$ Myr SEDs with different stellar masses (at $t_{sf} = \infty$) of 0.03, 0.1, 0.5 and $2{\times}10^{10}$ $M_{\odot}$ for $E(B-V) = 0.0$ (dotted) and $E(B-V) = 0.15$ (solid). The thick solid line indicates the 'blue envelope' of Papovich et al. (2004), and suggests a color-magnitude relation in which luminosity correlates with either age or dust. See the caption of Fig. 5.8 for further details.

et al. 2004a) and may imply a mass-extinction or a mass-metallicity relation rather than a relation with age (Bouwens et al. 2005b). Interpreting the slope-magnitude relation as a mass-extinction relation implies $E(B-V) \approx 0.13$ at $z_{850} \approx 23$ and $E(B-V) \approx 0.0$ at $z_{850} \approx 27$ for a fixed age of 70 Myr.

5.3.1.3 *Rest-frame UV to optical colors*

At $z \sim 4.1$, the filters i_{775}, z_{850} and K_S probe the rest-frame at ∼1500 Å, 1800 Å and 4300 Å, respectively. We detected 13 of the g_{475}-dropouts in the K_S-band at $> 2\sigma$. In Fig. 5.8 we show the i_{775}–K_S versus i_{775}–z_{850} color diagram. i_{775}–K_S color is more sensitive to the effects of age and dust than i_{775}–z_{850}, due to its longer lever arm in wavelength. Comparing the colors to the best-fit LBG SED from Papovich et al. (2001) redshifted to $z \sim 4$ shows that the observed colors are consistent with ages in the range 10-100 Myr, although there will be degeneracy with dust. Non-detections in the K_S-band suggests that more than 50% of the g_{475}-dropouts have ages less than 70 Myr, with a significant fraction less than 30 Myr. The radio galaxy is among the reddest objects, although it has large gradients in i_{775}–K_S among its various stellar and AGN components (see Zirm et al. 2005). The age of ∼ 100 Myr was derived based on its average i_{775}–K_S color, it may actually consist of stellar components that are both significantly older and younger than 100 Myr, and does not rule out a significantly higher mass-weighted age for the galaxy as a whole.

In Fig. 5.9 we plot the i_{775}–K_S versus K_S color-magnitude diagram. Papovich et al. (2004) found evidence for a trend of generally redder colors for galaxies that are brighter in K_S in GOODS. The effect is not likely to be a selection effect because the objects are selected in the UV. Papovich et al. (2004) suggest that age and/or dust of LBGs at $z \sim 3-4$ may increase with increasing rest-frame optical luminosity. Our data are consistent with that conclusion.

5.3.1.4 Sizes

We measured r_{hl} in z_{850} using SExtractor by analysing the growth curve for each object out to $2.5 \times r_{\texttt{Kron}}$. Excluding the exceptionally large radio galaxy, the measured radii range from unresolved ($\sim 0\farcs07$) to $0\farcs42$, corresponding to physical diameters of $\lesssim 7$ kpc at $z \sim 4$. The average radius is $0\farcs17$ or ~ 1.4 kpc. If we divide our sample into two magnitude bins each containing an approximately equal number of objects (achieved by placing a cut at z_{850}=26.1 magnitude), the mean r_{hl} are $0\farcs21 \pm 0\farcs01$ (error represents the standard deviation of the mean) and $0\farcs14 \pm 0\farcs01$ in the bright and faint bins, respectively. The difference is expected to be largely due to a larger flux loss in the fainter sample (see Fig. 5.3), although fainter galaxies are also likely to be smaller because of the $r_{200} \sim V_c \sim L^{1/3}$ luminosity-size relationship, where r_{200} is the virial radius and V_c is the circular dark matter halo velocity (see Mo et al. 1998).

The i_{775}-band morphologies of the g_{475}-dropouts are shown in Fig. 5.10. A separate section will be devoted to a nonparametric analysis of these morphologies and a comparison to field samples (see Sect. 5.4).

5.3.2 Lyα galaxies

Venemans et al. (2002) found an overdensity of LAEs ($EW_{0,Ly\alpha} > 15$Å), all spectroscopically confirmed to lie within 625 ± 150 km s^{-1} of $z = 4.11$. All of the 12 LAEs in the ACS field have been detected in r_{625}, i_{775} and z_{850} (see Table 7.2).

5.3.2.1 Star formation rates

The z_{850} magnitudes are in the range 25.3–27.4, corresponding to a luminosity range of $\sim 0.2-1.0L_*$. The SFRs are $\sim 1-14$ $M_\odot$ yr^{-1} with a median of 5.1 $M_\odot$ yr^{-1} (not including the effect of dust). Venemans et al. (2005) calculated the SFRs from Lyα using SFR ($M_\odot$ yr^{-1}) $= 8.7L_{Ly\alpha}$ (erg s^{-1})$/1.12 \times 10^{41}$, from Kennicutt (1998) with the standard assumption of case B recombination (Brocklehurst 1971,$L_{H\alpha}/L_{Ly\alpha} = 8.7$ for gas that is optically thick to H I resonance scattering and no dust). In general, we find good agreement between the SFRs calculated from the UV compared to Lyα with a median UV-to-Lyα SFR ratio of 1.3.

5.3.2.2 UV continuum colors

The UV slopes, β_{iz}, of the Lyα emitters are indicated in Fig. 5.7 (stars). The slope can be constrained relatively well for the four brightest emitters, which have -2.1 ± 0.4, -2.0 ± 0.6, -1.9 ± 0.7, and -2.5 ± 0.5. The LAE slopes scatter around the β_{iz}-magnitude relation for the g_{475}-dropouts found in Sect. 5.3.1.2, with a sample average of -1.7 ± 1.2. These slopes are consistent with a flat (in f_ν) continuum, thereby favouring relatively low ages and little dust.

5.3.2.3 Rest-frame UV to optical colors

None of the 11 LAEs covered were detected in K_S at the $> 2\sigma$ level. We created a stack of the K_S-band fluxes for the 5 LAEs that fell in the deepest part of our NIR image. The subsample had $25.3 < z_{850} < 26.4$ and $\langle(i_{775}-z_{850})\rangle \approx 0.0$. We obtained a 3σ detection for the stack finding $K_S = 25.8^{+0.46}_{-0.32}$ and hence i_{775}–$K_S \approx 0.0$. We compared this to a stack of 12 g_{475}-dropouts with a similar range in z_{850} magnitudes and i_{775}–z_{850} colors, which gave a 7σ detection with $K_S = 25.14^{+0.16}_{-0.13}$ and i_{775}–$K_S \approx 0.7$. The results from the stacks have been indicated in Figs. 5.8 and 5.9. The difference in the i_{775}–K_S color is significant at $\sim 2\sigma$. A difference between the K_S luminosities of LBGs and LAEs is highly interesting given the very similar UV magnitudes/colors of the two subsamples. A possible interpretation is

Table 5.3 — Properties of the $z \sim 4$ Lyman break sample.

ID	α_{J2000}	δ_{J2000}	$(g_{475}-r_{625})^a$	$(r_{625}-z_{850})^a$	$(i_{775}-z_{850})^a$	$z_{850}{}^b$	$r_{hl,z}$	SFR^c_{UV}
2707/RG	13:38:26.05	–19:42:30.47	3.42 ± 0.17	-0.61 ± 0.03	0.09 ± 0.03	23.05 ± 0.05	$0''.62$	$93.7^{+2.71}_{-2.63}$
367	13:38:32.75	–19:44:37.27	1.70 ± 0.06	0.52 ± 0.02	0.07 ± 0.02	23.10 ± 0.02	$0''.20$	$94.7^{+1.10}_{-1.09}$
1991	13:38:27.84	–19:43:15.19	1.88 ± 0.25	0.43 ± 0.08	0.05 ± 0.07	24.43 ± 0.12	$0''.42$	$28.8^{+2.24}_{-2.08}$
3018	13:38:24.31	–19:42:58.06	1.73 ± 0.14	0.29 ± 0.06	-0.01 ± 0.05	24.49 ± 0.07	$0''.20$	$34.2^{+1.19}_{-1.15}$
3216	13:38:22.37	–19:43:32.41	1.86 ± 0.15	0.33 ± 0.05	0.10 ± 0.05	24.54 ± 0.06	$0''.21$	$26.3^{+0.92}_{-0.89}$
3116	13:38:24.21	–19:42:41.85	1.55 ± 0.14	0.36 ± 0.06	-0.00 ± 0.06	24.67 ± 0.06	$0''.20$	$25.4^{+0.93}_{-0.90}$
959	13:38:32.67	–19:43:3.673	1.88 ± 0.25	0.55 ± 0.07	0.28 ± 0.07	24.73 ± 0.09	$0''.23$	$18.2^{+1.19}_{-1.12}$
2913	13:38:23.68	–19:43:36.59	1.77 ± 0.22	0.47 ± 0.07	-0.01 ± 0.06	24.94 ± 0.10	$0''.26$	$24.2^{+1.16}_{-1.11}$
2152	13:38:26.92	–19:43:27.60	1.56 ± 0.17	0.15 ± 0.08	-0.01 ± 0.08	24.97 ± 0.15	$0''.32$	$22.4^{+1.74}_{-1.62}$
2799	13:38:24.88	–19:43:7.415	1.72 ± 0.17	0.19 ± 0.07	-0.03 ± 0.07	25.03 ± 0.09	$0''.18$	$18.6^{+0.97}_{-0.92}$
2439	13:38:25.35	–19:43:43.65	1.69 ± 0.24	0.46 ± 0.09	0.14 ± 0.08	25.08 ± 0.10	$0''.25$	$17.7^{+1.03}_{-0.97}$
3430	13:38:21.21	–19:43:41.99	1.74 ± 0.22	0.49 ± 0.08	-0.03 ± 0.07	25.10 ± 0.09	$0''.16$	$17.0^{+0.88}_{-0.83}$
2407	13:38:24.35	–19:44:29.15	1.54 ± 0.21	0.43 ± 0.09	0.04 ± 0.08	25.11 ± 0.11	$0''.26$	$15.6^{+1.04}_{-0.97}$
2839	13:38:25.90	–19:42:18.39	2.23 ± 0.45	0.75 ± 0.09	0.12 ± 0.07	25.14 ± 0.10	$0''.15$	$15.6^{+0.98}_{-0.92}$
1252	13:38:31.98	–19:42:37.47	1.57 ± 0.16	0.39 ± 0.07	-0.03 ± 0.06	25.25 ± 0.08	$0''.11$	$16.3^{+0.70}_{-0.67}$
227	13:38:33.02	–19:44:47.57	1.57 ± 0.17	-0.06 ± 0.09	-0.14 ± 0.09	25.29 ± 0.19	$0''.23$	$20.4^{+1.22}_{-1.15}$
2710/L9	13:38:25.10	–19:43:10.77	1.78 ± 0.25	0.49 ± 0.09	-0.02 ± 0.07	25.34 ± 0.08	$0''.14$	$14.4^{+0.60}_{-0.58}$
1815	13:38:29.01	–19:43:3.275	1.67 ± 0.24	0.27 ± 0.11	0.01 ± 0.10	25.50 ± 0.12	$0''.17$	$11.8^{+0.80}_{-0.75}$
1152	13:38:32.62	–19:42:25.15	> 2.13	0.48 ± 0.14	-0.19 ± 0.11	25.57 ± 0.20	$0''.28$	$15.0^{+1.28}_{-1.18}$
2755	13:38:24.95	–19:43:16.89	1.78 ± 0.53	0.36 ± 0.19	0.12 ± 0.18	25.59 ± 0.21	$0''.33$	$10.3^{+1.40}_{-1.23}$
3304	13:38:23.67	–19:42:27.37	1.66 ± 0.33	0.56 ± 0.12	0.08 ± 0.10	25.60 ± 0.12	$0''.15$	$10.2^{+0.77}_{-0.71}$
1819	13:38:29.61	–19:42:38.19	1.98 ± 0.33	0.39 ± 0.10	0.15 ± 0.09	25.60 ± 0.15	$0''.14$	$11.0^{+0.97}_{-0.89}$
3159	13:38:22.21	–19:43:50.13	> 1.59	0.49 ± 0.23	0.11 ± 0.20	25.63 ± 0.16	$0''.41$	$7.83^{+1.04}_{-0.92}$
309	13:38:34.77	–19:43:27.59	1.55 ± 0.27	0.20 ± 0.13	0.06 ± 0.12	25.69 ± 0.15	$0''.21$	$10.1^{+0.92}_{-0.85}$
1808	13:38:30.04	–19:42:22.51	1.61 ± 0.27	0.36 ± 0.11	-0.10 ± 0.10	25.71 ± 0.12	$0''.15$	$10.1^{+0.73}_{-0.68}$
3670	13:38:20.73	–19:43:16.32	2.09 ± 0.47	0.50 ± 0.12	0.07 ± 0.10	25.81 ± 0.11	$0''.14$	$8.77^{+0.61}_{-0.57}$
633/L25	13:38:34.96	–19:42:24.95	1.68 ± 0.33	0.32 ± 0.13	0.00 ± 0.12	25.81 ± 0.15	$0''.24$	$9.94^{+0.78}_{-0.72}$
2524	13:38:24.47	–19:44:7.263	> 2.01	0.60 ± 0.14	-0.02 ± 0.12	25.86 ± 0.21	$0''.17$	$13.3^{+1.03}_{-0.96}$
1461	13:38:31.37	–19:42:30.95	> 1.97	0.56 ± 0.15	0.07 ± 0.13	25.89 ± 0.15	$0''.20$	$8.22^{+0.77}_{-0.70}$
3177	13:38:22.97	–19:43:16.07	1.61 ± 0.35	0.27 ± 0.16	0.12 ± 0.15	25.99 ± 0.23	$0''.18$	$8.70^{+1.09}_{-0.97}$
1668	13:38:26.93	–19:44:53.25	> 1.82	0.72 ± 0.17	0.16 ± 0.13	25.99 ± 0.16	$0''.17$	$5.58^{+0.73}_{-0.64}$
358	13:38:32.12	–19:45:4.687	2.00 ± 0.54	0.48 ± 0.15	0.03 ± 0.13	25.99 ± 0.19	$0''.20$	$7.87^{+0.87}_{-0.79}$
2569	13:38:26.38	–19:42:43.55	1.94 ± 0.44	0.36 ± 0.14	0.03 ± 0.13	26.04 ± 0.15	$0''.13$	$7.08^{+0.64}_{-0.59}$
3131	13:38:25.27	–19:41:55.49	> 2.15	0.28 ± 0.15	-0.09 ± 0.14	26.04 ± 0.19	$0''.16$	$8.29^{+0.83}_{-0.75}$

[a] Isophotal colors. The limits are 2σ.
[b] Total magnitudes.
[c] SFR estimated from the UV continuum flux (i_{775}).

discussed in Sect. 5.6.

5.3.2.4 *Sizes and morphologies*

We calculated $r_{hl,r}$ from the r_{625}-band, the filter that includes Lyα, and compared it to the r_{hl} of the continuum calculated from the z_{850}-band (Table 7.2). The mean r_{hl} are $0''.13$ in r_{625} and $0''.12$ in z_{850}. At $z = 4.1$, the measured angular sizes correspond to physical radii of < 3 kpc, with a mean value of ~ 1 kpc. We do not find evidence for the sources to be more extended in r_{625} than they are in z_{850}, suggesting that Lyα emission is distributed in a very similar way to the continuum. One exception is source L7 which has $r_{hl,r} = 0''.18$ compared to $r_{hl,i} = 0''.13$ and $r_{hl,z} = 0''.11$.

We have measured the r_{hl} from a sample of 17 field stars in a similar magnitude range. The stars were selected on the basis of SExtractor

Table 5.3 —- *Continued*

ID	α_{J2000}	δ_{J2000}	$(g_{475}-r_{625})^a$	$(r_{625}-z_{850})^a$	$(i_{775}-z_{850})^a$	$z_{850}{}^b$	$r_{hl,z}$	SFR^c_{UV}
2527	13:38:27.99	–19:41:44.07	1.79 ± 0.29	0.28 ± 0.11	-0.13 ± 0.10	26.11 ± 0.22	0.″07	$10.8^{+0.89}_{-0.83}$
2347	13:38:27.99	–19:42:12.22	1.59 ± 0.40	0.42 ± 0.17	0.32 ± 0.16	26.14 ± 0.19	0.″14	$5.63^{+0.79}_{-0.69}$
2358	13:38:24.12	–19:44:47.21	1.70 ± 0.42	0.36 ± 0.16	-0.12 ± 0.15	26.15 ± 0.16	0.″14	$6.28^{+0.66}_{-0.60}$
307	13:38:32.80	–19:44:46.47	2.02 ± 0.49	0.30 ± 0.15	-0.04 ± 0.13	26.17 ± 0.22	0.″15	$9.76^{+0.87}_{-0.80}$
2989	13:38:22.90	–19:43:59.01	1.93 ± 0.29	-0.17 ± 0.13	-0.22 ± 0.13	26.21 ± 0.15	0.″12	$6.61^{+0.59}_{-0.54}$
552/L21	13:38:33.56	–19:43:36.00	1.50 ± 0.32	-0.00 ± 0.18	-0.16 ± 0.18	26.22 ± 0.19	0.″18	$4.75^{+0.79}_{-0.68}$
507	13:38:34.26	–19:43:12.20	> 1.92	0.78 ± 0.15	0.10 ± 0.11	26.22 ± 0.12	0.″12	$6.50^{+0.47}_{-0.44}$
3564	13:38:23.34	–19:41:51.44	1.82 ± 0.49	-0.05 ± 0.23	-0.02 ± 0.23	26.22 ± 0.29	0.″32	$6.64^{+1.11}_{-0.95}$
540	13:38:33.26	–19:43:49.45	1.85 ± 0.52	-0.07 ± 0.24	-0.08 ± 0.24	26.28 ± 0.26	0.″23	$5.65^{+0.94}_{-0.80}$
2480	13:38:27.25	–19:42:30.43	1.78 ± 0.40	0.26 ± 0.15	-0.04 ± 0.14	26.30 ± 0.21	0.″11	$8.26^{+0.75}_{-0.69}$
2712	13:38:26.54	–19:42:12.01	1.73 ± 0.43	0.48 ± 0.15	-0.10 ± 0.13	26.34 ± 0.18	0.″12	$7.77^{+0.60}_{-0.56}$
2494	13:38:25.39	–19:43:34.79	1.61 ± 0.33	0.32 ± 0.15	-0.14 ± 0.13	26.35 ± 0.19	0.″09	$6.55^{+0.66}_{-0.60}$
2708	13:38:24.13	–19:43:50.55	> 1.94	-0.03 ± 0.23	-0.04 ± 0.23	26.39 ± 0.22	0.″23	$3.89^{+0.75}_{-0.63}$
538/L20	13:38:32.83	–19:44:6.934	> 2.17	0.37 ± 0.15	0.13 ± 0.14	26.44 ± 0.16	0.″11	$5.12^{+0.53}_{-0.48}$
1843	13:38:29.54	–19:42:38.83	1.82 ± 0.44	0.11 ± 0.18	-0.21 ± 0.17	26.47 ± 0.21	0.″12	$5.44^{+0.65}_{-0.58}$
1876	13:38:30.04	–19:42:27.78	> 1.61	0.40 ± 0.23	0.03 ± 0.21	26.48 ± 0.25	0.″17	$5.05^{+0.82}_{-0.71}$
375	13:38:32.71	–19:44:38.30	> 1.58	0.35 ± 0.25	0.09 ± 0.23	26.49 ± 0.27	0.″19	$2.93^{+0.89}_{-0.68}$
1655	13:38:29.52	–19:43:10.60	> 2.02	0.46 ± 0.15	0.27 ± 0.14	26.51 ± 0.18	0.″10	$4.69^{+0.55}_{-0.50}$
1339/L14	13:38:28.72	–19:44:36.98	> 1.88	0.37 ± 0.18	0.24 ± 0.18	26.52 ± 0.18	0.″13	$4.29^{+0.54}_{-0.48}$
286	13:38:34.08	–19:43:58.08	1.63 ± 0.45	0.47 ± 0.17	-0.20 ± 0.14	26.52 ± 0.19	0.″10	$5.43^{+0.55}_{-0.50}$
3133	13:38:23.75	–19:42:56.64	> 1.95	0.16 ± 0.20	0.04 ± 0.19	26.53 ± 0.27	0.″14	$5.95^{+0.80}_{-0.70}$
1800	13:38:29.65	–19:42:39.80	> 1.92	0.16 ± 0.20	-0.01 ± 0.19	26.56 ± 0.26	0.″14	$3.72^{+0.79}_{-0.65}$
3486	13:38:21.49	–19:43:21.68	1.82 ± 0.45	0.23 ± 0.17	-0.06 ± 0.16	26.61 ± 0.21	0.″10	$4.84^{+0.59}_{-0.53}$
2874/L4	13:38:22.46	–19:44:33.67	1.88 ± 0.27	-0.35 ± 0.15	-0.14 ± 0.16	26.68 ± 0.23	0.″08	$4.83^{+0.59}_{-0.53}$
1211	13:38:33.53	–19:42:9.188	> 1.73	0.21 ± 0.24	0.19 ± 0.24	26.72 ± 0.27	0.″13	$2.39^{+0.73}_{-0.56}$
1203	13:38:31.76	–19:42:53.82	1.72 ± 0.45	0.42 ± 0.17	0.04 ± 0.15	26.73 ± 0.26	0.″07	$4.20^{+0.66}_{-0.57}$
2571	13:38:23.70	–19:44:32.20	> 1.75	0.09 ± 0.25	-0.00 ± 0.25	26.76 ± 0.23	0.″14	$1.63^{+0.59}_{-0.43}$
1265	13:38:28.64	–19:44:52.16	> 2.08	0.22 ± 0.18	0.36 ± 0.19	26.82 ± 0.18	0.″11	$2.38^{+0.41}_{-0.35}$
1712	13:38:27.93	–19:44:5.602	1.57 ± 0.25	-0.10 ± 0.14	-0.26 ± 0.14	26.83 ± 0.31	0.″09	$6.78^{+0.66}_{-0.60}$
3013	13:38:24.18	–19:43:3.364	1.54 ± 0.42	0.18 ± 0.21	0.05 ± 0.21	26.85 ± 0.30	0.″12	$3.79^{+0.69}_{-0.59}$
1866	13:38:29.33	–19:42:44.09	> 1.63	0.19 ± 0.26	0.24 ± 0.27	26.86 ± 0.30	0.″14	$2.75^{+0.69}_{-0.55}$
1290	13:38:32.15	–19:42:25.57	> 1.54	0.24 ± 0.26	-0.05 ± 0.24	26.88 ± 0.29	0.″17	$4.00^{+0.66}_{-0.56}$

[a] Isophotal colors. The limits are 2σ.
[b] Total magnitudes.
[c] SFR estimated from the UV continuum flux (i_{775}).

stellarity index of 1.0. Four of the LAEs (L4, L11, L20, L22) have a r_{hl} in both bands that is indistinguishable from that of the stars. The UV luminosities of these unresolved LAEs are no different than those of the resolved ones. It is therefore unlikely that they contain an AGN nucleus that significantly overwhelms the host galaxy, making it appear unresolved. The light is probably due to unresolved stellar regions with $r_{hl} \lesssim 500$ pc. If we restrict ourselves to resolved sources only, the mean r_{hl} are 0.″15 in both r_{625} and z_{850}.

The morphologies at rest-frame ~ 1500Å are shown in Fig. 7.5 (see also Miley et al. (2004)). Two sources (L16 & L25) have double nuclei separated by $\sim 0.''5$ (~ 3 kpc) that are connected by faint, diffuse emission. This is suggestive of merging systems.

5.4 Morphological analysis

In order to quantify the wide range in ACS continuum morphologies as observed in Fig. 5.10, we have carried out a nonparametric morphological analysis of the g_{475}-dropout sample. Fol-

Table 5.4 — Properties of the spectroscopically confirmed Lyα emitters.

ID	α_{J2000}	δ_{J2000}	z_{spec}	$(g_{475}-r_{625})^a$	$(r_{625}-z_{850})^a$	$(i_{775}-z_{850})^a$	$z_{850}{}^b$	$r_{hl,r}$	$r_{hl,z}$	SFR^c_{UV}
RG	13:38:26.05	–19:42:30.47	4.105	3.42 ± 0.17	-0.61 ± 0.03	0.09 ± 0.03	23.05 ± 0.05	$0\farcs60$	$0\farcs62$	$93.7^{2.71}_{2.63}$
L4	13:38:22.46	–19:44:33.67	4.095	1.88 ± 0.27	-0.35 ± 0.15	-0.14 ± 0.16	26.68 ± 0.23	$0\farcs09$	$0\farcs08$	$4.83^{0.59}_{0.53}$
L7	13:38:24.78	–19:41:33.66	4.106	> 1.26	0.65 ± 0.29	0.32 ± 0.25	27.20 ± 0.49	$0\farcs18$	$0\farcs11$	$3.22^{0.85}_{0.67}$
L8	13:38:24.86	–19:41:45.49	4.102	> 1.47	0.37 ± 0.27	-0.26 ± 0.23	26.51 ± 0.30	$0\farcs12$	$0\farcs16$	$6.25^{0.88}_{0.77}$
L9	13:38:25.10	–19:43:10.77	4.100	1.78 ± 0.25	0.49 ± 0.09	-0.02 ± 0.07	25.34 ± 0.08	$0\farcs12$	$0\farcs14$	$14.4^{0.60}_{0.58}$
L11	13:38:26.16	–19:43:34.31	4.101	1.56 ± 0.18	0.11 ± 0.09	-0.08 ± 0.09	25.94 ± 0.10	$0\farcs08$	$0\farcs09$	$8.95^{0.48}_{0.46}$
L14	13:38:28.72	–19:44:36.98	4.102	> 1.88	0.37 ± 0.18	0.24 ± 0.18	26.52 ± 0.18	$0\farcs13$	$0\farcs13$	$4.29^{0.54}_{0.48}$
L16	13:38:29.66	–19:43:59.82	4.102	1.43 ± 0.23	0.22 ± 0.12	-0.00 ± 0.11	25.54 ± 0.16	$0\farcs16$	$0\farcs19$	$11.4^{1.10}_{1.00}$
L17	13:38:29.86	–19:43:25.84	4.093	> 1.57	0.21 ± 0.27	0.44 ± 0.29	27.37 ± 0.28	$0\farcs11$	$0\farcs10$	$1.33^{0.40}_{0.31}$
L20	13:38:32.83	–19:44:6.934	4.100	> 2.17	0.37 ± 0.15	0.13 ± 0.14	26.44 ± 0.16	$0\farcs09$	$0\farcs11$	$5.12^{0.53}_{0.48}$
L21	13:38:33.56	–19:43:36.00	4.097	1.50 ± 0.32	-0.00 ± 0.18	-0.16 ± 0.18	26.22 ± 0.19	$0\farcs12$	$0\farcs18$	$4.75^{0.79}_{0.68}$
L22	13:38:34.14	–19:42:52.68	4.096	> 1.82	0.79 ± 0.16	0.13 ± 0.13	26.64 ± 0.14	$0\farcs07$	$0\farcs08$	$4.69^{0.38}_{0.35}$
L25	13:38:34.96	–19:42:24.95	4.093	1.68 ± 0.33	0.32 ± 0.13	0.00 ± 0.12	25.81 ± 0.15	$0\farcs25$	$0\farcs24$	$9.94^{0.78}_{0.72}$

[a] Isophotal colors. The limits are 2σ.

[b] Total magnitudes.

[c] SFR estimated from the UV continuum flux (i_{775}).

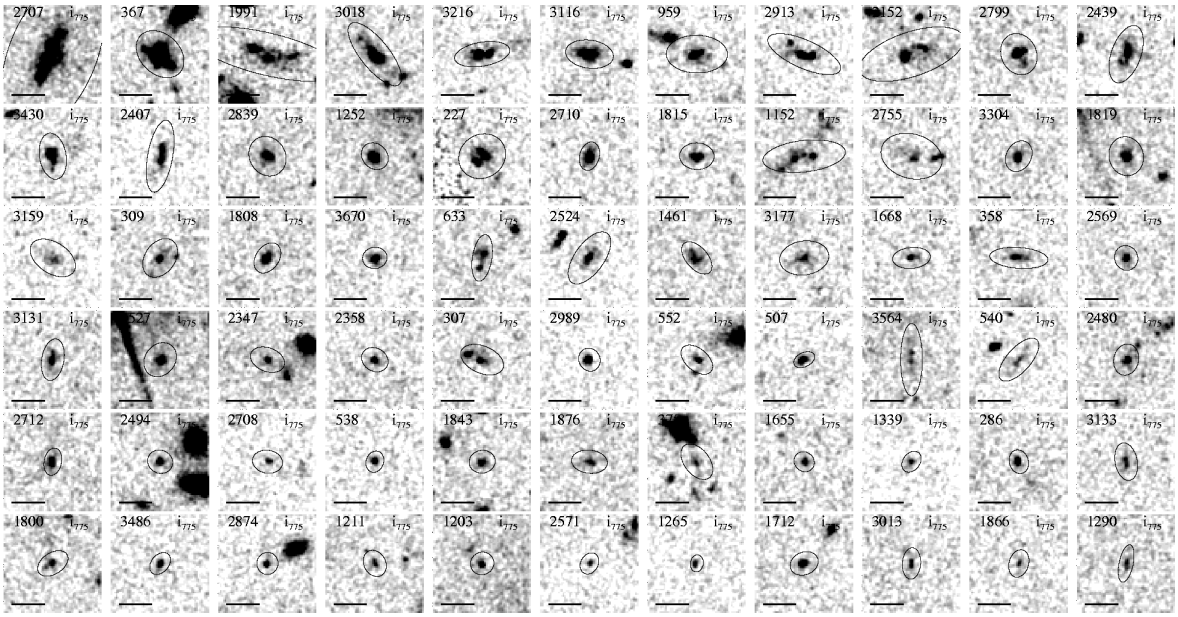

Figure 5.10 — i_{775} postage stamps ($3'' \times 3''$) of the g_{475}-dropout sample. The images have been smoothed using a Gaussian kernel of $0.''075$ (FWHM). Kron apertures are indicated. The scale bars measure $1''$. North is up, East is to the left.

lowing Lotz et al. (2004) we determined the following morphological coefficients. 1) The Gini coefficient (G), a statistic for the relative distribution of an object's flux over its associated pixels, 2) M_{20}, the normalised second order moment of the brightest 20% of a galaxy's pixels, and 3) concentration (C), the ratio of the circular radii containing 20% and 80% of the total flux. The exact formulae have been adopted from Lotz et al. (2004) with some minor modifications.

To improve the S/N of our sample we coadded the i_{775} and z_{850} images, giving a total exposure time of 23500 s. To further improve the S/N per pixel the images were binned using a 2×2 binning scheme. Pixels were flagged as belonging to an object if they were inside one 'Petrosian radius' (Petrosian 1976). This ensures that the morphological analysis is relatively insensitive to varying surface brightness limits and S/N among different objects (Lotz et al. 2004). After some initial tests, we maximized the number of g_{475}-dropouts with sufficient $(S/N)_{pixel}$ by setting the free Petrosian parameter η to 0.3. We measured the morphologies for a total of 15 of the g_{475}-dropouts that had $(S/N)_{pixel} > 3$, which included the radio galaxy. The C coefficients were all determined within a maximum radius of $1.5 \times r_p$. We used SExtractor's segmentation maps to mask out all pixels suspected of belonging to unrelated sources. Errors on the coefficients were determined using Monte Carlo simulations. The value of each pixel was modified in such a way that the distribution of values were normally distributed with a standard deviation equal to that given by the RMS image value for the corresponding pixel.

In Fig. 5.12 we plot the distributions of the morphological parameters derived for the TN1338 g_{475}-dropouts (blue points). The radio galaxy (large circle) has non-average values in each of the parameter spaces, owing to its complex morphology as described by Zirm et al. (2005). To compare the morphologies of the g_{475}-dropouts in TN1338 we have applied the morphological analysis also to a sample of $z \sim 4$ LBGs selected in our GOODS CDF-S simulations (see Sect. 5.2.7). However, the morpho-

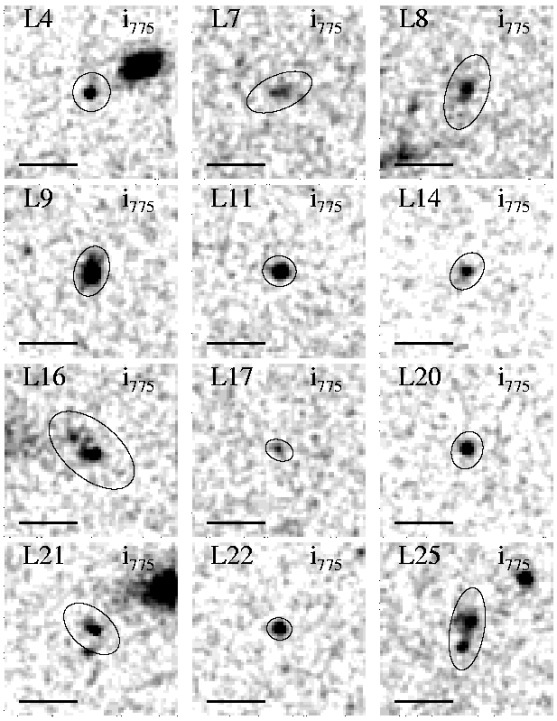

Figure 5.11 — i_{775} postage stamps ($3'' \times 3''$) of the twelve spectroscopically confirmed Lyα emitters of Venemans et al. (2002). See the caption of Fig. 5.10 for details.

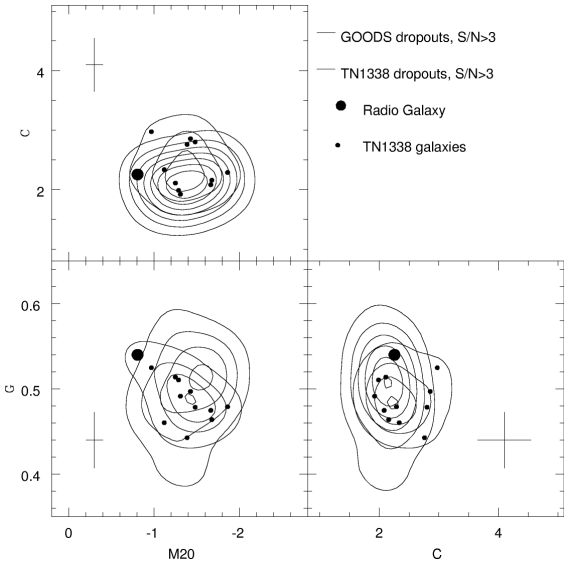

Figure 5.12 — The morphological Gini coefficient (G), M_{20}, and concentration (C) for g_{475}-dropouts in TN1338 (blue points and contours), and g_{475}-dropouts from GOODS (red contours). The radio galaxy is indicated by the large circle.

logical parameters were measured in the original, stacked i_{775} and z_{850} images from GOODS in case the morphologies were not preserved during the construction of the simulated images (Sect. 5.2.7). Fig. 5.12 indicates that both the centroids and the spread of the TN1338 parameter distributions (indicated with the blue contours) coincide with that of the parameter distributions determined from GOODS (red contours).

5.5 Evidence for an overdensity associated with TN J1338-1942 at $z = 4.1$?

5.5.1 Surface density distribution

In Fig. 5.13 we show the angular distribution of the g_{475}-dropouts in TN1338. Contours of the local object surface density compared to the average field surface density illustrate that the g_{475}-dropouts lie predominantly in a filamentary structure. Another density enhancement is located near the top edge of the image. Interestingly, both peaks in the object surface density distribution coincide with an extremely bright $\sim 6L^*$ LBG. One of these is the radio galaxy, which takes a central position in the largest concentration of g_{475}-dropouts in the field. Moreover, about half of the dropouts lie in a $2\farcm1 \times 2\farcm1$ region that includes the radio galaxy.

The subsample of g_{475}-dropouts detected in K_S are located only in the high density regions, most notably in the clump to the left of the radio galaxy. The objects detected in K_S are also the brightest objects in the rest-frame UV. The filamentary distribution of the dropouts is not reflected by the angular distribution of the 12 LAEs, which are distributed more uniformly over the field. In fact, 8 of the emitters lie in regions that are underdense compared to the overall distribution of g_{475}-dropouts.

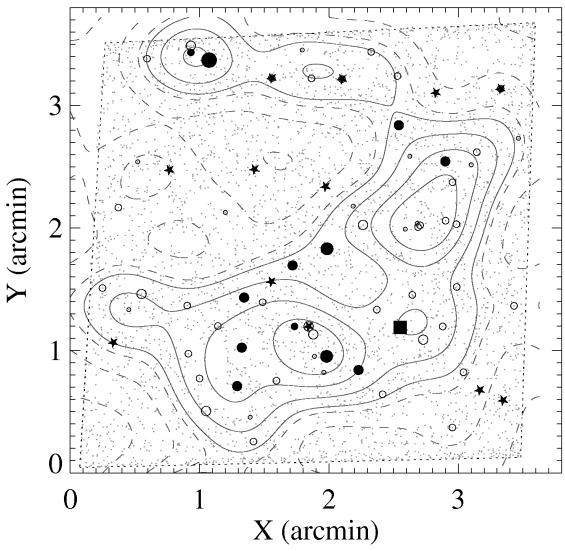

Figure 5.13 — Object map of the g_{475}-dropout candidates (circles), TN J1338–1942 (square), Lyα emitters (stars) and the detection catalog (points). g_{475}-dropouts detected in K_S are indicated by filled circles. Larger circles indicate brighter objects in z_{850}. The contours represent density fluctuations $\Delta \equiv (\Sigma - \bar{\Sigma})/\bar{\Sigma}$ of –1, –0.5, –0.1 (dashed contours) and +0.1, +0.5, +1, +1.5 (solid contours), achieved by smoothing the object map with a Gaussian of width 36″, or 250 kpc (FWHM), using equal weights. LAEs that are not in the g_{475}-dropout sample were not included in the density contours.

5.5.2 Comparison with 'field' LBGs from GOODS

Here we will test whether the suggestive structure of g_{475}-dropouts in TN1338 represent an overdensity of star-forming galaxies associated with TN J1338–1942, similar to the overdensity of LAEs discovered by Venemans et al. (2002). To determine the 'field' surface density of g_{475}-dropouts we have extracted a control sample by applying our selection criteria to the simulated images based on B_{435}-dropouts in the GOODS CDF-S as described in §5.2.7. A mosaic of the GOODS CDF-S fields is shown in Fig. 5.14. Points indicate the filamentary nature of the angular distribution of LBGs at $z \sim 4$. At $z_{850} < 27.0$ there are a total of 361 g_{475}-dropouts in the transformed CDF-S in an area of 159 arcmin^2, giving an average surface density of 2.27 arcmin^{-2}, and 1.82 arcmin^{-2}, and 1.16 arcmin^{-2} for $z_{850} < 26.5$ and $z_{850} < 26.0$, respectively. The surface density of g_{475}-dropouts in TN1338 is approximately 2.5$\times$ higher for each magnitude cut (5.64 arcmin^{-2}, 4.36 arcmin^{-2}, and 2.74 arcmin^{-2}, respectively).

What is the significance of this factor 2.5 surface overdensity? LBGs belong to a galaxy population that is strongly clustered at every redshift (Porciani & Giavalisco 2002; Ouchi et al. 2004), with non-negligible field-to-field variations. In our particular case, it is interesting to estimate the chance of finding a particular number of g_{475}-dropouts in a single $3\farcm4 \times 3\farcm4$ ACS pointing. Analysing each of the 15 GOODS tiles individually, the lowest number of g_{475}-dropouts encountered was 12, and the highest was 37 to z_{850}=27.0. Next, we measured the number of objects in $\sim$ 500 randomly placed, square 11 arcmin^2 cells in the GOODS mosaic shown in Fig. 5.14. The cells were allowed to overlap so that the chance of finding the richest pointing possible was 100%. In Fig. 7.12 (*top panel*) we show the histogram of counts-in-cells for the three different magnitude cuts. In each case the number of objects in TN1338 (indicated by the dashed lines) falls well beyond the high-end tail of the distribution, with none of the cells randomly drawn from GOODS containing as many objects (the highest being 41, 35, and 24 for z_{850}<27.0, 26.5, 26.0). Approximating the distributions with a Gaussian function (strictly spoken, this is only valid in the absence of higher order clustering moments, as well as non-linear clustering at very small scales), we find a surface overdensity of 2.5 at $5-6\sigma$ significance with respect to the simulated GOODS CDF-S[7]. The measured standard deviations were corrected by 4% to take into account

[7] We also selected a g_{475}-dropout sample on the basis of a SExtractor detection image that included the g_{475}-band image (as opposed to only $r_{625}i_{775}z_{850}$). Due to the addition of mostly noise (for g_{475}-dropouts) this sample included less objects, and we found a surface overdensity of ~ 2 at $\gtrsim 3\sigma$. This is slightly less significant, because the sample size in the simulations remained practically constant when selecting on $g_{475}r_{625}i_{775}z_{850}$. This suggests that the simulations may contain some extra crosstalk between filters as a result of the interpolation, and should be investigated a little further.

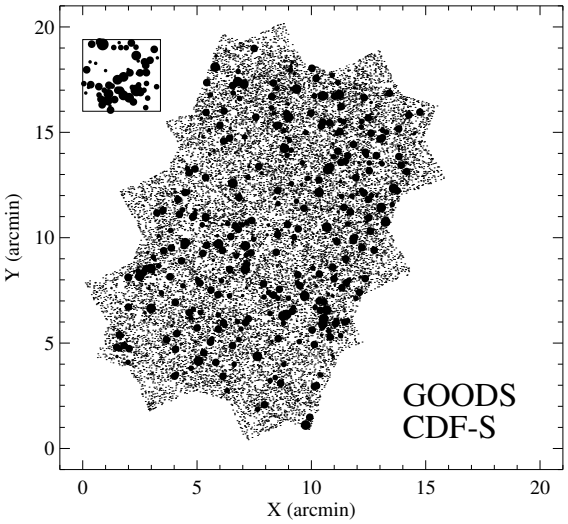

Figure 5.14 — Distribution of $z \sim 4$ LBGs in the GOODS CDF-S with $z_{850} \leq 27.0$ (circles). Larger symbols correspond to brighter objects. The inset in the top left shows the $3\farcm4 \times 3\farcm4$ TN1338 field and the distribution of g_{475}-dropouts at the same scale as the GOODS CDF-S for comparison.

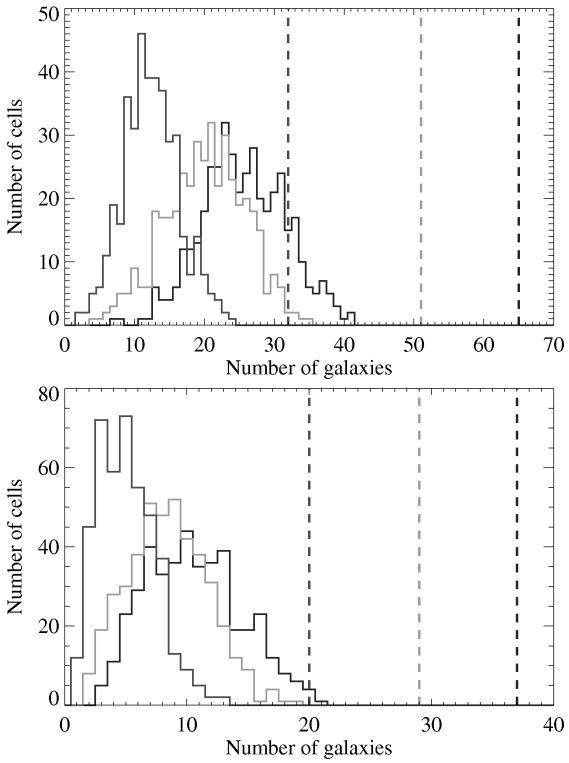

Figure 5.15 — Counts in cells analysis of $z \sim 4$ LBGs in the GOODS simulations compared to TN1338. *Top panel:* Histograms of the number of objects in square cells the size of TN1338 ($3\farcm4 \times 3\farcm4$) for z_{850}<27.0 (blue, right), 26.5 (green, middle) and 26.0 (red, left). The number of g_{475}-dropouts in TN1338 are indicated by the vertical lines of corresponding color. *Bottom panel:* Same as top, but for $2\farcm1 \times 2\farcm1$ cells. The number of g_{475}-dropouts in TN1338 exceeds the number encountered in GOODS for every limiting magnitude or field size.

that the counts in cells distribution will appear narrower due to the fact that our control field is not infinitely large.

Comparable significance for an overdensity is found if we focus on a smaller region of 4.4 arcmin^2, where more than half of the g_{475}-dropouts are located (see Fig. 5.13). Drawing $2\farcm1 \times 2\farcm1$ regions from the GOODS CDF-S field (Fig. 7.12, *bottom panel*) yielded a maximum of 21, 19 and 13 objects for the three magnitude cuts, respectively. The region in TN1338 corresponds to surface overdensities of 3.4, 3.2, and 4.0, but with $\sim 5\sigma$ significance due to the fact that the counts-in-cells distribution function is much wider due to the relatively small cell size compared to the fluctuations in the surface density of LBGs (bottom panel).

We have not applied the counts in cells to simulations of the GOODS HDF-N, since it has been shown that the northern GOODS field is $\sim 17\%$ less rich in B_{435}-dropouts compared to its southern counterpart (Bouwens et al. 2005b). We conclude that the number of g_{475}-dropouts in TN1338 represents a highly significant overdensity with respect to the 314 arcmin^2 GOODS fields. Below we will further investigate implications of large-scale structure and cosmic variance.

5.5.3 $w(\theta)$ and sub-halo clustering

The two-point correlation function is one of the most powerful tools to study the large-scale distribution of high redshift galaxies. Recent measurements of the clustering of LBGs at $3 < z < 5$ show that the angular correlation function, $w(\theta)$, deviates from the classical power-law at small angular scales. This behaviour is

expected in the regime where non-linear clustering within single halos dominates over the large-scale clustering between halos. This effect has now been shown to be present (at least in a statistical sense) in large LBG samples (Ouchi et al. 2005a; Lee et al. 2005), although the contribution from each individual halo is quite small due to the relatively small halo occupations of LBGs as well as projection effects.

The structure found in TN1338 provides a unique opportunity to test the contribution of the one-halo term to $w(\theta)$ within a single, overdense field. We measured $w(\theta)$ using the estimator $w(\theta) = [A_1 DD(\theta) - 2A_2 DR(\theta) + RR(\theta)]/RR(\theta)$ with $A_1 = N_r(N_r - 1)/(N_g(N_g - 1))$ and $A_2 = (N_r - 1)/2N_g$ (Landy & Szalay 1993). We used 25 random catalogs of 10000 sources each, and the 1σ errors on $w(\theta)$ were estimated from the standard deviation among 32 bootstrap samples of the original data (Ling et al. 1986)[8]. When the field size is relatively small, the average density of a clustered distribution is overestimated because the field where the clustering is being measured is also the field where the average density has to be estimated from. We therefore estimated the integral constraint (IC) for the ACS/WFC field, $IC/A_w = \sum_i RR(\theta_i)\theta_i^{-\beta} / \sum_i RR(\theta_i) = 0.073$, where we assumed a fixed slope of $\beta = 0.6$. The result is plotted in Fig. 5.16. We used bins of $10''$, but excluded the separations of $\theta < 1''$. Since we do not expect any signal in the large-scale, 2-halo clustering due to the finiteness of our sample, we have safely applied the IC to the data points using the large-scale clustering amplitude $A_w \approx 0.6$ for B-dropouts in GOODS at $z_{850} \lesssim 26.5$ measured by Lee et al. (2005). At $\theta > 20''$ $w(\theta)$ is consistent with no clustering at all. At $\theta < 20''$ the two datapoints lie above the large-scale clustering amplitude. The scale at which we find a positive signal agrees well with the expected location of an upturn in $w(\theta)$ due to sub-halo clustering (Ouchi et al. 2005a; Lee et al. 2005).

To test the significance of possible sub-halo clustering in the field of TN1338, we constructed a mock field having large-scale clustering properties resembling those of LBGs at $z \sim 4$. We used the formalism of Soneira & Peebles (1978) to create an object distribution with a choice two-point angular correlation function. The procedure is as follows. First a random position is chosen. This forms the center of a pair of points that are placed with a random position angle and separation θ_1. Each point forms the center for a new pair with separation $\theta_2 = \theta_1/\lambda$ and random position angles. This process is repeated until L levels, each level contributing 2^L points with separations θ_1/λ^{L-1} to the 'cluster'. Next, a new cluster center is randomly chosen in the field, and the cluster is again populated with a depth of L levels. This is repeated until the mock field contains N clusters. The resulting point distribution will have a power-law two-point angular correlation function with its slope determined by the choice of λ, and its smallest and largest angular scales determined by the point separations at the first and the last levels, respectively. Because we need both many levels to get sufficient signal in $w(\theta)$ at all angular scales, and many clusters to get sufficient coverage of the area, the method above produces far too many points at first. It is therefore common to introduce a parameter, f, which is the probability that each point makes it into the final sample when drawing a random subsample. We then calculate the number of clusters N necessary to match a particular surface density given this f. The amplitude of the angular correlation function, A_w, solely depends on the choice of f, since the clusters are randomly distributed with respect to each other. We iteratively created mock samples with different f and measured $w(\theta)$ until the best-fit amplitude matched the amplitude of the correlation function that we wish to model (corrected for the IC). The size of the mock field was set to $17' \times 17'$ with a surface density of ≈ 5 arcmin^{-2} to match the

[8] In our case, deriving unweighted bootstrap errors is expected to significantly overestimate the errors, since it does not take into account that each of the g_{475}-dropouts in TN1338 was already selected to have a secure $> 5\sigma$ detection. We therefore conservatively allowed only the 15 faintest objects in the sample to be randomly subsampled by the bootstrap resampling. The brighter sources were always retained in the bootstrap subsamples.

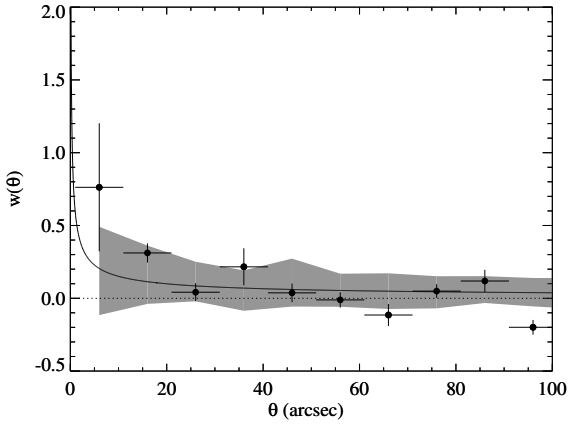

Figure 5.16 — The angular two-point correlation function for g_{475}-dropouts in the TN1338 field. The solid line indicates the angular correlation function $w(\theta) = 0.6\theta^{-0.6}$, as measured for B_{435}-dropouts with $z_{850} \lesssim 26.5$ in GOODS (Lee et al. 2005). The shaded region indicates the 1σ spread in $w(\theta)$ at each θ that was measured among 25 $3\farcm4 \times 3\farcm4$ fields of the same geometry and source density as the TN1338 field extracted from a $17' \times 17'$ mock catalog with $w(\theta) \approx 0.6\theta^{-0.6}$.

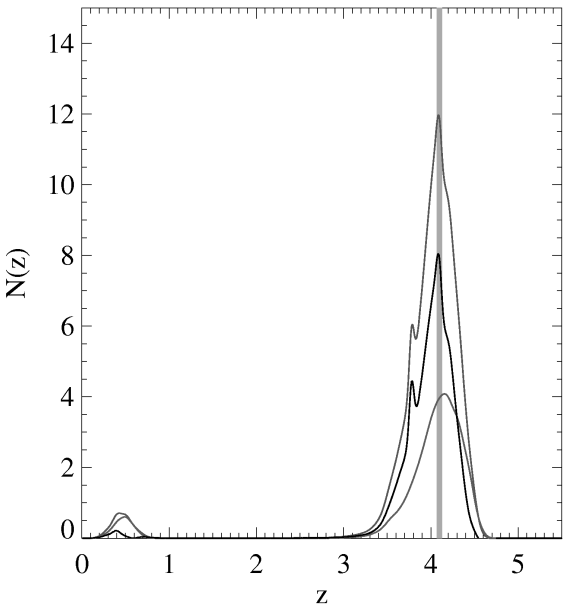

Figure 5.17 — Total z_B probability distributions for g_{475}-dropouts in TN1338 (blue, top curve) and in GOODS CDF-S (red, bottom curve). The area under the blue curve is equal to the number of objects in the TN1338 sample. The red curve for GOODS has been normalised to the area of the TN1338 field. The GOODS curve was subtracted from the TN1338 curve to bring out the residuals of the redshift distribution for TN1338 (black, middle curve). The residual z_B peak at the redshift of the radio galaxy and LAEs (shaded region). Another secondary peak lies at $z_B \approx 3.8$, the redshift of the other $\sim 6L^*$ object in the field. The peak at $z \sim 0.5$ are due to the alternative probability that a fraction of the g_{475}-dropouts could be 4000Å break objects.

density found in TN1338. To model the result of Lee et al. (2005), $w(\theta) \approx 0.6\theta^{-0.6}$, we required an f of 0.001 (with $\theta_1 = 8\farcm3$ and $L = 13$). Having modeled the observed two-point statistics successfully, we extracted 25 $3\farcm4 \times 3\farcm4$ 'ACS' fields from the mock sample and measured the mean $w(\theta)$ and its standard deviation. The result is indicated in Fig. 5.16 (shaded region). The mean $w(\theta)$ corresponds well to the large-scale clustering that was built into the much larger total mock field (solid line). For $\theta < 10''$ there is a 2σ discrepancy between the clustering observed in TN1338 and the expected clustering of a similarly sized mock field. It is likely that the subclustering in the TN1338 field is the result of galaxies that are physically interacting on scales that are smaller than the typical halo scale sizes (see Sect. 5.6.2.2).

5.5.4 Spectroscopy and photometric redshifts

Excluding the radio galaxy, 6 of the LAEs confirmed by Venemans et al. (2002) are also in our photometrically selected LBG candidate sample. These high equivalent width Lyα LBGs lie in a narrow redshift interval ($\Delta z \approx 0.03$) centered on the redshift of the radio galaxy. We further obtained spectroscopic redshifts for three of the candidate LBGs in our sample. The spectrum of the $\sim 6L^*$ object #367 shows several absorption lines typical for LBGs at a redshift of 3.830 ± 0.002 (Fig. 5.18). Object #3018 was found to have a redshift of $z = 3.911 \pm 0.004$, based on the presence of (faint) Lyα in emission, and O I/Si II λ1303 and C IIλ1334 in absorption. Candidate #959 has strong Lyα (as confirmed by its asymmetry) at a redshift of $z = 3.92 \pm 0.01$. We also attempted to obtain a spectrum of object #3216. A very faint continuum was detected, but the S/N was insufficient to determine the redshift. Although the redshifts of these three

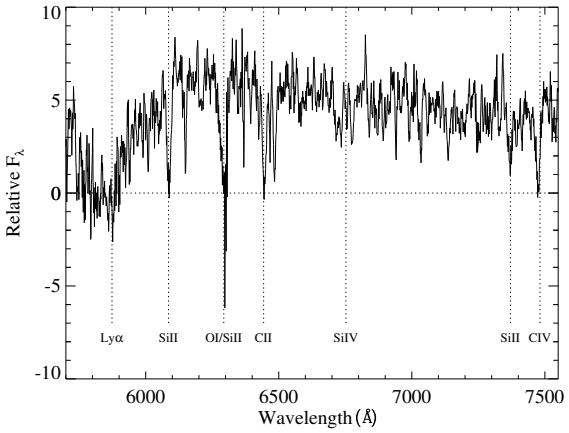

Figure 5.18 — VLT/FORS2 spectrum of the Lyman break galaxy #367 with a redshift of 3.830 ± 0.002.

LBGs in particular indicate no physical association with the radio galaxy and Lyα emitters, the spectroscopic results confirm that our g_{475}-dropout selection criteria successfully identify LBGs at $z \approx 4$.

We have computed the photometric redshifts of the g_{475}-dropouts in TN1338 and the 'simulated' g_{475}-dropouts in GOODS. We let BPZ output the full redshift probability distribution for each object, $P_i(z)$, and summed over all the objects to get the total redshift probability distribution. In this manner, information about lower redshift likelihoods can be retained, and can the S/N of the overall photometric redshift distribution be improved because objects are not forced to only their best-fit value of z_B. The result is shown in Fig. 5.17. The area under the curves is equal to the total number of objects found in a 11.7 arcmin^2 area. According to BPZ the fraction of galaxies at $z \sim 0.5$ totals $\sim 4\%$ of the candidate $z \sim 4$ sample in GOODS. The true contamination fraction is likely to be somewhat higher (Giavalisco et al. 2004a; Bouwens et al. 2005b). The difference in the areas under the two curves reflects the factor ~ 2.5 overdensity of the TN1338 field. The peak of the z_B distribution lies at $z = 4.1$, which is a good match to the average redshift of the radio galaxy and the LAEs. The peak redshift for the g_{475}-dropouts from GOODS lies at a slightly higher redshift of $z_B \approx 4.2$. While the photometric redshift distribution of GOODS appears rather Gaussian, z_B is significantly steeper at $z \approx 4.1$ for the g_{475}-dropouts in TN1338. The narrowness of the distribution and the overdensity can be illustrated by subtracting the GOODS z_B distribution from that of TN1338 (black curve in Fig. 5.17). The photometric redshift distribution is further evidence that a significant fraction of these objects is likely to be physically related to the LAEs that are clustered around the radio galaxy. $N(z)$ has a second peak around $z \approx 3.8$, although it contains much less objects. Interestingly, its redshift corresponds to the other $\sim 6L^*$ object in the field.

5.6 Summary and Discussion

5.6.1 Properties of LBGs and LAEs

5.6.1.1 SFRs, UV(-optical) colors, and masses

We studied the star forming properties of 66 g_{475}-dropouts to z_{850}= 27, and 12 LAEs (6 of which were also in the g_{475}-dropout sample). The SFRs were in the range 1–100 M$_\odot$ yr^{-1}, with LAEs being limited to < 14 M$_\odot$ yr^{-1}. Applying an average extinction ($E(B-V) = 0.1$) yields SFRs of up to ~ 300 M$_\odot$ yr^{-1}.

The LBGs and LAEs have very blue continua ($\beta_{iz} \approx -2$) when averaged over the entire sample. We derived a UV-slope magnitude relation of $\beta_{iz} = (-0.16 \pm 0.05) z_{850} + (2.16 \pm 1.26)$, such that the slopes of $L \gtrsim L^*$ LBGs are consistent with the average slopes determined for mildly reddened LBGs at $z \sim 3$ redshifted to $z = 4$ (Papovich et al. 2001; Shapley et al. 2003,see also Bouwens et al. (2005b)). The $\beta_{iz} - z_{850}$ relation can be interpreted as a SFR- or mass-extinction relation implying $E(B-V) \approx 0.13$ at $z_{850} \approx 23$ and $E(B-V) \approx 0.0$ at $z_{850} \approx 27$ for a fixed age of ~ 70 Myr.

We also derived rest-frame UV-optical colors, and estimated LBG ages in the range 10–100 Myr, with $\sim 50\%$ of the LBGs having ages < 50 Myr, with respect to our base template (exponentially declining, $\tau = 10$ Myr, $Z = 0.2 Z_\odot$ and $E(B-V) = 0.16$ from Papovich et al. 2001).

We also found evidence for a relation in i_{775}–K_S vs. K_S, similar as found for B_{435}-dropouts in GOODS (Papovich et al. 2004). This is likely to be interpreted as a stellar mass-age and/or mass-dust relation, in the sense that the more massive galaxies have higher optical luminosities and redder UV-optical colors due to aging and/or dust.

None of the LAEs was detected in the K_S-band, but we found a 3σ detection through stacking. The stacked magnitude of $K_S = 25.8^{+0.44}_{-0.32}$ implied i_{775}–$K_S \approx 0.0$, while a stack of LBGs with similar UV magnitudes gave a 7σ detection of $K_S = 25.14^{+0.16}_{-0.13}$ and i_{775}–$K_S \approx 0.7$. Such a significant difference in the K_S magnitude while having similar i_{775} and i_{775}–z_{850} can only be explained if the LAEs are both younger as well as less massive than those LBGs (mass/age tracks have been indicated in Fig. 5.9). While it has been suggested before that Lyα emission can only escape during a relatively short, dustless phase of star-formation, a mass difference would imply that the LAEs and LBGs are entirely different populations, at least in this field.

The observed range in K_S-band magnitudes in TN1338 of $K_S \sim 26 - 22$ implies stellar masses (at $t_{sf} = \infty$) ranging from $\sim 3 \times 10^8$ for LAEs and the faintest LBGs to $\sim 2 \times 10^{10}$ $M_\odot$ for the radio galaxy and the brightest LBGs (Fig. 5.9).

To summarize, our "cluster" sample is in fair agreement with the rest-frame UV and UV-optical color-magnitude relations of field samples, suggesting that age (or dust) – while clearly correlated with the rest-frame UV/optical luminosity – is only weakly linked to environment.

5.6.1.2 Sizes and morphologies

For $L \geq L^*$ galaxies we found a mean half-light radius of $0\farcs22$ (~ 2 kpc). Although this is slightly smaller than the average size reported by Ferguson et al. (2004) based on a GOODS B_{435}-dropout sample, Ferguson et al. (2004) measured r_{hl} out to much larger circular annuli. The results are consistent when we apply a small aperture correction from Fig. 5.3. The mean r_{hl} of the g_{475}-dropouts is comparable to that of B_{435}-dropouts culled from the UDF and GOODS fields by Bouwens et al. (2004a), and is therefore consistent with the $\propto (1+z)^{-1.05\pm0.21}$ size scaling law that connects U_{300}-B_{435}-,V_{606}-, and i_{775}-dropouts at fixed luminosities (Bouwens et al. 2004a). The r_{hl} of the $L < L^*$ LAEs and LBGs are comparable (~ 1.5 kpc).

Our morphological classifications showed that the g_{475}-dropouts span a wide range of morphologies that are highly dissimilar to local Hubble types, but not dissimilar to B_{435}-dropouts in GOODS studied by Lotz et al. (2004, 2005).

We found no evidence for AGN among the LAEs, similar to a large field sample at $z \sim 4.5$ studied by Wang et al. (2004). On the other hand, several of the LAEs in the protocluster near radio galaxy MRC 1138–262 at $z = 2.16$ have been detected with *Chandra* indicating that the AGN fraction of such protoclusters could be significant (Pentericci et al. 2002; Croft et al. 2005). Upcoming Chandra observations of TN1338 will enable us to establish which of the LBGs/LAEs may harbor AGN.

5.6.2 Properties of the protocluster

5.6.2.1 Clustering segregation

We have presented evidence for an overdensity of g_{475}-dropouts in TN1338, and that this population has significant sub-clustering across the ACS field. The radio galaxy lies in a ~ 7.5 (comoving) Mpc 'filament' formed by the majority of the g_{475}-dropouts. The discovery of this substructure with ACS ties in closely with the clustering seen at larger scales. Intema et al. (2005) present the large-scale distribution of relatively bright B-dropouts towards TN1338 in a $25' \times 25'$ field observed with the Subaru Telescope, showing several significant density enhancements amidst large voids.

In contrast, Venemans et al. (2002); Venemans et al. (2005), using data from two $7' \times 7'$ VLT/FORS fields, found that the LAEs are relatively randomly distributed. Based on the absence of substructure and their small velocity dispersion they concluded that the LAEs might

just be breaking away from the local Hubble flow. Additional evidence for this might be contained in the fact that the LAEs in the much smaller ACS field seem to prefer regions that are generally devoid of the UV-selected LBGs. We showed evidence that LAEs are generally younger (and possibly less massive) than objects in our UV-selected sample. Also, g_{475}-dropouts that were detected in K_S are both brighter and redder than LAEs, suggesting that objects with both higher ages or dust and larger stellar masses lie in the densest regions of the TN1338 field. This hints towards the formation of an age-density or mass-density relation in TN1338, analogous to the morphology-density relations or red-sequence relations observed at low redshift.

5.6.2.2 *Halo sizes*

We have compared the clustering of the g_{475}-dropouts to that expected based on the large-scale, two-halo contribution to $w(\theta)$ measured for B_{435}-dropouts in clustered mock samples. We found an excess of clustering at the smallest angular scales ($\theta < 20''$), which is expected when $w(\theta)$ is dominated by non-linear sub-halo clustering at small scales (Ouchi et al. 2005a; Lee et al. 2005). These radii of $\sim 0.3 - 0.6$ (co-moving) Mpc are similar to the virial radii, r_{200}, of dark matter halos with masses of 10^{12-13} $M_\odot$ (see Ouchi et al. 2005a), where r_{200} is defined as the radius of a sphere in which the mean density is $200\times$ the mean density of the Universe (Mo & White 2002). The linear bias, b, within these radii can reach values of $> 10 - 50$, compared to a bias of $2.5 - 4$ for the field (Ouchi et al. 2005a; Lee et al. 2005). Together with the overdensity this explains the large number and sub-clustering of the g_{475}-dropouts in TN1338. The amplitude of the sub-halo correlation suggests that the occupation number of the protocluster "halo" is much higher than that of field halos on average, similar to what is expected from numerical simulations (e.g. Kravtsov et al. 2004).

TN1338 is further exceptional in the sense that it contains two $\sim 6L^*$ LBGs, while there are only a few of such objects in the two GOODS fields combined. One is the radio galaxy at $z = 4.11$. The second object (#367) lies at a redshift of $z = 3.83$, and is also associated with a small enhancement in the g_{475}-dropout surface density. Possibly, the TN1338 field therefore contains not one, but *two* overlapping, large-scale structures at $z \sim 4$. Given their overall strong clustering properties and cosmic variance, $z \sim 4$ LBGs will likely have significant field-to-field variations even on angular scales larger than currently probed by GOODS (Somerville et al. 2004). Future deep, wide surveys will demonstrate the uniqueness of protocluster structures such as found in the TN1338 field. Based on shallower samples, albeit of significantly larger areas, it has been found that the surface density of TN1338-like concentrations are comparable to that expected based on the co-moving volume densities of local clusters (e.g. Steidel et al. 1998; Shimasaku et al. 2003; Ouchi et al. 2005; Intema et al. 2005). Observations of these kind of systems could constrain the halo occupation distribution at the very high mass end.

5.6.2.3 *Mass of the overdensity*

A proper determination of the mass of the TN1338 protocluster requires a good estimate of the total volume density, which depends on the actual redshift distribution of the LBGs and LAEs. We were not able to confirm any additional LBGs at the redshift of the radio galaxy. Not only due to the faintness of the targets, but also because all objects with high equivalent width Lyα, the most efficient method of confirming high redshift objects, had already been found previously. We nevertheless indirectly obtained redshifts of the 6 g_{475}-dropouts that are also in the Lyα sample (excluding the radio galaxy). From the redshift distribution of LBGs in the GOODS simulations we expect 2.33 field LBGs at a redshift of $z = 4.1$ with $|z - \delta z| < 0.03$. The volume overdensity in TN1338 is then $\delta_g \equiv (\rho - \bar{\rho})/\bar{\rho} = 1.6$, which can be considered to be a lower limit since it assumes that no other g_{475}-dropouts lie within δz of $z = 4.1$. Alternatively, given that only 20%–25% of field LBGs have high equivalent width Lyα to be detected

as a LAE (Steidel et al. 2000), the 10 LAEs (with $z_{850} < 27$) associated with TN1338 would represent 40–50 LBGs (including LAEs) in a relatively narrow redshift range. Note that if we subtract the average number of g_{475}-dropouts expected in a TN1338-sized field (~ 26) from the number of g_{475}-dropouts observed, the surplus indeed amounts to ~ 40 g_{475}-dropouts. This is independent confirmation of the results of Venemans et al. (2002) that were based on LAEs alone.

If we assume that the LBGs in TN1338 have the same overdensity as measured for the LAEs by Venemans et al. (2002), the surface overdensity in TN1338 would be $\delta_g \approx 3.5$. We can relate the true mass overdensity, δ_m, to the observed g_{475}-dropout overdensity, δ_g, through $1 + b\delta_m = |C|(1 + \delta_g)$, where $C = 1 + f - f(1 + \delta_m)^{1/3}$ (with $f = \Omega_m(z)^{4/7}$) corrects for redshift-space distortion due to peculiar velocities assuming that the structure is just breaking away from the Hubble expansion (Steidel et al. 1998). Taking $b \sim 3$ for B_{435}-dropouts with $z_{850} < 26 - 27$ from Lee et al. (2005) gives $\delta_m \sim 0.8$ for $\delta_g = 1.5$. This can be related to a total mass of $M \simeq (1 + \delta_m)\bar{\rho}V \gtrsim 10^{14}$ $M_\odot$, where $\bar{\rho}$ is the present-day mean density of the Universe. The main uncertainty here is the total volume occupied by the mass overdensity, which could well span beyond the current ACS field (Venemans et al. 2002; Intema et al. 2005). The mass overdensity corresponds to a linear overdensity of $\delta_L \sim 0.5$, which when evolved to the present epoch corresponds to a linear overdensity of $\delta_L \sim 2$ (see Steidel et al. 2005). This exceeds the linear collapse threshold of $\delta_c = 1.69$, so the structure will have virialized by $z = 0$. Taken together with the large estimate for its mass the term 'protocluster' is justified.

5.6.2.4 *Redshift evolution of the overdensity*

In a subsequent paper, we will compare the number densities, masses, and total SFRs of galaxies in protoclusters observed at a wide range of redshifts to the properties of massive clusters at $z \lesssim 1$ extrapolated to the early Universe (Overzier et al., in prep.). The progenitors of galaxy clusters must have undergone rapid and intense star-formation (and possibly AGN activity) at $z \gtrsim 2$. The star formation in these 'protoclusters' is not only responsible for the buildup of the present-day stellar mass in cluster galaxies, but also for the chemical enrichment of the ICM (Ettori 2005). The ages of the stellar populations in massive red-sequence galaxies at $z \sim 1$ are sufficiently high for them to be formed at redshifts $2 < z < 6$ (e.g. Blakeslee et al. 2003; Mei et al. 2006). Simulations have indicated that there are significant differences between the redshift of formation and redshift of assembly for the stellar mass in massive early-type galaxies: De Lucia et al. (2006) found that for elliptical galaxies with stellar mass larger than 10^{11} $M_\odot$ the median redshift at which 50% of the stars were formed is ~ 2.5, but the median redshift when those stars were actually assembled into a single galaxy lies only at ~ 0.8. In the same paper, they showed that the star formation properties of ellipticals depend strongly on the environment. For elliptical galaxies in clusters, the average ages can be up to 2 Gyr higher than those of similar mass ellipticals in the field. For an elliptical that is ~ 1 Gyr older compared to the field, 50% of its stellar mass will already have been formed at $z \sim 4$. This stellar mass is likely to be formed in much smaller units, while the number of major mergers is considered to be relatively small (a few).

It is likely that the stellar mass formed by protocluster galaxies will end up in quiescent cluster early-types at lower redshifts, in accordance with the color-magnitude relation. However, there is a significant discrepancy between the masses of the LBGs and LAEs (both in protoclusters and in the field) and the masses of cluster ellipticals of $\gtrsim 10$. On the other hand, the number densities of LBGs found in e.g. TN1338 is a few times larger than the number of early-types on the red-sequence at $z \sim 1$, indicating that they can contribute still significant stellar mass through merging. Alternatively, protocluster fields may host other, older galaxies of significant mass, analogous to the population of distant red galaxies found at $2 < z < 4$ (e.g. Franx et al. 2003; van Dokkum et al. 2003; Webb et al. 2005). These objects are believed to be the

aged and reddened descendants of LBGs that were UV luminous only at $z \gtrsim 5 - 6$, and are therefore missed by the current object selection.

Recent numerical simulations of CDM growth predict that quasars at $z \sim 6$ may lie in the center of very massive dark matter halos of $\sim 4 \times 10^{12}\ M_{\odot}$ (Springel et al. 2005). They are surrounded by many fainter galaxies, that will evolve into massive clusters of $\sim 4 \times 10^{15}\ M_{\odot}$ at $z = 0$ (Springel et al. 2005). The discovery of galaxy clustering associated with luminous radio galaxies and quasars at $z > 2$ is consistent with that scenario (e.g. Stiavelli et al. 2005; Overzier et al. 2006; Zheng et al. 2006; Venemans et al. 2005, this paper).

Acknowledgments

We thank Masami Ouchi for invaluable discussions and reading through the manuscript. We thank Ryan Quadri and Huib Intema for their contributions.

ACS was developed under NASA contract NAS 5-32865, and this research has been supported by NASA grant NAG5-7697 and by an equipment grant from Sun Microsystems, Inc. The Space Telescope Science Institute is operated by AURA Inc., under NASA contract NAS5-26555. We are grateful to K. Anderson, J. McCann, S. Busching, A. Framarini, S. Barkhouser, and T. Allen for their invaluable contributions to the ACS project at JHU.

References

Adelberger, K. L., Steidel, C. C., Giavalisco, M., Dickinson, M., Pettini, M., & Kellogg, M. 1998, ApJ, 505, 18
Barmby, P. et al. 2004, ApJ, 154, 97
Benítez, N. 2000, ApJ, 536, 571
Benítez, N. et al. 2004, ApJ, 150, 1
Bertin, E., & Arnouts, S. 1996, A&AS, 117, 393
Best, P. N., Lehnert, M. D., Miley, G. K., & Röttgering, H. J. A. 2003, MNRAS, 343, 1
Blakeslee, J. P., Anderson, K. R., Meurer, G. R., Benítez, N., & Magee, D. 2003a, in ASP Conf. Ser. 295: Astronomical Data Analysis Software and Systems XII, 257
Blakeslee, J. P., Anderson, K. R., Meurer, G. R., Benítez, N., & Magee, D. 2003b, in ASP Conf. Ser. 295: Astronomical Data Analysis Software and Systems XII, 257–+
Bouwens, R., Broadhurst, T., & Illingworth, G. 2003a, ApJ, 593, 640
Bouwens, R. J., Illingworth, G. D., Blakeslee, J. P., Broadhurst, T. J., & Franx, M. 2004a, ApJ, 611, L1
Bouwens, R. J., Illingworth, G. D., Blakeslee, J. P., & Franx, M. 2005a, Submitted to ApJ
Bouwens, R. J., Illingworth, G. D., Broadhurst, T. J., Meurer, G., Blakeslee, J. P., Franx, M., & Ford, H. 2005b, Submitted to ApJ
Bouwens, R. J. et al. 2003b, ApJ, 595, 589
—. 2004b, ApJ, 606, L25
—. 2004c, ApJ, 616, L79
Brocklehurst, M. 1971, MNRAS, 153, 471
Bruzual, G., & Charlot, S. 2003, MNRAS, 344, 1000
Cimatti, A., Andreani, P., Röttgering, H., & Tilanus, R. 1998, Nature, 392, 895
Coe, D., Benitez, N., Sanchez, S., Jee, M., Bouwens, R., & Ford, H. 2005, Submitted to AJ
Coleman, G. D., Wu, C.-C., & Weedman, D. W. 1980, ApJ, 43, 393
Conselice, C. J. 2003, ApJ, 147, 1
Croft, S., Kurk, J., van Breugel, W., Stanford, S. A., de Vries, W., Pentericci, L., & Röttgering, H. 2005, AJ, 130, 867
Daddi, E. et al. 2002, A&A, 384, L1
Dawson, S. et al. 2004, ApJ, 617, 707
De Breuck, C. et al. 2004, A&A, 424, 1
De Breuck, C., van Breugel, W., Stanford, S. A., Röttgering, H., Miley, G., & Stern, D. 2002, AJ, 123, 637
De Lucia, G., Kauffmann, G., Springel, V., White, S. D. M., Lanzoni, B., Stoehr, F., Tormen, G., & Yoshida, N. 2004, MNRAS, 348, 333
De Lucia, G., Springel, V., White, S. D. M., Croton, D., & Kauffmann, G. 2006, MNRAS, 366, 499
Dey, A., van Breugel, W., Vacca, W. D., & Antonucci, R. 1997, ApJ, 490, 698
Dickinson, M. et al. 2004, ApJ, 600, L99
Dressler, A., Smail, I., Poggianti, B. M., Butcher, H., Couch, W. J., Ellis, R. S., & Oemler, A. J. 1999, ApJ, 122, 51
Elston, R., Rieke, G. H., & Rieke, M. J. 1988, ApJ, 331, L77
Ettori, S. 2005, MNRAS, 362, 110
Ferguson, H. C. et al. 2004, ApJ, 600, L107
Ford, H. C. et al. 1998, in Proc. SPIE Vol. 3356, p. 234-248, Space Telescopes and Instruments V, Pierre Y. Bely; James B. Breckinridge; Eds., 234–248
Francis, P. J. et al. 2001, ApJ, 554, 1001
Franx, M. et al. 2003, ApJ, 587, L79
Giavalisco, M., & Dickinson, M. 2001, ApJ, 550, 177
Giavalisco, M. et al. 2004a, ApJ, 600, L103
—. 2004b, ApJ, 600, L93
Giavalisco, M., Steidel, C. C., Adelberger, K. L., Dickinson, M. E., Pettini, M., & Kellogg, M. 1998, ApJ, 503, 543
Goto, T. et al. 2005, ApJ, 621, 188
Hall, P. B. et al. 2001, AJ, 121, 1840
Holden, B. P. et al. 2005, ApJ, 620, L83
Intema, H., Venemans, B., Kurk, J., Ouchi, M., Kodama, T., Röttgering, H., Miley, G., & Overzier, R. 2005, Submitted to A&A
Kashikawa, N. et al. 2005, ArXiv Astrophysics e-prints
Kauffmann, G., White, S. D. M., Heckman, T. M., Ménard, B., Brinchmann, J., Charlot, S., Tremonti, C., & Brinkmann, J. 2004, MNRAS, 353, 713

Keel, W. C., Cohen, S. H., Windhorst, R. A., & Waddington, I. 1999, AJ, 118, 2547
Kennicutt, R. C. 1998, ApJ, 498, 541
Kinney, A. L., Calzetti, D., Bohlin, R. C., McQuade, K., Storchi-Bergmann, T., & Schmitt, H. R. 1996, ApJ, 467, 38
Kogut, A. et al. 2003, ApJ, 148, 161
Kravtsov, A. V., Berlind, A. A., Wechsler, R. H., Klypin, A. A., Gottlöber, S., Allgood, B., & Primack, J. R. 2004, ApJ, 609, 35
Kron, R. G. 1980, ApJ, 43, 305
Kurk, J., Röttgering, H., Pentericci, L., Miley, G., & Overzier, R. 2003, New Astronomy Review, 47, 339
Landy, S. D., & Szalay, A. S. 1993, ApJ, 412, 64
Lee, K., Giavalisco, M., Gnedin, O., Somerville, R., Ferguson, H., Dickinson, M. E., & Ouchi, M. 2005, Submitted to ApJ(astro-ph/0508090)
Ling, E. N., Barrow, J. D., & Frenk, C. S. 1986, MNRAS, 223, 21P
Lotz, J., Madau, P., Giavalisco, M., Primack, J., & Ferguson, H. 2005, ApJIn Press (astro-ph/0509106)
Lotz, J. M., Primack, J., & Madau, P. 2004, AJ, 128, 163
Möller, P., & Fynbo, J. U. 2001, A&A, 372, L57
Madau, P. 1995, ApJ, 441, 18
Madau, P., Ferguson, H. C., Dickinson, M. E., Giavalisco, M., Steidel, C. C., & Fruchter, A. 1996, MNRAS, 283, 1388
Madau, P., Pozzetti, L., & Dickinson, M. 1998, ApJ, 498, 106
McCarthy, P. J. et al. 2001, ApJ, 560, L131
Mei, S., et al. 2006, ApJ, 639, 81
Meurer, G. R., Heckman, T. M., & Calzetti, D. 1999, ApJ, 521, 64
Miley, G. K. et al. 2004, Nature, 427, 47
Mo, H. J., Mao, S., & White, S. D. M. 1998, MNRAS, 295, 319
Mo, H. J., & White, S. D. M. 2002, MNRAS, 336, 112
Monaco, P., Møller, P., Fynbo, J. P. U., Weidinger, M., Ledoux, C., & Theuns, T. 2005, A&A, 440, 799
Mullis, C. R., Rosati, P., Lamer, G., Böhringer, H., Schwope, A., Schuecker, P., & Fassbender, R. 2005, ApJ, 623, L85
Oke, J. B. 1971, ApJ, 170, 193
Ouchi, M. et al. 2005a, Submitted to ApJ(astro-ph/0508083)
—. 2005b, ApJ, 620, L1
—. 2004a, ApJ, 611, 660
—. 2004b, ApJ, 611, 685
Overzier, R. et al. 2006, ApJ, 637, 1
Papovich, C., Dickinson, M., & Ferguson, H. C. 2001, ApJ, 559, 620
Papovich, C. et al. 2004, ApJ, 600, L111
Pascarelle, S. M., Windhorst, R. A., Driver, S. P., Ostrander, E. J., & Keel, W. C. 1996, ApJ, 456, L21
Pentericci, L., Kurk, J. D., Carilli, C. L., Harris, D. E., Miley, G. K., & Röttgering, H. J. A. 2002, A&A, 396, 109
Pentericci, L. et al. 2000, A&A, 361, L25
Pentericci, L., McCarthy, P. J., Röttgering, H. J. A., Miley, G. K., van Breugel, W. J. M., & Fosbury, R. 2001, ApJ, 135, 63
Petrosian, V. 1976, ApJ, 209, L1
Pickles, A. J. 1998, PASP, 110, 863
Porciani, C., & Giavalisco, M. 2002, ApJ, 565, 24
Postman, M., ACS IDT, ACS IDT, ACS IDT, ACS IDT, ACS IDT, & ACS IDT. 2005, ApJ, Accepted for publication
Rhoads, J. E., Malhotra, S., Dey, A., Stern, D., Spinrad, H., & Jannuzi, B. T. 2000, ApJ, 545, L85
Sánchez, S. F., & González-Serrano, J. I. 1999, A&A, 352, 383
—. 2002, A&A, 396, 773
Schlegel, D. J., Finkbeiner, D. P., & Davis, M. 1998, ApJ, 500, 525
Shapley, A. E., Steidel, C. C., Pettini, M., & Adelberger, K. L. 2003, ApJ, 588, 65
Sheth, R. K., & Tormen, G. 1999, MNRAS, 308, 119
Shimasaku, K. et al. 2003, ApJ, 586, L111
Sirianni, M. et al. 2005, Submitted to PASP
Somerville, R. S., Lee, K., Ferguson, H. C., Gardner, J. P., Moustakas, L. A., & Giavalisco, M. 2004, ApJ, 600, L171
Soneira, R. M., & Peebles, P. J. E. 1978, AJ, 83, 845
Spergel, D. N. et al. 2003, ApJ, 148, 175
Springel, V. et al. 2005, Nature, 435, 629
Stanford, S. A., Eisenhardt, P. R., & Dickinson, M. 1998, ApJ, 492, 461
Stanway, E. R., Bunker, A. J., & McMahon, R. G. 2003, MNRAS, 342, 439
Steidel, C. C., Adelberger, K. L., Dickinson, M., Giavalisco, M., Pettini, M., & Kellogg, M. 1998, ApJ, 492, 428
Steidel, C. C., Adelberger, K. L., Giavalisco, M., Dickinson, M., & Pettini, M. 1999, ApJ, 519, 1
Steidel, C. C., Adelberger, K. L., Shapley, A. E., Erb, D. K.and Reddy, N. A., & Pettini, M. 2005, ApJ in Press (astro-ph/0502432), 626, 44
Steidel, C. C., Adelberger, K. L., Shapley, A. E., Pettini, M., Dickinson, M., & Giavalisco, M. 2000, ApJ, 532, 170
Steidel, C. C., Giavalisco, M., Pettini, M., Dickinson, M., & Adelberger, K. L. 1996, ApJ, 462, L17
Stiavelli, M. et al. 2005, ApJ, 622, L1
Szalay, A. S., Connolly, A. J., & Szokoly, G. P. 1999, AJ, 117, 68
Thompson, D., Aftreth, O., & Soifer, B. T. 2000, AJ, 120, 2331
van Dokkum, P. G. et al. 2003, ApJ, 587, L83
van Dokkum, P. G., Franx, M., Fabricant, D., Illingworth, G. D., & Kelson, D. D. 2000, ApJ, 541, 95
Venemans, B. 2005, Ph. D. Thesis, University of Leiden
Venemans, B. P. et al. 2002, ApJ, 569, L11
—. 2005, A&A, 431, 793
—. 2006, Accepted by A&A
—. 2004, A&A, 424, L17
Villar-Martín, M. et al. 2005, MNRAS, L112
Wang, J. X. et al. 2004, ApJ, 608, L21
Webb, T. et al. 2005, Accepted by ApJ(astro-ph/0511598)
Webb, T. M. et al. 2003, ApJ, 582, 6
Wold, M., Armus, L., Neugebauer, G., Jarrett, T. H., & Lehnert, M. D. 2003, AJ, 126, 1776
Wuyts, S., van Dokkum, P. G., Kelson, D. D., Franx, M., & Illingworth, G. D. 2004, ApJ, 605, 677
Yan, H., & Windhorst, R. A. 2004, ApJ, 612, L93
Zheng, W., et al. 2006, ApJ, In Press (astro-ph/0511734)
Zirm, A. W. et al. 2005, ApJ, 630, 68

Chapter 6

Feedback and brightest cluster galaxy formation: ACS observations of the radio galaxy TN J1338–1942 at $z = 4.1$

Abstract. We present deep optical imaging of the $z = 4.1$ radio galaxy TN J1338–1942, obtained using the Advanced Camera for Surveys (ACS) onboard the *Hubble Space Telescope* as well as ground-based near-infrared imaging data from European Southern Observatory (ESO) Very Large Telescope (VLT). The radio galaxy is known to reside within a large galaxy overdensity (both in physical extent and density contrast). There is good evidence that this 'protocluster' region is the progenitor of a present-day rich galaxy cluster. TN J1338 is the dominant galaxy in the protocluster in terms of size and luminosity (in both the optical and near-infrared) and therefore seems destined to evolve into the brightest cluster galaxy. The high spatial resolution ACS images reveal several kiloparsec-scale features within and around the radio galaxy. The continuum light is aligned with the radio axis and is resolved into two clumps in the i_{775} and z_{850} bands. These components have luminosities $\sim 10^9 L_\odot$ and sizes of a few kpc. The estimated nebular continuum, scattered light, synchrotron- and inverse-Compton scattering contributions to the aligned continuum light are only a few percent of the observed total, indicating that the observed flux is likely dominated by forming stars. The estimated star formation rate for the whole radio galaxy is $\sim 200\ M_\odot\ \mathrm{yr}^{-1}$. A simple model in which the jet has triggered star formation in these continuum knots is consistent with the available data. A striking, but small, linear feature is evident in the z_{850} aligned light and may be indicative of a large-scale shock associated with the advance of the radio jet. The rest of the aligned light also seems morphologically consistent with star formation induced by shocks associated with the radio source, as seen in other high-z radio galaxies (e.g., 4C 41.17). An unusual feature is seen in Lyα emission. A wedge-shaped extension emanates from the radio galaxy perpendicularly to the radio axis. This 'wedge' naturally connects to the surrounding asymmetric, large-scale (~ 100 kpc) Lyα halo. We posit that the wedge is a starburst-driven superwind, associated with the first major epoch of formation of the brightest cluster galaxy. The shock and wedge are examples of feedback processes due to both active galactic nucleus and star formation in the earliest stages of massive galaxy formation.

A. W. Zirm, R. A. Overzier, G. K. Miley, J. P. Blakeslee, M. Clampin, C. De Breuck, R. Demarco, H. C. Ford, G. F. Hartig, N. Homeier, G. D. Illingworth, A. R. Martel, H. J. A. Röttgering, B. Venemans, D. R. Ardila, F. Bartko, N. Benítez, R. J. Bouwens, L. D. Bradley, T. J. Broadhurst, R. A. Brown, C. J. Burrows, E. S. Cheng, N. J. G. Cross, P. D. Feldman, M. Franx, D. A. Golimowski, T. Goto, C. Gronwall, B. Holden, L. Infante, R. A. Kimble, J. E. Krist, M. P. Lesser, S. F. Mei, F. Menanteau, G. R. Meurer, V. Motta, M. Postman, P. Rosati, M. Sirianni, W. B. Sparks, H. D. Tran, Z. I. Tsvetanov, R. L. White & W. Zheng
The Astrophysical Journal, **630**, 68 (2005)

6.1 Introduction

The most massive galaxies in the local Universe reside in the centers of rich clusters. Within the context of hierarchical models of biased galaxy formation, the mass of a galaxy and its clustering properties are naturally connected via the initial density fluctuations (e.g., Kaiser 1984). Therefore, not only locally, but throughout cosmic time, massive galaxies mark the densest regions of the Universe. The study of young overdensities at high redshift ('protoclusters') then also traces the history of the future brightest cluster galaxies.

Many observing programs, spanning wavelengths from radio to X-ray, have been devoted to identifying galaxy overdensities over a large range of redshifts (e.g., Postman et al. 1996; Scharf et al. 1997; Stanford et al. 1997; Rosati et al. 1998; Oke et al. 1998; Rosati et al. 1999; Holden et al. 1999; Kurk et al. 2000; Pentericci et al. 2000a; Holden et al. 2000; Donahue et al. 2001; Francis et al. 2001; Stanford et al. 2002; Postman et al. 2002; Donahue et al. 2002; Mullis et al. 2003; Miley et al. 2004). To date, the most distant protoclusters have been found at $z \sim 5$ (Shimasaku et al. 2003; Venemans et al. 2004). Do these very young overdensities already contain a dominant, massive galaxy?

There are several observational clues to the mass of a high-redshift galaxy. One is the observed *K*-band magnitude, which probes the rest-frame optical out to $z \sim 4$. Another is the presence of a high-luminosity active nucleus (a supermassive accreting black-hole), which implies the existence of a large spheroidal host galaxy at least locally (Magorrian et al. 1998; Gebhardt et al. 2000; Ferrarese & Merritt 2000). High-redshift radio galaxies (HzRGs) are bright at the *K* band and harbor powerful nuclei (Jarvis et al. 2001a; De Breuck et al. 2002; Willott et al. 2003; Jarvis & McLure 2002). Therefore, the fields surrounding HzRGs are important targets for studying the earliest examples of massive galaxies and clusters. Using a narrowband Lyα imaging program, Miley and collaborators discovered an overdensity of star-forming galaxies around all four radio galaxies observed to sufficient depth, out to $z = 5.2$ (Venemans et al. 2004). The resulting set of protoclusters is the subject of several ongoing studies. This discovery also implies that the radio galaxies are the seeds of the brightest cluster galaxies.

The brightest cluster galaxies (BCGs) are the most massive galaxies known in the local universe, with stellar masses in excess of $10^{12} M_{\odot}$ (Jørgensen et al. 1996; Bernardi et al. 2003). The luminosities and sizes of BCGs are not drawn from the same distributions as the majority of the galaxy population (Oegerle & Hoessel 1991). BCGs at low redshift lie on the extrapolated fundamental plane of elliptical galaxies (Oegerle & Hoessel 1991). The surface brightness profiles of some BCGs, the cD galaxies, extend out to hundreds of kpcs. These shallow power-law stellar envelopes blur the distinction between the galaxy and the diffuse intracluster light. Such extreme sources are clearly very useful laboratories for studying the processes inherent in massive galaxy and cluster formation. In fact, several authors have shown that the observed buildup of BCGs can provide key constraints on the hierarchical theory of galaxy formation (Aragon-Salamanca et al. 1998; Burke et al. 2000). The present discrepancies between the predicted (using semi-analytic models) and observed abundance of massive galaxies imply that fundamental processes are not being accounted for in the current models (Cole et al. 2000; Baugh et al. 2003; Somerville et al. 2004). One possibility to solve this discrepancy is to postulate the existence of strong interactions between accreting black-holes, star formation, and their host galaxy and surroundings (i.e., "feedback").

Galaxies that host powerful radio sources are peculiar in several respects. The most striking property is the radio-optical 'alignment effect'. This effect is the strong tendency of the rest-frame ultraviolet continuum light of the radio host to be aligned with the axis defined by the radio source. Several explanations for this behavior have been put forward: recent star formation induced by the radio jet, nebular continuum from emission-line gas that is photoion-

ized or shock-ionized by the active galactic nucleus (AGN), light from the central engine scattered into the line of sight by either dust or electrons, and Inverse Compton scattering of the microwave background or other local photon fields (McCarthy et al. 1987; Chambers et al. 1987; Daly 1992; Dickson et al. 1995). These explanations of the alignment, but particularly the jet-induced star formation, are excellent examples of feedback on the galaxy formation process.

The giant ($\sim$100 kpc) Lyα emitting halos surrounding distant radio galaxies may be an observable consequence of feedback from galaxy formation (e.g., van Ojik et al. 1997; Reuland et al. 2003). The enormous line luminosities of these objects, often in excess of 10^{44} ergs s^{-1}, imply they are massive reservoirs of gas (Kurk et al. 2000; Steidel et al. 2000). What is the origin of this gas: outflow from the galaxy or infall of primordial material? There are several pieces of circumstantial evidence that these halos are connected with the AGN. The halos are often aligned with the FRII radio axis, and in some cases Lyα emission is directly associated with radio structures (Kurk et al. 2003). Perhaps photoionization by the AGN or shocks due to the radio source expansion are responsible for the extended line emission. Spectroscopically, Lyα absorption is seen in addition to the bright halo emission (e.g., van Ojik et al. 1997; Wilman et al. 2004). There is a good correlation between the amount of absorption and the size of the radio source (Jarvis et al. 2001b). A possible scenario is that a neutral hydrogen shell initially surrounds the radio source but is subsequently ionized during the growth of the radio source. There are also some halos known that do not contain a bright radio source (Steidel et al. 2000), suggesting that perhaps the halo phenomenon is associated with the more general processes of galaxy formation rather than being specific to active nuclei.

The radio galaxy TN J1338–1942 ($z = 4.1$ De Breuck et al. 1999) resides in one of the youngest protoclusters known (Venemans et al. 2002; Miley et al. 2004). This galaxy lies within a large Lyα halo that shows unusually asymmetric morphology when compared to other similar radio sources (Venemans et al. 2002). In this paper we present high spatial resolution Hubble Space telescope (*HST*) Advanced Camera for Surveys (ACS) imaging of this radio galaxy. These data provide the clearest view of a young BCG to date. Images in four broadband filters (g_{475}, r_{625}, i_{775} and z_{850}) have been obtained. The resulting magnitudes and colors have been used to apply the 'Lyman break' technique to select galaxies at the same redshift as the radio galaxy (Miley et al. 2004). The exquisite spatial resolution of *HST* ACS allows us to study the detailed morphology of the radio galaxy. Using these data we present a scenario that describes the observed morphology (both continuum and Lyα) and the measured kiloparsec-scale colors and magnitudes within a self-consistent formation framework for TN J1338–1942 (hereafter TN J1338).

This paper is structured as follows: we describe the observations and data reduction in § 6.2, we present the results of our analysis of the combined multiwavelength dataset in § 6.3, and discuss these results in § 6.4. We adopt the 'concordance' cosmology (Spergel et al. 2003) with $\Omega_m = 0.27$, $\Omega_\Lambda = 0.73$ and $H_0 = 71$ km s^{-1} Mpc^{-1}. Within this cosmology, the angular scale at the redshift of TN J1338, $z = 4.1$, is 7.0 kpc arcsec^{-1}. We use the AB magnitude system (Oke & Gunn 1983), except where noted.

6.2 Observations and Data Reduction

6.2.1 ACS Imaging

The ACS data of TN J1338 were taken with two primary goals in mind: first, to enable color-selection of faint protocluster members using the Lyman break technique, and second, to investigate the detailed morphological structure of the brightest protocluster galaxies, including the radio galaxy. To achieve these goals, images were taken in four broadband filters: g_{475} (F475W), r_{625} (F625W), i_{775} (F775W) and z_{850} (F805LP). The g_{475} band is below the Lyman-break for galaxies at $z \gtrsim 4.1$. The r_{625} band con-

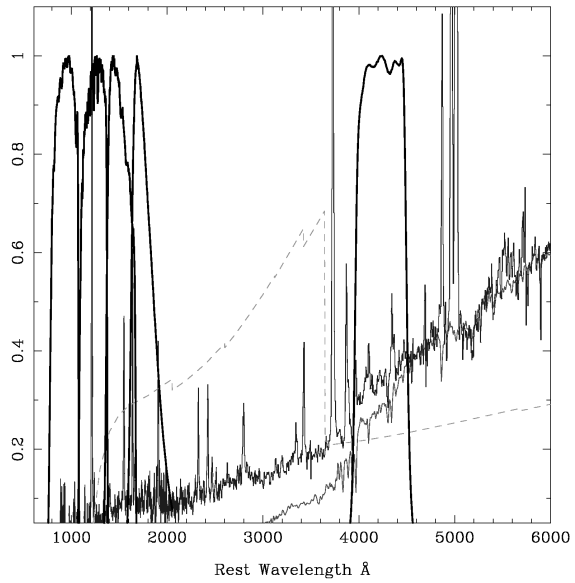

Figure 6.1 — Rest-frame wavelengths covered by the ACS and ground-based near-infrared filters. Shown left to right are the filter curves for the F475W, F625W, F775W, F850LP, and K_S bandpasses (black curves). Also shown for comparison are the characteristic spectra of the nebular continuum emission (green dashed), high-redshift radio galaxies in general (upper blue curve; McCarthy 1993) and an older (1 Gyr) stellar population (lower red curve).

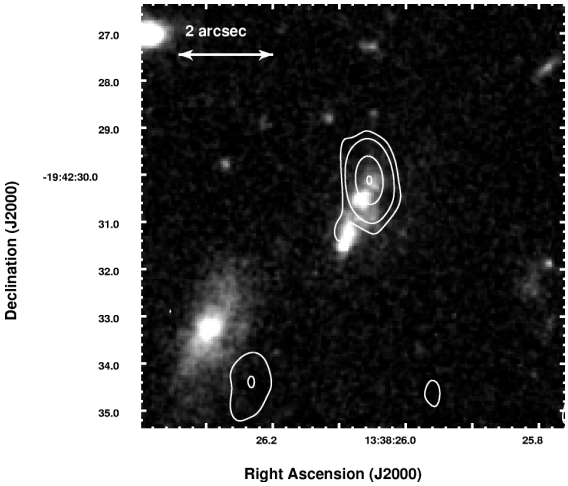

Figure 6.2 — Color composite image of the r_{625}, i_{775} and z_{850} images from ACS, with the VLA 5 GHz radio map overlaid. Notice the blue wedge emanating from the southwestern side of the radio galaxy, this appears only in the r_{625} band and is likely due entirely to Lyα emission. The rest of the emission is clearly aligned with the axis defined by the two radio lobes. The continuum in the i_{775} and z_{850} bands is dominated by the two clumps along the same axis.

tains (and for the case of the radio galaxy, is dominated by) the Lyα emission line. Both the i_{775} and z_{850} bands are relatively unaffected by bright emission lines (see Table 6.1). However, we note that one emission line, C III] λ1909, may be affecting the z_{850} band morphology of the radio galaxy. The g_{475}, r_{625} and i_{775} observations were carried out between 2002 July 8 and 12 and the z_{850} images between 2003 July 11 and 12 with the Wide Field Channel of the ACS. The total observing time of 18 orbits was split between the broadband filters 9400 s in g_{475}, 9400 s in r_{625}, 11700 s in i_{775}, and 11800 s in z_{850}. Each orbit was split into two 1200 s exposures to facilitate the removal of cosmic rays. The g_{475} dropouts were selected using the g_{475}, r_{625} and i_{775} bands as described in Miley et al. (2004) and Overzier et al., in prep. This effort was very successful and confirmed the presence of a galaxy overdensity around TN J1338. In this paper we present the first discussion of the radio galaxy itself and its role as the dominant protocluster galaxy.

The ACS data were reduced using the ACS pipeline science investigation software (*Apsis*; Blakeslee et al. 2003a), developed for the ACS Guaranteed Time Observation (GTO) program. After the initial flat-fielding of the images through CALACS at Space telescope Science Institute (STScI), the *Apsis* processing steps include the empirical determination of image offsets and rotations, the rejection of cosmic rays, the combining of images through "drizzling", and object detection and photometry using SExtractor (Bertin & Arnouts 1996). The final images have a scale of $0\farcs05$ pixel^{-1}, and (2σ) limiting (AB) magnitudes of 28.46 (g_{475}), 28.23 (r_{625}), 28.07 (i_{775}), and 27.73 (z_{850}) in 0.2 arcs^2 apertures (corrected for Galactic extinction).

6.2.2 VLT Optical Imaging and Spectroscopy

Deep VLT FORS2 (Focal Reducer and Spectrograph 2) images ($6\farcm8 \times 6\farcm8$) of the TN J1338 field were made in 2001 March in both the broad-

band R filter ($\lambda_c = 6550$ Å, $\Delta\lambda_{FWHM} = 1650$ Å) and a custom narrowband filter ($\lambda_c = 6195$ Å, $\Delta\lambda_{FWHM} = 60$ Å) to target the redshifted Lyα emission line (Venemans et al. 2002). The 1σ limiting surface brightnesses are 28.6 and 29.2 per arcs^2 for the narrow and broad bands respectively. These images were used to identify candidate Lyα-emitting galaxies (Venemans et al. 2002). For the current paper, these images are used to elucidate the larger scale structure of the Lyα emission and to compare it to the structures seen in the ACS images.

A follow-up spectroscopy program using FORS2 in multiobject mode was carried out in 2001 May. These spectra have a dispersion of 1.32 Å pixel^{-1} (using the 600RI grism) and cover the wavelength range from 5300 to 8000 Å. Candidate Lyα galaxies were placed on two slit masks (Venemans et al. 2002). The radio galaxy itself was included on both slitmasks providing a deep spectrum along the radio axis which covers both the Lyα and C IV λ1549 emission lines.

6.2.3 VLT Near-Infrared Imaging

Our K_S band images of TN J1338 were obtained in two separate observing runs. One on 2002March 24–26 collected 2.1 hr of total exposure time using the Infrared Spectrometer and Array camera (ISAAC) on UT1 of the VLT. The sond run, using the same instrument, was done in service mode at VLT between the nights of 2004 May 27 and June 13. The total exposure time for this run was 5.7 hr. All the data were processed, sky-subtracted and combined using the XDIMSUM package within IRAF[1] (Tody 1993). The final image has a scale of 0.148″pixel^{-1}, a seeing of 0.″5, and a (2σ, 1 arcsec^2 aperture) limiting magnitude of 25.6. ISAAC has some geometrical distortion across the face of the detector. We have not corrected the distortion in detail because the K_S morphology of the radio galaxy matches features seen in the continuum ACS observations.

[1]IRAF is distributed by the National Optical Astronomy Observatories, which are operated by the Association of Universities for Research in Astronomy, Inc., under cooperative agreement with the National Science Foundation.

The K_S band is the only band that probes wavelengths longward of the 4000 Å break, beyond which an old stellar population should dominate the emergent flux (see Figure 6.1). It should be noted, however, that the bandpass is not entirely at $\lambda > 4000$ Å. However, these data still provide a crucial point on the spectral energy distribution (SED) of the radio galaxy.

6.2.4 Radio Imaging

The radio source TN J1338 was originally selected because of its ultrasteep spectrum (between 365 MHz and 1.4 GHz) which has been shown to be an indicator of high redshift (De Breuck et al. 2000b). The first radio data were culled from the Texas and NVSS (NRAO VLA Sky Survey) catalogs (Douglas et al. 1996; Condon et al. 1998). Follow-up observations were made with the Very Large Array (VLA) at 4.71 and 8.46 GHz in 1998 March (Pentericci et al. 2000b). The noise levels are 25 and 50 μJy beam^{-1} for the 8 and 5 GHz maps, respectively. The resolution is 0.″23 for the 8 GHz map and 0.″43 for the 5 GHz map. These are the primary radio data used in this paper (see overlay in Figure 6.2). The radio source has three distinct components at both these frequencies; the northwest ($S^{NW}_{4.7GHz} = 21.9$ mJy) and southeast ($S^{SE}_{4.7GHz} = 1.1$ mJy) lobes (separated by 5.″5) and the likely radio core ($S^{core}_{4.7GHz} = 0.3$ mJy) located very close (1.″4) to the northwest lobe (De Breuck et al. 1999). The radio source is highly asymmetric, with the northwest lobe nearly 20 times brighter at 4.7 GHz than the southeast lobe. The radio asymmetry may indicate an asymmetry in the ambient medium (McCarthy et al. 1991).

6.2.5 Image Registration

The center position, orientation and angular resolution all differ between the ground-based and space-based data sets. To facilitate comparison amongst these data sets, we registered them all to a common reference frame and pixel scale. The ACS images were registered with respect to each other in the ACS GTO pipeline. We chose the ACS r_{625} frame as this common grid.

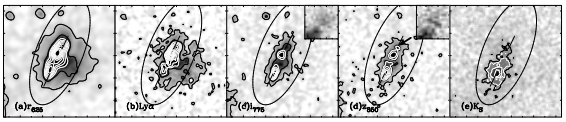

Figure 6.3 — Four optical and one near-infrared images used in this paper. North is up and east to the left. Each cutout is 4.″5 on a side. From left to right: The r_{625} ACS image, the same image but continuum-subtracted, the i_{775} ACS image, the z_{850} ACS image and finally the K_S image from VLT. All the ACS images have been smoothed with a 1.5 pixel Gaussian kernel. The arrow in panel (d) marks the linear feature which is likely a large-scale shock, which is also shown unsmoothed in the inset. The two lines indicate the radio axis and the ellipse is the Kron aperture used for photometry of the entire radio galaxy.

For the ground-based R and K_S data this registration requires interpolation from plate scales of 0.″201 and 0.″148 pixel^{-1} to 0.″05 pixel^{-1}, respectively. The shifts, rotations and rebinning were all done in a single interpolation step using the IRAF tasks *geomap* and *geotran*. We fitted a general coordinate transformation using second-order polynomials in both axes. The rms deviations of the data from the fits were on the order of 0.3 input pixels (0.″04) for the K_S image and 0.07 input pixels (0.″01) for the FORS2 narrow and broad band images. The calculated transformations were done using 'sinc' interpolation within *geotran*. At least 15-20 unsaturated stars were matched within the ACS r_{625} band and each of the ground-based images to calculate the appropriate transformations. We applied these transformations to the ground-based R-band, narrowband and K_S-band images.

The optical/near-infrared frame is defined by stellar positions and that of the radio image is defined by the positions of radio point sources (quasars). The radio image of the TN J1338 field is sparse, so a direct matching of sources will not produce a robust transformation between the two frames, particularly when we do not want to use the radio galaxy itself. Therefore the accuracy limit to the radio-optical registration is determined solely by the systematic error in the optical reference frame. To better quantify this we have used two different optical frames, those of the USNO and the GSC-2.0, and compared the astrometric solutions using each one to the radio data. This gives us a conservative amplitude of 0.″3 to the error on the position of the radio core with respect to the optical structures in the ACS and ground-based data. Therefore, we can confidently associate the radio core with the region near the peak of the K_S-band flux and at one tip of the ACS galaxy.

6.2.6 Continuum subtraction

To model the continuum in the r_{625} band we have used a power-law extrapolation from the relatively emission line-free i_{775} and z_{850} bands. While these filters are not strictly line-free due to the presence of C IV λ1549 in the i_{775} band, He II λ1640 in both passbands and, to a lesser extent, C III] λ1909 in the z_{850} band, none of these lines are expected to dominate the continuum (based on spectroscopic data, see Table 6.1). We assume that the continuum follows a simple power-law in $F_\lambda (\propto \lambda^\beta)$ that extrapolates through to the ACS r_{625} bandpass, VLT R-band and narrowbands. We have accounted for the intergalactic absorption shortward of the emission line and the relative throughputs of the filter curves.

Light at wavelengths shorter than Lyα is easily absorbed by neutral hydrogen located between the source and the observer. This will greatly affect the amount of continuum light detected in any bandpass shortward of the emission line. We have therefore adopted the model of the intergalactic hydrogen optical depth presented in Madau (1995): $\tau_{\rm eff} = 0.0036(\lambda_{\rm obs}/\lambda_\beta)^{3.46}$. This is the optical depth due to Lyα forest lines, and not due to higher order Lyman series or metal lines. These two opacity sources make negligible contributions to the total optical depth at this redshift (Madau 1995). We integrate this attenuation over the filter curve shortward of Lyα to determine the amount of continuum flux absorbed in the intergalactic medium (IGM). This correction decreases the amount of continuum by 23.9%, 16.9% and 36.2% in the ACS r_{625}band, the VLT R-band and the VLT narrowbands, respectively. In addition, the continuum flux detected in the images is affected by the filter throughput

curves. The extrapolation from continuum measured in some filters (in our case, the ACS i_{775} and z_{850}) to other bandpasses depends on the relative filter curves. We have used the total integrated throughputs to correct for the differential sensitivities. The final value of β for the entire radio galaxy is -1.32 (or $\alpha = 0.62$, where $F_\nu \propto \nu^\alpha$).

6.3 Results

The ACS and VLT images are shown in Figure 6.3. The rest-frame ultraviolet morphology of TN J1338 is complex and multi-faceted. The radio galaxy exhibits the usual alignment between its continuum, line emission and radio axis (Chambers et al. 1987; McCarthy et al. 1987; Best et al. 1998). Two kilopars-sized clumps along the radio axis dominate the continuum structure in the i_{775} and z_{850} bands. This is similar to many powerful 3CR radio galaxies at $z \sim 1$ (Best et al. 1998; Zirm 2003; Zirm et al. 2003). In the r_{625} band, the ACS image reveals both concentrated and diffuse Lyα emitting regions. In this Section we quantify the line and continuum flux distributions for the radio galaxy by performing photometry in a set of varied apertures.

6.3.1 Estimating the Contributions to the Aligned Light

The presence of a powerful radio source has several effects on the emitted spectrum. As mentioned above, at least three of these effects tend to align the observed continuum emission with the axis defined by the double radio lobes. Any remaining continuum flux we attribute to a young stellar population.

Ionized gas emits not only emission lines, but also continuum photons from two-photon recombination, bremsstrahlung recombination, and standard recombination. For a given gas temperature and density, this nebular continuum spectrum can be calculated (see Figure 6.1). Observationally, the normalization of the nebular spectrum is determined by using the emission-line spectrum. For TN J1338–1942 we have a spectrum which was taken along the radio axis and that spatially averages the entire optical extent of the radio galaxy (RG). Ideally one would measure Balmer recombination emission lines. These lines directly correspond to the nebular continuum. At $z = 4.1$, these lines have shifted out of the optical window visible from the ground. As a 'Balmer proxy', we use the He II λ1640 emission line (Vernet et al. 2001), which has a flux of $\approx 1.7 \times 10^{-16}$ ergs s^{-1} cm^{-2} (2004, C. De Breuck, private communication). Assuming the He II Hβ ratio ($= 3.18$) from a high-redshift RG composite spectrum (McCarthy 1993), we estimate the Hβ flux to be 5.4×10^{-17} ergs s^{-1} cm^{-2}. If these emission lines arise in a 15,000 K gas, at densities low enough that collisional de-excitation is negligible, then the corresponding nebular continuum flux densities in the r_{625}, i_{775} and z_{850} bands are 1.5×10^{-31}, 3.1×10^{-31}, and 3.8×10^{-31} ergs s^{-1} cm^{-2} Hz^{-1}, respectively. Thus, at its brightest the nebular continuum averaged over the entire galaxy is only z_{850}(AB)$= 27.4$, much fainter than even the individual components of TN J1338. We subtract the nebular continuum from all quoted magnitudes and fluxes by scaling the subtracted amounts for the subcomponents by their estimated Lyα flux.

The same population of electrons that is responsible for the radio synchrotron emission can also Inverse Compton (IC) scatter ambient photon fields. The primary seed photons are those making up the cosmic microwave background (CMB), with sondary contributions from the synchrotron photons themselves (synchrotron self-Compton [SSC]) and other AGN emission. By assuming equipartition to calculate the magnetic field in the northern radio lobe of TN J1338, we find a B field on the order of a few hundred mG. If we use the extrapolation to the rest-frame UV as calculated by Daly (1992), this translates to an IC-CMB contribution of only a few times 10^{-31} ergs s^{-1} cm^{-2} Hz^{-1}, or fainter than 28 mag (AB). The estimated energy density in the synchrotron field is similar to that of the CMB at this high redshift, so SSC adds a similar amount to the aligned continuum. These two contributions combined are negligible. As

with the spectroscopy above, these values are spatially averaged over the entire galaxy.

Optical spectropolarimetry of the entire galaxy reveals a polarization of $5 \pm 3\%$ (2004, C. De Breuck, private communication). This value is much lower (about a factor of 2) than similar measurements of $z \sim 1$ RGs (e.g., Dey et al. 1996; Cimatti et al. 1996, 1997; Solórzano-Iñarrea et al. 2004), but similar to other powerful RGs at $z \sim 4$ (Dey et al. 1997). The amount of scattered light is related to the percent polarization by the intrinsic polarization, P_i. The value of P_i depends on the type of scatterer (either dust or electrons) and the geometry of the scattering, neither of which is well constrained for TN J1338. Therefore, we can only put the lower limit on the percentage of scattered light of 5%. However, we also note that for $z \sim 1$ 3CR radio galaxies the observed polarizations are high and suggest that P_i is also high. We therefore conclude that for TN J1338, the aligned continuum contains some scattered light ($\sim 10\%$) but is substantially diluted by unpolarized sources. We have already shown that neither the nebular continuum nor the IC scattering can account for this dilution.

Clear evidence for the presence of young stellar populations in radio galaxies has proven difficult to find. The same spectral region, the ultraviolet, where massive stars are brightest coincides with the bright region of the AGN SED. Therefore, the detection depends on being able to find stellar-specific features in very deep spectra (e.g., the SVλ1502 photospheric absorption feature in 4C 41.17 at $z = 3.8$; Dey et al. 1997). Existing spectra of TN J1338 do not show such features. In this case the presence of young massive stars must be inferred from the UV excess after subtracting the other known contributors to the aligned light. As we have shown above, there seems to be such an excess in TN J1338, which implies the existence of many young stars. We examine this result further below.

6.3.2 Large-Aperture Photometry

To perform integrated photometry over the whole galaxy, we used a Kron aperture (Kron 1980) to approximate a total galaxy magnitude in the ACS and VLT images. This enables easy comparisons between the space-based and ground-based observations of TN J1338. This aperture is optimized to be as large as possible while still retaining a high signal-to-noise ratio. The magnitudes were determined using SExtractor (Bertin & Arnouts 1996). The *Apsis* pipeline deblends the radio galaxy into two distinct objects. We therefore reset the SExtractor deblending parameters to maintain the radio galaxy as a single object. We overplot the aperture in Figure 6.3. The total magnitudes within this aperture are listed in Table 6.1.

The radio galaxy is > 1.4 mag brighter than the next brightest dropout or Lyα emitting galaxy (within similarly defined apertures). This is true even in the K_S-band, where the light from older stars is presumed to dominate the emission rather than processes related to the AGN. Therefore, the radio galaxy is surely identified as the dominant and likely most massive galaxy within the protocluster and the probable progenitor of a present-day BCG.

6.3.3 Rest-frame Optical Surface Brightness Profile

The K_S-band samples the rest-frame optical continuum emission, mostly longward of the 4000 Å break and shortward of the potentially bright [O II] $]\lambda\lambda 4959, 5007$ and Hβ lines. At these wavelengths it is likely that the galaxy luminosity is dominated by older, low-mass stars. We show the final ISAAC image of the radio galaxy in Figure 6.3e and the raw surface brightness profile of the radio galaxy and a star in this band in Figure 6.4. This profile is centered on the peak of the K_S-band light. It is clear that the galaxy is resolved, but it is not possible to measure the size of the galaxy robustly from these data. A simple $r^{\frac{1}{4}}$ law fit roughly estimates the effective radius at $0\farcs7$ or ~ 5 kpc. This is considerably smaller than the corresponding radii of

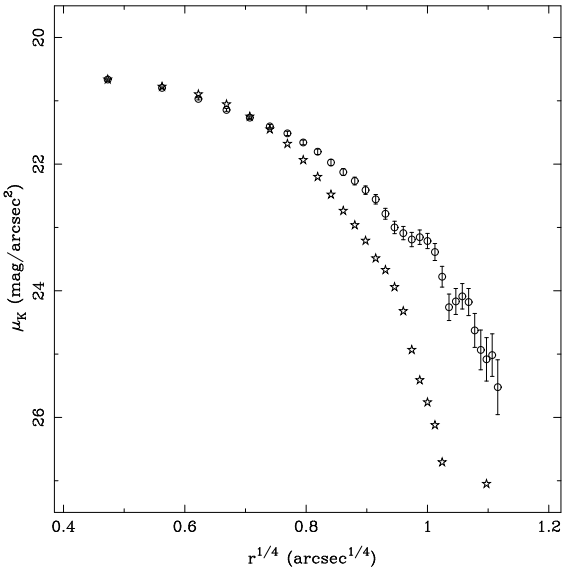

Figure 6.4 — K_S–band surface brightness profile for TN J1338, extracted in circular apertures (circles), along with that of a star measured in the same manner (stars). The radio galaxy is clearly extended and there is some indication that the profile may follow a de Vaucouleurs law. However, these data does not have sufficient spatial resolution to decisively determine the form of the surface brightness profile.

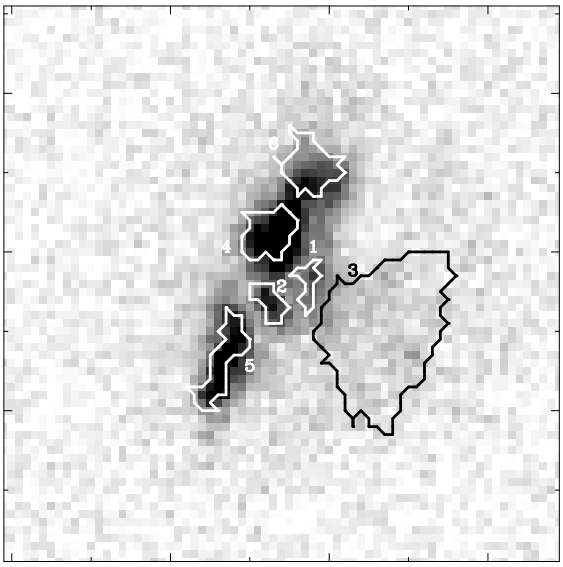

Figure 6.5 — Segmentation map of the galaxy showing the labelled individual clumps. North is up and east to the left. This cutout is 3.″5 on a side, with major tickmarks every arcsond.

local BCGs (e.g., Graham et al. 1996). In fact, the observed morphology in the K_S image is very similar to that seen in the ACS i_{775} band. The galaxy is highly elongated and is nearly perfectly aligned with the radio axis. There are no bright emission lines within the bandpass, and none of the continuum processes discussed above are bright in the K_S-band. Therefore, we conclude that the stellar distribution is aligned with the radio axis.

6.3.4 Multi component Decomposition and Diffuse Light

The rest-frame ultraviolet morphology of TN J1338 can be decomposed into several discrete components. To better understand the morphology of the galaxy, we have extracted multiband photometry of these individual components. We divided the radio galaxy into distinct regions, both in the line-dominated r_{625} band and in the continuum-dominated i_{775} band. The resulting segmentation map is shown in Figure 6.5. The regions are numbered 1–6. Regions 1, 2 and 3 (the 'wedge') are found only in the emission line-ominated r_{625} band. Conversely, regions 4 and and 5 are most prominent in the continuum bands (i_{775} and z_{850}). Finally, region 6 contains a linear feature in z_{850}.

For each region we have measured the magnitude in each ACS band and in the ACS Lyα (continuum subtracted r_{625}) image. Using these values we have derived the UV continuum slope and line flux independently for each portion of the galaxy. In addition, we have measured the magnitudes in the K_S-band for the two primary continuum clumps visible in the ACS data (regions 4 and 5). The $(i_{775}–K_S)_{AB}$ color for region 5 is ~ 0.2 mag redder than region 4. The sum of the light contained within these clumps is about one magnitude fainter in the i_{775} band than the total radio galaxy, indicating that there is some "diffuse" light detected in these high angular resolution images. This remains the case in the z_{850} band, with the extended light appar-

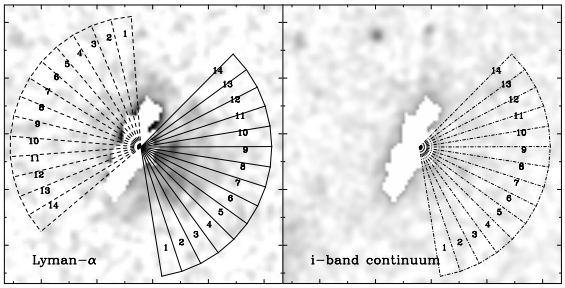

Figure 6.6 — Azimuthal bins used to measure the profile shown in Figure 6.7, overlaid on the continuum-subtracted r_{625} (left) and i_{775} (right) images.

ently having the same color as the mean color of the entire galaxy. The magnitudes and Lyα fluxes are presented in Columns 3-6 of Table 6.2.

6.3.5 Azimuthal Binning

While the aligned light is a common feature of high-redshift radio galaxies, the wedge of extended line emission to the southwest of the radio galaxy (region 3 in Figure 6.5) is unusual. We have measured the azimuthal surface brightness distribution of this feature by extracting photometry in angular bins. The bins are shown in Figure 6.6. The angular regions are sized and placed to cover the entire visible extent of the wedge and to be small enough to accentuate the internal structure of the feature. The flux in each bin was summed using the IRAF task polyphot. The corresponding errors were calculated by performing the same aperture photometry on the error maps. The pixels within the radio galaxy (as defined by the extent of the i_{775} band continuum) were masked out. The resulting flux histogram is shown in Figure 6.7 for the wedge (solid line), the opposite side of the galaxy in the line image (the 'anti-wedge'; dashed line) and for the i_{775} band continuum in the wedge region (dotted line).

The bins covering the wedge show a clear excess of flux with respect to both the opposite side of the galaxy and to the continuum. There also appears to be some structure those for the azimuthal profile. The azimuthal profile has relatively sharp cutoffs at either side. There is no

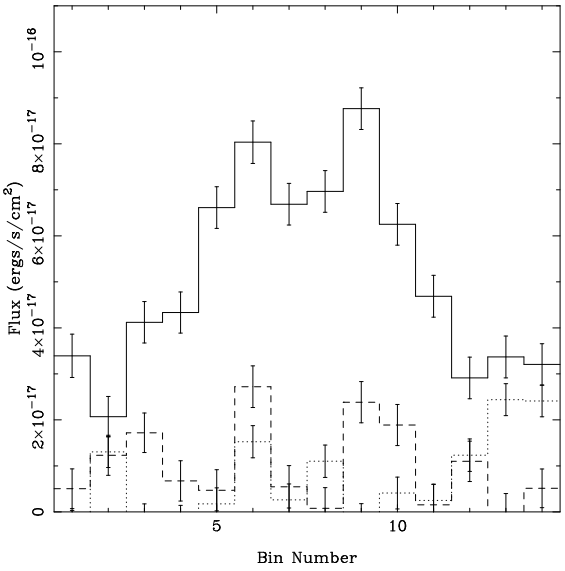

Figure 6.7 — Azimuthal profile of the wedge (solid line), antiwedge (dashed line) and i_{775} continuum (dotted line). Note the sharp cutoff on either side of the wedge and the possible substructure (radial filaments) in the profile.

evidence for limb brightening toward the edges of the wedge. However, the spatial resolution (~ 1.5 kpc bin^{-1}) is insufficient to resolve a thin shell of limb-brightened emission.

6.3.6 Semicircular Annuli

To measure the radial profile of the wedge we have constructed semicircular annuli which cover the same region(s) as the angular bins above (Figure 6.8). We have increased the width of the annuli towards the outer edge of the wedge to maintain constant signal-to-noise ratio per annulus. The annular photometry again shows that the line emission is significantly brighter in the wedge than on either the opposite side of the galaxy or in the continuum. The surface-brightness profiles for the wedge (solid line), anti-wedge (dashed line), and continuum (dotted line) are shown in Figure 6.9. The errors for each data point were derived by performing identical photometry on the corresponding error map. There does not seem to be evidence for limb brightening toward the outer edge of the

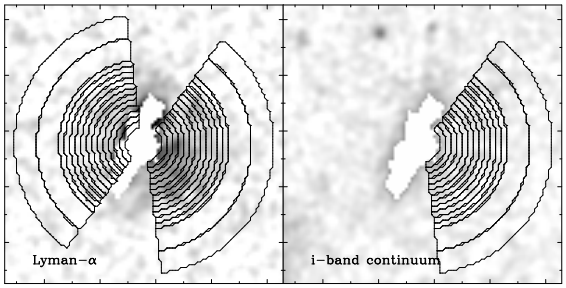

Figure 6.8 — Semicircular annuli used to measure the radial profile of the wedge in Lyα (left). The same annuli were also used on the antiwedge side of the galaxy and on the *i*-band continuum image (right). North is up and east to the left. Each cutout is 5″ on a side, with major tickmarks separated by 1″. The radial dependence of all three are shown in Fig. 6.9.

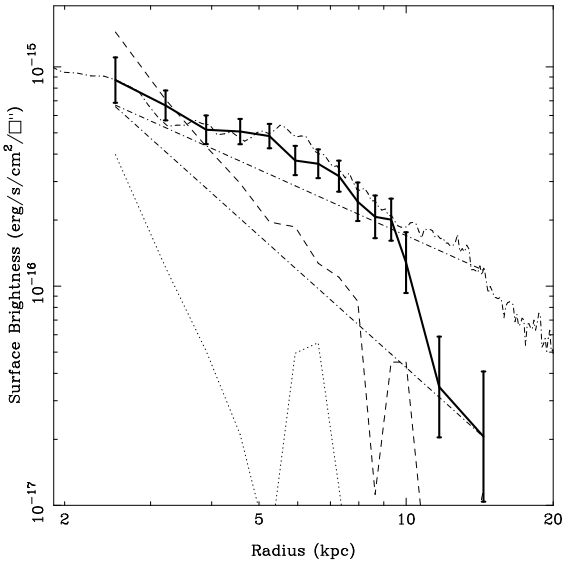

Figure 6.9 — Radial surface brightness profile for the wedge (solid line), antiwedge (dashed line) and continuum (dotted line) annuli. The profile derived from the GALEX data for M82 normalized to the TN J1338 wedge is plotted as a dot-dashed line. The two straight dot-dashed lines are power laws of slope -1 and -2. There is a clear excess of flux in the wedge between radii of 3.5 and 10 kpc. The slope follows the GALEX profile and the $\alpha = -1$ power law well out to 10 kpc. At 10 kpc, the wedge profile falls off rather sharply, but the errors are large.

wedge. Also shown are power-law profiles of the form SB(r) $\propto r^{\alpha}$ with α values of -1 and -2 (dot-dashed lines). The wedge profile has a profile much closer to the $\alpha = -1$ curve. We consider these profiles further in the discussion.

6.4 Discussion

The unparalleled spatial resolution provided by *HST* and the Advanced Camera for Surveys has allowed us to observe kiloparsec-scale structures within the radio galaxy TN J1338–1942 at $z = 4.1$. The rest-frame ultraviolet continuum and line emission of the host galaxy is morphologically complex and consists of several distinct components. In this Section we discuss these features and their implications for the formation of this galaxy and attempt to construct a possible scenario for the ongoing processes in this source.

6.4.1 Ongoing Star Formation

Are we witnessing the formation of the bulk of the final stellar mass in this radio galaxy? Previous studies based on ground-based optical and millimeter imaging suggest that the current star formation rate (SFR) within TN J1338 is very high, on the order of several hundred $M_{\odot}$ yr^{-1} (Venemans et al. 2002; De Breuck et al. 2004). The current study not only confirms this estimate, under different assumptions, but also determines the spatial gradients in star formation activity. This new spatial information allows us to constrain both the timescale and possible physical origin of the current star formation episode.

There are two methods to estimate the SFR in TN J1338 using the ACS imaging data: one using the Lyα luminosity and the other using the UV continuum luminosity. Both estimates are based on the assumption that the UV light we see from the galaxy is due solely to star formation. As we have shown earlier, the UV continuum is relatively unpolluted by the nonstellar contributors to the aligned light. Conversely, for the line emission, the high observed equivalent widths argue in favor of nonstellar excitation (e.g., Charlot & Fall 1993). Therefore, the line emission provides an upper limit (modulo

dust extinction) to the SFR, while the UV continuum provides a lower limit. The comparison of these two derived values provides an estimate of the mean SFR for each portion of the galaxy.

For a given Lyα flux, we calculate the corresponding Balmer line flux and hence the SFR (Kennicutt 1998). This SFR is a lower limit locally due to Lyα being a resonantly scattered line and very susceptible to dust. For example, the Lyα flux of the wedge (region 3 in Figure 6.5) is 3.3×10^{-16} ergs s^{-1} cm^{-2}, corresponding to an intrinsic luminosity of 5.2×10^{43} ergs s^{-1} at $z = 4.1$. If we adopt a Case B Lyα/Hα ratio of 8.7 (Brocklehurst 1971) and use the relation between Hα line flux and SFR, we find that region 3 is forming stars at a rate of $40\,M_\odot$ yr^{-1}. The analogous results for the other regions are listed in Table 6.2. The total Kron Lyα SFR is $290\,M_\odot$ yr^{-1}. The sum of the individual SFRs does not equal this total, underpredicting it by $\approx 90\,M_\odot$ yr^{-1}. There is a considerable amount of low surface brightness line emission even within the Kron aperture ($\sim 18 \times 7$ kpc). We have not corrected for the observed HI absorption (De Breuck et al. 1999; Wilman et al. 2004).

The i_{775} and z_{850} band probe the rest-frame UV of TN J1338–1942 at ~ 1500 and ~ 1775 Å, respectively. We can use the ACS continuum magnitudes to estimate the current SFR, under the assumptions that the UV luminosity is dominated by the light from late O early B stars on the main sequence. We measure total (Kron) SFRs of 86 and 96 $M_\odot$ yr^{-1} for the i_{775} and z_{850} bands, respectively, assuming a Salpeter Initial Mass Function (IMF). The derived SFRs are lower limits, since they are dependent on the amount and the distribution of dust present in the UV emitting regions. The slope of the UV continuum can also be used to measure the extinction. We measure the slope of the continuum from the i_{775}–z_{850} color and use a template spectrum of a typical star-forming galaxy redshifted to $z = 4.1$ to convert the measured slope to a color excess, $E(B-V)$. For the template spectrum we have used the stellar population synthesis models of Bruzual & Charlot (2003) to create a typical Lyman break galaxy spectrum with an exponentially declining star formation history (with time constant, $\tau = 10$ Myr), an age of 70 Myr, 0.2 $Z_\odot$ metallicity, and a Salpeter IMF. The parameters of this template are taken from the best-fit SED at $z \sim 3$ of Papovich et al. (2001). We varied the dust content by applying the attenuation curve of Calzetti et al. (2000) to this template. We find $E(B-V) = 0.12$, yielding a dust-corrected SFR of $\sim 220\ M_\odot$ yr^{-1}, in good agreement with the emission line estimate above. If we repeat this calculation for each discrete region of the galaxy [allowing for $E(B-V)$ and SFR to change for each; see Table 6.2], we again find evidence for diffuse UV light and star formation. The sum of the SFRs for all the regions again falls short of the total by a factor of 4.5, "missing" $170\,M_\odot$ yr^{-1}.

6.4.1.1 *Shocks and Jet-Induced Star Formation*

One of the primary explanations for the alignment effect is that the passage of the radio jet through the interstellar gas induces star formation (e.g., Rees 1989). Strong large-scale shocks associated with the expanding radio source overpressure molecular gas clouds, which then collapse to form stars. The presence of powerful shocks in radio galaxies at $z \lesssim 2$ has been inferred via their ultraviolet emission-line ratios (e.g., Best et al. 2000; De Breuck et al. 2000a). For TN J1338, most of the important diagnostic emission lines are unobservable from the ground. However, we can use morphological information to search for possible signatures of shock processes in this radio galaxy.

In these respects, useful analogies can be drawn between TN J1338 at $z = 4.1$ and 4C 41.17 at $z = 3.8$. The shock properties of 4C 41.17 were studied and modeled in detail by Bicknell et al. (2000). In addition to *HST* imaging of 4C 41.17, these authors also used deep emission-line spectra and high angular resolution radio imaging to study the relationship between the radio source, the gas, and the stars. We apply a similar analysis to TN J1338.

A bow shock is formed at the tip of the advancing radio jet (cf. Figure 3 in Bicknell et al.

(2000)). Due to the unresolved radio structure we cannot robustly determine the location of the jet interaction. We assume that region 4 in the continuum ACS image is the primary site where the jet has shocked or is still impacting the gas. This continuum knot is very blue and has a morphological structure which is suggestive of jet-cloud interaction, namely, a paraboloid oriented along the radio axis. From the spatially-resolved optical images we estimate the interaction area to be $\sim 2 \times 10^{44}$ cm^2 by assuming the emission we see is emitted by a spherical shell. The jet is most likely well collimated and therefore the area of the jet itself is much smaller than the total; we assume 10%. If we assume that most of the momentum flux of the jet is dissipated in this interaction, the shock velocity (see Eq. 1 of Bicknell et al.) will be greater than:

$$v_{\rm sh} \gtrsim 300 - 2000 F_{\rm E,46}^{1/2} \beta_{\rm jet}^{-1/2} n_{\rm H}^{-1/2} {\rm km\ s^{-1}} \quad (6.1)$$

where $F_{\rm E,46}$ is the energy flux of the jet in units of 10^{46} ergs s^{-1}, $\beta_{\rm jet}$ is the relativistic Doppler parameter, and $n_{\rm H}$ is the hydrogen density per cm^3 in the cloud. Comparison between model and observed C IV $\lambda\lambda 1548, 1550$ doublet fluxes can help to constrain the pre shock gas density and the energy flux of the jet. Assuming that the ACS UV/Lyα image also shows the spatial distribution of C IV, we can constrain the area from which the line is being emitted. We use the observed C IV Lyα flux ratio to convert the Lyα image to a "C IV" image. If we follow Bicknell et al. (2000) and take A_p to be the projection of the true area of the shock A_{sh} in region 4 and predict the C IV line luminosity for our estimated shock velocity we find

$$L({\rm C\ IV}) \approx 2 \times 10^{42} [\frac{\alpha({\rm C\ IV})}{0.01}] n_H (\frac{A_{sh}}{A_p})^{-1} {\rm ergs\ s^{-1}} \quad (6.2)$$

where α(C IV) is the radiative efficiency of the C IV doublet. By comparing this to the observed line luminosity (4.8×10^{42} ergs s^{-1}), we estimate that the pre shock electron number density to be on the order of $n_{\rm H\,I} = 3$ cm^{-3}.

We have estimated the SFR produced by the jet-cloud interaction in region 4. To determine whether these shocks can lead to SFRs in excess of a couple dozen M$_\odot$ yr^{-1} (for region 4), we parameterize the jet-induced star formation as follows.

$${\rm SFR} = 26 (\frac{\epsilon}{0.01})(\frac{f_{\rm gas}}{1.0})(\frac{\rho}{3{\rm cm^3}}) {\rm A_{sh,44}} v_{\rm sh,1000}\, {\rm M_\odot\ yr^{-1}} \quad (6.3)$$

We have taken the ambient pre shock gas number density, ρ, to be 3 cm^{-3}, as inferred above using the line luminosity. The area of the shock front is taken from the image itself, and the shock velocity was assumed to be between the extremes possible in Equation 6.1 above. The efficiency with which the shocked gas is converted into stars is denoted by ϵ, and the gas volume filling factor is denoted by $f_{\rm gas}$. The assumption of filling factor on the order of unity is most likely incorrect globally in the galaxy but is more likely to be realistic in this limited region, where the gas is approximately uniform. We conclude that jet-cloud interactions could be responsible for the observed star formation in TN J1338.

The existing radio imaging data of TN J1338 does not have sufficient angular resolution to make direct correspondence with specific features in the ACS images. However, since the radio structure clearly overlaps the optical galaxy, the comparison with 4C 41.17 and our assumption of a physical connection between the radio and optical structures are likely to be justified.

6.4.2 The 'Wedge'

The coupling and regulation of star formation and nuclear activity in forming galaxies and their interaction with their environments (i.e., feedback) is a key issue in modern astrophysics. At low redshift, imaging and spatially resolved spectrocopic observations of starbursting galaxies show that supernovae-driven outflows, the so-called superwinds, are common among this population (e.g., Heckman et al. 1990). Whether such outflows actually achieve escape velocity and enrich the IGM is still an outstanding ques-

tion (Heckman 2000; Heckman et al. 2000; Martin 2004). However, these winds, along with nuclear outflows, are the only processes observed to transport material into the outer halos of galaxies and are therefore prime candidates for injecting the metals and energy that are observed in the IGM. At high redshift, at which these processes are likely to be even more prevalent due to the higher global SFRs, the strongest evidence for the presence of outflows is spectroscopic. However, the spectroscopic features observed are of ambiguous origin and could be due to inflow, outflow or rotation (e.g., van Ojik et al. (1997), but see also Adelberger et al. (2003)). Spatially resolved imaging of the emission-line gas can provide a more certain indication of outflow if the gas is collimated or exhibits the bipolar morphology of low-redshift superwinds. In the next Sections we consider several possible origins for the wedge: the photoionization cone of an AGN or young stellar population, insitu star formation, scattering by dust, or an ionized outflow associated with a starburst (i.e., a superwind).

6.4.2.1 *Photoionization*

In several low-redshift Seyfert galaxies, cone-shaped regions of high ionization are observed, consistent with photoexcitation by an active nucleus (e.g., Wilson & Tsvetanov 1994). In some cases these cones extend to distances of 15-20 kpc from the nucleus, similar to the size of the Lyα wedge seen in our ACS image (Wilson & Tsvetanov 1994). Both the ionized cone and our wedge have high equivalent width. We derive a lower limit to the Lyα rest-frame equivalent width of 650Å for the wedge emission. Furthermore, powerful radio galaxies are known on the basis of emission-line diagnostics and imaging of low-redshift sources, to photoionize their surroundings. Generally, both the line and UV continuum emission are elongated and aligned with the radio axis, particularly at $z > 0.7$ (McCarthy et al. 1987; Chambers et al. 1987).

Conversely, however, the principal wedge axis is perpendicular to that of the radio source. The unified model for AGNs posits that the observed radiation is anisotropic (Antonucci 1993) due to a combination of obscuration close to the nucleus and the intrinsically anisotropic radiation. For radio-loud galaxies, this preferential radiation axis is traced by the line connecting the dual radio lobes. The misalignment of the wedge therefore argues against photoionization due to the AGN or shocks due to the radio jet. Furthermore, the most likely position of the accreting black hole powering the radio emission and therefore also the primary source of hard ionizing radiation is where the radio core and K_S-band surface brightness peak coincide. The apex of the wedge does not coincide with this position. It is possible that a sond AGN (this one radio-quiet), coinciding with region 4 in Figure 6.5, could ionize the wedge. However, this additional black hole would have to have its primary axis roughly perpendicular to the radio-loud AGN and be much less luminous at K_S-band. While not impossible, this explanation is ad hoc and not preferred.

6.4.2.2 *In Situ Star Formation or Galaxy Interaction*

Ongoing star formation within the wedge itself and perhaps extending into the outer Lyα halo (outside the Kron radius) would also produce bright line emission. However, there is a robust upper limit to the Lyα equivalent width produced by normal massive stars of $W_\lambda = 400$ Å (Charlot & Fall 1993). For the wedge we estimate a significantly higher equivalent width. We also note that dust extinction will decrease the observed equivalent width from its true value; the resonant scattering of Lyα photons increases their optical depth relative to continuum photons. This equivalent width argument also applies to tidal debris ejected from the galaxy via a merger or interaction. It therefore seems unlikely that stars are directly responsible for the wedge emission.

6.4.2.3 *Superwind: Comparison with M82*

In Heckman et al. (1990) the authors use their observations of local starburst galaxies to determine the minimal condition for driving a

galactic-scale outflow powered by supernovae explosions, or a superwind. They phrase this criterium in terms of the star formation rate per unit area (Σ_{SFR}) and empirically determine the minimum to be $\Sigma_{SFR} \geq 0.1\,M_\odot\ yr^{-1}\ kpc^{-2}$. If we adopt this minimal value for TN J1338 and apply it to the resolved area where we see the wedge emerging from the galaxy (assuming a circular region seen in projection), we derive a lower limit to the SFR over this same area of $1.5\,M_\odot\ yr^{-1}$. Above we have shown that the SFR for this galaxy greatly exceeds this limit, even in region 4, where the wedge may originate.

Galactic-scale winds have been observed in detail around local starburst galaxies, of which M82 is a well-studied example (e.g., Heckman et al. 1990). Morphologically, these superwinds are bipolar structures emanating from the galaxy nucleus and along the minor axis of the galaxy. They are detected as emission-line filaments, extended X-ray lobes, and bipolar thermal dust emission (Heckman et al. 1990). In M82, the emission-line gas is photoionized in the innermost regions and is primarily shock-excited in the outskirts. The optically emitting gas flows from M82 in filaments that trace the biconical surface. The outflows have double-peaked emission lines (due to the two surfaces of the cone being separated in velocity) and also, depending on geometry and spectral resolution, emission lines with blueshifted absorption. On the basis of these spectroscopic signatures, galactic winds seem to be a generic feature of high-redshift star-forming galaxies (Pettini et al. 2001). All the existing spectroscopy of TN J1338 has been taken along the radio axis, where the dynamics of the gas are presumably dominated by the AGN outflow and jet-cloud interactions (see above and e.g., Villar-Martín et al. 1999; Solórzano-Iñarrea et al. 2001). So we must rely on morphology alone to infer the presence of a superwind emanating from this radio galaxy along the wedge.

Comparison of the recent ultraviolet *Galaxy Evolution Explorer* (GALEX) image of M82 (Hoopes et al. 2005) with our TN J1338 image reveals a striking degree of similarity (Figure 6.10). The scales of the two outflows are somewhat different; in M82 the narrowest collimated Section is only 1.5 kpc across, while in TN J1338 the similarly defined region is approximately twice that. The surface brightness profile is also similar between the wedge and the M82 far-UV outflow (see Figure 6.9). The shallow drop-off of emission-line surface brightness is consistent with having shock ionization dominate at these large radii rather than photoionization by a central source.

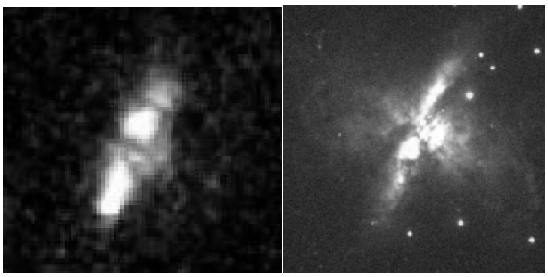

Figure 6.10 — *Left*: Color composite of r_{625}, i_{775} and z_{850} ACS images. *Right*: *GALEX* near-UV (*red*) and far-UV (*blue* composite image of M82, showing the bipolar outflow. In this case the far-UV is interpreted as being continuum light from the starburst that is scattered by dust mixed with the outflowing gas (Hoopes et al. 2005). Note the great similarity between the morphologies of the two objects,which suggests that the wedge emanating from TN J1338 is also a starburst-driven outflow.

Why do we see only one side of the presumably bipolar outflow? This could be due to obscuration of the line emission on one side of the galaxy. If the radio galaxy is flattened (perpendicular to the plane of the sky) and inclined with respect to the line of sight, then any dust in the galaxy would naturally obscure the side tilted away from the observer. This is the primary explanation for the observed asymmetry in the bipolar superwind in M82 (Shopbell & Bland-Hawthorn 1998). Alternatively, the lack of line emission on the northeast side may be due to a strong gradient in the ambient gas density.

Alternatively, if the pressure is higher on the northeast side of the galaxy, a situation which could arise due to the motion of the radio galaxy within the protocluster medium, i.e., ram pressure, then the outflow would be impeded on

this side of the galaxy. Marcolini et al. (2004) have made simulations (albeit for dwarf galaxies) that show that motion through the IGM does not greatly affect the dynamics of galactic outflows until the ram pressure becomes comparable to the static thermal pressure of the galactic ISM. This result should be extendable to the case of TN J1338. To estimate the thermal pressure in the galaxy, we must first estimate a density for the gas. If we assume that the observed Lyα emission is due to Case B recombination at $T = 15000$K, then we can use the fiducial Lyα/Hα ratio of ~ 10 to deduce the number of ionized hydrogen atoms. Given the observed geometry of the wedge, we can assume further that the emitting gas is contained in the surface of a cone with half-angle 30° and length 10 kpc. The thickness of the gas layer cannot be larger than a few hundred pc due to the absence of significant limb brightening in the azimuthal profile of the wedge. Consequently, the number density and mass of ionized hydrogen are

$$n_e = 1.0 L_{H\beta,41}^{1/2} V_{\mathrm{cone,kpc^3}}^{-1/2} \ \mathrm{cm}^{-3} \quad (6.4)$$

$$M_{\mathrm{H\ II}} = 7.6 \times 10^8 \mu_p L_{H\beta,41}^{1/2} V_{\mathrm{cone,kpc^3}}^{1/2} \ \mathrm{M}_{\odot} \quad (6.5)$$

where μ_p is the mean particle mass, which we have taken to be the proton mass, and $L_{H\beta,41}$ is the $H\beta$ luminosity in units of 10^{41} ergs s^{-1}. The true electron density is likely to be higher than this, but only within smaller clouds or filaments as is seen in the M82 outflow. The resulting thermal pressure is equivalent to the ram pressure produced by a relative velocity of 300 km s^{-1} (if the surrounding gas has a density 1/1000 times of that in the wedge). This provides some evidence that the radio galaxy is not in the center of the galaxy overdensity and that motion toward the center would provide the requisite ram pressure (Intema et al. 2005, in prep.). We conclude that the wedge is likely to be a supernova-driven ouflow, with the current episode of star formation possibly triggered by the radio jet. This superwind is one-sided due to ram pressure inhibiting the flow on one side.

6.4.3 The Outer Lyα Halo

In Figure 6.11, the extended Lyα (out to ~ 100 kpc), as detected in the very deep VLT narrow-band image, is shown as contours. The TN J1338 halo is somewhat has an asymmetric plume that is aligned with the radio axis. It is clear from the underlying ACS image showing the wedge that there is a natural connection between the high surface brightness wedge (out to 20–30 kpc) and the larger scale lower surface brightness halo along the southwest direction. However, the halo at larger distances appears to be aligned with the radio axis of TN J1338. What is the relation, if any, between the wedge and the large-scale Lyα structure?

If the wedge is an outflow, as we conclude above, the resulting bubble will stall at some radius where gravity and the amount of swept-up intergalactic matter balance the input energy. The gas deposited at this radius would naturally flow along the boundary of the excavated cavity and follow any density gradients in the ambient medium. The halo-radio alignment would then be a natural consequence if lower density regions were preferentially along the radio axis. This would be the case if either the current radio source extended farther out in radius than our current radio observations indicate or the radio source was previously (either during this same accretion episode or during an earlier one) much larger and had excavated the region along the radio axis. However, there is no evidence in the current radio data for a relic radio source at larger distances. In any case, if the ionized gas has originated in the starburst, the observed alignment implies that the AGN had already imprinted the region before the starburst was triggered. We discuss this possibility and its implications further in the next Section.

6.4.4 A Self-Consistent Scenario

The host galaxy of the powerful radio source TN J1338–1942 at $z = 4.1$ is unique. It is arguably the youngest BCG known to date and has been the subject of several multiwavelength investigations. In this paper we have presented imaging from *HST* ACS which reveals several

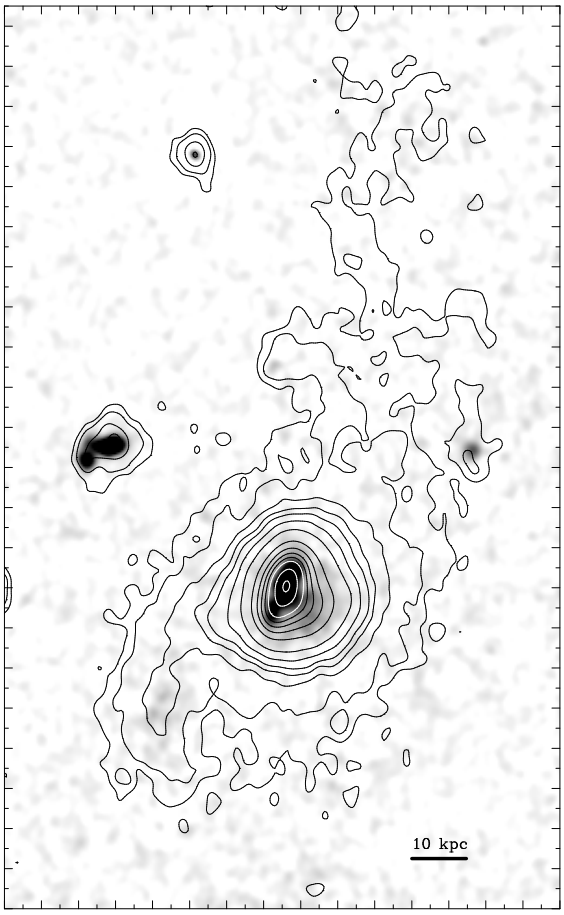

Figure 6.11 — Continuum-subtracted ACS *r*-band image overlaid with the VLT narrowband image (contours). North is up and east to the left. The fiducial bar in the bottom right of the image is 10 kpc long. The field of view is $15'' \times 22\farcs5$, each major tickmark is separated by one arcsond. Note the correspondence between the wedge and the larger scale structure of the halo seen in the ground-based image. The filament extending to the north is aligned with the radio axis, although it extends far beyond the northern lobe.

interesting morphological and broadband spectral features in this radio galaxy. In this Section we attempt to construct a plausible and self-consistent story of the past, present, and future of TN J1338.

The host galaxy of TN J1338 appears to be forming stars at a high rate. None of the non-stellar processes known to produce the alignment effect in other galaxies can be dominant in this case. The ACS data presented here reveals a morphology that is consistent with most of the star formation being triggered by the passage of the radio jet. In Figure 6.12 we show a color-color diagram for the discrete regions within the radio galaxy. The color difference between regions 4 and 5 may be an age effect (region 4 is also bluer in i_{775}–K_S). We use the overplotted model colors in Fig. 6.12 to derive an age difference between the two regions. The model has constant star formation with 0.4 solar metallicity and $E(B-V) = 0.1$, the ages are labeled at timesteps of 1, 10, 100, and 1000 Myr. We estimate from the comparison between the model points and the data that the age difference is between 25 and 200 Myr. This matches, within the (large) errors the shock travel time from the radio core (in region 5) to the jet-cloud interaction in region 4 (a distance of ~ 7 kpc with a 300 km s^{-1} shock). We do not see very extended star formation which may be triggered by the expanding radio cocoon. The energy injection from the AGN may be rather isolated to these few nodes along the radio jet itself. Therefore, we suspect that the large-scale Lyα gas has an origin apart from the AGN, namely, in the newly formed stars.

Once the prodigious star formation is initiated, the supernova explosions expel the ionized gas into the surrounding media by means of a superwind. In addition, ram pressure is stripping the gas from the star-forming regions as the radio galaxy moves through the ICM and IGM. This gas remains ionized primarily via shock excitation at the interface between the outflow and the ambient intergalactic gas. At a distance of approximately 20–30 kpc from the nucleus, the outflow reaches pressure equilibrium with the IGM. The gas rapidly cools at this interface, consistent with the boundary to the Lyα halo observed at this region. This cooling gas follows the density gradients in the IGM. The very low surface brightness line emission seen to the northeast of the radio galaxy, which is aligned with the radio axis, is probably gas that originated in the outflow, cooled, and is now being re-excited by low-luminosity shocks

associated with the radio source.

The observed rest-frame B magnitude of TN J1338 is approximately 1.5-2 mag brighter than that of the six BCGs at $z \sim 1$ observed with ACS (Postman et al. 2005). If we use the same star formation model as above (constant for 1 Gyr and 0.4 solar metallicity) and age the galaxy from 1 Gyr at $z = 4.1$ to 5.2 Gyr at $z = 1$ the galaxy fades by 3.3 mag. This would imply that some additional star formation or merging must occur during those 4.2 Gyrs for TN J1338 to match the luminosity of the $z \sim 1$ BCGs. This is certainly not surprising. It is interesting to note as well, that several of these BCGs have a nearby bright companion of almost equal luminosity ($\Delta M \lesssim 0.1$ mag), with which it seems to be destined to merge. The resulting increase in luminosity would nearly make up the 1 mag of extra fading seen for the 1 Gyr constant star formation model.

It is debatable whether one should attempt to draw conclusions for an entire population of sources (either BCGs or radio galaxies in this case) based on observations of a single example. TN J1338 may be a galaxy in a special phase of its evolution; alternatively, it may be a special source whose history cannot be generalized to describe other galaxies. However, studies of ensembles of radio galaxies, including their luminosity functions and duty cycles, suggest that the space density of radio source hosts at high-z are roughly in agreement with the density of BCGs at low redshift and the density of non-RG overdensities at $z \sim 3$ (West 1994; Venemans et al. 2002)

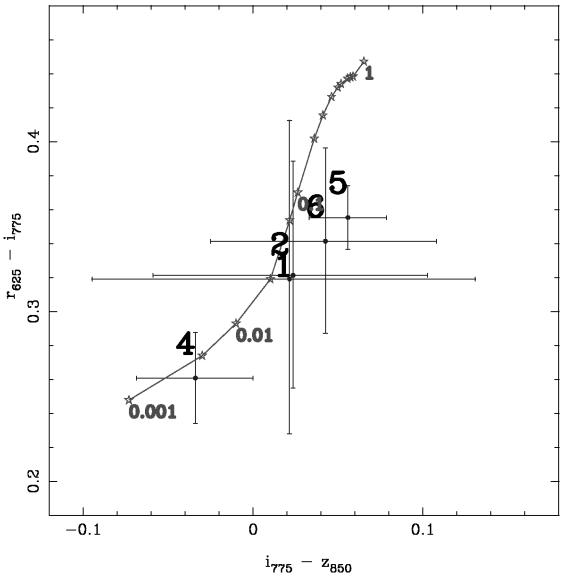

Figure 6.12 — Color-color diagrams of r_{625}–i_{775} vs. i_{775}–z_{850} for the individual regions in TN J1338. We have excluded the wedge (region 3) from this plot since it is a clear outlier, r_{625}–$i_{775} = -0.11$ and i_{775}–$z_{850} = -0.39$. The estimated Lyα flux has been subtracted from the r_{625} magnitude for each region using a continuum fit to the i_{775}–z_{850} color. The overplotted red line shows the colors for a constant star formation model with ages indicated in Gyr, $E(B-V) = 0.1$, and $Z = 0.4 Z_{\odot}$.

6.5 Conclusions and Future

The host galaxy of powerful radio source TN J1338–1942 shows signatures of several feedback processes that connect the black hole, stellar host, and intergalactic medium. The elongated and multicomponent ultraviolet continuum is aligned with the FRII radio axis and is likely to be due to emission from young stars being formed along the jet axis. Interpretation of this light in terms of jet-induced star formation is consistent with the observations. There is, however, also evidence for considerable star formation outside the highest surface brightness regions. If the current star formation rate has been constant over the jet travel time from the radio core to the site of the presumed jet-cloud interaction, this process could have produced in excess of 10^{11} $M_{\odot}$ of stars. Data from the *Spitzer Space Telescope* will allow us to determine the total stellar mass of TN J1338 and help verify our hypothetical star formation history.

We interpret the ACS wedge of Lyα emission as a superwind driven by the winds and supernova explosions associated with prodigious star formation activity. This outflow connects with the larger scale Lyα halo. The initial source of the halo gas is then within the starburst and is possibly enriched. Deep spectroscopy from the ground along the wedge axis would help us determine the ionization mechanism more defini-

Table 6.1 — Kron Aperture Photometry

Bandpass	AB Magnitude	Estimated Line Contamination[a]
g_{475}	25.92 ± 0.28	$\lesssim 0.05$ mag[a]
r_{625}	22.46 ± 0.01	~ 1.3 mag (Lyα)
i_{775}	23.23 ± 0.03	~ 0.3 mag (C IVλ1549,He IIλ1640)
z_{850}	23.11 ± 0.04	~ 0.2 mag (He IIλ1640,C III] λ1909)
K_S	21.9 ± 0.2	$\lesssim 0.01$ mag[b]

[a] Calculated using the observed spectrum of TN J1338–1942
[b] Calculated assuming the composite spectrum of McCarthy (1993)

Table 6.2 — Six Easy Pieces

ID	Piece	AB Magnitude			Lyα Flux (10^{-16}	Lyα	Extinction	SFR
		r_{625}[a]	i_{775}	z_{850}	ergs/s/cm^2)	EW_0 (Å)	$E(B-V)$	UV (Lyα)[b]
1	Line 1	27.14	26.82	26.80	1.17	448	0.02	3 (17)
2	Line 2	27.66	27.34	27.32	0.80	492	0.02	2 (12)
3	Wedge	26.19	26.36	26.81	4.20	645	0.0	3 (61)
4	Continuum 2	25.74	25.48	25.51	3.73	390	0.0	9 (54)
5	Continuum 1	25.33	24.98	24.92	1.69	121	0.06	24 (24)
6	Shock	26.54	26.20	26.15	2.45	536	0.04	7 (35)

[a] Calculated for the Lyα subtracted image, where the line flux is determined from power-law continuum fits to the i_{775} and z_{850} bands for each piece
[b] Star formation rate as calculated by the UV continuum magnitude and the Lyα flux (in parenthesis)

tively. In particular, covering the Lyα, C IV, He II and C III] emission lines may enable us to also measure the enrichment of the outflowing gas. An ongoing ACS program using the narrow-band (ramp) filter (PI: W. van Breugel) to image several high-redshift radio galaxies in Lyα will discover how prevalent such wedge features are in this population.

Acknowledgments

We thank M. Seibert, C. Hoopes and the rest of the GALEX team for providing their M82 images ahead of publication. We gratefully acknowledge M. Lehnert for helpful discussions and the anonymous referee for valuable comments. THE ACS was developed under NASA contract NAS 5-32865, and this research has been supported by NASA grant NAG5-7697 and by an equipment grant from Sun Microsystems, Inc. The Space Telescope Science Institute is operated by the Association of Universities for research in Astronomy (AURA) Inc., under NASA contract NAS5-26555. We are grateful to K. Anderson, J. McCann, S. Busching, A. Framarini, S. Barkhouser, and T. Allen for their invaluable contributions to the ACS project at the Johns Hopkins University.

References

Adelberger, K. L., Steidel, C. C., Shapley, A. E., & Pettini, M. 2003, ApJ, 584, 45
Antonucci, R. 1993, ARA&A, 31, 473

Aragon-Salamanca, A., Baugh, C. M., & Kauffmann, G. 1998, MNRAS, 297, 427
Baugh, C. M., Benson, A. J., Cole, S., Frenk, C. S., & Lacey, C. 2003, in The Mass of Galaxies at Low and High Redshift, ed. R. Bender & A. Renzini, ESO Springer, 91
Bernardi, M., et al. 2003, AJ, 125, 1866
Bertin, E. & Arnouts, S. 1996, A&AS, 117, 393
Best, P. N., Longair, M. S., & Röttgering, H. J. A. 1998, MNRAS, 295, 549
Best, P. N., Röttgering, H. J. A., & Longair, M. S. 2000, MNRAS, 311, 23
Bicknell, G. V., Sutherland, R. S., van Breugel, W. J. M., Dopita, M. A., Dey, A., & Miley, G. K. 2000, ApJ, 540, 678
Blakeslee, J. P., Anderson, K. R., Meurer, G. R., Benítez, N., & Magee, D. 2003a, in ASP Conf. Ser. 295: Astronomical Data Analysis Software and Systems XII 257
Blakeslee, J. P., et al. 2003b, ApJ, 596, 143
Brocklehurst, M. 1971, MNRAS, 153, 471
Bruzual, G. & Charlot, S. 2003, MNRAS, 344, 1000
Burke, D. J., Collins, C. A., & Mann, R. G. 2000, ApJ, 532, 105
Calzetti, D., Armus, L., Bohlin, R. C., Kinney, A. L., Koornneef, J., & Storchi-Bergmann, T. 2000, ApJ, 533, 682
Chambers, K. C., Miley, G. K., & van Breugel, W. 1987, Nature, 329, 604
Charlot, S. & Fall, S. M. 1993, ApJ, 415, 580
Cimatti, A., Dey, A., van Breugel, W., Antonucci, R., & Spinrad, H. 1996, ApJ, 465, 145
Cimatti, A., Dey, A., van Breugel, W., Hurt, T., & Antonucci, R. 1997, ApJ, 476, 677
Cole, S., Lacey, C. G., Baugh, C. M., & Frenk, C. S. 2000, MNRAS, 319, 168
Condon, J. J., Cotton, W. D., Greisen, E. W., Yin, Q. F., Perley, R. A., Taylor, G. B., & Broderick, J. J. 1998, AJ, 115, 1693
Daly, R. A. 1992, ApJ, 386, L9
De Breuck, C., et al. 2004, A&A, 424, 1
De Breuck, C., Röttgering, H., Miley, G., van Breugel, W., & Best, P. 2000a, A&A, 362, 519
De Breuck, C., van Breugel, W., Minniti, D., Miley, G., Röttgering, H., Stanford, S. A., & Carilli, C. 1999, A&A, 352, L51
De Breuck, C., van Breugel, W., Röttgering, H. J. A., & Miley, G. 2000b, A&AS, 143, 303
De Breuck, C., van Breugel, W., Stanford, S. A., Röttgering, H., Miley, G., & Stern, D. 2002, AJ, 123, 637
Dey, A., Cimatti, A., van Breugel, W., Antonucci, R., & Spinrad, H. 1996, ApJ, 465, 157
Dey, A., van Breugel, W., Vacca, W. D., & Antonucci, R. 1997, ApJ, 490, 698
Dickson, R., Tadhunter, C. Shaw, M., Clark, N., & Morganti, R. 1995, MNRAS, 273, L29
Donahue, M., et al. 2001, ApJ, 552, L93
Donahue, M., et al. 2002, ApJ, 569, 689
Douglas, J. N., Bash, F. N., Bozyan, F. A., Torrence, G. W., & Wolfe, C. 1996, AJ, 111, 1945
Ferrarese, L. & Merritt, D. 2000, ApJ, 539, L9
Fragile, P. C., Murray, S. D., Anninos, P., & van Breugel, W. 2004, ApJ, 604, 74
Francis, P. J., et al. 2001, ApJ, 554, 1001
Gebhardt, K., et al. 2000, ApJ, 539, 13
Graham, A., Lauer, T. R., Colless, M., & Postman, M. 1996, ApJ, 465, 534
Heckman, T. M. 2000, in Gas and Galaxy Evolution, ed. J. Hibbard, M. Rupen, & J. van Gorkom, Volume 240 PASP, 345
Heckman, T. M., Armus, L., & Miley, G. K. 1990, ApJ, 74, 833
Heckman, T. M., Lehnert, M. D., Strickland, D. K., & Armus, L. 2000, ApJ, 129, 493
Holden, B. P., et al. 2000, AJ, 120, 23
Holden, B. P., Nichol, R. C., Romer, A. K., Metevier, A., Postman, M., Ulmer, M. P., & Lubin, L. M. 1999, AJ, 118, 2002
Hoopes, C. G., et al. 2005, ApJ, 619, 99
Jarvis, M. J. & McLure, R. J. 2002, MNRAS, 336, L38
Jarvis, M. J., Rawlings, S., Eales, S., Blundell, K. M., Bunker, A. J., Croft, S., McLure, R. J., & Willott, C. J. 2001a, MNRAS,326, 1585
Jarvis, M. J., et al. 2001b, MNRAS, 326, 1563
Jørgensen, I., Franx, M., & Kjærgaard, P. 1996, MNRAS, 280, 167
Kaiser, N. 1984, ApJ, 284, 9
Kennicutt, R. C. 1998, ARA&A, 36, 189
Kron, R. G. 1980, ApJ, 43, 305
Kurk, J., Röttgering, H., Pentericci, L., Miley, G., & Overzier, R. 2003, New Astronomy Review, 47, 339
Kurk, J. D., et al. 2000, A&A, 358, L1
Madau, P. 1995, ApJ, 441, 18
Magorrian, J., et al. 1998, AJ, 115, 2285
Marcolini, A., Brighenti, F., & D'Ercole, A. 2004, MNRAS, 352, 363
Martin, C. L. 2004, ApJ in press, astro-ph/0410247
McCarthy, P. J. 1993, ARA&A, 31, 639
McCarthy, P. J., van Breugel, W., & Kapahi, V. K. 1991, ApJ, 371, 478
McCarthy, P. J., van Breugel, W., Spinrad, H., & Djorgovski, S. 1987, ApJ, 321, L29
Mellema, G., Kurk, J. D., & Röttgering, H. J. A. 2002, A&A, 395, 13
Miley, G. K., et al. 2004, Nature, 427, 47
Mullis, C. R., et al. 2003, ApJ, 594, 154
Oegerle, W. R. & Hoessel, J. G. 1991, ApJ, 375, 15
Oke, J. B. & Gunn, J. E. 1983, ApJ, 266, 713
Oke, J. B., Postman, M., & Lubin, L. M. 1998, AJ, 116, 549
Papovich, C., Dickinson, M., & Ferguson, H. C. 2001, ApJ, 559, 620
Pentericci, L., et al. 2000a, A&A, 361, L25
Pentericci, L., Van Reeven, W., Carilli, C. L., Röttgering, H. J. A., & Miley, G. K. 2000b, A&AS, 145, 121
Pettini, M., Shapley, A. E., Steidel, C. C., Cuby, J., Dickinson, M., Moorwood, A. F. M., Adelberger, K. L., & Giavalisco, M. 2001, ApJ, 554, 981
Postman, M., Lauer, T. R., Oegerle, W., & Donahue, M. 2002, ApJ, 579, 93
Postman, M., Lubin, L. M., Gunn, J. E., Oke, J. B., Hoessel, J. G., Schneider, D. P., & Christensen, J. A. 1996, AJ, 111, 615
Postman, M., et al. 2005, ApJ, 623, 721
Rees, M. J. 1989, MNRAS, 239, 1
Reuland, M., et al. 2003, ApJ, 592, 755

Rosati, P., della Ceca, R., Norman, C., & Giacconi, R. 1998, ApJ, 492, L21
Rosati, P., Stanford, S. A., Eisenhardt, P. R., Elston, R., Spinrad, H., Stern, D., & Dey, A. 1999, AJ, 118, 76
Scharf, C. A., Jones, L. R., Ebeling, H., Perlman, E., Malkan, M., & Wegner, G. 1997, ApJ, 477, 79
Shimasaku, K., et al. 2003, ApJ, 586, L111
Shopbell, P. L. & Bland-Hawthorn, J. 1998, ApJ, 493, 129
Solórzano-Iñarrea, C., Best, P. N., Röttgering, H. J. A., & Cimatti, A. 2004, MNRAS, 351, 997
Solórzano-Iñarrea, C., Tadhunter, C. N., & Axon, D. J. 2001, MNRAS, 323, 965
Somerville, R. S., et al. 2004, ApJ, 600, 135
Spergel, D. N., et al. 2003, ApJ, 148, 175
Stanford, S. A., Eisenhardt, P. R., Dickinson, M., Holden, B. P., & De Propris, R. 2002, ApJ, 142, 153
Stanford, S. A., Elston, R., Eisenhardt, P. R., Spinrad, H., Stern, D., & Dey, A. 1997, AJ, 114, 2232
Steidel, C. C., Adelberger, K. L., Shapley, A. E., Pettini, M., Dickinson, M., & Giavalisco, M. 2000, ApJ, 532, 170
Tody, D. 1993, in Astronomical Society of the Pacific Conference Series 173
van Ojik, R., Röttgering, H. J. A., Miley, G. K., & Hunstead, R. W. 1997, A&A, 317, 358
Venemans, B. P., et al. 2002, ApJ, 569, L11
Venemans, B. P., et al. 2004, A&A, 424, L17
Vernet, J., Fosbury, R. A. E., Villar-Martín, M., Cohen, M. H., Cimatti, A., di Serego Alighieri, S., & Goodrich, R. W. 2001, A&A, 366, 7
Villar-Martín, M., Tadhunter, C., Morganti, R., Axon, D., & Koekemoer, A. 1999, MNRAS, 307, 24
West, M. J. 1994, MNRAS, 268, 79
Willott, C. J., Rawlings, S., Jarvis, M. J., & Blundell, K. M. 2003, MNRAS, 339, 173
Wilman, R. J., Jarvis, M. J., Röttgering, H. J. A., & Binette, L. 2004, MNRAS, 351, 1109
Wilson, A. S. & Tsvetanov, Z. I. 1994, AJ, 107, 1227
Zirm, A. W. 2003. Stellar hosts, aligned light and polarization of high-redshift radio galaxies.Ph. D. thesis, Johns Hopkins University
Zirm, A. W., Dickinson, M., & Dey, A. 2003, ApJ, 585, 90

Chapter 7

Clustering of star-forming galaxies near a radio galaxy at $z = 5.2$

Abstract. We present *HST* ACS observations of the most distant radio galaxy known, TN J0924–2201 at $z = 5.2$. This radio galaxy has six spectroscopically confirmed Lyα emitting companion galaxies and appears to lie within an overdense region. The radio galaxy is marginally resolved in i_{775} and z_{850} showing continuum emission aligned with the radio axis, similar to what is observed for lower redshift radio galaxies. Both the half-light radius and the UV star formation rate are comparable to the typical values found for Lyman break galaxies at $z \sim 4 - 5$. The Lyα emitters are sub-L^* galaxies, with deduced star formation rates of $1 - 10\ M_\odot\ \mathrm{yr}^{-1}$. One of the Ly$\alpha$ emitters is only detected in Lyα. Based on the star formation rate of $\sim 3\ \mathrm{M}_\odot\ \mathrm{yr}^{-1}$ calculated from Lyα, the lack of continuum emission could be explained if the galaxy is younger than ~ 2 Myr and is producing its first stars.

Observations in $V_{606}i_{775}z_{850}$ were used to identify additional Lyman break galaxies associated with this structure. In addition to the radio galaxy, there are 22 V_{606}-break ($z \sim 5$) galaxies with $z_{850}<26.5$ (5σ), two of which are also in the spectroscopic sample. We compare the surface density of ~ 2 arcmin^{-2} to that of similarly selected V_{606}-dropouts extracted from GOODS and the UDF parallel fields. We find evidence for an overdensity to very high confidence ($> 99\%$), based on a counts-in-cells analysis applied to the control field. The excess suggests that the V_{606}-break objects are associated with a forming cluster around the radio galaxy.

R. A. Overzier, G. K. Miley, R. J. Bouwens, N. J. G. Cross, A. W. Zirm, N. Benítez, J. P. Blakeslee, M. Clampin, R. Demarco, H. C. Ford, G. F. Hartig, G. D. Illingworth, A. R. Martel, H. J. A. Röttgering, B. Venemans, D. R. Ardila, F. Bartko, L. D. Bradley, T. J. Broadhurst, D. Coe, P. D. Feldman, M. Franx, D. A. Golimowski, T. Goto, C. Gronwall, B. Holden, N. Homeier, L. Infante, R. A. Kimble, J. E. Krist, S. Mei, F. Menanteau, G. R. Meurer, V. Motta, M. Postman, P. Rosati, M. Sirianni, W. B. Sparks, H. D. Tran, Z. I. Tsvetanov, R. L. White & W. Zheng
The Astrophysical Journal, **637**, 58 (2006)

7.1 Introduction

Where can we find the progenitors of the galaxy clusters that populate the local universe? The evolution of rich galaxy clusters has been studied out to $z \sim 1.4$ (Mullis et al. 2005). These clusters have been discovered primarily via their bright X-ray emission, the signature of virialized gas within a deep gravitational potential well. Follow-up observations have revealed that some of the galaxy populations in distant clusters are relatively old, as evidenced by, for example, the tight scatter in the color-magnitude relation for early-type galaxies (e.g. Stanford et al. 1998; Blakeslee et al. 2003a; Wuyts et al. 2004; Holden et al. 2005) and the mild evolution of the morphology density relation for cluster elliptical galaxies since $z \sim 1$ (Postman et al. 2005). This suggests that an interesting epoch of cluster formation could lie at higher redshifts. Several good examples of overdensities of galaxies at $1.5 \lesssim z \lesssim 6$, possibly the progenitors of clusters, exist in the literature (e.g. Pascarelle et al. 1996; Steidel et al. 1998; Keel et al. 1999; Steidel et al. 2000; Francis et al. 2001; Möller & Fynbo 2001; Sánchez & González-Serrano 2002; Shimasaku et al. 2003; Ouchi et al. 2005; Steidel et al. 2005). These structures have been found often as by-products of large-area field surveys using broad or narrow band imaging, or by targeting luminous radio sources.

One technique for finding distant galaxy overdensities is based on the empirical evidence that powerful radio galaxies are among the most massive forming galaxies at high redshift (e.g. De Breuck et al. 2002; Dey et al. 1997; Pentericci et al. 2001; Zirm et al. 2003). In the standard cold dark matter (CDM) universe model, massive galaxies and galaxy clusters are associated with the most massive dark matter halos within the large-scale structure. It has been found that massive black holes are a key ingredient of local massive galaxies, and that their mass scales in proportion to the mass of the spheroidal component of the host galaxy (Magorrian et al. 1998; Gebhardt et al. 2000; Ferrarese & Merritt 2000). Radio galaxies may therefore demarcate the location of forming clusters, analogous to the suggested scaling relations between halo, host galaxy, and black hole mass at low redshift. A program with the Very Large Telescope (VLT) of the European Southern Observatory to search for galaxy overdensities around luminous high-redshift radio galaxies through deep narrow-band Lyα imaging and spectroscopy has indeed revealed that the radio galaxies are often accompanied by large numbers of line-emitting galaxies (Pentericci et al. 2000; Kurk et al. 2003; Venemans et al. 2002, 2004; Venemans et al. 2005).

We have started a study with the *Advanced Camera for Surveys* (ACS) on the *Hubble Space Telescope* (*HST*; Ford et al. 1998) to survey some of these Lyα-selected protoclusters[1]. Our goal is to augment our study of emission-line objects by deep broad band observations to search for Lyman break galaxies (LBGs). Observations of the radio galaxy protocluster TN J1338–1942 at $z = 4.1$ have shown that the overdensity of Lyα emitters discovered by Venemans et al. (2002) is accompanied by a similar overdensity of LBGs, allowing us to assess distinct galaxy populations in overdense regions (Miley et al. 2004, Overzier et al., in prep.). The radio galaxy TN J1338–1942 was found to have a complex morphology, showing clear signs of active galactic nucleus (AGN) feedback on the forming ISM (interstellar medium) and a starburst-driven wind possibly feeding the gaseous halo that surrounds the galaxy (Zirm et al. 2005). The Lyα emitters have relatively faint UV continua and small angular sizes compared to the generally brighter LBG population in field studies (e.g. Ferguson et al. 2004; Bouwens et al. 2004a).

TN J0924–2201 at $z = 5.19$ is the most distant radio galaxy known (van Breugel et al. 1999; De Breuck et al. 2000). Following the successes obtained in identifying Lyα galaxy overdensities around our sample of powerful high-redshift radio galaxies at $2.2 < z < 4.1$, Venemans et al. (2004) have probed the distribution of Lyα

[1] The term "protocluster" has no strict definition in literature. It is commonly used to describe galaxy overdensities at high redshift with mass estimates that are comparable to those of galaxy clusters, but without any detectable X-ray emission from a hot, virialized intracluster medium.

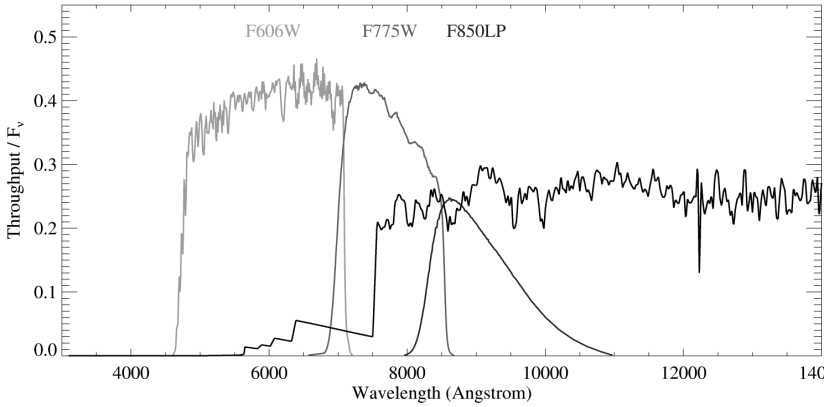

Figure 7.1 — Total effective throughput of the *HST* ACS filterset used in our observations. The SED template shown is the *SB*2 template from Benítez (2000), redshifted to $z = 5.19$, taking into account the attenuation of the IGM following the prescription of Madau et al. (1996). The Lyman break occurs between filters V_{606} and i_{775} for galaxies at $z \sim 5$.

emitters around TN J0924–2201: there are six spectroscopically confirmed companions within a (projected) radius of 2.5 Mpc and a (rest frame) 1000 km s^{-1} from the radio galaxy, corresponding to a surface overdensity of 1.5–6 with respect to the field. This overdensity is comparable to that of radio galaxy/Lyα protoclusters at lower z and supports the idea that radio galaxies conspicuously identify groups or cluster-like regions in the very early universe.

In this paper we present the results of a follow-up study of the galaxy overdensity near TN J0924–2201 through high resolution imaging observations obtained with *HST* ACS. The primary goal of these observations was to look for an enhancement in the surface density of LBGs in the field of TN J0924–2201, which would generally be missed by the selection based on the presence of a Lyα emission line alone. LBGs and Lyα emitters are strongly clustered at $z = 3 - 5$ and are highly biased relative to predictions for the dark matter distribution (Giavalisco et al. 1998; Adelberger et al. 1998; Ouchi et al. 2004). The biasing becomes stronger for galaxies with higher rest-frame UV luminosity (Giavalisco & Dickinson 2001). In an excellent, all-encompassing census of the clustering properties of LBGs, Ouchi et al. (2004) found that the bias may also increase with redshift and dust extinction, in addition to UV luminosity. By comparing the number densities of LBGs to that of dark halos predicted by Sheth & Tormen (1999), they concluded that $z = 4$ LBGs could be hosted by halos of $1 \times 10^{11} - 5 \times 10^{12}$ M$_\odot$ (see also Hamana et al. 2004) and that the descendants of those halos at $z = 0$ have masses that are comparable to the masses of groups and clusters.

The structure of this paper is as follows. In Sect. 2 we describe our observations and data analysis. Sect. 3 subsequently deals with the host galaxy of the radio source, the spectroscopically confirmed Lyα emitters, and our sample of $z \sim 5$ LBGs. In Sect. 4 we discuss the evidence that suggests that TN J0924–2201 may pinpoint a young galaxy cluster, and we present our conclusions in Sect. 5. We use a cosmology in which $H_0 = 72$ km s^{-1} Mpc^{-1}, $\Omega_M = 0.27$, and $\Omega_\Lambda = 0.73$ (Spergel et al. 2003). In this universe, the luminosity distance is 49.2 Gpc, and the angular scale size is 6.2 kpc arcsec^{-1} at $z = 5.2$. The look-back time is 12.2 Gyr, corresponding to an epoch when the Universe was approximately 8% of its current age.

7.2 ACS Observations, data reduction and photometry

7.2.1 TN J0924–2201

We surveyed the field surrounding TN J0924–2201 with a single pointing of the Wide-Field Channel (WFC) of *HST* ACS. The field position was chosen in order to maximize the number of spectroscopically confirmed Lyα emitters in the field. The radio galaxy is located at $\alpha_{J2000} = 9^h24^m19.90^s$, $\delta_{J2000} = -22^\circ01'42.0''$, and four of the Ly$\alpha$ emitters fall within the 11.7 arcmin^2 field. The field has an extinction value $E(B-V) = 0.057$ determined from the dust maps of Schlegel et al. (1998). The observations were carried out between 29 May and 8 June 2003, as part of the ACS Guaranteed Time Observing (GTO) high redshift cluster program. The total observing time of 14 orbits was split over the V_{606} (9400 s), i_{775} (11800 s), and z_{850} (11800 s) broadband filters, bracketing redshifted Lyα at 7527 Å. The filter transmission curves are indicated in Fig. 7.1. Each orbit was split into two 1200 s exposures to facilitate the removal of cosmic rays. A color image of the field is shown in Fig. 7.2.

The data were processed through CALACS at Space Telescope Science Institute (STScI) and the ACS pipeline science investigation software *Apsis* (Blakeslee et al. 2003b) that was developed by and for the ACS GTO team. By default *Apsis* provides final drizzled images with a pixel scale of $0\farcs05$ pixel^{-1}. However, to match the image scale of the public data release of the GOODS data (our main comparison dataset), we drizzled the science images onto a frame with a pixel scale of $0\farcs03$ pixel^{-1}. Fig. 7.3 (left panels) shows the limiting magnitudes for each filter as a function of aperture diameter and signal-to-noise ratio (S/N). The 2σ limiting magnitudes in a square aperture of 0.2 arcsec^2 are ~ 29.0 in V_{606}, ~ 28.5 in i_{775}, and ~ 28.0 in z_{850}. There is no significant difference in the detection limits for the $0\farcs05$ pixel^{-1} dataset and the $0\farcs03$ pixel^{-1} data set. The total filter exposure times, extinctions and zeropoints (Sirianni et al. 2005) are listed in Table 7.1.

7.2.2 GOODS public data

We used the public imaging data from the Great Observatories Origins Deep Survey (GOODS; Giavalisco et al. 2004) as a control field for our data. Similar to TN J0924–2201, GOODS has observations in V_{606}, i_{775} and z_{850}, and is comparably deep. We downloaded the V1.0 mosaicked images release[2] for the GOODS Chandra Deep Field South (CDF-S) and Hubble Deep Field North (HDF-N) regions. Details on how these images were produced can be found in Giavalisco et al. (2004). In total we used an area of ~ 314 arcmin^2 from this survey (see Sect. 7.4.1), roughly 27 times larger than a single ACS pointing. We used the zeropoints given by Giavalisco et al. (2004) for this dataset. Fig. 7.3 (bottom panels) shows that the depth is comparable to that of our TN J0924–2201 observations. A summary of the GOODS observations is provided in Table 7.1.

7.2.3 UDF parallels

We also used the two ACS parallels to the Hubble Ultra Deep Field (UDF) Near Infrared Camera and Multi-Object Spectrometer (NICMOS) observations (GO-9803; R. I. Thompson et al.) for comparison[3]. The observations consist of two parallel fields with pointings of $\alpha_{J2000} = 3^h32^m46.0^s$, $\delta_{J2000} = -27^\circ54'42.3''$ (UDF-P1) and $\alpha_{J2000} = 3^h32^m1.0^s$, $\delta_{J2000} = -27^\circ48'3.5''$ (UDF-P2). The heavily dithered images were trimmed down to only the central regions, covering 11.7 arcmin^2 for each parallel field. The data were reduced using *Apsis* at the default output scale of $0\farcs05$ pixel^{-1}. The UDF parallels reach about 0.5–1 magnitudes deeper in each filter compared to both TN J0924–2201 and GOODS (see Fig. 7.3). Details on the observations are given in Table 7.1.

7.2.4 Object detection and photometry

Object detection and photometry was done using the Source Extractor (SExtractor) software package of Bertin & Arnouts (1996). We used

[2] http://www.stsci.edu/science/GOODS/

[3] Available through MAST (http://archive.stsci.edu/)

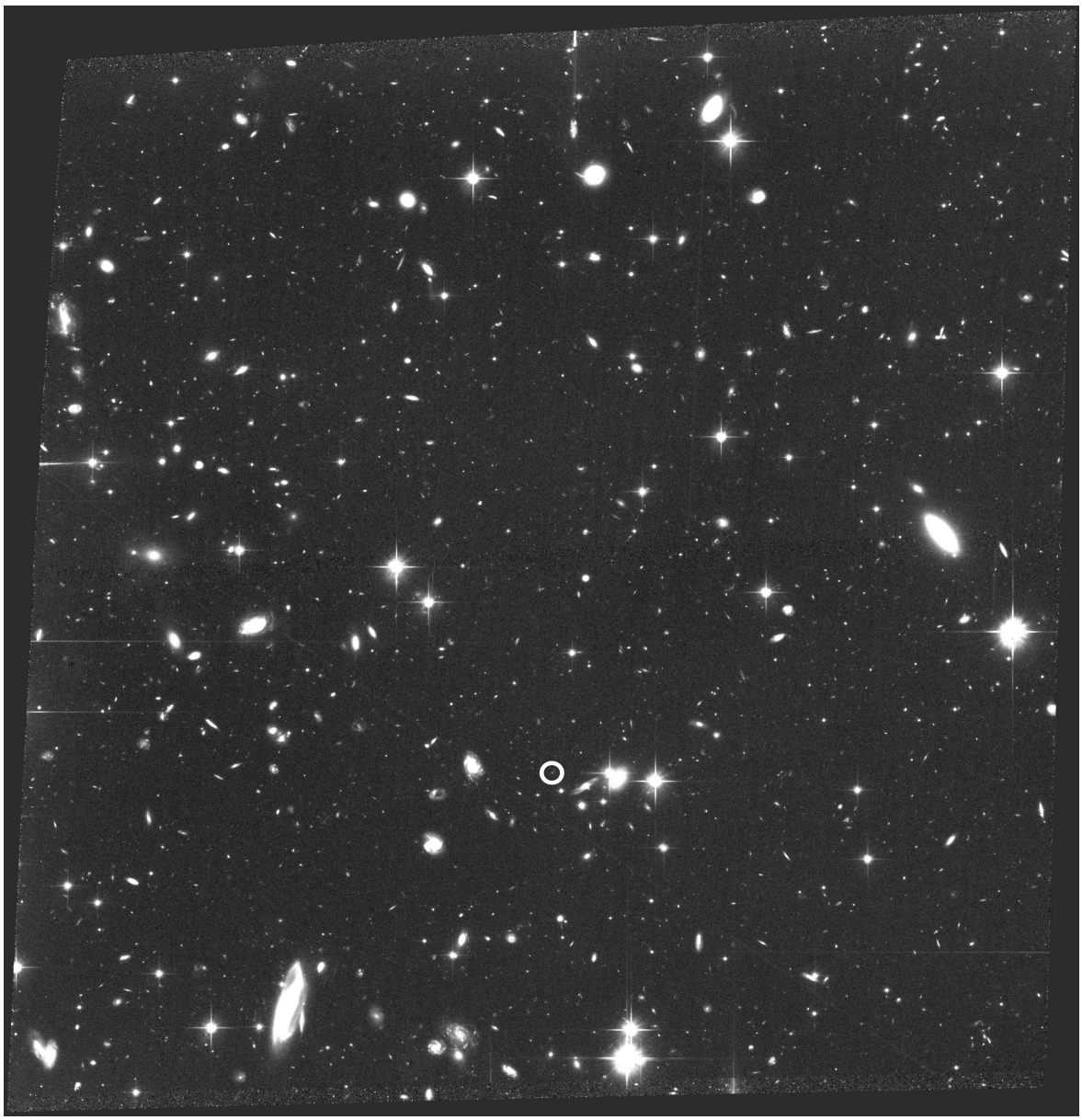

Figure 7.2 — ACS color image showing V_{606} in blue, i_{775} in green, and z_{850} in red. The field measures 11.7 arcmin^2. The position of the radio galaxy TN J0924–2201 is indicated by the circle.

SExtractor in double-image mode, where object detection and aperture determination are carried out on the so-called detection image, and the photometry is carried out on the individual filter images. The z_{850}-band was used as the detection image. Photometric errors are calculated using the root mean square (rms) images that contain the final error per pixel for each output science image. The rms images correctly reflect the pixel variation when images are stacked in

Table 7.1 — Observational Data

Field	Filter	T_{exp} (s)	A (mag)	Zeropoint (mag)	Area (arcmin^2)
TN J0924–2201	V_{606}	9400	0.167	36.4262[a]	11.7
TN J0924–2201	i_{775}	11800	0.115	35.8202[a]	11.7
TN J0924–2201	z_{850}	11800	0.080	35.0228[a]	11.7
GOODS CDF-S	V_{606}	5120	0.023	26.4934[b]	156
GOODS CDF-S	i_{775}	5120	0.017	25.6405[b]	156
GOODS CDF-S	z_{850}	10520	0.012	24.8432[b]	156
GOODS HDF-N	V_{606}	5000	0.035	26.4934[b]	158
GOODS HDF-N	i_{775}	5000	0.024	25.6405[b]	158
GOODS HDF-N	z_{850}	10660	0.018	24.8432[b]	158
UDF-PARALLEL 1	V_{606}	22300	0.023	37.3571[a]	11.7
UDF-PARALLEL 1	i_{775}	41400	0.016	37.1970[a]	11.7
UDF-PARALLEL 1	z_{850}	59800	0.012	36.8038[a]	11.7
UDF-PARALLEL 2	V_{606}	20700	0.026	37.2763[a]	11.7
UDF-PARALLEL 2	i_{775}	41400	0.018	37.1970[a]	11.7
UDF-PARALLEL 2	z_{850}	62100	0.013	36.8448[a]	11.7

[a]Zero point for the total exposure (Sirianni et al. 2005).
[b]Zero point for a 1 s exposure (Giavalisco et al. 2004).

the absence of noninteger pixel shifts or corrections for the geometric distortion. For the fields at a scale of $0\farcs03$ pixel^{-1} (TN J0924–2201 and GOODS), the main parameters influencing the detection and photometry are essentially the same as the parameters that were used to construct the GOODS r1.1z public data set source catalog (see Giavalisco et al. 2004): we initially considered all detections with a minimum of 16 connected pixels each containing >0.6 times the standard deviation of the local background (giving a S/N of >2.4). SExtractor's deblending parameters were set to `DEBLEND_MINCONT` = 0.03, `DEBLEND_NTHRESH` = 32. The publicly available inverse variance images provided by the GOODS team were converted to rms images to ensure that the absolute standard deviations per pixel were used by SExtractor. For the UDF parallel data sets that were drizzled on a scale of $0\farcs05$ pixel^{-1}, we detected objects using a minimum of five connected pixels at a threshold of 1.1× the rms of the local background (nominal S/N>2.4) and setting `DEBLEND_MINCONT` = 0.1 and `DEBLEND_NTHRESH` = 8.

After this initial detection we rejected all objects with S/N less than 5 in z_{850}, where we define S/N as the ratio of counts in the isophotal aperture to the errors on the counts. The remaining objects were considered real objects. Galactic stars appear to closely overlap with galaxies in the V_{606}–i_{775}, i_{775}–z_{850} color-color plane (see section 3.4). We initially rejected all point sources on the basis of high SExtractor stellarity index, e.g., setting S/G<0.85 (nonstellar objects with high confidence).

We used SExtractor's `MAG_AUTO` to estimate total object magnitudes within an aperture radius of $2.5 \times r_{\rm Kron}$ (Kron 1980), but calculated galaxy colors from the isophotal magnitudes measured by SExtractor within the aperture defined by the isophotal area of the object in the z_{850}-band. These procedures are optimal for (faint) object detection and aperture photometry with ACS (Benítez et al. 2004). We measured half-light radii defined as the radius that contains half of the total light using annular photometry out to $2.5 \times r_{\rm Kron}$ (performed by SExtractor). The total magnitudes and half-light

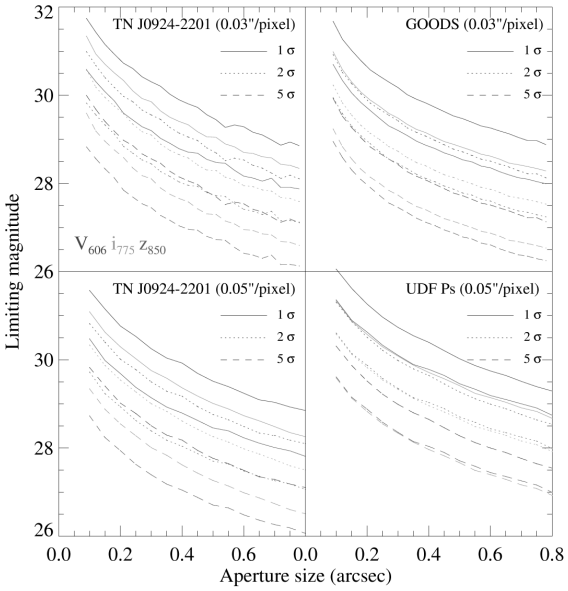

Figure 7.3 — Depth as a function of square aperture diameter for the different data sets. Curves give the 1σ (solid), 2σ (dotted), and 5σ (dashed) limiting magnitudes in V_{606} (blue), i_{775} (green), and z_{850} (red).

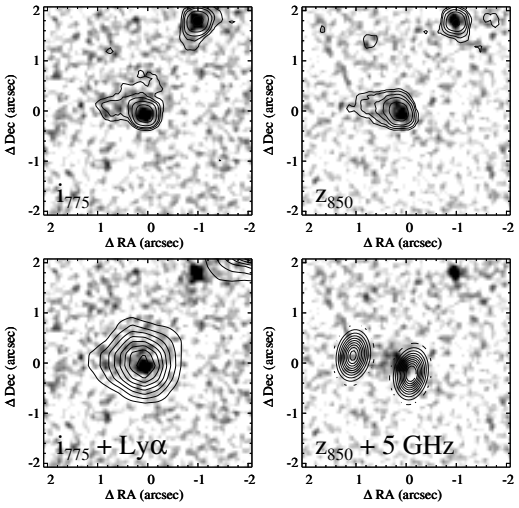

Figure 7.4 — *HST* ACS images of radio galaxy TN J0924–2201. *Top left:* The i_{775}-band image with contours of the same image smoothed using a $0\farcs15$ (FWHM) Gaussian to enhance the faint tail. *Top right:* Same as top left, but for the z_{850}-band. *Bottom left:* i_{775}-band image in gray scale with contours representing the ground-based narrowband Lyα image (with a seeing of $\sim$0.8″ (FWHM)). *Bottom right:* z_{850}-band image in gray scale with contours of the 4.86 GHz radio image overlaid (C. De Breuck 2005, private communications). Throughout this paper, all ACS gray scale postage stamps have been smoothed using a Gaussian kernel of 0.075″ (FWHM). The continuum, Lyα, and radio emission are all aligned.

radii have not been corrected for the amount of light missed outside the apertures, unless stated otherwise (see Benítez et al. 2004; Giavalisco et al. 2004,Overzier et al., in prep. for aperture corrections applied to ACS observations). All colors and magnitudes quoted in this paper have been corrected for foreground extinction and are in the AB system of Oke (1971).

7.2.5 Photometric redshifts

We used the Bayesian Photometric Redshift code (BPZ) of Benítez (2000) to obtain estimates for galaxy redshifts, z_B. For a complete description of BPZ and the robustness of its results, we refer the reader to Benítez (2000) and Benítez et al. (2004). Our library of galaxy spectra is based on the elliptical, intermediate- (*Sbc*) and late-type spiral (*Scd*) and irregular templates of Coleman et al. (1980), augmented by starburst galaxy templates with $E(B-V) \sim 0.3$ ($SB2$) and $E(B-V) \sim 0.45$ ($SB3$) from Kinney et al. (1996), and two simple stellar population (SSP) models with ages of 5 and 25 Myr from Bruzual & Charlot (2003). The latter two templates have been found to improve the accuracy of BPZ for very blue, young high-redshift galaxies in the UDF (Coe et al., in prep.). BPZ makes use of the parameter ODDS, defined as $P(|z - z_B| < \Delta z)$, which gives the total probability that the true redshift is within an uncertainty Δz. For a Gaussian probability distribution a 2σ confidence interval centered on z_B would get an ODDS of > 0.95. The empirical accuracy of BPZ is $\sigma \approx 0.1(1 + z_B)$ for objects with $I_{814} \lesssim 24$ and $z \lesssim 4$ observed in the $B_{435}V_{606}I_{814}$-bands with ACS to a depth comparable to our observations (Benítez et al. 2004). Note that we will be applying BPZ to generally fainter objects at $z \sim 5$ observed in $(B_{435})V_{606}i_{775}z_{850}$. The true accuracy for such a sample has yet to be determined em-

pirically.

7.3 Results

7.3.1 Radio galaxy TN J0924–2201

The radio galaxy TN J0924–2201 was not detected in V_{606} due to the attenuation of flux shortward of Lyα by the intergalactic medium (IGM). We derive a 2σ upper limit of 28.3 magnitude within $r_{\rm Kron}$. The galaxy is detected in the other filters with total magnitudes of $i_{775}= 26.0 \pm 0.1$ and $z_{850}= 25.5 \pm 0.1$ and colors of V_{606}–$i_{775}> 2.7$ and i_{775}–$z_{850}= 0.4 \pm 0.1$ (Table 7.2).

The radio galaxy's V_{606}–i_{775} color is affected by the relatively large equivalent width of Lyα ($EW_0 = 83$ Å, Venemans et al. (2004)). In the i_{775}- and z_{850}-bands, the galaxy consists of a compact object with a $\sim 1''$ tail extending toward the east, which we have made visible by smoothing the ACS images shown in Fig. 7.4 using a Gaussian kernel of $0\farcs15$ (FWHM). Also shown is the narrowband Lyα from Venemans et al. (2004) in contours superposed on the ACS i_{775}-band (Fig. 7.4, bottom left). The narrowband image was registered to the ACS image using a nearby star $\sim 3''$ to the northwest of the radio galaxy. The main component observed with ACS is entirely embedded in the $\sim 1\farcs5$ (~ 9 kpc) Lyα halo (compared to a seeing of $0\farcs8$). The lower right panel of Fig. 7.4 shows the VLA 4.86 GHz radio contours (C. De Breuck, private communications) overlaid on the ACS z_{850}-band image. The relative astrometry could not be determined to better than $0\farcs5$. We find good correspondence between the orientations of the radio emission and the extended ACS emission. This is analogous to the alignment of both the UV continuum and emission lines with the radio seen in other HzRGs at lower redshifts, which can be due to (a combination of) scattered light, emission lines, and, possibly, jet-induced star formation (e.g., Best et al. 1998; Bicknell et al. 2000; Zirm et al. 2005, and references therein). Several emission lines common to high-redshift radio galaxies fall within the z_{850} transmission curve (C IV, He II). Based on a composite radio galaxy spectrum, we estimate that the contribution of these lines is at most ~ 0.2 mag in z_{850}. If the continuum is further dominated by the emission of young, hot stars with little dust, we derive a star formation rate (SFR) of 13.3 $M_\odot$ yr^{-1}. This SFR is comparable to that of normal star-forming galaxies at $z \sim 4-6$ (e.g., Steidel et al. 1999; Papovich et al. 2001; Ouchi et al. 2004a; Giavalisco et al. 2004a; Bouwens et al. 2004b).

7.3.2 Properties of Lyα emitting galaxies at $z \approx 5.2$

In this section we study some of the properties of the four Lyα-emitting galaxies from Venemans et al. (2004). The morphologies in the three bands are shown in Fig. 7.5, and their photometric properties are summarized in Table 7.2. All four Lyα emitters were detected in i_{775}, the filter that includes Lyα, with one object (2688) being solely detected in this filter. The UV continuum magnitudes measured from the z_{850}-band are all fainter than 25.8 magnitudes, making them fainter than the faintest galaxies in the $z \sim 5$ GOODS LBG sample from Ferguson et al. (2004). This implies that this population of Lyα galaxies is confined to luminosities of $\lesssim 0.7\ L^*$, where L^* is the characteristic continuum luminosity of $z = 3$ LBGs from Steidel et al. (1999). Two emitters have a luminosity of $\lesssim 0.3\ L^*$. It is evident that the selection of these Lyα galaxies is biased in two important ways. One, the sample is naturally biased toward galaxies with high equivalent width of Lyα, and second, it is biased toward the fainter end of the LBG luminosity function. This finding seems consistent with that of Shapley et al. (2003) who found evidence that Lyα equivalent width increases toward fainter continuum magnitudes in their spectroscopic $z \sim 3$ LBG sample. The faint UV continuum of these Lyα-emitting galaxies is similar to that observed for Lyα galaxies associated with other radio galaxies (Venemans et al. 2004; Miley et al. 2004,Overzier et al., in prep.).

7.3.2.1 Continuum slopes

We can use the accurate ACS photometry, together with the narrowband Lyα flux densi-

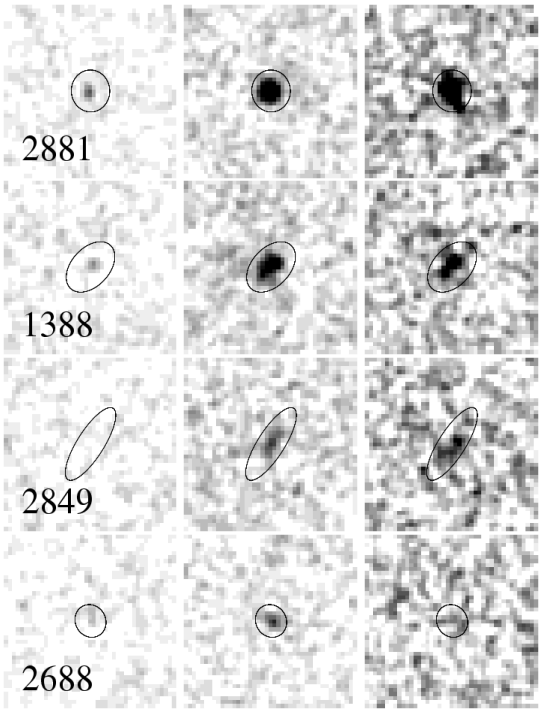

Figure 7.5 — Left to right: V_{606},i_{775} and z_{850} images of the four spectroscopically confirmed Lyα emitters of Venemans et al. (2004). The images have been smoothed using a Gaussian kernel of 0.075″ (FWHM). Kron apertures determined from the i_{775}-band image are indicated. The images are $2'' \times 2''$ in size.

ties, to try to sharpen the constraints on the Lyα EW and to determine the continuum slope ($f_\lambda \propto \lambda^\beta$) of these emitters. To this end, we follow the procedures detailed in Venemans et al. (2005) to subsequently derive the UV slope β, the strength of the continuum, the contribution of Lyα to i_{775}, and its (restframe) equivalent width, EW_0. We take into account that for a source at $z = 5.2$ a fraction $Q_{775} \approx 0.68$ of the i_{775} flux is absorbed by intervening neutral hydrogen (Madau 1995) and note that this fraction is virtually independent of β. The uncertainties on β and EW_0 were obtained by propagating the individual errors on the measured magnitudes using a Monte Carlo method and fitting the resulting distributions with a Gaussian. For object 2881, the brightest in our sample, we find good constraints on both the UV slope and the Lyα EW, $\beta = -0.8 \pm 0.6$ and $EW_0 = 39 \pm 7$. The continuum seems redder than the average slope of $\beta = -1.8 \pm 0.2$ of V_{606}-dropouts in GOODS found by Bouwens et al. (2005b). However, we cannot rule out the possibility that the Lyα flux in i_{775} has been oversubtracted due to the presence of faint, extended Lyα in the VLT narrowband Lyα image (point spread function (PSF) of $\sim 0.''8$) not detected with ACS (PSF of $\sim 0.''1$). This could have caused the slope calculated above to be shallower than it in fact is. We were not able to place tight constraints on the two fainter objects, Nos. 1388 and 2849, detected in i_{775} and z_{850}, and refer to Venemans et al. (2005), who find $EW_0 \sim 50$ Å with large errors under the assumption of a flat (in f_ν, i.e., $\beta = -2$) spectrum.

7.3.2.2 Star formation rates

Using the emission-line–free UV flux at 1500Å measured in z_{850}, we derive star formation rates (SFRs) using the conversion between UV luminosity and SFR for a Salpeter initial mass function (IMF) given in Madau et al. (1998):

$$\mathrm{SFR} = \frac{L_{1500\mathring{A}}[\mathrm{erg\ s^{-1}Hz^{-1}}]}{8 \times 10^{27}} M_\odot\ \mathrm{yr}^{-1} \qquad (7.1)$$

We find 5.9 and 3.0 $M_\odot$ yr^{-1} for objects 1388 and 2849. Object 2881 has a SFR of 9.7 $M_\odot$ yr^{-1}, quite comparable to that derived for the radio galaxy (see Sect. 7.3.1). These SFRs are considered to be lower limits, since the presence of dust is likely to absorb the (rest frame) UV luminosities observed. The Lyα-to-continuum SFR ratios are in the range 0.7–3. The Lyα SFRs were derived following the standard assumption of case B recombination, valid for gas that is optically thick to H I resonance scattering (Venemans et al. 2005).

As modeled by Charlot & Fall (1993), high equivalent width Lyα is expected for a relatively brief period in young ($\sim 10^{7-9}$ yr), nearly dust-free galaxies. However, the general understanding is that, regardless of the effects of dust, the UV continuum is a better probe of the SFR than Lyα, given the large cross section to resonance

scattering for the latter. While the Lyα profile can be severely diminished, depending on the geometry of the system, the gas density, and the dust contents, the *enhancement* of Lyα flux over UV flux is also not ruled out, at least theoretically. Young galaxies may consist of a two-phase medium (e.g., Rees 1989), effectively thin to Lyα photons scattering off the surfaces of clouds that are optically thick to unscattered UV photons (Neufeld 1991). For the Lyα emitters found in overdensities associated with radio galaxies, we find that the SFRs derived from the UV and Lyα are generally of a similar order of magnitude (e.g., this paper, Venemans et al. 2005,Overzier et al., in prep.). It is unlikely that geometry, dust, and scattering medium all conspire so that the SFRs derived from Lyα and the continuum will be comparable. More likely it implies that both the UV and Lyα offer a relatively clear view (e.g., little dust and simple geometry) toward the star-forming regions of these galaxies.

7.3.2.3 Sizes

Except for source 2688, which we discuss in detail below, the sources are (slightly) resolved in i_{775} and z_{850}. The half-light radii measured in z_{850} are 0.″10–0.″16, implying that the (projected) physical half-light diameters are $<$2.5 kpc, where we have applied a correction for the degree to which half-light radii as measured by SExtractor are underestimated for objects with $z_{850} \approx 26$, based on profile simulations (Overzier et al., in prep). The sizes are comparable to the sizes we have measured for Lyα emitters associated with radio galaxies at $z = 3.13$ and 4.11 (Miley et al. 2004; Venemans et al. 2005, Overzier et al. in prep.). We find no evidence for dominant active nuclei among these Lyα emitters.

7.3.3 A galaxy without UV continuum

Object 2688 from Venemans et al. (2004) is particularly interesting. It is the faintest object in our Lyα sample ($i_{775} \approx 28$), and it is not detected in z_{850} at the 2σ level ($z_{850} > 28.4$). Likewise, there is no detection in V_{606}. Assuming $\beta \approx -2$, which is appropriate for a dustless, young (1–100 Myr) galaxy, correcting for the Lyα emission in the i_{775}-band would place this object's magnitude close to the detection limit in i_{775}. This implies that the i_{775} flux is solely that of Lyα, with an EW_0 of $>$ 100 Å. What physical processes could explain its peculiar observed properties?

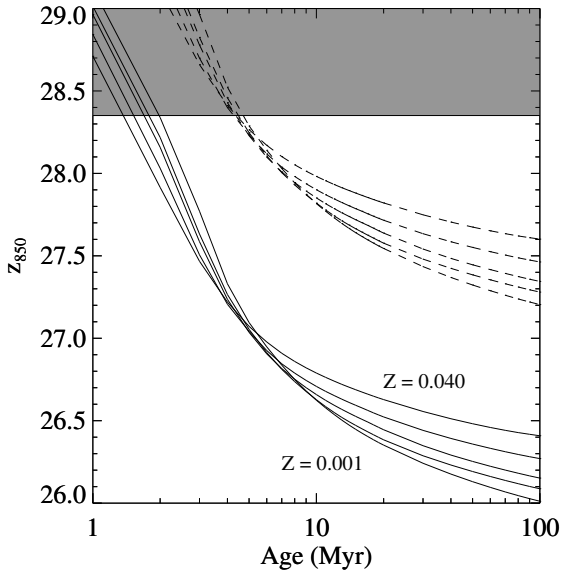

Figure 7.6 — Plot of z_{850} continuum magnitude as a function of age for a continuous star formation model with a SFR of 3 $M_\odot$ yr^{-1} from Starburst99 (Leitherer et al. 1999) (Salpeter IMF with $M_l = 1\ M_\odot$ and $M_u = 100\ M_\odot$). Bttom to top: Metallicities of the models are 0.001, 0.004, 0.008, 0.02, and 0.04. The shaded box demarcates the 2σ limit on the z_{850} magnitude within the Kron aperture of Lyα emitter 2688. Dashed lines indicate similar models, but with a SFR of only 1 $M_\odot$ yr^{-1}. The nondetection in z_{850} may indicate that object 2688 has an age of only a few Myr.

• **Young star-forming galaxy?** If object 2688 is a young star-forming galaxy, the observed equivalent width of Lyα should be a function of the age of the stellar population. Venemans et al. (2004) estimated the SFR in 2688 from its Lyα luminosity and found $\sim 3\ M_\odot$ yr^{-1}. Based on a population synthesis model for a young stellar population with a SFR of 3 $M_\odot$ yr^{-1} (Salpeter IMF, $M_l = 1 M_\odot$, and $M_u = 100 M_\odot$) shown in Fig. 7.6, our robust limit on the z_{850}-band ($\sim$ 1465 Å rest frame) would be surpassed within only $\sim$ 2 Myr (Leitherer et al. 1999). A comparably young object was found by Ellis et al. (2001)

at $z = 5.6$. In this case, the lensing amplification by the cluster Abell 2218 also enabled placing a strong upper limit on the object size of 150 pc, consistent with it being a typical H II region. Given the nondetection of 2688 in z_{850}, it is difficult to place an upper limit on the size of this object. If we take the physical half-light diameter of 2.5 kpc derived for the other Lyα emitters as an extreme upper limit on the size, it is not likely that star formation can progress over such a large size within only a few Myr. Whether the actual size of the Lyα emitting in 2688 is similar to that of typical H II regions is unclear given the extremely thin detection in i_{775}.

• **Outflow?** Extended emission-line regions seem to be a common feature of both local and high-redshift star-forming galaxies. Locally, some of the emission is produced in galactic scale outflows. Empirically, there is a lower limit to the surface density of star formation necessary to launch such a galactic wind of 0.1 $M_\odot$ yr^{-1} kpc^{-2} (Heckman et al. 1990). For 2688 we calculate a SFR surface density of $>$ 0.5 $M_\odot$ yr^{-1} kpc^{-2}. Therefore, the observed high equivalent width Lyα may be a result of outflowing gas, while the galaxy itself may be obscured and older than the strong upper limit of a few Myr derived for the above scenario.

• **AGN?** The equivalent width of Lyα could also be boosted by the presence of an active nucleus. TN J0924–2201 itself has a Lyα $EW_0 = 83$ Å, close to the lower limit derived for object 2688. While there is no evidence for a bright nuclear point source in 2688, it could be easily obscured by circumnuclear dust, particularly at rest frame ultraviolet wavelengths. Because the spectrum only has narrow Lyα, it could be a faint narrow-line quasar. Several of the Lyα emitters in the protocluster near radio galaxy MRC 1138–262 at $z = 2.16$ have been detected with *Chandra* indicating that the AGN fraction of such protoclusters could be significant. In contrast, Wang et al. (2004) found no evidence of AGNs among a large field sample of $z \approx 4.5$ Lyα emitters observed in the X-ray.

7.3.4 Selection of V_{606}-dropouts

Galaxies without a significant excess of Lyα (i.e., rest frame $EW_{Ly\alpha} < 20$Å) constitute $\sim 75\%$ of LBG samples (Shapley et al. 2003) and hence are missed by selection based purely on the presence of Lyα emission. To circumvent this inherent bias in Lyα surveys, galaxies can be selected on the basis of broadband colors that straddle the Lyman break for some specific redshift range. Unfortunately, having only a few filters, the Lyman break selection provides only a crude selection in redshift space due to photometric scatter and uncertainty in the underlying spectral energy distributions (SEDs). This is especially important when we want to test for the presence of LBGs within a relatively narrow redshift range of the radio galaxy.

Giavalisco et al. (2004a) selected V_{606}-dropouts from the GOODS fields using the criteria:

$$\begin{aligned}&[(V_{606} - i_{775}) \geq 1.5 + 0.9 \times (i_{775} - z_{850}) \ \vee \\ &(V_{606} - i_{775}) \geq 2.0] \ \wedge \ (i_{775} - z_{850}) \leq 1.3 \ \wedge \\ &(V_{606} - i_{775}) \geq 1.2 \end{aligned} \quad (7.2)$$

where $\vee$ and $\wedge$ are the logical OR and AND operators. Although we use these selection criteria to select V_{606}-dropout samples from our datasets, we use a slightly modified selection window when discussing the clustering statistics of V_{606}-dropouts with respect to the radio galaxy (Sect. 7.4.1). We can tighten the color constraints given in Eq. 7.2 to effectively remove relatively blue objects that are likely to be at redshifts much lower than we are interested in ($z \approx 5.2$), as well as relatively red objects at much higher redshifts. We required

$$0.0 \leq (i_{775} - z_{850}) \leq 1.0 \quad (7.3)$$

in addition to Eq. 7.2 to reject galaxies at $z \lesssim 4.8$ and $z \gtrsim 5.5$, based on the color-color track of a 10^8 yr constant star-forming model of $0.4Z_\odot$ metallicity. The resulting selection window is indicated in Fig. 7.7 (shaded area). The selection window of (Giavalisco et al. 2004a) as given in Eq. 7.2 has been indicated for comparison (dashed line).

Table 7.2 — Properties of the spectroscopically confirmed Lyα emitters.

ID[a]	α_{J2000}	δ_{J2000}	V_{606}–i_{775}[b]	i_{775}–z_{850}[b]	z_{850}[c]	z_{spec}^{d}	$r_{hl,i}^{e}$	$r_{hl,z}^{f}$	SFR[g]
RG[h]	09:24:19.89	–22:01:41.23	> 2.7	0.4 ± 0.1	25.45 ± 0.12	5.199	0.″19	0.″23	$14^{+2.2}_{-1.9}$
2881[i]	09:24:23.87	–22:03:43.97	2.5 ± 0.3	0.4 ± 0.1	25.80 ± 0.09	5.168	0.″09	0.″11	$9.7^{+0.6}_{-0.6}$
1388[i]	09:24:16.66	–22:01:16.41	2.2 ± 0.4	0.1 ± 0.2	26.33 ± 0.17	5.177	0.″12	0.″15	$5.9^{+0.8}_{-0.6}$
2849[i]	09:24:24.29	–22:02:30.11	> 1.9	-0.3 ± 0.4	27.06 ± 0.25	5.177	0.″13	0.″16	$3.0^{+0.8}_{-0.6}$
2688[i]	09:24:25.65	–22:03:00.27	1.2 ± 0.4	< -0.5	> 28.35	5.173	0.08″	–	< 1

[a] IDs are from Venemans et al. (2005).
[b] Isophotal color, using 2σ limits in V_{606}.
[c] Kron magnitude.
[d] Spectroscopic redshifts from Venemans et al. (2005).
[e] Half-light radius measured in i_{775}.
[f] Half-light radius measured in z_{850}.
[g] SFR measured in z_{850} in $M_\odot$ yr^{-1}.
[h] Detection based on the z_{850} image.
[i] Detection based on the i_{775} image.

Unlike GOODS and the UDF parallel fields, there are no observations in B_{435} for our field, which makes it impossible to remove low-redshift contamination by requiring a maximum upper limit on detections in B_{435} (e.g., $S/N < 2$). The estimates for the low-redshift contamination fraction of V_{606}-dropouts from GOODS amount to $\sim 10 - 30\%$ (Bouwens et al. 2005b). We note, however, that in some cases low-redshift objects that have made it into the selection window can still be rejected on the basis of their high relative brightness and/or large sizes in the $V_{606}i_{775}z_{850}$-bands during visual inspection.

7.3.5 Properties of V_{606}-dropouts in the field of TN J0924–2201

The V_{606}–i_{775} versus i_{775}–z_{850} diagram of the objects that meet our selection criteria is shown in Fig. 7.7 compared to the entire $V_{606}i_{775}z_{850}$ sample. Also shown are the color-color tracks of several standard SEDs and the stellar locus. We find 23 V_{606}-dropouts down to a limiting magnitude of z_{850}= 26.5. The radio galaxy (object 1396) and the two brightest Lyα emitters (objects[4] 449 and 1844) passed the V_{606}-dropout selection criteria. Table 7.3 lists the coordinates, colors, and magnitudes of the LBG candidates. Fig. 7.8 shows the z_{850}-band image with the positions of the V_{606}-dropouts (blue circles) and the Lyα emitters (red squares).

7.3.5.1 SFRs and continuum slopes

Our limiting magnitude in z_{850} corresponds to $\sim 0.5\ L^*$ (taking into account the average amount of flux missed). We calculated SFRs from the emission-line–free UV flux measured in z_{850}. The SFRs range from 5–42 $M_\odot$ yr^{-1} if there is no dust (see Table 7.3). We calculated an average UV slope ($f_\lambda \propto \lambda^\beta$) for the entire sample from the i_{775}–z_{850} color and find $\langle\beta\rangle = -2.4$, with a standard deviation of 1.7 for the sample. Here we have assumed a redshift of $z = 5.2$ to convert between magnitudes and the actual flux densities of the continuum in i_{775}. However, this assumed redshift is critical to the calculation of β, due to its large dependence on the amount of Lyα forest absorption in i_{775}: the average i_{775}–z_{850} color corresponds to slopes ranging from $\langle\beta\rangle = -1.3$ at $z = 5.0$ to $\langle\beta\rangle = -4.0$ at $z = 5.4$. The average slope of $\langle\beta\rangle = -2.4$, which we measured, is consistent with the average slope of V_{606}-dropouts ($\beta = -1.8 \pm 0.2$) in GOODS (Bouwens et al. 2005b).

It is impossible to fit both the redshift and the

[4] IDs 2881 and 1388 in Table 7.2 and Venemans et al. (2004)

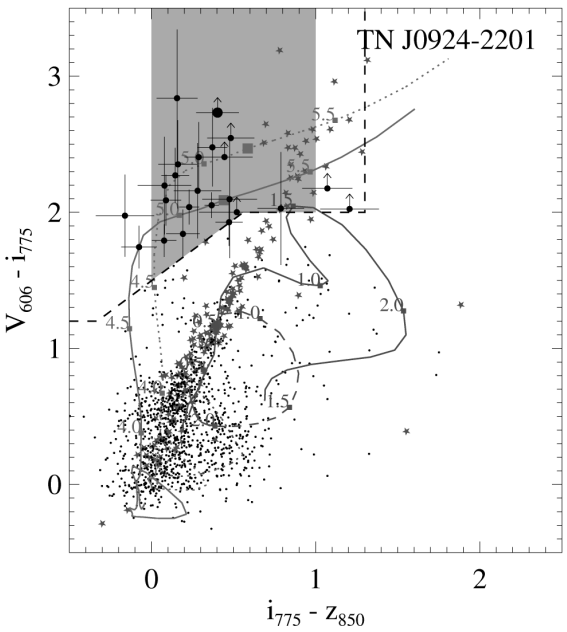

Figure 7.7 — Color-color diagram V_{606}–i_{775} vs. i_{775}–z_{850} for TN J0924–2201 candidate LBGs (solid circles) relative to objects from the full catalog ($z_{850}< 26.5$ with $S/N > 5$). The radio galaxy is indicated by the large circle. The black dashed line bounds the selection window of Giavalisco et al. (2004a). The shaded region marks the selection window used for the clustering statistics of V_{606}-dropouts at $z \approx 5.2$ (see Sect. 7.4.1). The spectral tracks are from an elliptical (red solid line), a Sbc (red dashed line), a Scd (red dotted line), and a 100 Myr constant star formation model with $E(B-V) = 0.0$ (blue solid line) and $E(B-V) = 0.15$ (blue dotted line). Redshifts are indicated along the tracks. The redshift of the overdensity of Venemans et al. (2004) is marked by blue squares ($z = 5.2$). The position of the stellar locus is illustrated by the green stars (objects having $S/G > 0.85$). All colors were set to their 2σ limits (limits and error bars for field objects have been omitted for clarity).

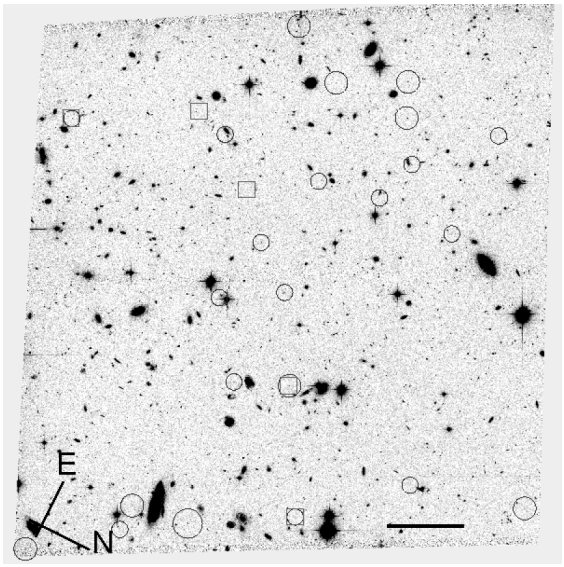

Figure 7.8 — ACS z_{850} image showing the positions of the V_{606}-break objects with blue circles. The size of the circles scales with the total z_{850} magnitude of the LBGs, where the smallest circles correspond to objects with $z_{850}> 25.5$, and the largest correspond to objects brighter than $z_{850}< 24.5$. The positions of the spectroscopically confirmed Lyα emitters from Venemans et al. (2004) are indicated with red squares. TN J0924–2201 is located roughly $0.5'$ from the image center toward the bottom of the image (this is both a Lyα emitter and a V_{606}-break object). The scale bar at the bottom measures $0.'5$.

spectral slope independently. In the following, we assume that $z = 5.2$ and that the value of the spectral slope is largely determined by dust, rather than age or metallicity. We have parameterized $E(B-V) - \beta_{iz}$ for a base template consisting of a 100 Myr old ($z_f \approx 5.6$) SED with 0.2 $Z_\odot$ metallicity that has been forming stars at a continuous rate (from Bruzual & Charlot 2003). The template was reddened by applying increasing values of $E(B-V)$ using the recipe of Calzetti et al. (2000). The measured slopes are consistent with modest absorption by dust of $E(B-V) \sim 0-0.4$, with the lower values preferred, given the mean slope of the sample. In some cases we also found negative values of $E(B-V)$. This suggests that the color might be bluer than that of the base template used or that the redshift is off.

Bouwens et al. (2005b) found evidence for evolution in the mean UV slope from $z \sim 5$ ($\beta = -1.8 \pm 0.2$) to $z \sim 2.5$ ($\beta = -1.4 \pm 0.1$) (see also Lehnert & Bremer 2003; Ouchi et al. 2004a; Papovich et al. 2004; Bouwens et al. 2006). They have interpreted this as an evolution in the dust content rather than age or metallicity, based on the plausible assumption that any change in these parameters by significantly large factors seems unlikely, given that the universe only doubles in age over this redshift interval and the

gradual process of galaxy formation. Reducing the dust content by a factor of ~ 2 from $z \sim 3$ to 5 can explain the relatively blue continuum of the V_{606}-dropouts.

7.3.5.2 Sizes

We have measured half-light radii in z_{850}. A Gaussian fit to the size distribution gives a $\langle r_{hl,z} \rangle = 0\farcs16$, with standard deviation $0\farcs05$. The mean half-light radius corresponds to ~ 1.2 kpc at $z \sim 5$. Note that our sample is biased against $z \sim 5$ AGN point sources, since they would be rejected based on their high stellarities. If we divide our sample in two magnitude ranges, $z_{850}=$ $24.2 - 25.5$ and $z_{850}= 25.5 - 26.5$, the mean half-light radii for the two bins are $0\farcs20$ and $0\farcs14$, respectively.

While it cannot entirely be ruled out that fainter LBGs are intrinsically smaller, the observed difference between the two bins can most likely be explained by the effect of surface brightness dimming in two ways: 1) the fraction of light that is missed in aperture photometry is larger for fainter sources, and 2) the incompleteness is higher for larger sources at a fixed magnitude (see, e.g., Bouwens et al. 2004b; Giavalisco et al. 2004). The mean half-light radius of $z_{850}< 25.8$ LBGs at $z \sim 5$ in GOODS is $\langle r_{hl,z} \rangle \approx 0\farcs27$, as measured by Ferguson et al. (2004). However, Ferguson et al. (2004) measured half-light radii using maximum apertures approximately 4 times larger than ours, which inevitably results in slightly larger half-light radii. Calculating the half-light radius using our method and our own sample of $z \sim 5$ LBGs from the GOODS field (Sect. 7.4.1) gives $\langle r_{hl,z} \rangle =$ $0\farcs17 \pm 0.06$ (with $0\farcs20 \pm 0.08$ and $0\farcs16 \pm 0.05$ for the brighter and fainter magnitude bins, respectively), consistent with the sizes we find in the TN J0924–2201 field.

The V_{606}, i_{775}, and z_{850} morphologies are shown in Fig. 7.9. Three objects (119, 303, and 444) have a clear double morphology. Based on the large V_{606}-dropout sample from GOODS (Sect. 7.4.1), we would expect roughly 1.5 of such systems in our field, indicating that our field might be relatively rich in merging systems. A more detailed, comparative analysis of sizes and morphologies of LBGs and Lyα emitters in radio galaxy protoclusters at $2 < z < 5.2$ will be given elsewhere.

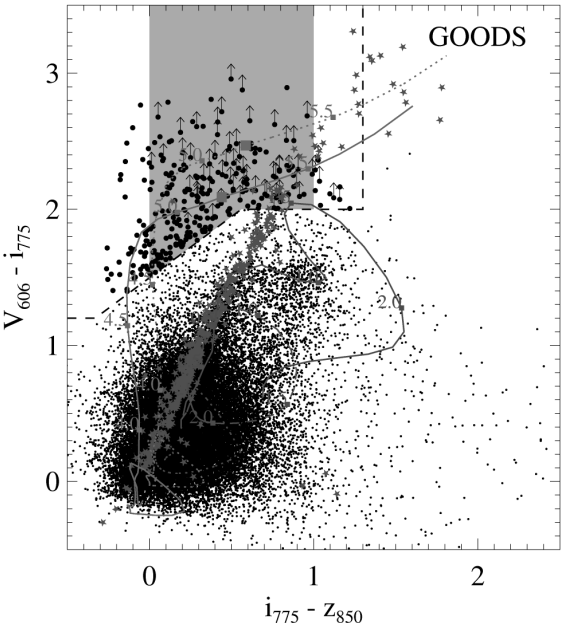

Figure 7.10 — Color-color diagram of GOODS. See the legend of Fig. 7.7 for details.

7.3.5.3 Point sources

The Galactic stellar locus runs through our V_{606}-dropout selection window (green stars in Fig. 7.7). We found ~ 14 stellar objects that pass our selection criteria, if we let go of the requirement of relatively low stellarity index, as measured by SExtractor. However, the additional objects we found were all brighter than z_{850}=25.0, and the majority were scattered around the red end of the stellar locus. No new objects with high stellarity were found at fainter magnitudes. Therefore, we believe that we have not missed a significant population of (unresolved) $z \sim 5$ AGNs in this field.

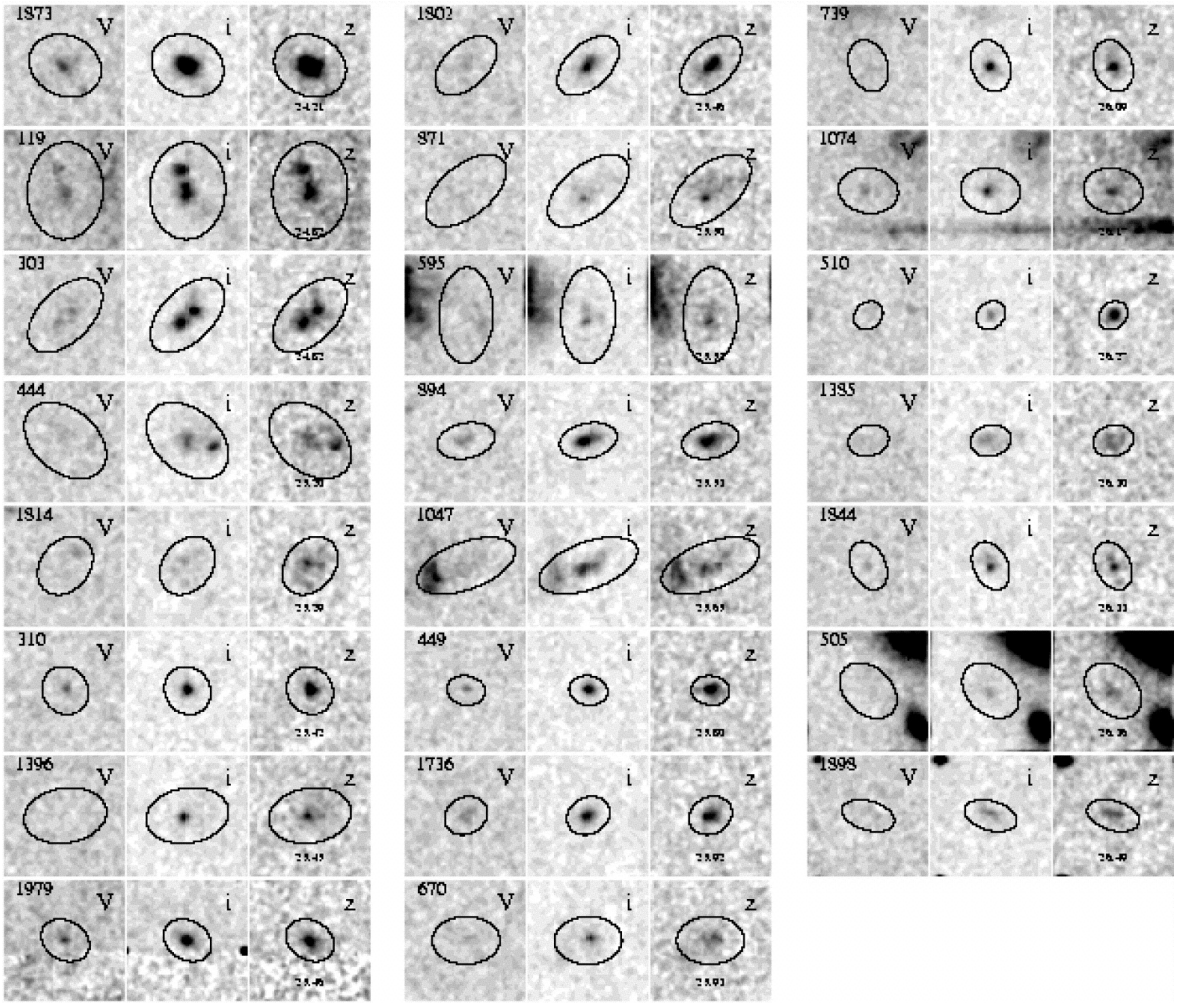

Figure 7.9 — Left to right: *HST* ACS postage stamps showing V_{606}, i_{775}, and z_{850} of the $z \sim 5$ LBG sample. Each image measures $2'' \times 2''$, corresponding to $\sim 13 \times 13$ kpc at $z \sim 5$. The Kron aperture defined by the light distribution in z_{850} has been indicated. The images have been smoothed using a Gaussian kernel of $0.075''$ (FWHM).

7.4 Discussion

7.4.1 An overdensity of V_{606}-dropouts associated with TN J0924–2201?

In this section we test whether the overdensity of Lyα emitters near TN J0924–2201 found by Venemans et al. (2005) is accompanied by an overdensity of V_{606}-dropout galaxies. To establish what the surface density is of V_{606}-dropouts in the "field," we have applied our selection criteria to the GOODS and the UDF parallel fields. The color-color diagram for the objects in the GOODS fields is shown in Fig. 7.10. The GOODS and UDF parallel fields cover a total area of ~ 337 arcmin^2 compared to ~ 12 arcmin^2 for TN J0924–2201. At $z_{850} < 26.5$ the numbers of V_{606}-dropouts satisfying our selection criteria are 277 for the combined GOODS fields, and 8 and 16 objects in the UDF-P1 and UDF-P2 fields, respectively. Similar to Bouwens et al. (2005b), we find that the number of V_{606}-

Table 7.3 — Properties of V_{606}-dropouts in the field of TN J0924–2201.

ID	α_{J2000}	δ_{J2000}	V_{606}–i_{775}[b]	i_{775}–z_{850}[b]	z_{850}[c]	$r^d_{hl,z}$	SFR[e]	z^f_B
1873	09:24:15.17	–22:01:53.2	2.05 ± 0.09	0.37 ± 0.04	24.21 ± 0.04	0.″18	42	$5.19^{+0.73}_{-0.73}$
119	09:24:29.06	–22:02:41.1	1.79 ± 0.12	0.08 ± 0.07	24.82 ± 0.09	0.″24	24	$4.74^{+0.68}_{-0.68}$
303	09:24:29.03	–22:01:53.2	2.04 ± 0.13	0.23 ± 0.06	24.82 ± 0.07	0.″22	24	$4.86^{+0.69}_{-0.69}$
444	09:24:28.11	–22:01:47.4	2.35 ± 0.32	0.16 ± 0.12	25.20 ± 0.11	0.″28	17	$4.93^{+0.70}_{-0.70}$
1814	09:24:19.78	–22:59:58.1	> 2.18	1.07 ± 0.15	25.29 ± 0.09	0.″24	16	$5.56^{+0.77}_{-0.77}$
310	09:24:28.10	–22:02:18.1	1.93 ± 0.18	0.47 ± 0.08	25.42 ± 0.08	0.″11	14	$5.23^{+0.73}_{-0.73}$
1396/								
RG[a]	09:24:19.91	–22:01:41.7	> 2.73	0.40 ± 0.13	25.45 ± 0.12	0.″23	13	$5.16^{+0.72}_{-0.72}$
1979	09:24:12.50	–22:02:45.5	2.09 ± 0.19	0.09 ± 0.09	25.46 ± 0.12	0.″14	13	$4.90^{+0.69}_{-0.69}$
1802	09:24:14.92	–22:02:15.8	2.41 ± 0.26	0.29 ± 0.09	25.46 ± 0.10	0.″15	13	$5.01^{+0.71}_{-0.71}$
871	09:24:25.76	–22:01:11.4	2.03 ± 0.41	0.79 ± 0.14	25.50 ± 0.13	0.″23	13	$5.39^{+0.75}_{-3.90}$
595	09:24:27.00	–22:01:37.6	> 2.55	0.48 ± 0.14	25.53 ± 0.14	0.″23	12	$5.21^{+0.73}_{-0.73}$
894	09:24:23.15	–22:02:16.6	2.27 ± 0.20	0.15 ± 0.08	25.53 ± 0.09	0.″15	12	$4.92^{+0.70}_{-0.70}$
1047	09:24:22.19	–22:01:59.6	1.74 ± 0.16	-0.08 ± 0.11	25.65 ± 0.15	0.″20	11	$4.76^{+0.68}_{-0.68}$
449/								
2881[a]	09:24:23.89	–22:03:44.4	2.48 ± 0.29	0.37 ± 0.09	25.80 ± 0.09	0.″11	9.7	$5.13^{+0.72}_{-0.72}$
1736	09:24:18.92	–22:00:42.2	1.84 ± 0.18	0.19 ± 0.11	25.92 ± 0.12	0.″11	8.6	$4.77^{+0.68}_{-0.68}$
670	09:24:25.41	–22:02:07.2	2.16 ± 0.35	0.28 ± 0.14	25.93 ± 0.16	0.″17	8.5	$5.02^{+0.71}_{-0.71}$
739	09:24:25.76	–22:01:43.0	2.84 ± 0.50	0.16 ± 0.12	26.09 ± 0.15	0.″12	7.4	$4.94^{+0.70}_{-0.70}$
1074	09:24:21.24	–22:02:21.6	1.98 ± 0.30	-0.16 ± 0.18	26.17 ± 0.18	0.″18	6.9	$4.79^{+0.68}_{-0.68}$
510	09:24:28.81	–22:01:12.2	> 2.02	1.21 ± 0.18	26.27 ± 0.12	0.″09	6.2	$5.62^{+0.78}_{-0.78}$
1385	09:24:19.31	–22:02:01.8	2.10 ± 0.43	0.48 ± 0.17	26.30 ± 0.15	0.″15	6.1	$5.18^{+0.73}_{-0.73}$
1844/								
1388[a]	09:24:16.68	–22:01:16.8	2.20 ± 0.36	0.08 ± 0.16	26.33 ± 0.17	0.″15	5.9	$4.87^{+0.69}_{-0.69}$
505	09:24:25.42	–22:02:48.0	> 2.00	0.52 ± 0.23	26.36 ± 0.22	0.″16	5.8	$5.23^{+0.73}_{-1.18}$
1898	09:24:14.17	–22:02:15.9	> 2.41	0.44 ± 0.17	26.49 ± 0.19	0.″12	5.1	$5.18^{+0.73}_{-0.73}$

[a] The alternative ID refers to Venemans et al. (2005) and Table 7.2.
[b] Isophotal color, using 2σ limits in V_{606}
[c] Kron magnitude.
[d] Half-light radius measured in z_{850}.
[e] UV star formation rate measured in z_{850} in $M_\odot$ yr^{-1}.
[f] Bayesian photometric redshift.

dropouts is 10% higher in the HDF-N compared to the CDF-S due to cosmic variance. We derive an average surface density of 0.9 arcmin^{-2} for the field, consistent with Giavalisco et al. (2004a) and the publicly available GOODS Version 1.1 catalogs, which we have used to cross-check our results. The V_{606}-dropout surface density of 2.0 arcmin^{-2} in the TN J0924–2201 field is twice as high, while the overall object surface densities at $z_{850} < 26.5$, $S/N > 5$, and $S/G < 0.85$ are fairly constant: 106, 119, and 98 arcmin^{-2} for the GOODS CDF-S, HDF-N, and TN J0924–2201 fields, respectively.

What is the significance of this factor of 2 surface overdensity? LBGs are known to be strongly clustered at every redshift (Porciani & Giavalisco 2002; Ouchi et al. 2004) and are known to have large field-to-field variations. In our particular case, it is interesting to calculate the probability of finding a certain number of V_{606}-dropouts in a single ACS pointing. Here we use the additional constraint on the i_{775}–z_{850} color specified in Eq. 7.3 and which is indicated by the shaded areas in Figs. 7.7

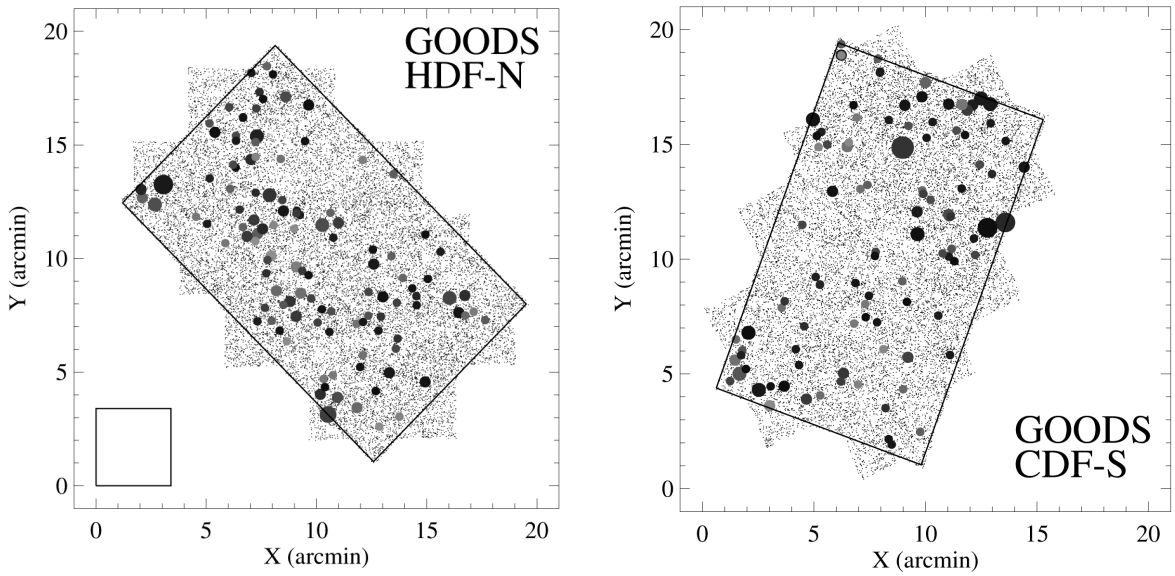

Figure 7.11 — Angular distribution of V_{606}-break objects (solid circles) in the GOODS HDF-N field (left panel) and the CDF-S field (right panel), compared to the photometric sample as a whole (points). The V_{606}-dropouts have been color coded corresponding to their i_{775}–z_{850} colors (dark blue corresponds to i_{775}–$z_{850} \approx 0.0$, dark red corresponds to i_{775}–$z_{850} \approx 1.0$), which can be taken as a rough measure of the relative redshifts. The size of the symbols scales with z_{850} magnitude (the smallest symbols correspond to $z_{850} > 26.0$, the largest symbols to $z_{850} < 24.0$). The total area of the GOODS fields is ~ 314 arcmin^2 (area within the solid lines). The size of a single $3\farcm4 \times 3\farcm4$ ACS pointing as obtained for TN J0924–2201 has been indicated to the left of the GOODS HDF-N field for comparison.

and 7.10. The angular distributions of the 218 GOODS V_{606}-dropouts satisfying these criteria are shown in Fig. 7.11. The distribution appears filamentary with noticeable "voids" that are somewhat smaller than one ACS pointing. To the bottom left of the GOODS HDF-N mosaic in Fig. 7.11 we have indicated the size of a single $3\farcm4 \times 3\farcm4$ ACS pointing for comparison. We measured the number of LBGs in 1000 (500 for each GOODS field) square 11.7 arcmin^2 cells placed at random positions and orientation angles. The cells were allowed to overlap and are therefore not totally independent. The histogram of counts-in-cells is shown in Fig. 7.12. The number of LBG candidates in TN J0924–2201 falls on the extreme right of the expected distribution based on GOODS (indicated by the red arrow). None of the cells randomly drawn from the CDF-S contained 19 objects (the highest being 14), while the chance of finding 19 objects in a single pointing in the HDF-N was slightly over 1%. Combining these results, TN J0924–2201 is overdense at the $> 99\%$ level with respect to GOODS.

As shown in Fig. 7.13, the excess in the TN J0924–2201 field over that of the GOODS sample (normalized to the same area) is primarily due to objects having i_{775}–$z_{850} \sim 0.0 - 0.5$. This clustering observed in the i_{775}–z_{850} color distribution suggests that the significance of the surface overdensity is in fact much higher than the $> 99\%$ estimated above, given that $\sim 30\%$ of the GOODS V_{606}-dropouts populate the color diagram at i_{775}–$z_{850} > 0.5$, compared to only $\sim 10\%$ of the TN J0924–2201 candidates. The most significant number excess manifests itself around i_{775}–$z_{850} \approx 0.5$, which matches the expected color of an LBG spectrum at the redshift of the radio galaxy, assuming a typical slope of $\beta \approx -2$ (the approximate redshift for such a template spectrum is indicated on the top axis of Fig. 7.13). Two of the three previously known protoclus-

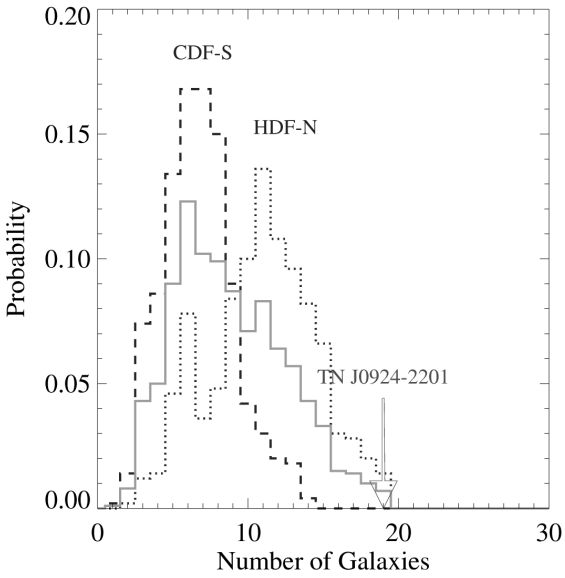

Figure 7.12 — Histogram of counts-in-cells for the GOODS fields. The number of V_{606}-break objects were counted in 500 randomly placed, square cells of 11.7 arcmin^2 in both the CDF-S (dashed line) and the HDF-N (dotted line). The sum of the GOODS histograms is indicated (solid line). The total probability that one finds 19 objects in a single pointing in GOODS amounts to $\sim 1\%$. The number of V_{606}-break objects detected in the TN J0924–2201 field (red arrow) is anomalously high compared to GOODS. This is evidence for a population of V_{606}-dropouts associated with the radio galaxy and the Lyα emitters of Venemans et al. (2004).

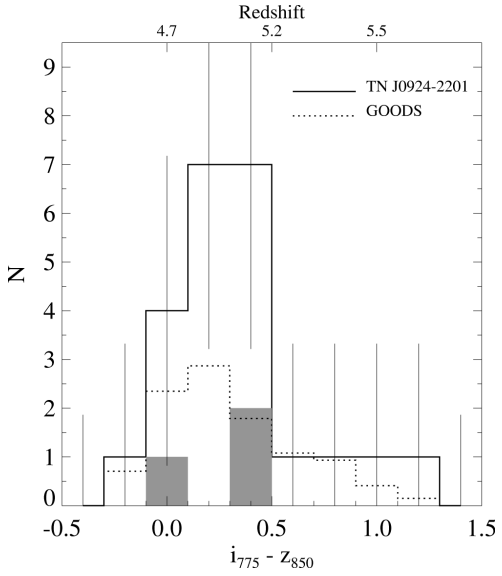

Figure 7.13 — Plot of the i_{775}–z_{850} color distribution of the TN J0924–2201 sample (solid curve). The GOODS color distribution, normalized to the area of the TN J0924–2201 field, is shown for comparison (dotted curve). The error bars are Poissonian in the low-count regime (Gehrels 1986). The i_{775}–z_{850} color of the radio galaxy and the two Lyα emitters included in the TN J0924–2201 sample are indicated by the shaded regions. The overdensity in the TN J0924–2201 field is most prominent at $0.0 < i_{775}–z_{850} < 0.5$. A slight excess in the number counts is seen around $i_{775}–z_{850} \approx 0.5$, which corresponds to $z \approx 5.2$ (see top axis) for typical values of β (i.e., –1.5 to –2).

ter members that are in the V_{606}-dropout sample also lie near this color (shaded regions in Fig. 7.13). Estimates of the photometric redshifts with BPZ also show a preference for $z \approx 5.2$ and slightly lower redshifts, although the errors on z_B are quite large (~ 0.7, Fig. 7.14 & Table 7.3). The subclustering in i_{775}–z_{850} and the photometric redshifts provide further evidence that the overdensity is associated with the radio galaxy and the Lyα emitters.

We can derive the V_{606}-dropout number densities from the comoving volume occupied by the objects. For the comoving volume one usually defines an effective volume, V_{eff}, that takes into account the magnitude and color incompleteness. We estimated the effective redshift distribution, $N(z)$, associated with our selection criteria by running BPZ on the $B_{435}V_{606}i_{775}z_{850}$ photometry of the large GOODS V_{606}-dropouts sample. The redshift distribution is shown in Fig. 7.15, where we have also indicated the sum of the redshift probability curves of each object to maintain information on secondary maxima, as well as the uncertainties associated with each object. Our effective redshift distribution is slightly narrower than the redshift distribution of Giavalisco et al. (2004a) (indicated by the dashed line in Fig. 7.15), due to our additional constraint on i_{775}–z_{850}. Because we only used objects for which z_B was relatively secure (i.e., objects having ODDS> 0.95), as well as using the full z_B probability curves to construct Fig. 7.15, we believe that our $N(z)$ is a good approximation to the true underlying redshift distribution. While our $N(z)$ could appear too narrow

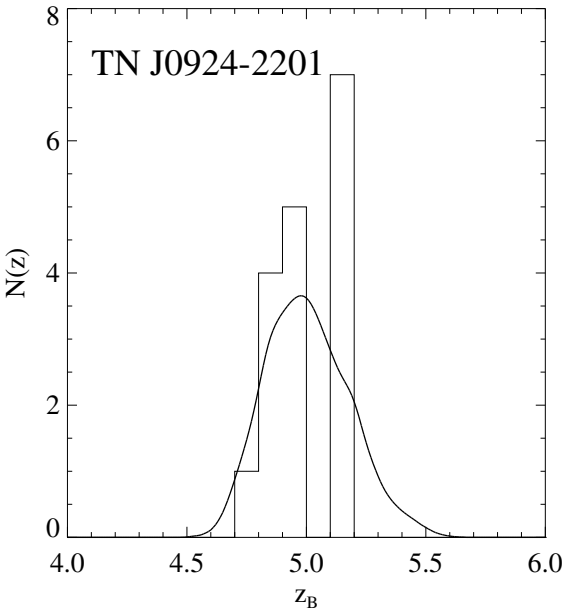

Figure 7.14 — Bayesian photometric redshift histogram for V_{606}-dropouts in TN J0924–2201 having $0.0 < i_{775}{-}z_{850} < 1.0$ and ODDS> 0.95. BPZ was used with the standard redshift prior that is based on the magnitudes of galaxies in the HDF-N (see Benítez et al. 2004). The total z_B probability distribution (thick solid curve) has also been indicated.

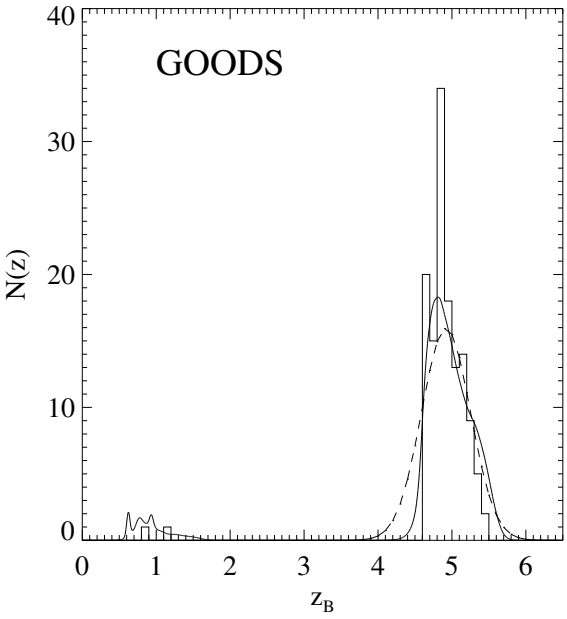

Figure 7.15 — Photometric redshift histogram for the GOODS sample. Although the sample was selected using only the $V_{606}i_{775}z_{850}$ passbands, redshifts were calculated using the full $B_{435}V_{606}i_{775}z_{850}$ catalog. The total z_B probability distribution (thick solid curve) suggests a low-redshift contamination of $\sim 9\%$. The redshift distribution of Giavalisco et al. (2004a) has been indicated for comparison (dashed curve). Our distribution is narrower because of the additional constraints on $i_{775}{-}z_{850}$ (Eq. 7.3).

if the errors on z_B are significantly underestimated, we can expect it to be narrower than that of Giavalisco et al. (2004a) in any case. The total probability of contamination seen around $z \sim 1$ amounts to $\sim 10\%$. This is similar to the number of objects in the GOODS sample for which the S/N in B_{435} is > 2.

Using the effective $N(z)$, the comoving volume for the combined GOODS fields becomes $\sim 5.5 \times 10^5$ Mpc^3. Here it is assumed that the selection efficiency at the peak of the redshift distribution is close to unity. Taking into account an incompleteness of $\sim 50\%$ for $z_{850} < 26.5$ (from Giavalisco et al. 2004a) gives an effective volume twice as small and a GOODS V_{606}-dropout volume density of 8×10^{-4} Mpc^{-3}. For TN J0924–2201, the effective volume is $\sim 1 \times 10^4$ Mpc^3, giving a number density of 2×10^{-3} Mpc^{-3} if all galaxies are spread out across the volume. If, on the other hand, a significant fraction (e.g., $\gtrsim$50%) of the objects are associated with the radio galaxy and Lyα emitters (assuming an effective protocluster volume of 8×10^2 Mpc^3 at $\bar{z} = 5.2$ with $\Delta z = 0.03$), we find a volume density of $\gtrsim 1 \times 10^{-2}$ Mpc^{-3} and a SFR density of $\gtrsim 1 \times 10^{-1}$ M$_\odot$ yr^{-1} Mpc^{-3}. This is at least a 10-fold increase compared to that of the field.

One may wonder what the cosmic variance implies for a field as large as GOODS. Somerville et al. (2004) have presented a useful recipe for deriving the cosmic variance based on the clustering of dark matter halos in the analytic CDM model of Sheth & Tormen (1999). Once the number density and mean redshift of a given population are known, one can derive the bias parameter, b, and calculate the variance of the galaxy sample, $\sigma_g = b\sigma_{DM}$, where σ_{DM} is the variance of the dark matter. A number density

of $\sim 1 \times 10^{-3}$ Mpc^{-3} corresponds to $b \approx 4$ and a variance $\sigma_{DM} \approx 0.07$ for dark matter halos at $z \sim 5$. This would imply that the upper limit for the cosmic variance of V_{606}-dropouts in a field as large as one of the GOODS fields is $\sim 30\%$. The difference in the object densities that we found was $\sim 10\%$ between the two GOODS fields. Assuming that the CDF-S represents the absolute minimum of the allowed range would imply that new fields may be discovered showing significantly more subclustering on the scale of a single ACS pointing than currently observed. In the other extreme case, that the HDF-N represents the absolute maximum, the TN J0924–2201 field should exhibit one of the highest surface densities of V_{606}-dropouts expected.

The surface overdensity of Lyα emitters around TN J0924–2201 was 1.5–6 compared to the field (Venemans et al. 2004). Our results would be marginally consistent with the lower value of ~ 2. However, only two of the Lyα emitters are bright enough to be included in our LBG sample. If the fraction of LBGs with high rest-frame equivalent width Lyα in protoclusters is similar to that of the field (Shapley et al. (2003) find $\sim 25\%$), about 6 additional (i.e., non-Lyα) 'protocluster' LBGs are expected among our sample of 16 candidates (19 when including the radio galaxy and the two Lyα emitters). Such an overdensity could easily be accommodated given the relative richness of LBGs in this field, although its ultimate verification must await spectroscopic follow-up.

Based on the clustering statistics of relatively bright ($z' < 25.8$) $Vi'z'$-selected LBGs at $z \sim 5$, Ouchi et al. (2004) found that these objects are likely to be hosted by very massive dark matter halos of $\sim 10^{12}$ M$_\odot$. The halo occupation number for these LBGs is almost unity, implying that almost every halo of this mass is expected to host a UV-bright LBG. Our sample contains several V_{606}-dropouts that have $z_{850} < 25.0$ (the brightest being 1873, with $z_{850} = 24.2$), implying present-day halo masses of $\langle M(z = 0) \rangle > 10^{14}$ M$_\odot$. Whether any of these objects are associated with the radio galaxy should be confirmed by spectroscopy.

7.4.2 The host galaxy of TN J0924–2201

The high radio luminosity of TN J0924–2201 indicates that it hosts a supermassive black hole, which must have acquired its mass in less than ~ 1 Gyr. However, in many other respects we found that it appears unremarkable when compared to general LBGs at a similar redshift. Although there is a wide dispersion in the properties of the highest redshift radio galaxies (e.g., Rawlings et al. 1996; Dey et al. 1997; Reuland et al. 2003; Zirm et al. 2005), it might be interesting to naively compare TN J0924–2201 to TN J1338–1942 at $z = 4.1$, also studied with ACS (Zirm et al. 2005). The optical host of TN J0924–2201 is almost 2 magnitudes fainter (at similar rest-frame wavelengths) than TN J1338–1941. There are several V_{606}-dropouts in our sample that have brighter magnitudes (and therefore higher SFRs) than the radio source, while TN J1338–1942 is by far the brightest object among the sample of associated g_{475}-dropouts found in that field (Miley et al. 2004). Likewise, TN J0924–2201 has a size comparable to the average size of V_{606}-dropouts (Bouwens et al. 2004b; Ferguson et al. 2004), while TN J1338–1942 is an exceptionally large ($\sim 2''$) galaxy. If TN J0924–2201 is to develop into a similar source within the ~ 400 Myr or so between $z \sim 5$ and ~ 4, it would require an increase in the projected radio source size by a factor of ~ 5, in Lyα luminosity by a factor of ~ 60, in SFR by a factor of ~ 10, and in UV size by at least a factor of 2. The recent detection of molecular gas (CO) by Klamer et al. (2005) suggests that there is $\sim 10^{11} M_\odot$ of gas mass present. The rapid enrichment that brought about this reservoir of molecular gas could have been facilitated by the early formation of the radio source and the triggering of massive star formation. The amount of gas present shows that there is plenty of material available to sustain a high SFR of several $100 M_\odot$ yr^{-1}, possibly allowing this source to undergo dramatic changes in its UV luminosity and morphology during certain stages of its evolution.

7.5 Conclusions

We have presented statistical evidence for an overdensity of star-forming galaxies associated with the radio galaxy TN J0924–2201. Our result is consistent with the overdensity of Lyα emitters discovered previously by Venemans et al. (2004) and is comparable to overdensities of Lyα emitters and LBGs found around other high-redshift radio galaxies. TN J0924–2201 could be a protocluster that will evolve into a cluster with a mass of $\sim 10^{14}$ $M_\odot$ at $z = 0$.

The existence of relatively massive structures in the early universe may not be uncommon, as suggested by, for example, the existence of quasars at even higher redshifts (e.g., Fan et al. 2003), the evidence for protoclusters out to $z < 6$, and the increasingly higher limit that can be set on the redshift of reionization. Regions of high mass concentrations are rare, strongly clustered objects at every redshift that underwent high amplification since the initial conditions (Kaiser 1984). Radio galaxies are suspected to be the sites of the formation of a massive galaxy. The evidence reported in this paper contributes to the hypothesis that redshift filaments and possibly groups or clusters of galaxies emerged together with these massive galaxies. In the radio-loud AGN unification model, the viewing angle relative to the jet determines whether a galaxy will be seen as a radio galaxy or as a radio-loud quasar (Barthel 1989). It is therefore expected that early galaxy overdensities could, in principle, also be found around high-redshift radio-loud quasars. Results indicate that the same may hold for at least some radio-quiet quasars at $z > 5$ too (Djorgovski et al. 1999, 2003,Stiavelli et al. 2005).

Although primordial galaxy overdensities so far discovered are not solely limited to fields that contain a luminous AGN (e.g. Steidel et al. 1999; Ouchi et al. 2005), they hold a strong connection to low-redshift clusters due to the presence of a supermassive black hole and possibly the development of a brightest cluster galaxy (Zirm et al. 2005). When the radio source has switched off, the host galaxy may become indistinguishable from other relatively massive, quiescent galaxies that may have been active in the past. The clustering properties and inferred halo masses of the brightest LBGs suggest that their descendants at $z = 0$ fall into groups and clusters of galaxies (Ouchi et al. 2004). Interestingly, the number densities of protoclusters, radio galaxies, and LBG redshift spikes have all been found to be consistent with the abundance of local clusters (e.g., Steidel et al. 1999; Venemans et al. 2002; Ouchi et al. 2005, and references therein). Structures such as TN J0924–2201 provide ideal comparisons with state-of-the-art *N*-body simulations. Springel et al. (2005) found that the descendants of the most massive objects at high redshift (presumed to be luminous quasars) can almost exclusively be identified with the most massive clusters at the current epoch. It might become possible to trace back cluster evolution from the well-studied regimes at $z \lesssim 1$ to slight overdensities at very high redshifts, possibly up to the epoch of reionization.

Acknowledgments

RAO is very grateful to Masami Ouchi for invaluable discussions, to Mike Dopita for discussion of Fig. 7.6, and to Carlos De Breuck for providing the radio map of TN J0924–2201 shown in Fig. 7.4. We thank the anonymous referee for helping to improve the manuscript.

ACS was developed under NASA contract NAS 5-32865, and this research has been supported by NASA grant NAG5-7697 and by an equipment grant from Sun Microsystems, Inc. The Space Telescope Science Institute (STScI) is operated by AURA Inc., under NASA contract NAS5-26555. We are grateful to K. Anderson, J. McCann, S. Busching, A. Framarini, S. Barkhouser, and T. Allen for their invaluable contributions to the ACS project at the Johns Hopkins University.

References

Adelberger, K. L., Steidel, C. C., Giavalisco, M., et al. 1998, ApJ, 505, 18
Barthel, P. 1989, Scientific American, 260, 20
Benítez, N. 2000, ApJ, 536, 571

Benítez, N., Ford, H., Bouwens, R., et al. 2004, ApJ, 150, 1
Bertin, E. & Arnouts, S. 1996, A&AS, 117, 393
Best, P. N., Longair, M. S., & Röttgering, H. J. A. 1998, MNRAS, 295, 549
Bicknell, G. V., Sutherland, R. S., van Breugel, W. J. M., et al. 2000, ApJ, 540, 678
Blakeslee, J. P., Anderson, K. R., Meurer, G. R., Benítez, N., & Magee, D. 2003a, in ASP Conf. Ser. 295: Astronomical Data Analysis Software and Systems XII, 257
Blakeslee, J. P., Franx, M., Postman, M., et al. 2003b, ApJ, 596, L143
Bouwens, R. J., Illingworth, G. D., Blakeslee, J. P., Broadhurst, T. J., & Franx, M. 2004a, ApJ, 611, L1
Bouwens, R. J., Illingworth, G. D., Blakeslee, J. P., & Franx, M. 2005a, ApJ, In Press (astro-ph/0509641)
Bouwens, R. J., Illingworth, G. D., Broadhurst, T. J., et al. 2005b, Submitted to ApJ
Bouwens, R. J., Illingworth, G. D., Thompson, R. I., et al. 2004b, ApJ, 606, L25
Bruzual, G. & Charlot, S. 2003, MNRAS, 344, 1000
Calzetti, D., Armus, L., Bohlin, R. C., et al. 2000, ApJ, 533, 682
Charlot, S. & Fall, S. M. 1993, ApJ, 415, 580
Coleman, G. D., Wu, C.-C., & Weedman, D. W. 1980, ApJ, 43, 393
De Breuck, C., van Breugel, W., Röttgering, H. J. A., & Miley, G. 2000, A&AS, 143, 303
De Breuck, C., van Breugel, W., Stanford, S. A., et al. 2002, AJ, 123, 637
Dey, A., van Breugel, W., Vacca, W. D., & Antonucci, R. 1997, ApJ, 490, 698
Djorgovski, S. G., Odewahn, S. C., Gal, R. R., Brunner, R. J., & de Carvalho, R. R. 1999, in Astronomical Society of the Pacific Conference Series, 179
Djorgovski, S. G., Stern, D., Mahabal, A. A., & Brunner, R. 2003, ApJ, 596, 67
Ellis, R., Santos, M. R., Kneib, J., & Kuijken, K. 2001, ApJ, 560, L119
Fan, X., Strauss, M. A., Schneider, D. P., et al. 2003, AJ, 125, 1649
Ferguson, H. C., Dickinson, M., Giavalisco, M., et al. 2004, ApJ, 600, L107
Ferrarese, L. & Merritt, D. 2000, ApJ, 539, L9
Ford, H. C., Bartko, F., Bely, P. Y., et al. 1998, in Proc. SPIE Vol. 3356, p. 234-248, Space Telescopes and Instruments V, Pierre Y. Bely; James B. Breckinridge; Eds., 234–248
Francis, P. J., Williger, G. M., Collins, N. R., et al. 2001, ApJ, 554, 1001
Gebhardt, K., Bender, R., Bower, G., et al. 2000, ApJ, 539, L13
Gehrels, N. 1986, ApJ, 303, 336
Giavalisco, M. & Dickinson, M. 2001, ApJ, 550, 177
Giavalisco, M., Dickinson, M., Ferguson, H. C., et al. 2004a, ApJ, 600, L103
Giavalisco, M., Ferguson, H. C., Koekemoer, A. M., et al. 2004b, ApJ, 600, L93
Giavalisco, M., Steidel, C. C., Adelberger, K. L., et al. 1998, ApJ, 503, 543
Hamana, T., Ouchi, M., Shimasaku, K., Kayo, I., & Suto, Y. 2004, MNRAS, 347, 813
Heckman, T. M., Armus, L., & Miley, G. K. 1990, ApJ, 74, 833
Holden, B. P., van der Wel, A., Franx, M., et al. 2005, ApJ, 620, L83
Kaiser, N. 1984, ApJ, 284, L9
Keel, W. C., Cohen, S. H., Windhorst, R. A., & Waddington, I. 1999, AJ, 118, 2547
Kinney, A. L., Calzetti, D., Bohlin, R. C., et al. 1996, ApJ, 467, 38
Klamer, I. J., Ekers, R. D., Sadler, E. M., et al. 2005, ApJ, 621, L1
Kron, R. G. 1980, ApJ, 43, 305
Kurk, J., Röttgering, H., Pentericci, L., Miley, G., & Overzier, R. 2003, New Astronomy Review, 47, 339
Lehnert, M. D. & Bremer, M. 2003, ApJ, 593, 630
Leitherer, C., Schaerer, D., Goldader, J. D., et al. 1999, ApJ, 123, 3
Möller, P. & Fynbo, J. U. 2001, A&A, 372, L57
Madau, P. 1995, ApJ, 441, 18
Madau, P., Ferguson, H. C., Dickinson, M. E., et al. 1996, MNRAS, 283, 1388
Madau, P., Pozzetti, L., & Dickinson, M. 1998, ApJ, 498, 106
Magorrian, J., Tremaine, S., Richstone, D., et al. 1998, AJ, 115, 2285
Miley, G. K., Overzier, R. A., Tsvetanov, Z. I., et al. 2004, Nature, 427, 47
Mullis, C. R., Rosati, P., Lamer, G., et al. 2005, ApJ, 623, L85
Neufeld, D. A. 1991, ApJ, 370, L85
Oke, J. B. 1971, ApJ, 170, 193
Ouchi, M., Shimasaku, K., Akiyama, M., et al. 2005, ApJ, 620, L1
Ouchi, M., Shimasaku, K., Okamura, S., et al. 2004a, ApJ, 611, 660
—. 2004b, ApJ, 611, 685
Papovich, C., Dickinson, M., & Ferguson, H. C. 2001, ApJ, 559, 620
Papovich, C., Dickinson, M., Ferguson, H. C., et al. 2004, ApJ, 600, L111
Pascarelle, S. M., Windhorst, R. A., Driver, S. P., Ostrander, E. J., & Keel, W. C. 1996, ApJ, 456, L21
Pentericci, L., Kurk, J. D., Röttgering, H. J. A., et al. 2000, A&A, 361, L25
Pentericci, L., McCarthy, P. J., Röttgering, H. J. A., et al. 2001, ApJ, 135, 63
Porciani, C. & Giavalisco, M. 2002, ApJ, 565, 24
Postman, M., et al. 2005, ApJ, 623, 721
Rawlings, S., Lacy, M., Blundell, K. M., et al. 1996, Nature, 383, 502
Rees, M. J. 1989, MNRAS, 239, 1
Reuland, M., van Breugel, W., Röttgering, H., et al. 2003, ApJ, 592, 755
Sánchez, S. F. & González-Serrano, J. I. 2002, A&A, 396, 773
Schlegel, D. J., Finkbeiner, D. P., & Davis, M. 1998, ApJ, 500, 525
Shapley, A. E., Steidel, C. C., Pettini, M., & Adelberger, K. L. 2003, ApJ, 588, 65
Sheth, R. K. & Tormen, G. 1999, MNRAS, 308, 119
Shimasaku, K., Ouchi, M., Okamura, S., et al. 2003, ApJ, 586,

L111
Sirianni, M., et al. 2005, PASP, 117, 1049
Somerville, R. S., Lee, K., Ferguson, H. C., et al. 2004, ApJ, 600, L171
Spergel, D. N., Verde, L., Peiris, H. V., et al. 2003, ApJ, 148, 175
Springel, V., White, S. D. M., Jenkins, A., et al. 2005, Nature, 435, 629
Stanford, S. A., Eisenhardt, P. R., & Dickinson, M. 1998, ApJ, 492, 461
Steidel, C. C., Adelberger, K. L., Dickinson, M., et al. 1998, ApJ, 492, 428
Steidel, C. C., Adelberger, K. L., Giavalisco, M., Dickinson, M., & Pettini, M. 1999, ApJ, 519, 1
Steidel, C. C., Adelberger, K. L., Shapley, A. E., Erb, D. K., Reddy, N. A., & Pettini, M. 2005, ApJ, 626, 44
Steidel, C. C., Adelberger, K. L., Shapley, A. E., et al. 2000, ApJ, 532, 170
van Breugel, W., De Breuck, C., Stanford, S. A., et al. 1999, ApJ, 518, L61
Venemans, B. P., Kurk, J. D., Miley, G. K., et al. 2002, ApJ, 569, L11
Venemans, B. P., Röttgering, H. J. A., Miley, G. K., et al. 2005, A&A, 431, 793
Venemans, B. P., Röttgering, H., Overzier, R., et al. 2004, A&A, 424, L17
Wang, J. X., Rhoads, J. E., Malhotra, S., et al. 2004, ApJ, 608, L21
Wuyts, S., van Dokkum, P. G., Kelson, D. D., Franx, M., & Illingworth, G. D. 2004, ApJ, 605, 677
Zirm, A., Overzier, R., Miley, G., et al. 2005, ApJ, 630, In press
Zirm, A. W., Dickinson, M., & Dey, A. 2003, ApJ, 585, 90

Chapter 8

Clustering of i_{775} dropout galaxies at $z \sim 6$ in GOODS and the UDF

Abstract. We measured the angular clustering among a sample of 506 i_{775} dropout galaxies obtained from deep ACS fields to study clustering at $z \sim 6$. For our largest and most complete subsample ($L \gtrsim 0.5L^*_{z=6}$), we detected clustering at $\sim 94\%$ significance. We derive a (co-moving) spatial correlation length of $r_0 = 3.6^{+1.7}_{-2.5}\ h_{72}^{-1}$ Mpc and bias $b = 3.6^{+1.3}_{-2.2}$, using an accurate model for the redshift distribution. No clustering could be detected in the much deeper but significantly smaller UDF sample. We compare our findings to Lyman break galaxies at $z \sim 3-5$ at a fixed luminosity. Our best estimate of the bias parameter implies that i_{775} dropouts are hosted by dark matter halos having masses of $\sim 10^{11}\ M_\odot$, consistent with the typical mass of halos hosting V_{606} dropouts at $z \sim 5$. We evaluate a recent claim by Lee et al. (2005) that at $z \gtrsim 5$ star formation might have occurred more efficiently compared to that at $z = 3-4$. This may provide an explanation for the very mild evolution observed in the rest frame UV luminosity density between $z = 6$ and 3. Although our results are consistent with the star formation efficiency also being higher at $z \sim 6$, our errors are too large to find conclusive evidence for this.

R. A. Overzier, R. J. Bouwens, G. D. Illingworth & M. Franx
Submitted to *The Astrophysical Journal Letters*

8.1 Introduction

The Advanced Camera for Surveys (ACS, Ford et al. 1998) aboard the *Hubble Space Telescope* has made the detection of star-forming galaxies at $z \sim 6$ (i_{775} dropouts) relatively easy. The largest sample of i_{775} dropouts currently available (Bouwens et al. 2006) comes from the Great Observatories Origins Deep Survey (GOODS, Giavalisco et al. 2004), allowing the first quantitative analysis of galaxies only 0.9 Gyr after recombination[1] (Stanway et al. 2003; Bouwens et al. 2003; Yan & Windhorst 2004; Dickinson et al. 2004; Malhotra et al. 2005,see also Shimasaku et al. 2005; Ouchi et al. 2005). Bouwens et al. (2006) found evidence for strong evolution of the luminosity function between $z \sim 6$ and 3, while the (unextincted) luminosity density at $z \sim 6$ is only $\sim 0.8\times$ lower than that at $z \sim 3$. Some i_{775} dropouts have significant Balmer breaks, indicative of stellar populations of >100 Myr in age and masses comparable to those of present-day L^* galaxies (Eyles et al. 2005; Yan et al. 2005). These i_{775} dropouts may end up as relatively red galaxies at $z = 2 - 4$ (Franx et al. 2003).

Through the study of the clustering we can address fundamental cosmological issues that cannot be answered from the study of galaxy light alone. The strength of clustering and its evolution with redshift relates to the bias of galaxies, relative to the underlying dark matter. The two-point angular correlation function (ACF) has been used to measure the clustering of Lyman break galaxies (LBGs) at $z = 3 - 5$ (e.g. Adelberger et al. 1998; Arnouts et al. 1999; Magliocchetti & Maddox 1999; Giavalisco & Dickinson 2001; Ouchi et al. 2001; Arnouts et al. 2002; Porciani & Giavalisco 2002; Ouchi et al. 2004; Adelberger et al. 2005; Hildebrandt et al. 2005; Allen et al. 2005; Kashikawa et al. 2006). These studies have found that LBGs are highly biased with respect to the dark matter ($b \simeq 2 - 8$), and that this biasing depends strongly on rest frame UV luminosity, as well as, to a lesser extent, on dust and redshift. Recently, using both wide and deep surveys, the clustering statistics of LBGs have reached the level of sophistication at which one can measure two physically different contributions. At small angular scales the ACF is dominated by the highly non-linear clustering of galaxies within single dark matter halos, whereas at large scales its amplitude tends to the 'classical' clustering of galaxies residing in different halos (Ouchi et al. 2005a; Lee et al. 2005), as explained by the framework of the halo occupation distribution (e.g. Zehavi et al. 2004; Hamana et al. 2004). A detailed understanding of the clustering properties of galaxies at $z \sim 6$ is also important for the interpretation of overdensities recently observed towards luminous $z \sim 6$ quasars and in the field (Ouchi et al. 2005; Stiavelli et al. 2005; Wang et al. 2005; Zheng et al. 2006). These overdensities may demarcate structures that preceeded the present-day massive galaxies and clusters (Springel et al. 2005). Our aim here is to 'complete' the census of clustering to $z \sim 6$ as follows. In Sections 2 and 3 we describe the sample, and present our measurements of the ACF. In Section 4 we derive cosmological quantities, and discuss our findings.

[1] Throughout this letter we use a cosmology [Ω_M, Ω_Λ, h_{72}, n, σ_8]=[0.27,0.73,1.0,1.0,0.9] with $H_0 = 72\,h_{72}$ km s^{-1} Mpc^{-1}.

8.2 Data

The present analysis is based on the sample of i_{775} dropouts described in detail by Bouwens et al. (2006). We used the ACS data from the GOODS v1.0 release, which was processed together with a substantial amount of overlapping pointings that have since become available, i.e., the Ultra Deep Field (UDF) parallel fields (Thompson et al. 2005), Galaxy Evolution from Morphology and Spectral energy distributions (GEMS; Rix et al. 2004), and supernovae search data (Riess et al., Perlmutter et al., in preparation), using 'Apsis' (Blakeslee et al. 2003). The 10σ detection limit was 27.5 in z_{850} in a $0\farcs2$ diameter aperture. We also used a deep sample of i_{775} dropouts selected from the UDF (Beckwith et al., in preparation), which had a 10σ detection limit of 29.2. The final areas are listed in Table 8.1. The i_{775}-dropout distribution in the GOODS fields is shown in Fig. 8.1.

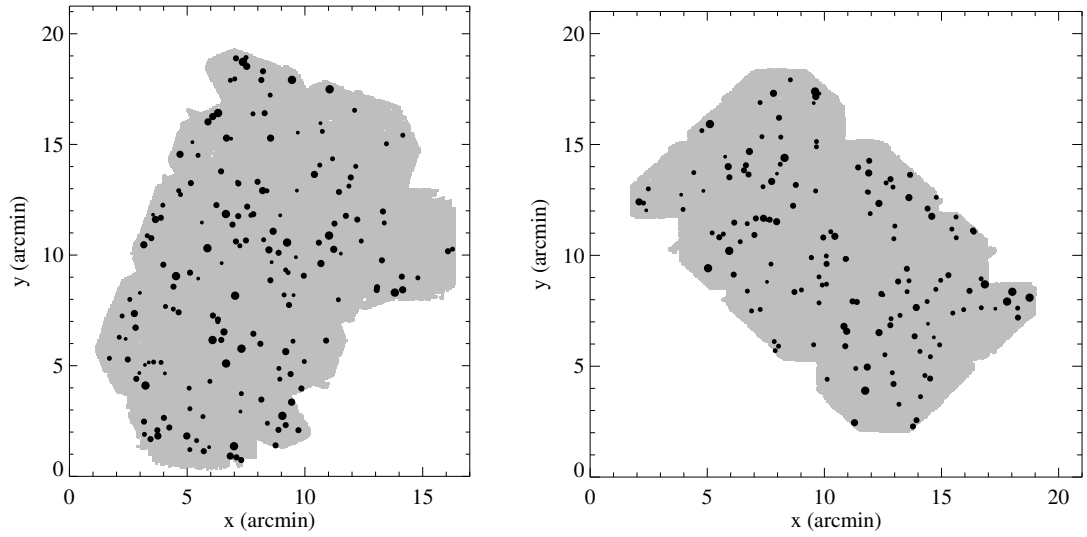

Figure 8.1 — The distributions of i_{775}-dropouts in the GOODS CDFS (left panel) and HDFN (right panel) fields.

Objects were selected by requiring (i_{775}–z_{850})>1.3, and (V_{606}–z_{850})>2.8 or non-detections (<2σ) in V_{606} to exclude lower redshift interlopers. Point sources were removed based on high stellarity parameters >0.75. The estimated remaining contamination due to photometric scatter, red interlopers, and stars is ∼7% to z_{850}=28.0, of which 2% is due to stars (see Bouwens et al. (2006) for details). The effective redshift distributions for GOODS and the UDF are shown in Fig. 8.2. The effective rest frame UV luminosity of the sample is $L \approx 0.5L^*_{z=6}$ for z_{850}∼27.5 (Bouwens et al. 2006). Note that the luminosity is quite sensitive to redshift due to forest attenuation entering z_{850} at $z > 6$, with $L^*_{z=6}$ corresponding to z_{850}∼26.5 (∼28) at $z = 5.5$ ($z = 6.5$).

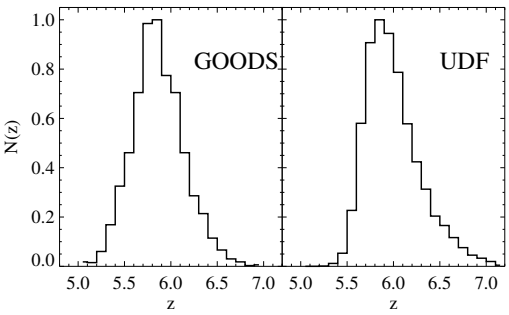

Figure 8.2 — The redshift distributions of i_{775} dropouts in our GOODS (left panel) and UDF (right panel) selections (estimated by projecting a complete UDF B_{435} dropout sample scaled to the sizes and colors as found for the i_{775} dropout sample to $z \sim 5-7$, see Bouwens et al. (2006) for details). As a result of a more significant photometric scatter in (i_{775}–z_{850}), the selection extends to lower redshifts in GOODS than it does for the UDF.

8.3 The angular correlation function

We measured the ACF, $w(\theta)$, defined as the excess probability of finding two sources in the solid angles $\delta\Omega_1$ and $\delta\Omega_2$ separated by the angle θ, over that expected for a random Poissonian distribution (Peebles 1980). We used the estimator $w(\theta) = [DD(\theta) - 2DR(\theta) + RR(\theta)]/RR(\theta)$ of Landy & Szalay (1993), where $DD(\theta)$, $DR(\theta)$ and $RR(\theta)$ are the number of pairs of sources with angular separations between θ and $\theta+\Delta\theta$ measured in the data, random, and data-random cross catalogs, respectively. We used 16 random catalogs containing ∼100× more sources than the data catalog of

similar angular geometry. Errors on $w(\theta)$ were bootstrapped (Ling et al. 1986). We assumed a power-law ACF of the form $w(\theta)=A_w\theta^{-\beta}$ and determined its amplitude, A_w, by fitting the function $w(\theta)=A_w\theta^{-\beta}-IC$. The integral constraint ($IC=\int\int w(\theta)d\Omega_1 d\Omega_2/\Omega^2$, where Ω is the survey area) was $0.033A_w$ for GOODS, and $0.074A_w$ for the UDF. We did not attempt to fit the slope of the ACF and assumed $\beta = 0.6$ based on the results of Lee et al. (2005). The ACF was fitted over the range 10″–300″ (10″–200″ for the UDF), corresponding to roughly 0.4–10 h_{72}^{-1} Mpc comoving at $z \sim 6$. The lower value of 10″ is larger than the virial radius of a 10^{12} $M_\odot$ halo to ensure that we are measuring the large-scale clustering (and not receiving a contribution at small scales from the sub-halo component). Because the results of the fits are sensitive to the size of the bins used, we determined the amplitude and its error from Monte Carlo simulations. Each datapoint was randomly varied according to a normal distribution with standard deviation equal to its bootstrap error, and the bin size was varied within the range 5″–50″. The final amplitude and the error are the mean and standard deviations among the fits that had $A_w > 0$. We note that if the 7% of contamination in the sample has a uniform distribution, the measured amplitude should be multiplied by ∼1.16 to yield the corrected clustering amplitude.

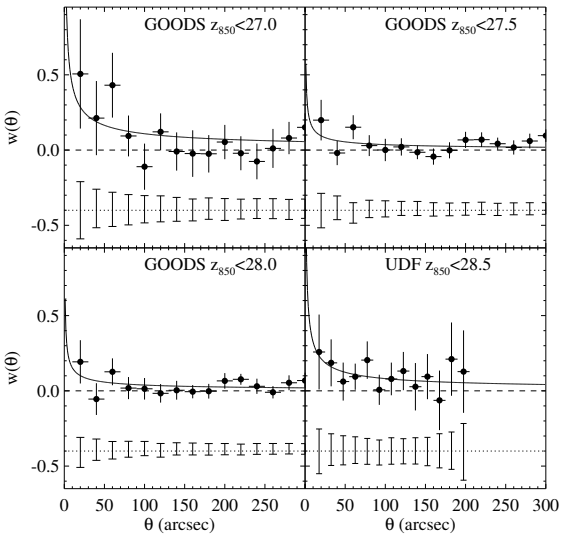

Figure 8.3 — The ACF of i_{775} dropouts from GOODS and the UDF. Points indicate the measurements corrected using the integral constraint for GOODS with z_{850}<27 (top left), z_{850}<27.5 (top right) and z_{850}<28 (bottom left), and for the UDF with z_{850}<28.5 (bottom right). Errors (1σ) were bootstrapped. The best-fit power-laws were obtained through Monte Carlo simulations of the measurements at $\theta > 10''$ (lines). The mean and standard deviations among 1000 Poissonian distributions are indicated by the empty error bars, offset by –0.4 in the vertical direction for clarity. In the UDF, the measurements become very uncertain at $\theta \gtrsim 200''$ since we are reaching the approximate angular extent of that field.

8.3.1 Results from GOODS

Fig. 8.3 shows the ACF in GOODS for various limiting z_{850}-magnitudes. The fit results are given in Table 8.1. A positive signal was measured out to $\theta \sim 50'' - 100''$, most notably among the 172 i_{775} dropouts in the z_{850}<27.0 sample, which had a best-fit amplitude of $A_w = 1.7 \pm 1.2$. For the fainter samples we found $A_w \approx 0.6 \pm 0.5$. Because the objects were selected from data of uniform depth, any signal in the ACF is unlikely to be caused by instrumental variations in the object surface density. Given the large errors on A_w, it is useful to ask whether the $w(\theta)$ observed at $\theta \lesssim 1'$ could be the result of shot noise in a random object distribution. We created 1000 random distributions with the same geometry and the same number of points as our data, and calculated the ACF in each of the random samples. The mean and standard deviation at each θ is plotted in Fig. 8.3 (offset by –0.4). We calculate the chance of reproducing the observed clustering in the random realizations, using the average $w(\theta)$ measured over the first four bins ($\theta < 100''$) as a gauge of this clustering. We find a chance of 0.1% for the z_{850}<27.0 sample. The random occurrences are respectively 6% and 11% for the fainter samples.

Another test of the measured clustering was as follows. We used the formalism of Soneira & Peebles (1978) to create mock samples with a choice ACF in two dimensions. A $250' \times 250'$ mock field with similar surface density

as the i_{775} dropouts allowed us to mimick the measured A_w to an accuracy of 98%, determined from a fit. Next, we randomly extracted 100 mock 'GOODS' surveys and measured the mean $w(\theta)$ and its standard deviation using identical binning and fitting as for the real sample. Fig. 8.4 demonstrates that the amplitude of the observed $w(\theta)$ at $\theta \lesssim 1'$ lies within $\lesssim 1\sigma$ of the expected amplitudes for our model ACF, but also illustrates the large scatter in the extracted amplitudes due to the small sample size (shaded region in Fig. 8.4).

In the above analysis we restricted ourselves to clustering at $\theta \geq 10''$. Our measurements also showed an excess of pair counts at $\theta < 10''$. Upon closer inspection it was found that the excess was strictly limited to $\theta < 5''$, with $w(2\farcs5) \sim 2.0 \pm 0.9$. The excess is consistent with an enhancement of $w(\theta)$ due to sub-halo clustering (Ouchi et al. 2005; Lee et al. 2005) to 1.7σ confidence, but the exact amplitude cannot be determined accurately due to the small number of pairs (11 pairs at $z_{850} < 28.0$). A similar small-scale excess was found by Shimasaku et al. (2006) in the distribution of Lyα emitters at $z = 5.7$.

8.3.2 Results from the UDF

The analysis is hampered by the relatively small number of sources available, owing to its $\sim 30\times$ smaller area compared to GOODS, although its greater depth (1.5 mag) partially makes up for this lack of area. Fig. 8.3 (bottom right) shows the ACF obtained from the 52 i_{775} dropouts in our $z_{850} < 28.5$ UDF sample. The best-fit amplitude is $A_w = 1.3 \pm 1.2$. The $z_{850} < 29.0$ sample containing 95 objects gave a best-fit $A_w = 0.3 \pm 0.5$. As with GOODS, we created 1000 random 'UDF' fields to measure the effect of shot noise. The results are indicated again in the bottom right panel of Fig. 8.3. In about 13% of the random fields, $w(\theta)$ was equal to or greater than the $w(\theta)$ measured at $\theta < 1'$. The relatively large error and the small amplitude of our faintest UDF sample is likely the result of the small sample size and the strong luminosity dependence of clustering observed at lower redshifts (e.g. Kashikawa et al. 2006).

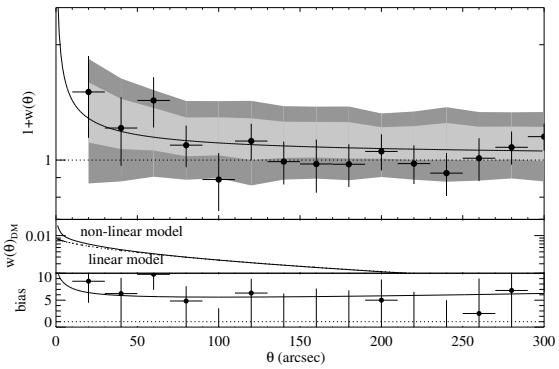

Figure 8.4 — The ACF and bias for the $z_{850} < 27$ sample. The top panel shows the clustering measurements (points), and the best-fit $w(\theta)$ (solid line). The shaded region indicates the range found among 100 mock samples extracted from a $250' \times 250'$ field with a built-in clustering amplitude as measured for the $z_{850} < 27$ sample at 1σ (light grey) and 2σ (dark grey). The middle panel shows the non-linear clustering of dark matter (Peacock & Dodds 1996), where the linear case has been indicated to illustrate the additional power at small θ in the non-linear model. The redshift distribution of Fig. 8.2 was used for Limber inversion of the dark matter clustering. The bottom panel shows the bias as a function of θ (points) and the bias for the best-fit ACF (solid line).

8.4 Derivation of cosmological quantities

While the uncertainties are large, our measurements can nevertheless be used to estimate the spatial correlation length, r_0, and bias, b, given the redshift selection functions (Fig. 8.2). We used the cosmological Limber equation adopted for our cosmology to invert A_w to obtain r_0 (Table 8.1). The clustering was assumed to be fixed in comoving coordinates across the redshift selection window. We found $r_0 \sim 4 \pm 2\, h_{72}^{-1}$ Mpc for the $z_{850} < 27.5$ and $z_{850} < 28$ samples. At $z_{850} < 27$, the best-fit value was $r_0 = 7.2^{+2.8}_{-3.7}\, h_{72}^{-1}$ Mpc, consistent with the fainter subsamples within the errors. These correlation lengths increase by ~ 10 percent if we apply the contamination correction derived in Section 3. Also, it is important to realise that except for the brightest sample, the samples are not independent. Therefore, if the brightest subsample is more strongly clustered, then the fainter samples must be more weakly clustered to yield the measured r_0.

We calculated the galaxy-dark matter bias, defined as $b(\theta) \equiv \sqrt{w(\theta)/w_{dm}(\theta)}$, where $w_{dm}(\theta)$ is the ACF of the dark matter as 'seen' through our redshift selection window. $w_{dm}(\theta)$ was calculated using the non-linear fitting function of Peacock & Dodds (1996) (middle panel of Fig. 8.4). In the bottom panel of Fig. 8.4 we have indicated the bias as a function of θ (points). Our best-fit ACF implies $b(\theta{\sim}30'')=6.2^{+1.8}_{-2.7}$ (solid line), with $b{\sim}4-5$ for the fainter samples. Applying the contamination correction yields values that are ∼5 percent higher.

It is important to evaluate how our results might be influenced by cosmic variance. For GOODS we estimate $\sigma_v{\sim}0.1$–0.2, while $\sigma_v{\sim}0.5$ for the UDF (σ_v being the square root of the cosmic variance), assuming a one-to-one correspondence between dark halos and galaxies as in Somerville et al. (2004). This shows that the GOODS i_{775} dropout sample is likely to be a fairly representative sample, while the UDF results may suffer significantly from the relatively small effective volume. For the UDF, the uncertainty on r_0 due to cosmic variance is likely of similar order of magnitude as the uncertainty in our current measurements. The small cosmic variance derived for GOODS indicates that for these fields, our results are dominated by the uncertainty in the measurements alone. While it is possible that the positive signal out to $\sim 1'$ is the result of strong sub-halo clustering (see Lee et al. 2005; Ouchi et al. 2005), the occurrence of such halos becomes increasingly rare with redshift and by limiting the fits to $\theta \gtrsim 10''$ we have suppressed the dominant contribution from sub-halo clustering.

We can directly compare our results to measurements performed by Lee et al. (2005) who found $b{\sim}3.3{\pm}0.5$ for faint V_{606} dropouts ($z \sim 5$) also from GOODS. At $z_{850}{\sim}27.5$ we probe approximately the same rest frame luminosity ($M_z \lesssim -19.5$) as their faintest (i.e. $z_{850}{\leq}27$) V_{606} dropout sample. To this limit, we measure a bias of $b = 3.6^{+1.3}_{-2.2}$, which suggests an average halo mass in the (1σ) range $\sim 1 \times 10^{10} - 3 \times 10^{11}$ $M_\odot$, assuming that the bias of the i_{775} dropouts corresponds to that of dark halos more massive than the average halo hosting them (Sheth & Tormen 1999). This range is similar to the average halo mass of V_{606} dropouts. Interestingly, Lee et al. (2005) found that at slightly higher rest frame luminosities ($M_z \lesssim -20$), the clustering of V_{606} dropouts is incompatible with that of U and B_{435} dropouts at $z = 3-4$, for which much stronger clustering is found and correspondingly a $\sim 10\times$ larger halo mass ($\sim 10^{12}$ $M_\odot$) is inferred, as shown in Fig. 8.5. Can we confirm this result using our brightest ($M_z \lesssim -20$) GOODS sample? The bias for this sample implies halo masses in the range $M \sim 5 \times 10^{10} - 2 \times 10^{12}$ $M_\odot$. Although our best values for r_0 and b are almost twice as high as for our fainter sample, the difference cannot be regarded as statistically significant. Focusing instead on the $z_{850}{<}$ 27.5 sample (which is our best estimate of the clustering of i_{775} dropouts given the large sample size and large relative completeness), the inferred halo mass is lower than that at $z = 4$ only at $\sim 1\sigma$ significance, owing to the relatively large error

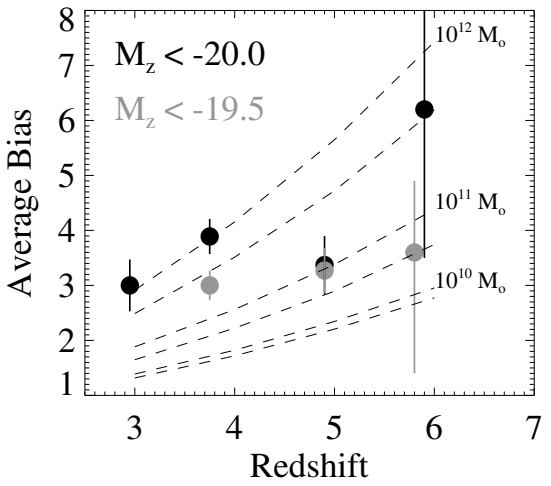

Figure 8.5 — Bias parameters of U, B_{435}, and V_{606}-dropouts as measured by Lee et al. (2005), compared to the bias estimated for the i_{775}-dropouts. Our best estimate for the halo mass at $z \sim 6$ is $\sim 10^{11}$ $M_\odot$, albeit with large errors. The estimate of the halo mass of the brightest ($M_z < -20$) V_{606}-dropouts at $z = 5$ is $\sim 10\times$ lower than that of B_{435}-dropouts at $z = 4$, but the errors at $z \sim 6$ are too large to conclude that this is generally true for luminous star-forming galaxies at $z \simeq 5-6$.

Table 8.1 — ACF and related physical quantities.

Sample	Area (arcmin^2)	N	A_w	r_0 (h_{72}^{-1} Mpc)	$b(30'')$
enhanced GOODS data					
<27.0	$320^\dagger$	172	1.72 ± 1.17	$7.2^{+2.8}_{-3.7}$	$6.2^{+1.8}_{-2.7}$
<27.5	$320^\dagger$	293	0.57 ± 0.49	$3.6^{+1.7}_{-2.5}$	$3.6^{+1.3}_{-2.2}$
<28.0	$320^\dagger$	331	0.61 ± 0.41	$3.8^{+1.4}_{-1.9}$	$3.7^{+1.1}_{-1.6}$
UDF data					
<28.5	$11^\dagger$	52	1.29 ± 1.22	$5.9^{+3.0}_{-4.9}$	$5.4^{+2.1}_{-4.1}$
<29.0	$11^\dagger$	95	0.29 ± 0.47	< 4.2	< 4.1

† Approximate areal coverage with the 10σ detection limit.

as well as to the fact that the decrease in the effective halo mass from $z = 4$ to 5 at these luminosities is not as dramatic as observed at luminosities of $M_z \lesssim -20$.

Lee et al. (2005) argued that star formation may have occurred more efficiently at higher redshifts ($z \sim 5$) than it did at $z \sim 3-4$, given that objects of comparable luminosity are found in less massive halos at $z \sim 5$. If this is true (and can be confirmed for galaxies at $z \gtrsim 6$), it would largely offset changes that are occurring in the mass function over this range. As such, this may provide at least a partial explanation for the mild evolution in the luminosity density from $z = 6$ to 3 (Bouwens et al. 2006).

In conclusion, we used the largest available sample of i_{775} dropouts to study clustering at $z \sim 6$. We found a small signal, although its amplitude is not well constrained due to the large errors on the individual datapoints. The present analysis is reminiscent of that performed at $z \sim 3-5$ based on the original Hubble Deep Fields. The clustering of galaxies at $z \sim 6$ will continue to be studied from large samples of relatively bright LBGs, as well as Lyα emitters selected using groundbased surveys of deep and wide fields (see e.g., Shimasaku et al. 2005, 2006). Although it might become possible in the near future to increase our sample size by a factor of $\sim 2-3$ by relaxing our current i_{775} dropout detection threshold, to perform an analysis at the same level of detail as currently performed at $z \sim 5$ would require another six GOODS fields, for $\sim$1200 arcmin^2 in total.

Acknowledgments

RAO is grateful for helpful discussions with Peter Katgert and Huub Röttgering, and the referee, Masami Ouchi, for his many good suggestions. ACS was developed under NASA contract NAS 5-32865, and this research has been supported by NASA grant NAG5-7697.

References

Adelberger, K. L., Steidel, C. C., Giavalisco, M., Dickinson, M., Pettini, M., & Kellogg, M. 1998, ApJ, 505, 18
Adelberger, K. L., Steidel, C. C., Pettini, M., Shapley, A. E., Reddy, N. A., & Erb, D. K. 2005, ApJ, 619, 697
Allen, P. D., Moustakas, L. A., Dalton, G., MacDonald, E., Blake, C., Clewley, L., Heymans, C., & Wegner, G. 2005, MNRAS, 360, 1244
Arnouts, S., Cristiani, S., Moscardini, L., Matarrese, S., Lucchin, F., Fontana, A., & Giallongo, E. 1999, MNRAS, 310, 540
Arnouts, S. et al. 2002, MNRAS, 329, 355
Blakeslee, J. P., Anderson, K. R., Meurer, G. R., Benítez, N., & Magee, D. 2003, in ASP Conf. Ser. 295: Astronomical Data Analysis Software and Systems XII, 257
Bouwens, R., Broadhurst, T., & Illingworth, G. 2003, ApJ, 593, 640
Bouwens, R. J., Illingworth, G. D., Blakeslee, J. P., & Franx, M. 2006, ApJ, In Press (astro-ph/0509641)
Dickinson, M. et al. 2004, ApJ, 600, L99
Eyles, L. P., Bunker, A. J., Stanway, E. R., Lacy, M., Ellis, R. S., & Doherty, M. 2005, MNRAS, 364, 443
Ford, H. C. et al. 1998, in Proc. SPIE Vol. 3356, p. 234-248, Space Telescopes and Instruments V, Pierre Y. Bely; James B. Breckinridge; Eds., 234–248

Franx, M., et al. 2003, ApJ, 587, L79
Giavalisco, M., & Dickinson, M. 2001, ApJ, 550, 177
Giavalisco, M. et al. 2004, ApJ, 600, L93
Hamana, T., Ouchi, M., Shimasaku, K., Kayo, I., & Suto, Y. 2004, MNRAS, 347, 813
Hildebrandt, H. et al. 2005, A&A, 441, 905
Kashikawa, N. et al. 2006, ApJ, 637, 631
Landy, S. D., & Szalay, A. S. 1993, ApJ, 412, 64
Lee, K.-S., Giavalisco, M., Gnedin, O., Somerville, R., Ferguson, H., Dickinson, M. E., & Ouchi, M. 2006, ApJ, In Press (astro-ph/0508090)
Ling, E. N., Barrow, J. D., & Frenk, C. S. 1986, MNRAS, 223, 21P
Magliocchetti, M., & Maddox, S. J. 1999, MNRAS, 306, 988
Malhotra, S., et al. 2005, ApJ, 626, 666
Ouchi, M., et al. 2001, ApJ, 558, L83
Ouchi, M. et al. 2005a, ApJ, 635, L117
—. 2005b, ApJ, 620, L1
—. 2004, ApJ, 611, 685
Peacock, J. A., & Dodds, S. J. 1996, MNRAS, 280, L19
Peebles, P. J. E. 1980, The large-scale structure of the universe (Princeton University Press, 1980. 435 p.)
Porciani, C., & Giavalisco, M. 2002, ApJ, 565, 24
Rix, H.-W. et al. 2004, ApJ, 152, 163
Sheth, R. K., & Tormen, G. 1999, MNRAS, 308, 119
Shimasaku, K., Ouchi, M., Furusawa, H., Yoshida, M., Kashikawa, N., & Okamura, S. 2005, PASJ, 57, 447
Shimasaku, K. et al. 2006, PASJ, In Press (astro-ph/0602614)
Somerville, R. S., Lee, K., Ferguson, H. C., Gardner, J. P., Moustakas, L. A., & Giavalisco, M. 2004, ApJ, 600, L171
Soneira, R. M., & Peebles, P. J. E. 1978, AJ, 83, 845
Springel, V. et al. 2005, Nature, 435, 629
Stanway, E. R., Bunker, A. J., & McMahon, R. G. 2003, MNRAS, 342, 439
Stiavelli, M. et al. 2005, ApJ, 622, L1
Thompson, R. I. et al. 2005, AJ, 130, 1
Wang, J. X., Malhotra, S., & Rhoads, J. E. 2005, ApJ, 622, L77
Yan, H. et al. 2005, ApJ, 634, 109
Yan, H., & Windhorst, R. A. 2004, ApJ, 612, L93
Zehavi, I. et al. 2004, ApJ, 608, 16
Zheng, W. et al. 2006, ApJ, 640, 574

Chapter 9

An overdensity of galaxies near the most distant radio-loud quasar

Abstract. A 5 arcmin^2 region around the luminous radio-loud quasar SDSS J0836+0054 ($z = 5.8$) hosts a wealth of associated galaxies, characterized by very red ($1.3 < i_{775} - z_{850} < 2.0$) color. The surface density of these $z \sim 5.8$ candidates is approximately 6 times higher than the number expected from deep ACS fields. This is one of the highest galaxy overdensities at high redshifts, which may develop into a group or cluster. We also find evidence for a substructure associated with one of the candidates. It has two very faint companion objects within $2''$, which are likely to merge. The finding supports the results of a recent simulation, which finds that luminous quasars at high redshifts lie on the most prominent dark-matter filaments and are surrounded by many fainter galaxies. The quasar activity from these regions may signal the buildup of a massive system.

W. Zheng, R. A. Overzier, R. J. Bouwens, R. L. White, H. C. Ford, N. Benítez, J. P. Blakeslee, L. D. Bradley, M. K. Jee, A. R. Martel, S. Mei, A. W. Zirm, G. D. Illingworth, M. Clampin, G. F. Hartig, D. R. Ardila, F. Bartko, T. J. Broadhurst, R. A. Brown, C. J. Burrows, E. S. Cheng, N. J. G. Cross, R. Demarco, P. D. Feldman, M. Franx, D. A. Golimowski, T. Goto, C. Gronwall, B. Holden, N. Homeier, L. Infante, R. A. Kimble, J. E. Krist, M. P. Lesser, F. Menanteau, G. R. Meurer, G. K. Miley, V. Motta, M. Postman, P. Rosati, M. Sirianni, W. B. Sparks, H. D. Tran & Z. I. Tsvetanov

The Astrophysical Journal, **640**, 574 (2006)

9.1 Introduction

The fluctuations in the cosmic microwave background temperature observed by the Wilkinson Microwave Anisotropy Probe (WMAP; Bennett et al. 2003) are believed to be the seeds for the first generation of baryonic objects, which eventually evolved into the stars, galaxies, and clusters seen in the current epoch. Several hundred galaxy candidates at $z \gtrsim 6$ have been found as i_{775}-dropout objects (Stanway et al. 2003; Yan & Windhorst 2004; Bouwens et al. 2003, 2005), characterized by a large color difference between the i_{775}- and z_{850}-band and faint magnitudes of approximately 26. The current best estimate of the average surface density of these galaxies is from the Great Observatories Origins Deep Survey (GOODS; Giavalisco et al. 2004), approximately 0.25 arcmin^{-2} to a z_{850}-band magnitude of 26.5 (Dickinson et al. 2004; Bouwens et al. 2005). In addition, at least a dozen of quasars have also been discovered at redshift $z \gtrsim 5.7$ (Fan et al. 2004), and their high luminosities suggest the presence of massive black holes of mass $> 10^9\ M_\odot$. The formation of such black holes at epochs less than one billion years after the big bang requires an extremely high accretion rate (Haiman & Loeb 2001).

According to the hierarchical model of galaxy formation (Press & Schechter 1974), massive baryonic objects are formed in the densest halos. The latest simulations of CDM growth (Springel et al. 2005) predict that $z \sim 6$ quasars may lie in the center of very massive dark matter halos of $\sim 4 \times 10^{12}$ M$_\odot$, which will grow into the most massive clusters of $\sim 4 \times 10^{15}$ M$_\odot$ at $z = 0$. Studying the clustering properties of young galaxies and quasars may provide insights into their formation history. Reports of clustering of galaxies at redshift $z \sim 6$ (Ouchi et al. 2005; Wang et al. 2005; Malhotra et al. 2005) suggest that the formation of large structures in the early universe may be more significant than the cold dark matter (CDM) models have predicted. Recently Stiavelli et al. (2005) reported that one of the most distant quasars, SDSS J1030+0524 at $z = 6.28$, exhibits an excess of associated galaxies. It has also been found that some radio galaxies harbor an enhanced number of associated galaxies. Venemans et al. (2002) and Miley et al. (2004) found a potential protocluster around TN J1338–1942, a radio galaxy at $z = 4.1$. Venemans et al. (2004) and Overzier et al. (2005) observed an excess of Lyα emitters (LAEs) and Lyman break galaxies (LBGs) in the field of TN J0924–2201, the most distant radio galaxy at $z = 5.2$. These reports confirm an empirical result that powerful, high-redshift radio galaxies are associated with massive forming galaxies (van Breugel et al. 1999). To explore the possibility that radio-loud quasars may also be a signpost of galaxy clustering at high redshifts, we initiated a project with the *Hubble Space Telescope (HST)* Advanced Camera for Surveys (ACS) to image the fields around some of the most distant radio-loud quasars.

The quasar SDSS J0836+0054 ($z = 5.82$; Fan et al. 2001) is the most distant radio-loud quasar known to date and is one of the most luminous. The object is detected in the Faint Images of the Radio Sky at 20 cm (FIRST) radio survey, with a total flux density at 1.4 GHz of 1.11 mJy. Very Large Array (VLA) and Max Planck Millimeter Bolometer Array (MPMBA)-IRAM observations (Petric et al. 2003) yield flux densities of 1.75 mJy at 1.4 GHz, 0.58 mJy at 5 GHz, and a non-detection at 250 GHz, with a 3σ upper limit of 2.9 mJy. It is a compact steep-spectrum radio source with a radio spectral index of -0.8. VLBI observations at ~ 10 mas angular resolution (Frey et al. 2003) show an apparent core-jet morphology, with no indication of multiple images produced by gravitational lensing. The quasar's enormous power at $M \sim -27.8$ in the rest-frame UV band implies a mass of the central black hole of 5×10^9 M$_\odot$, posing a challenge to the theoretical models on how such massive objects are formed in the very early universe.

Throughout the paper, we use AB magnitudes and assume the common values of cosmological parameters, $\Omega_m = 0.3$, $\Omega_\lambda = 0.7$, and H_0 = 70 km s^{-1} Mpc^{-1}.

Figure 9.1 — Composite *HST* ACS image of the field of the quasar SDSS J0836+0054. The quasar (Q) and the i_{775}-dropout candidates (A–G) are marked with open circles. The scale bar measures 50″ ($\sim$ 300 kpc of proper distance).

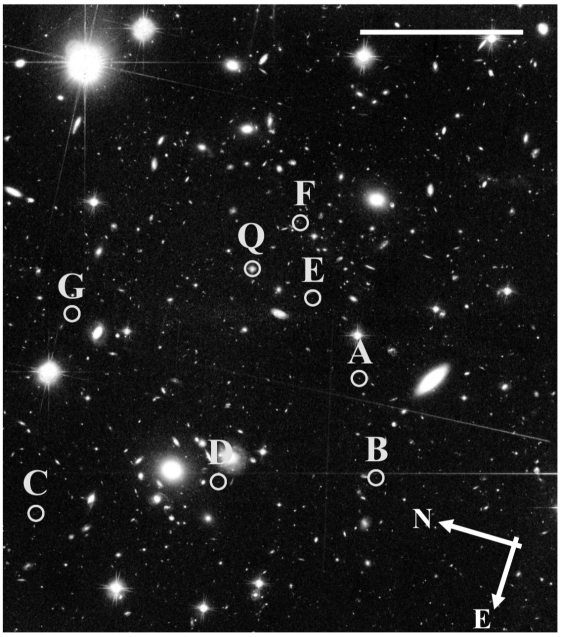

9.2 Data

The *HST* ACS observations of SDSS J0836+0054 were carried out on 2004 October 8 and November 17, with a total exposure of 10,778 s in the z_{850}-band and 4676 s in the i_{775}-band, at two different position angles. They were processed with the standard pipeline CALACS (Pavlovsky et al. 2005), then with APSIS (Blakeslee et al. 2003). These procedures carried out flat-fielding, removing bias, dark current, and cosmic ray events, correcting for geometrical distortion of the detectors, and drizzling the dithered images. The final images cover approximately 11.4 arcmin^2. The APSIS tasks determine the Galactic extinction of E(B-V)=0.05 from the dust maps of Schlegel et al. (1998) and applied 0.1 and 0.07 to i_{775}- and z_{850}-band magnitudes, respectively.

We used SExtractor (Bertin & Arnouts 1996) to find and parameterize sources from the science images and their rms counterparts. We first used the z_{850}-band as the detection image and then reran the task in a dual mode, namely to use the profile information in the z_{850}-band to link and constrain the parameter counterparts in the i_{775}-band image. The limiting magnitudes are similar to those of the GOODS fields, 26.5 mag in the z_{850}-band, for a 10σ detection of a source of 0.″2 in diameter. As shown in Table 1, we selected objects with a color $i_{775} - z_{850} > 1.3$ (MAG_ISO). Only sources with a star-galaxy index of $<$0.8 were considered (0 for galaxy and 1 for star). To further avoid contaminations from cosmic ray events, we only considered sources in the sky region that is covered by all six exposures in each band, which is approximately 10 arcmin^2. The limiting z_{850} magnitudes are MAG_AUTO as they allow us to collect most of the source flux, but the colors are determined with MAG_ISO, in order to maximize the signal-to-noise ratio (S/N). Extensive tests by Benítez et al. (2004) suggest that the colors of faint galaxies are more robust with MAG_ISO. The color selection threshold of 1.3 is chosen to avoid the contamination from low-redshift interlopers. Seven sources are listed, and five of them are i_{775}-faint objects, enabling us to separate them from objects at $z > 6$. Lyα emission at $6 < z < 7$ is at wavelengths redward of the i_{775}-band, and the $i_{775} - z_{850}$ color is at least 2.5 mag. No detection in the i_{775}-band is therefore anticipated. There are nine objects with $1.0 < i_{775} - z_{850} < 1.3$, which may be LAEs at $z \sim 5.8$ or galaxies at $z \sim 1$.

At a redshift of 5.8, 1″ corresponds to approximately 5.7 kpc, and the transverse dimension of the ACS field is approximately 1.1 Mpc. Along the line of sight, the proper distance between $z = 5.7$ and 5.9 is approximately 13 Mpc.

9.3 Results

We identified seven galaxy candidates with $z >$ 5.5 in the field of this quasar. Table 1 lists the properties of the candidates, along with that of the quasar, and Fig. 1 displays their positions. Object D is near a foreground cluster approximately 1′ south of the quasar. The cutout images of each candidate are shown in Fig. 2. We

Figure 9.2 — Cutout i_{775}- and z_{850}-band images of candidates. The image sizes are 2″. The objects are named alphabetically (see Table 1) as marked at the top left corner of each panel of paired images. The images of the quasar, at the bottom right panel, are marked as "Q." The band name is marked at the bottom left corner of each image. The contour at the center of each image marks the area where flux is collected for MAG_AUTO. The source color was calculated from MAG_ISO, which were derived from a compact core within the contour.

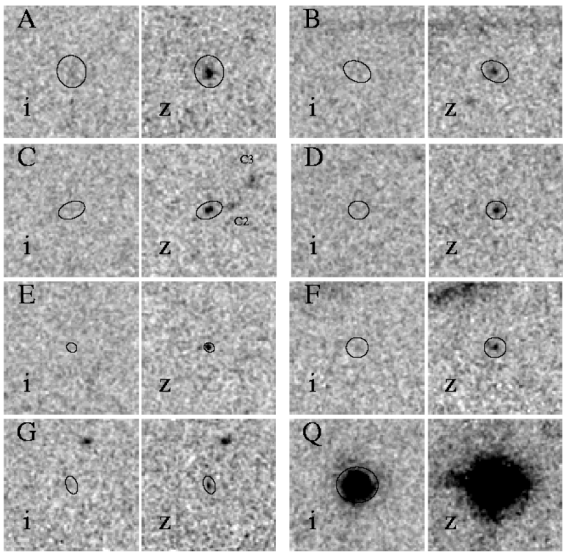

carried out a test on negative images (Dickinson et al. 2004) as spurious sources may be present even at S/N > 5. The i_{775}- and z_{850}-band images were multiplied by -1, and SExtractor tasks were carried out using the same detection parameters. No candidate was detected with the same selection criteria.

The Bayesian photometric redshifts (BPZ; Benítez 2000) were calculated with a calibrated template set of Benítez et al. (2004) supplemented by a very blue starburst template. These templates significantly improve the photometric redshift estimation for faint, high-z galaxies. The new features in BPZ identify multiple peaks of redshifts and assigns a probability to each of them. The values of the first-peak redshifts are listed in column (8) of Table 1.

While it is common to refer to objects with large $i_{775} - z_{850}$ color as "i_{775} dropouts", we can obtain a better redshift discrimination by selecting objects with strong $i_{775} - z_{850}$ breaks, but that are still detected in the i_{775}-band. At $z \sim 5.8$, the redshifted Lyα feature straddles both the i_{775}- and z_{850}-band. Because of the high throughput of ACS, most candidates at this redshift are expected to be detected in the i_{775}-band. As the redshift increases from 5.8 to 6.0, Lyα emission rapidly moves out of the i_{775}-band, and therefore, the $i_{775} - z_{850}$ color increases rapidly from magnitude ~ 1.5 to $\gtrsim 2.0$. Having set a detection limit of $z_{850} < 26.5$, we are able to secure a 2σ detection of sources with $i_{775} - z_{850} < 2.0$. We tested the reality of i_{775}-band detections by deliberately shifting the i_{775}-band image by ± 20 pixels along its row and column and then reran SExtractor. The source apertures defined by the z_{850}-band images would point to a nearby sky field, and in all the cases, the aperture source fluxes in the i_{775}-band were below S/N=1.4. We therefore conclude that an i_{775}-band detection at S/N > 2 is unlikely to be the result of random fluctuations. The detection in both bands

Figure 9.3 — Distribution of $i_{775} - z_{850}$ color for simulated galaxy spectra at redshift $z = 5.8$. The open region represents LAEs, and the hatched region LBGs. Our selection of $1.3 < i_{775} - z_{850} < 2.0$ is expected to include most LBGs but only about 1/3 of the LAEs.

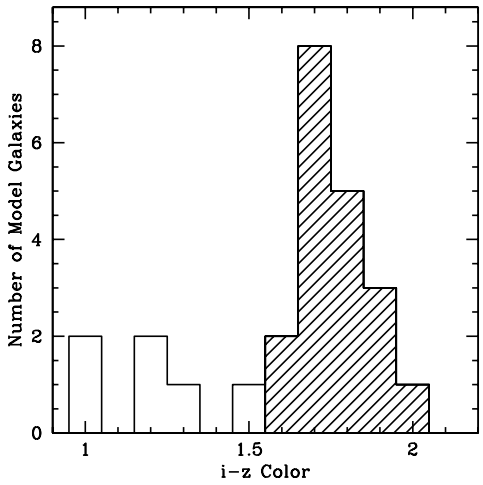

significantly enhances the confidence level and also enables us to exclude background galaxies at $z > 6$ (i_{775}- or i-dropouts). Objects B and G in Table 1 are not detected in the i_{775} band. They are likely background galaxies at $z > 6$ and not physically associated with the quasar.

Figure 9.4 — Field around object C in the z_{850} band. Two additional red objects are marked. The angular scale of $1''$ (~ 5.7 kpc of proper distance) is marked.

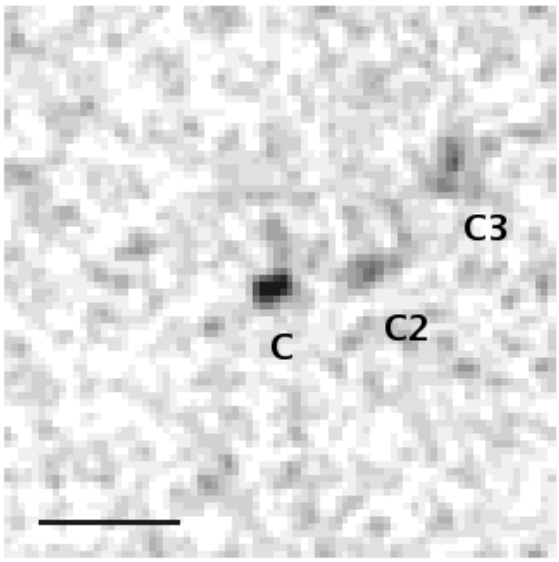

9.4 Discussion

The GOODS results (Dickinson et al. 2004; Bouwens et al. 2005) suggest that the surface density of i_{775}-dropouts and i_{775}-faint objects is approximately 0.25 arcmin^{-2}, to a limiting magnitude of $z_{850} \sim 26.5$. These objects are believed to be at redshifts $5.5 < z < 6.5$. Since we only select i_{775}-faint objects, the photometric redshifts of these objects only cover the range of $5.5 < z < 6$. From previous studies (Dickinson et al. 2004; Stiavelli et al. 2005; Bouwens et al. 2005) we estimate that approximately 60% of these objects are i_{775}-faint and the rest are i_{775}-dropouts. The surface density of i_{775}-faint objects is only ~ 0.15 arcmin^{-2}, or 1–2 in the ACS field of view. Since the chance of finding seven i_{775}-dropouts (including i_{775}-faint objects) in GOODS in a random ACS WFC-size cell (~ 11 arcmin^2) amounts to a few percent (Stiavelli et al. 2005), our finding of five i_{775}-faint objects (and two i_{775}-dropouts) in one ACS field suggests a significant source overdensity. Since all our candidates lie in a region of five arcmin^2 the actual factor of overdensity is approximately six with respect to GOODS, with no random cells drawn from GOODS containing seven objects (four being the highest using the sample of Bouwens et al. 2005). Although cosmic variance is expected to be nonnegligible even on scales as large as those probed by GOODS (Somerville et al. 2004), field to field variations cannot be determined empirically until larger surveys become available.

Our results provide new evidence for an excess of galaxies associated with quasars at $z \gtrsim 5.8$. Stiavelli et al. (2005) find seven candidates at $z \gtrsim 6$ in the field of a radio-quiet quasar at $z = 6.28$. Four out of these seven candidates are detected in the i_{775}-band, and are likely to be foreground galaxies at redshift $5.5 < z < 6$. The number of galaxies associated with the $z = 6.28$ quasar is at most three. We therefore believe that the five $z \sim 5.8$ candidates in the vicinity of quasar SDSS J0836+0054 represent a significant overdensity. Such an overdensity is consistent with the prediction of the Millennium Simulation (Springel et al. 2005) that a "first quasar" candidate at $z = 6.2$ lies on one of the most prominent dark matter filaments and is surrounded by a large number of other, much fainter galaxies. The quasar itself exhibits an $i_{775} - z_{850}$ color of 1.2, which is considerably smaller than that in the SDSS (2.2). This is because the i_{775}-band sensitivity of ACS detectors extends further to the red than that of the SDSS. The bulk of redshifted Lyα emission falls into that extended wavelength region beyond 8000 Å and boosts the i_{775}-band flux. We carried out color simulations of galaxies at $z \sim 5.8$, using the spectral evolution library of Bruzual & Charlot (2003). Among the 39 representative model templates, we chose 21 at age of 1.4 Gyr and younger, which included starburst models. We also added Lyα emission lines to the models

Table 9.1 — Objects with Large $i_{775} - z_{850}$ Color.

Object	R.A. (J2000)	Decl. (J2000)	z_{850}	S/N (i_{775})[a]	$i_{775} - z_{850}^{a}$	FWHM ($''$)	z_B^b
(1)	(2)	(3)	(4)	(5)	(6)	(7)	(8)
A	08 36 45.248	00 54 10.99	25.54 ± 0.10	3.2	1.91 ± 0.36	0.46	$5.8^{+1.4}_{-0.2}$
B[c]	08 36 47.053	00 53 55.90	26.00 ± 0.17	1.5	2.40 ± 0.97	0.39	$5.9^{+1.0}_{-1.0}$
C	08 36 50.099	00 55 31.16	26.24 ± 0.15	2.4	1.92 ± 0.60	0.29	$5.9^{+1.1}_{-0.5}$
C2	08 36 50.058	00 55 30.54	27.26 ± 0.39	1.5	2.42 ± 1.23	0.29	$5.9^{+1.1}_{-1.5}$
C3	08 36 50.010	00 55 30.27	26.82 ± 0.18	0.7	3.41 ± 3.43[d]	0.20	$7.0^{+0.0}_{-0.7}$
D	08 36 48.211	00 54 41.19	26.42 ± 0.14	2.2	1.84 ± 0.49	0.29	$5.8^{+1.2}_{-0.7}$
E	08 36 44.029	00 54 32.79	26.39 ± 0.16	2.3	1.61 ± 0.42	0.19	$5.2^{+1.7}_{-0.7}$
F	08 36 42.666	00 54 44.00	26.03 ± 0.17	2.6	1.64 ± 0.42	0.46	$5.7^{+1.2}_{-0.7}$
G[c]	08 36 45.962	00 55 40.53	26.36 ± 0.25	1.7	1.91 ± 0.63	0.43	$5.8^{+1.2}_{-0.8}$
Quasar	08 36 43.871	00 54 53.15	18.85 ± 0.02	22	1.19 ± 0.03	0.11	$5.7^{+0.1}_{-0.1}$

[a] Calculated using FLUX_ISO and MAG_ISO.
[b] Bayesian photometric redshift, at a 67% confidence level. First-peak redshifts are estimated with a preset upper limit of $z = 7.0$.
[c] i_{775}-dropout. Not considered as being associated with the quasar.
[d] Calculated using MAG_AUTO, as MAG_ISO yields no detection.

with ages of 25 Myr. The Lyα emission is assumed to have a line width FWHM=1000 km s^{-1} and varying equivalent widths 100 or 200 Å in the rest frame. All the model spectra are redshifted and corrected for intergalactic absorption. As shown in Fig. 3, the $i_{775} - z_{850}$ color peaks around 1.7 for LBGs and falls in the range $1.0 < i_{775} - z_{850} < 1.6$ for LAEs. Approximately 90% of the LBGs are selected by our criteria but only a fraction of LAEs.

The field around source "C" is interesting. The source seems to be a multiple system, as shown in Fig. 4. In its vicinity there are two red objects that are slightly fainter and are marked as "C2" and "C3". The two companion objects of source C are not among our initial sample, as they do not meet our selection criteria. However, they are in the vicinity of source C and share similarly red colors suggesting that they may be physically associated. The angular separation between these three sources is only $\sim 1\farcs7$ or ~ 10 kpc, suggestive of merging.

There is a slight chance that some of the candidates are reddened objects at lower redshifts. Red galaxies at $z \sim 1$ display a color of $0.9 \lesssim i_{775} - z_{850} \lesssim 1.1$ (Mei et al. 2006). Uncertainties in the $i_{775} - z_{850}$ color in our sample may introduce contaminations from red galaxies at $z \sim 1$. While it is possible that large uncertainties in magnitudes may lead to contamination from these galaxies, such an effect should also apply to the ACS images of the GOODS fields, because they used the same instrument and had comparable exposure times. As the GOODS fields exhibit a considerably lower surface density of i_{775}-faint objects than our field, the contamination level is low at $\sim 8\%$ (Bouwens et al. 2003). The so-called extremely red objects (ERO) can display sharply rising fluxes toward longer wavelengths in several adjacent bands. The lack of deep infrared images does not allow us to exclude such objects, but since the sizes and morphologies of our candidates do not fit either type, having neither pointlike nor rather diffuse profiles, we conclude that they are unlikely to be EROs. Malhotra et al. (2005) suggest that $\sim 90\%$ of sources with $i_{775} - z_{850} > 1.3$ and $z_{850} < 27$ are spectroscopically confirmed at red-

shift $z > 5.5$. The actual contamination rate is even lower when starlike objects are excluded.

Our finding complements a number of recent reports of overdensities of associated galaxies in the vicinities of radio galaxies at $z > 4$ (although not exclusively) and suggests a possibility of enhanced activities of clustering in the fields of radio sources at high redshifts. The galaxy candidates are more than a 100 times fainter than the quasar itself, and they form a good example of a hierarchical evolution. The detection of radio emission signals an environment that is rich in dark matter, thus harboring the formation of massive black holes.

9.5 Summary

The region around the radio-loud quasar SDSS J0836+0054 is rich in i_{775}-faint objects, which are candidates for galaxies at $z \sim 5.8$. The surface density of these objects is approximately 4–6 times higher than that of the GOODS fields, yielding one of the highest overdensities at $z \sim 6$ known to date. Our finding supports a hierarchical structure, as predicted by a recent simulation, in which luminous quasars are surrounded by fainter galaxies. Spectroscopic observations are needed to further confirm the association and enable us to estimate the volume density occupied by these sources. Future observations of this field in infrared bands will also provide information about the spectral energy distribution of these distant sources.

The observations add fresh evidence that quasars and radio galaxies are good beacons for finding protoclusters of young galaxies at high redshifts. Our measurements could provide the first constraint on the halo occupation number for LBGs in one of the most massive halos at high redshift, which will provide interesting an comparison to numerical simulations.

Acknowledgments

ACS was developed under NASA contract NAS 5-32865, and this research has been supported by NASA grant NAG5-7697 and by an equipment grant from Sun Microsystems, Inc. The Space Telescope Science Institute is operated by AURA Inc., under NASA contract NAS5-26555. We are grateful to K. Anderson, J. McCann, S. Busching, A. Framarini, S. Barkhouser, and T. Allen for their invaluable contributions to the ACS project at the Johns Hopkins University. We thank the anonymous referee for constructive comments.

References

Benítez, N, 2000, ApJ, 536, 571
Benítez, N. et al. 2004, ApJ, 150, 1
Bennett, C. L. et al. 2003, ApJ, 148, 97
Bertin E., & Arnouts S. 1996, A&A, 117, 393
Blakeslee, J. P., Anderson, K. R., Meurer, G. R., Benítez, N., & Magee, D. 2003, in Astronomical Data Analysis Software and Systems XII (San Francisco: ASP), eds. H. E. Payne, R. I. Jedrzejewski, & R. N. Hook, 295, 257
Bouwens, R. J. et al. 2003, ApJ, 595, 589
Bouwens, R. J., Illingworth, G. D., Blakeslee, J. P., & Franx, M. 2006, ApJ, in press (astro-ph/0509641)
van Breugel, W., De Breuck, C., Stanford, S. A., Stern, D., Röttgering, H., & Miley, G. 1999, ApJ, 518, L61
Bruzual, G., & Charlot, S. 2003, MNRAS, 344, 1000
Dickinson, M. et al. 2004, ApJ, 600, L99
Fan, X. et al. 2001, AJ, 122, 2833
Fan, X. et al. 2004, AJ, 128,515
Frey, S., Mosoni, L., Paragi, Z., & Gurvits, L. I. 2003, MNRAS, 343, L20
Giavalisco, M. et al. 2004, ApJ, 600,L93
Haiman, Z. & Loeb, A. 2001, ApJ, 552, 549
Malhotra, S. et al. 2005, ApJ, 626, 666
Mei, S., et al. 2006, ApJ, 639, 81
Miley, G. et al. 2004, Nature, 427, 47
Ouchi, M. et al. 2005, ApJ, 620, L1
Overzier, R. et al. 2006, ApJ, 637, 58
Pavlovsky, C. et al. 2005, "ACS Data Handbook", Version 4.0 (Baltimore: STScI)
Petric, A. O. et al. 2003, AJ, 126, 15
Press, W. H., & Schechter, 1974, ApJ, 187, 425
Schlegel, D., J., Finkbeiner, D. P., & David, M. 1998, ApJ, 500, 525
Somerville R. S., Lee K., Ferguson H. C., Gardner J. P., Moustakas L. A., & Giavalisco M. 2004, ApJ, 600, L171
Springel, V. et al. 2005, Nature, 435, 629
Stanway, E. R., Bunker, A. J., & McMahon, R. G. 2003, MNRAS, 342, 439
Stiavelli, M. et al. 2005, ApJ, 622, L1
Venemans, B. P. et al. 2002, ApJ, 569, L11
Venemans et al. 2004, A&A, 424, L17
Wang, J. X., Malhotra, S., & Rhoads, J. E. 2005, ApJ, 622, L77
Yan, H., & Windhorst, R. A. 2005, ApJ, 612, L93

Chapter 10

Protoclusters: observations, theory and modeling

Abstract. This chapter attempts to provide new constraints on the scenario for the formation of galaxy clusters, based, in part, on the observational evidence presented in this thesis. The chapter is structured in 3 parts. In part I, we compile the first overview of observational evidence for overdensities of galaxies between $z = 2$ and $z = 6$. The overdensities, estimated from the number densities of star-forming galaxies (Lyα emitting galaxies and Lyman break galaxies) relative to random fields, are $\sim 1 - 7$. If these structures were to collapse under the influence of their own gravity, their masses would be $\sim 10^{14}$ to 10^{15} $M_{\odot}$. Because this is comparable to the masses of clusters of galaxies in the local universe, we define the term 'protocluster' as being an object that meets the requirements for forming a bound object on the mass scale of a cluster prior to, or at, the present epoch, but which has not yet collapsed and virialized at the epoch corresponding to its observed redshift. In part II, we use simple theoretical descriptions for the growth of overdensities in a ΛCDM universe to study the evolution of the sample of candidate protoclusters compiled in part I. Using conservative estimates of the overdensities, we find that the majority of the structures are likely to collapse within a finite time. We identify several structures as meeting the requirements for virialization at $z \approx 0.5$, whereas others are expected to have fully collapsed by the present epoch. We compare the predicted abundance of dark halos as a function of their (linear) overdensities, mass and redshift, to the protocluster data. We find that the protoclusters lie in dark halos with number densities of 10^{-6} to 10^{-5} Mpc^{-3}, and conclude that they are associated with clusters that become virialized between $z \approx 0$ for $M \simeq 10^{15}$ $M_{\odot}$ and $z \approx 1$ for $M \simeq 10^{14}$ $M_{\odot}$. We show that this is in agreement with recent results from N-body simulations. We compare the extrapolated bias of dark halos hosting protoclusters and radio galaxies at $z \sim 3$ to the bias of Lyman break galaxies (LBGs) and distant red galaxies (DRGs) at $z = 3 - 6$. The bias of protoclusters at $z \sim 3$ ($b \sim 8$) implies that their present-day descendants lie in dark halos that are $\sim 5 - 10$ times more massive than those hosting the $z = 0$ descendants of luminous LBGs or DRGs, although even the latter populations are associated with group- or moderate clustertype environments at $z = 0$. In part III, we model the star formation history of cluster red sequence galaxies in order to compare their luminosities extrapolated to $z > 2$ to the protocluster data. We find that the total stellar mass in the cluster red sequence was built up over the redshift range $z \sim 10 - 2$ with star formation rates of several hundreds to a thousand of $M_{\odot}$ yr^{-1} assuming constant star formation. We show that there is good agreement with the star formation rates as measured for Lyα emitters and LBGs, and the total extrapolated star formation rates in protoclusters. Summarizing, the overdensities, the masses and the star formation rates of protocluster candidates are in general agreement with the properties expected for the progenitors of clusters in the local universe.

R. A. Overzier, G. K. Miley, H. J. A. Röttgering, S. Mei & B. P. Venemans (2006)

10.1 Introduction

The formation and evolution of structure in the universe is a fundamental research area in modern cosmology. Clusters of galaxies represent the most extreme deviation from initial conditions in the universe, and are therefore good laboratories for testing evolutionary scenarios for the formation of the large-scale structure, and their properties are closely tied to the cosmological parameters (Bahcall & Fan 1998). While clusters of galaxies have been studied extensively in the relatively nearby universe, their evolutionary history becomes obscure beyond roughly half the Hubble time. Their progenitors are extremely difficult to identify when the density contrast between the forming cluster and the field becomes very subtle, and mass condensations on the scales of clusters are extremely rare at any epoch (Kaiser 1984).

Overdensities of galaxies have been discovered out to $z \approx 6$ (e.g. Pascarelle et al. 1996; Steidel et al. 2005; Keel et al. 1999; Francis et al. 2001; Möller & Fynbo 2001; Venemans et al. 2002, 2004, 2005a,b; Shimasaku et al. 2003; Ouchi et al. 2005; Stiavelli et al. 2005). Some of these structures were found as by-products of wide field surveys using broad or narrow band imaging. Others were traced by a luminous radio galaxy or quasar that pinpointed the overdense regions (e.g. Steidel et al. 1998; Kurk et al. 2000; Pentericci et al. 2000; Venemans et al. 2002, 2004; Miley et al. 2004; Venemans et al. 2005a,b; Overzier et al. 2006a,b; Zheng et al. 2006). Although these structures are all overdense compared to the field, their derived physical properties are generally highly uncertain. In general, the galaxy overdensities are on the order of a few and imply group- or clusterlike masses of 10^{13-15} $M_\odot$, projected sizes of several to several tens of (comoving) Mpc, and in some cases measured velocity dispersions of a few hundred km s^{-1} determined from emission line galaxies. Because of the variation, as well as the uncertainties, in their sizes, topologies and masses they have been associated with overdense regions within the large-scale structure, such as filaments, or more special structures that are the progenitors of local clusters and galaxy groups.

The inferred total masses of the suspected protoclusters usually relies on the assumptions that (i) the overdensity measured for one tracer population of galaxies (usually Lyα emitters (LAEs) or Lyman break galaxies (LBGs)) is representative for the total underlying mass overdensity of the structure (its various components being dark matter, gas and other types of galaxies, besides the tracer population) and (ii) that the various other galaxy populations occupy the same volume that is occupied by the tracer population. These assumptions are at present difficult to verify without time-consuming spectroscopic campaigns over large areas of the sky. Can we use any other signatures expected from forming clusters to establish whether the high redshift galaxy overdensities observed are indeed the suspected sites of cluster formation? One of the tell-tale signs of clusters, at least in the relatively nearby universe, is their high luminosity and extended X-ray emission. However, the detectability of distant clusters using X-ray observations is proportional to $(1+z)^{-4}$, even when it is assumed that there is no evolution in cluster abundance, as well as their properties, with redshift. The most distant X-ray clusters that have been found (e.g. Rosati et al. 1998; Mullis et al. 2005) are expected to lie very close to the maximum redshift achievable by current surveys ($z \sim 1.5$). Because the X-ray luminosity of clusters is furthermore proportional to the square of the gas density within the virial radius of the cluster, and virialization is believed to have occurred by $z \sim 1-1.5$ (for the most distant and massive clusters known), little X-ray emission is expected from clusters or cluster progenitors beyond $z \simeq 2$. X-rays are therefore not useful as a tool for the identification of a (forming) cluster.

There is, however, another property of galaxy clusters that could serve as an indicator of its mass and overdensity at early epochs. The cluster red sequence or color-magnitude relation (CMR) is a preferred region in the magnitude (usually rest frame optical) versus color (usually rest frame $U-B$) diagram of the galaxies

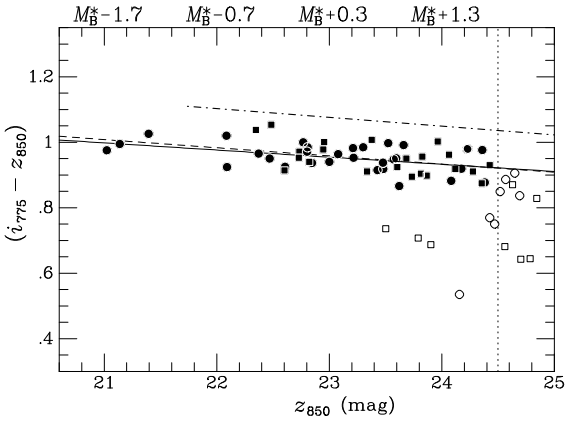

Figure 10.1 — Color-magnitude diagram of Cl1252–2927 at $z = 1.24$ within the central $2'$ of the cluster, with elliptical galaxies indicated by (filled) circles and S0 galaxies by squares. The lines indicate fits to the CMR for ellipticals only (solid line) and for all early-types (dashed). The dot-dashed line represents the relation for the Coma Cluster, transformed to these bandpasses at $z = 1.24$ assuming no evolution. The figure was taken from Blakeslee et al. (2003).

in clusters (see Fig. 10.1). The relation is formed almost exclusively by early-type galaxies. The existence of the red sequence implies that star formation ceased at a sufficiently early epoch to allow the colors redden passively up to the cluster age at the observed epoch. The early-type galaxies on the red sequence are the most massive and oldest galaxy constituents of clusters, even for clusters at $z \sim 1$, where masses of $\sim 10^{11}\ M_\odot$ and formation redshifts of $\sim 2-5$ are inferred (e.g. Ellis et al. 1997; van Dokkum et al. 2000; Stanford et al. 2002, 2005; Blakeslee et al. 2003, 2006; Holden et al. 2005; Postman et al. 2005; Mullis et al. 2005; Mei et al. 2006). The epoch of cluster formation is presumed to be marked by the violent build-up of the stellar mass contained in this early-type population. Constraints on the star formation history are (i) the color-magnitude relation, (ii) galaxy morphologies, (iii) the metal enrichment of the intra cluster medium (ICM), and (iv) the Butcher-Oemler effect (the empirical evidence that distant clusters have a higher fraction of relatively blue (late-type) galaxies than nearby clusters. **How do the star formation rates observed in protoclusters correspond to predictions based on the formation of these red sequence galaxies? Are the amplitudes of the galaxy overdensities observed consistent with what structure formation predicts for the progenitors of galaxy clusters?** The answers on these important questions may shed new light on the process of structure formation in the universe.

In this chapter we will attempt to address the questions raised above. The structure of this chapter is as follows. In Part I, we review the evidence of galaxy overdensities observed between $z = 2$ and 6, and summarize the main properties of the structures used in the subsequent parts of this chapter. In Part II, we review the theory of structure formation, and compare the evolution of overdensities associated with massive dark matter halos to the protocluster data compiled in Part I. We will investigate the abundances, bias and the likely present-day descendant populations of the halos hosting protoclusters with respect to other classes of high redshift objects. In Part III, we construct a simple 'toy model' for the star formation history of the red sequence population of galaxy clusters, and compare the evolution of the total luminosity as predicted by our model against the protocluster data.

10.2 Part I: A census of protoclusters

At present the investigation of candidate protocluster fields has resulted in the discovery of about 15 structures spanning the redshift range $z = 2-6$ (corresponding to ~ 2.5 Gyr of cosmic time). We have compiled an overview of the properties of 12 of the most convincing candidate protocluster objects discovered to date. Below we will briefly describe each target individually, ordered in increasing redshift, and refer to Table 10.1 for a compilation of the key parameters (overdensities and masses) of some of the structures used later in this chapter. The data was compiled from information on radio galaxy protocluster targets gathered by Venemans et al. (2005a), supplemented by data taken from this thesis, and from other targets from literature.

Table 10.1 — Observational data on protocluster candidates.

Object	z	Sample[a]	Field size[b] (arcmin^2)	δ_g^c	σ_v^d (km s^{-1})	M^e ($M_\odot$)	References[†]
PKS 1138–262	2.16	Lyα	7×7	3 ± 2	900 ± 240	3–4	1,2,3,4,5
HS1700–FLD	2.30	BX	8×8	$6.9^{+2.1}_{-2.1}$	–	14	6
MRC 0052–241	2.86	Lyα	7×7	$2.0^{+0.5}_{-0.4}$	980 ± 120	3–4	7
MRC 0943–242	2.92	Lyα	7×7	$2.2^{+0.9}_{-0.7}$	715 ± 105	4–5	7
SA22–FLD	3.09	LBG	9×18	$3.6^{+1.4}_{-1.2}$	–	10–14	8
		Lyα	9×9	5 ± 2	–	–	9
MRC 0316–257	3.13	Lyα	7×7	$2.3^{+0.5}_{-0.4}$	640 ± 195	3–5	7,10
TN J2009–3040	3.16	Lyα	7×7	$0.7^{+0.8}_{-0.6}$	515 ± 90	–	7
TN J1338–1942	4.11	Lyα	7×7 ($\times 2$)	$3.7^{+1.0}_{-0.8}$	265 ± 65	6–9	7,11
		LBG	3.4×3.4	$\sim 2 - 16$	–	–	12,13,14
SDF	4.86	Lyα	25×45	$2.0^{+1.0}_{-2.0}$	–	> 3	15
TN J0924–2201	5.19	Lyα	7×7	$1.5^{+1.6}_{-1.0}$	305 ± 110	4–9	7,16
		LBG	3.4×3.4	1.0 ± 0.5	–	–	17
SXDF-Object 'A'[f]	5.70	Lyα	60×60	$2.3^{+0.6}_{-0.6}$	~ 180	1–3	18
SDSS J0836+0054	5.82	LBG	3.4×3.4	$2.0^{+3.0}_{-1.5}$	–	1–6	19

[a]Method of sample selection: (Lyα) narrowband Lyα, (LBG) Lyman break technique, (BX) the 'BX' criteria of Adelberger et al. (2005).
[b]Approximate field size.
[c]Amplitude of the galaxy overdensity, $\delta_g = (\Sigma - \bar{\Sigma})/\bar{\Sigma}$, calculated from the surface overdensity (Σ) with respect to the average field density ($\bar{\Sigma}$). Except for HS1700–FLD and SA22–FLD where ample spectroscopic information was available, the overdensities quoted here do not infer any information on the velocity structure of the systems, and are therefore likely a lower limit to the true overdensities in real space.
[d]Velocity dispersion (where available).
[e]Inferred mass of the overdensity in units of 10^{14} $M_\odot$.
[f]Only the richest of the two $z = 5.7$ overdensities discovered in this field is listed.
[†]References: (1) Kurk et al. (2000), (2) Pentericci et al. (2000), (3) Pentericci et al. (2002), (4) Kurk et al. (2004a), (5) Kurk et al. (2004b), (6) Steidel et al. (2005), (7) Venemans et al. (2005a), (8) Steidel et al. (1998), (9) Steidel et al. (2000), (10) Venemans et al. (2005b), (11) Venemans et al. (2002), (12) Miley et al. (2004), (13) Zirm et al. (2005), (14) Overzier et al. (2006a), (15) Shimasaku et al. (2003), (16) Venemans et al. (2004), (17) Overzier et al. (2006b), (18) Ouchi et al. (2005), (19) Zheng et al. (2006).

10.2.1 The targets

• **PKS 1138–262 (z =2.16)** This $7' \times 7'$ field contains a significant overdensity of spectroscopically confirmed Lyα emitters around a massive radio galaxy (Kurk et al. 2000; Pentericci et al. 2000; Kurk et al. 2004a,b). Furthermore, the field has been found to be relatively rich in Hα emitting galaxies having different velocity and spatial distributions compared to the Lyα emitters, several spectroscopically confirmed X-ray sources (Pentericci et al. 2002; Croft et al. 2005), as well as candidate 4000Å break objects at the protocluster redshift, indicating that different galaxy populations already exist in clusters several Gyr before virialization. Being among the closest of the candidate protoclusters, this is a particularly important target for

linking high redshift protoclusters to clusters at low and intermediate redshifts ($z \sim 1$) in order to study morphological and kinematical evolution of galaxy clusters and their star formation histories. The host galaxy of the radio source has been found to consist of a massive component surrounded by a large concentration of smaller, disturbed objects, and the entire system in embedded in a 100 kpc halo of emission line gas (see Fig. 1.3 in this thesis).

• **HS1700–FLD (**$z = 2.30$**)** A highly significant overdensity at $z = 2.300 \pm 0.015$ was discovered in the course of a large spectroscopic campaign by Steidel et al. (2005) to select star-forming galaxies at $z = 2.3 \pm 0.4$. The structure corresponds to the largest, spectroscopically confirmed galaxy overdensity known at $z > 2$, and it is expected to become virialized by $z \sim 0$ on a mass scale of $\sim 10^{15}\ M_{\odot}$. Comparison between the best-fit spectral energy distributions of galaxies in the protocluster and the field suggests that the structure is relatively rich in evolved galaxies, as expected from simple theoretical predictions for accelerated structure formation (Steidel et al. 2005).

• **MRC 0052–241 (**$z = 2.86$**) and MRC 0943–242 (**$z = 2.92$**)** The $7' \times 7'$ fields towards both of these $z \approx 2.9$ radio galaxies are significantly rich in Lyα galaxies in a narrow redshift interval centred on that of the radio sources. The systems each have ~ 70 Lyα imaging candidates (of which > 20 spectroscopically identified), corresponding to galaxy overdensities of $\delta_g > 2$ and masses of $\sim 3 - 5 \times 10^{14}\ M_{\odot}$ (Venemans et al. 2005a).

• **SA22–FLD (**$z = 3.09$**)** This structure was serendipitously discovered by Steidel et al. (1998), following the presence of a significant 'spike' in the spectroscopic redshift distribution of a large sample of $z \sim 3$ Lyman break galaxies in this field ($9' \times 18'$). The derived number density of these structures implies that they are consistent with being the progenitors of moderately rich galaxy clusters in their early stages of evolution. Subsequent study of this field has shown a similar overdensity in Lyα galaxies, as well as the presence of several large Lyα 'blobs' associated with the protocluster (Steidel et al. 2000).

• **MRC 0316–257 (**$z = 3.13$**)** This structure consists of 31 confirmed Lyα emitters in a $7' \times 7'$ field centered on a powerful radio galaxy (Venemans et al. 2005a,b). Its velocity dispersion of ~ 600 km s^{-1}, roughly halfway between the typical velocity dispersion associated with the local Hubble flow at $z \gtrsim 3$ and that of massive virialized clusters at $z \lesssim 1$, possibly indicating that the structure is at an intermediate evolutionary stage.

• **TN 2009–3040 (**$z = 3.16$**)** This target is one of two of the least rich of the overdensities around radio galaxies found by Venemans et al. (2005a). Although due to its small overdensity it is not considered to be a candidate protocluster, the subclustering of Lyα emitters both in angular and velocity space suggests that they are physically linked to the radio galaxy, maybe in a group. We include it in our analysis below for comparison.

• **TN J1338-1942 (**$z = 4.11$**)** This is the richest structure among the radio galaxy-selected protocluster targets (Venemans et al. 2005a). Venemans et al. (2002) have estimated a mass of $\sim 10^{15}\ M_{\odot}$ based on the overdensity of Lyα emitters within a structure of ~ 2 Mpc in radius around the radio galaxy TN J1338–1942. The field has been shown to have a similar excess of Lyman break galaxies selected using HST/ACS over an $3.4' \times 3.4'$ area (see chapters 4, 5 & 6 of this thesis), indicating the enhanced star forming activity and clustering associated with the forming structure and the radio source (Miley et al. 2004; Zirm et al. 2005; Overzier et al. 2006b).

• **SDF (**$z = 4.86$**)** Strong clustering of Lyα emitters was found in a 20×50 Mpc (in co-moving units) elongated region in the Subaru Deep Field (SDF) using a narrowband centred on Lyα at $z = 4.86$ (Shimasaku et al. 2003). The overdensity and large structure size may signal the formation of a galaxy cluster.

• **TN J0924–2201 (**$z = 5.19$**)** This radio galaxy, the most distant known, has 6 spectroscopically confirmed Lyα emitting companion galaxies, and appears to lie within an overdense region (Venemans et al. 2004). Observations with

HST/ACS further indicated an excess of V_{606}-break ($z \sim 5$) objects to $\sim 99\%$ confidence, suggesting that the radio galaxy lies in a relatively rich environment, possibly a protocluster.

• **SXDF ($z = 5.70$)** Ouchi et al. (2005) discovered two overdense structures of ~ 1 Mpc in physical size of Lyα galaxies within the ~ 1 deg^2 Subaru/XMM-Newton Deep Field (SXDF), corresponding to a similar volume density of moderately rich clusters found in the present-day universe.

• **SDSS J0836+0054 ($z = 5.82$)** The most distant radio-loud quasar known, SDSS J0836+0054 is associated with a large number of candidate companion objects characterized by very red ($1.3 < i_{775} - z_{850} < 2.0$) color (Zheng et al. 2006,see chapter 8 of this thesis). The surface density in this field is approximately six times higher than the number expected from deep ACS fields, although the relatively small number statistics and lack of spectroscopic confirmation make it difficult to quantify the excess.

10.2.2 Derivation of the total mass

The large galaxy overdensities relative to the field observed in each of these structures can be translated into an estimate of the total mass of the structure (cf. Steidel et al. 1998; Venemans et al. 2005a) as follows. The observed galaxy overdensity, δ_g, relates to the mass overdensity, δ_m, through the bias parameter, b, that relates galaxies to the underlying dark matter:

$$1 + b\delta_m = |C|(1 + \delta_g), \tag{10.1}$$

where

$$C = 1 + f - f(1 + \delta_m)^{1/3}, f = \Omega_m(z)^{4/7} \tag{10.2}$$

is a correction for redshift-space distortion due to peculiar velocities assuming that the object is breaking away from the Hubble expansion (Steidel et al. 1998). Taking the typical bias values of $\sim 2 - 5$ as found for various populations of star-forming galaxies in protoclusters estimated from the clustering of these populations in large field surveys (e.g. Ouchi et al. 2004; Adelberger et al. 2005; Lee et al. 2005), typically yields $\delta_m \sim 0.2 - 2$ for the targets listed in Table 10.1. Assuming that this overdensity is representative for the true mass overdensity of the structure as a whole as measured within a certain structure volume (or surface area), the total mass is given by

$$M \simeq (1 + \delta_m)\bar{\rho}V, \tag{10.3}$$

where $\bar{\rho}$ is the present-day mean density of the Universe.

The mass estimates of the protocluster candidates are typically on the order of 10^{14-15} $M_\odot$ (see Table 10.1), similar to that of massive clusters. However, given that for typical cosmological surveys $V \gtrsim 10^{14-15}/\bar{\rho}$, the genuine progenitors of present-day clusters must be shown to have an overdensity sufficiently large in order for the structure to collapse and virialize by the current epoch. This will be the subject of the following section, where we shall consider the basic theory of structure formation in order to compare its predictions with the observed properties of protocluster candidates summarized above.

10.3 Part II: Theory of structure formation

The structure of this section is as follows. We first present the elements of the spherical collapse model, and use its predictions to investigate whether the properties of our candidate 'protoclusters' are consistent with the evolution of the structures into bound objects. Then, we use the framework of structure formation to investigate the evolution of cluster-like halo abundances, and compare its predictions to the available protocluster data.

10.3.1 Linear spherical collapse

In the local Universe, clusters of galaxies are gravitationally bound objects with masses of $\sim 10^{14-16}$ $M_\odot$ (bound objects with mass of a few times 10^{13} $M_\odot$ are usually referred to as 'galaxy groups'). We shall review aspects of the theoretical framework necessary to understand the for-

mation and evolution of galaxy clusters. Clusters are the result of the gravitational collapse of matter. Because most of this mass is in the form of (non-baryonic) dark matter, the theory of collapse can almost in its entirety be developed from the fluid dynamics of collisionless, non-dissipative systems. The current framework for the theory of collapse describes the growth of all structure in the universe as due to perturbations in the density field of an expanding universe with a non-zero cosmological constant. The theory predicts the mass distribution in the present-day universe from the amplitude of the initial perturbations at recombination as characterized by the matter power spectrum.

Although collapsed structures ranging from dwarf galaxies to massive galaxy clusters are highly non-linear systems, in explaining structure formation we can largely rely on the linear theory of spherical collapse (see, e.g., Peacock 1999). This is because the growth of cosmological structure proceeds approximately linearly up to the point of collapse. After collapse, the structure evolves non-linearly until it is virialized. In the linear collapse model, a uniform (top-hat) spherical overdense region with a density larger than the local critical density will behave like an isolated region that initially expands but then collapses to form a bound object. The turn-around time is the time at which the outermost shell of the system has reached its maximum radius, and decouples from the cosmic expansion resulting from the collapse. In this simplified model, the collapse is complete at twice the turn-around time. In reality, the object does not collapse to a singularity, but stabilizes after a finite time at the radius of virialization, roughly half the radius reached at maximum expansion (see Fig. 10.2). The critical overdensity predicted by the linear collapse model is $\delta_c \simeq 1.686$, which is almost independent of cosmology. This critical overdensity can be used as a simple criterion to study the collapse of density perturbations at different epochs and at different mass scales. Once the structure virializes, the true overdensity of the structure will be ~ 200, at which the linear model becomes insufficient to describe the dynamical evolution.

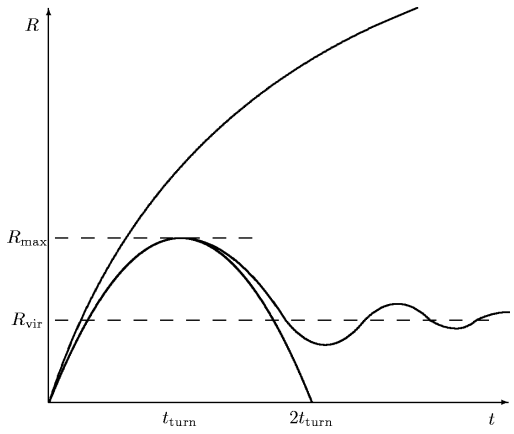

Figure 10.2 — Cartoon of the uniform (top-hat) model for spherical collapse (from Kaiser 2002). Each region in the universe will expand with time (open line), unless its local density exceeds the critical density. In this case, the perturbation reaches a maximum radius at the turn-around time, and collapses at twice that time (closed line). In reality, the overdensity does not collapse to zero, but stabilizes after a finite time at the radius of virialization, roughly half the radius reached at maximum expansion (wavy line).

10.3.2 Comparison between protocluster overdensities and the requirements for spherical collapse

Here we will investigate whether the matter overdensities estimated for protoclusters at $z = 2 - 6$ are sufficient for the structures to collapse, and, if so, at which epoch virialization takes place. As discussed in the previous section, gravitationally bound or collapsed objects of mass M are expected to have formed when their linear matter overdensity, δ_L, exceeds the critical density for collapse of 1.686. In order to make the comparison between δ_L used in the theory, and the matter overdensity, δ_m, that were estimated based on galaxy overdensities (δ_g) measured towards the protocluster targets discussed in the previous section, we use the approximation given by Mo & White (1996,see Bernardeau (1994) for a derivation) that relates the mass overdensity to the linearly extrapolated overdensity in the early stages of

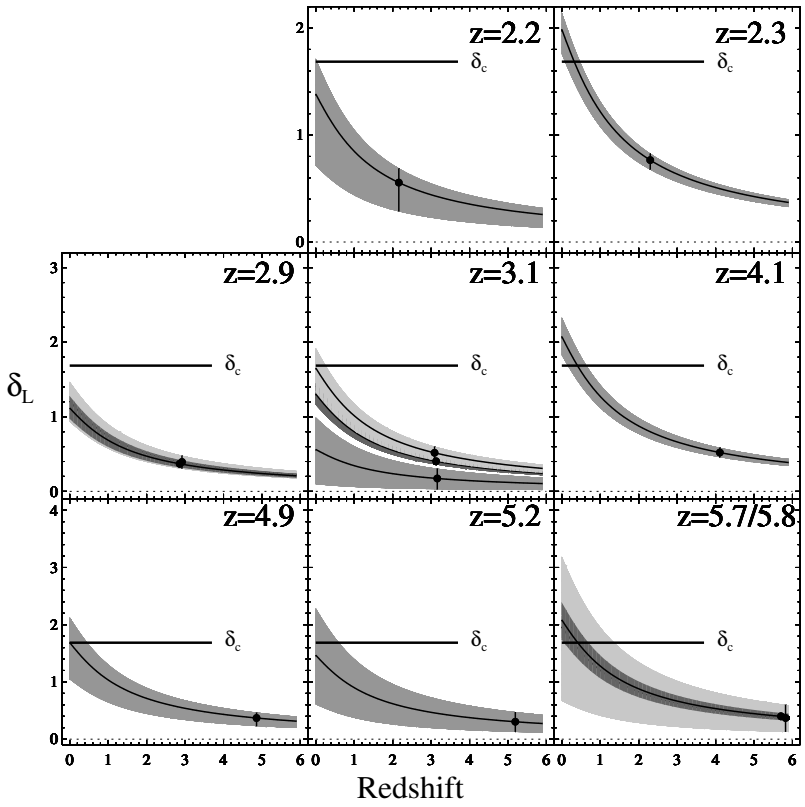

Figure 10.3 — Linear overdensities as a function of redshift based on the observational evidence for protocluster candidates as summarized in Table 10.1. Points with error bars show the linear overdensities corresponding to the measured galaxy overdensities (mostly from Lyα emitters) assuming spherical collapse, and the evolution of the overdensities with redshift is shown by the shaded regions (1σ range). The horizontal bar indicates the critical collapse treshold, $\delta_c = 1.686$, for forming bound objects. The available data suggests that the protocluster candidates have varying properties when evolved to the current epoch: some structures undergo collapse by $z \sim 0.5$, others by $z \approx 0$, while some structures are not dense enough for undergoing collapse even by $z = 0$. See text for details.

the (spherical) collapse:

$$\delta_L = -1.35(1+\delta_m)^{-2/3} + 0.78785(1+\delta_m)^{-0.58661} + -1.12431(1+\delta_m)^{-1/2} + 1.68647. \quad (10.4)$$

In Fig. 10.3 we present the linearly extrapolated overdensities determined from the protocluster data summarized in Section 10.2 (indicated by the points). For simplicity, the targets have been grouped in approximate redshift where appropriate. The shaded regions indicate the linear overdensities and their 1σ uncertainty when evolved to the present epoch based on the growth of the density perturbations according to

$$\delta_L(z_2) = \frac{D(z_2)\delta_L(z_1)}{D(z_1)}, \quad (10.5)$$

where

$$\begin{aligned} D(z) &= g(z)/[g(0)(1+z)], \quad (10.6)\\ g(z) &= \frac{5}{2}\Omega_{M,z}[\Omega_{M,z}^{4/7} - \Omega_{\Lambda,z} + \\ &\quad +(1+\Omega_{M,z}/2)(1+\Omega_{\Lambda,z}/70)]^{-1},\\ \Omega_{M,z} &= \Omega_M(1+z)^3/E^2(z),\\ \Omega_{\Lambda,z} &= \Omega_\Lambda/E^2(z),\\ E^2(z) &= [\Omega_\Lambda + (1-\Omega_\Lambda-\Omega_M)(1+z)^2 + \Omega_M(1+z)^3]. \end{aligned}$$

using the approximations to the cosmological growth in a ΛCDM universe given by Carroll et al. (1992).

In each of the panels of Fig. 10.3 we have indicated the critical linear overdensity for collapse. The simple extrapolation of the measured overdensities to later epochs illustrates a range of interesting aspects of these structures. Some of the structures (e.g. the targets HS1700–FLD at $z = 2.3$, TN J1338–1942 at $z = 4.1$ and SXDF at $z = 5.7$) have sufficiently large overdensities with relatively small uncertainties, that they are expected to have reached the collapse threshold well before the present epoch. For these objects, collapse is predicted to occur at $z \sim 0.5$. Most of the other structures are consistent with collapse by $z \sim 0$ (e.g., PKS 1138–262 at $z = 2.16$, SA22–FLD and MRC 0316–257 both at $z = 3.1$, SDF at $z = 4.9$, TN J0924–2201 at $z = 5.2$, and SDSS J0836+0054 at $z = 5.8$). Some of the overdensities observed seem too small for collapse even by $z = 0$, for example for 2009–3040 at $z = 3.1$, in agreement with the conclusion of Venemans et al. (2005a) that the overdensity is too small to qualify as a protocluster candidate.

Taking the results at face value, we have demonstrated that the current sample of protoclusters represents a class of objects that, generally speaking, meets the requirements for collapse on a mass scale that is comparable to that of galaxy clusters. How do the linear overdensities derived here, and the abundance of protoclusters observed, compare to the predicted halo abundances as a function of redshift and halo mass?

10.3.3 The evolution of mass fluctuations

Here we give the necessary ingredients for describing the evolution of mass fluctuations starting from the initial perturbations to the present (see, e.g., Peebles 1980; Peacock 1999; Mo & White 2002; Kaiser 2002; Tozzi 2006). Because the predictions for structure formation rely heavily on the cosmology, observational cosmologists have had to struggle with widely varying model predictions depending on which cosmological model was used. Currently, theory predictions have become considerably more reliable due to the vastly improved accuracy of the fundamental cosmological parameters. In the discussion below we will use the concordance ΛCDM cosmology, $\Omega_M = 0.3$, $\Omega_\lambda = 0.7$, $h = 0.7$, $H_0 = 100h$ km s^{-1}.

Because the cosmic density field is approximated to be linear, at any moment we can relate a given mass to the radius of a spherical volume in which that mass is contained

$$R(M) = \left(\frac{3M}{4\pi\bar{\rho}_0}\right)^{1/3}, \tag{10.7}$$

where $\bar{\rho}_0$ is the current average density of the universe. Under the assumption of Gaussian fluctuations in the density field (as predicted by inflation), the entire mass field can be characterized only by its variance

$$\sigma^2(M) = \frac{4\pi}{(2\pi)^3}\int_0^\infty \frac{dk}{k} k^3 P_{lin}(k) W^2(kR), \tag{10.8}$$

where $\sigma(M)$ is the rms value of the density fluctuations on mass scale M when smoothed with a top-hat filter of radius R having a Fourier transform of $W(x) = (3/x^3)[\sin x - x\cos x]$, and $P_{lin}(k)$ is the linear power spectrum of density fluctuations extrapolated to $z = 0$. We used a ΛCDM power spectrum of the form $P_{lin}(k) \propto k^n T_k^2(q)$ with $n = 1$ and the matter transfer function

$$\begin{aligned} T_k(q) &= \frac{\ln(1+2.34q)}{2.34q} \\ &\quad \times[1+3.89q+(16.1q)^2+ \\ &\quad +(5.46q)^3+(6.71q)^4]^{-1/4}, \\ q &= (k/h)\Gamma, \\ \Gamma &= \exp(\Omega_B + \sqrt{2H_0}\Omega_B/\Omega_M)/\Omega_M H_0 c \end{aligned} \tag{10.9}$$

from Bardeen et al. (1986); Sugiyama (1995). The power spectrum is normalized by requiring that the present-day rms mass fluctuation in a sphere of radius 8 h^{-1} Mpc is $\sigma_8 = 0.9$.

The above prescriptions for mass fluctuations can be used to predict the number density of present-day bound structures such as galaxy clusters, and their evolution at different epochs. This problem is usually addressed by studying the mass function $n(M, z)dM$, which describes the number density of bound objects

with masses between M and $M + dM$ at redshift z, or $N(> M, z)$, which is the number density of objects more massive than M. Although the collapse and virialization of overdensities are nonlinear in nature, the process of collapse is unlikely to change the total mass contained by the overdensity filtered on a scale R. Therefore, the mass function can be constructed from the number density of regions that have an overdensity $\delta > \delta_c$.

In the theory pioneered by Press & Schechter (1974), the halo abundance as a function of mass and redshift can be approximated using the *unconditional mass function* derived by Sheth & Tormen (1999); Sheth et al. (2001); Sheth & Tormen (2002):

$$\nu f(\nu) = 2A\left(1 + \frac{1}{\nu'^{2p}}\right)\left(\frac{\nu'^2}{2\pi}\right)^{1/2} \exp\left(-\frac{\nu'^2}{2}\right), \tag{10.10}$$

where $\nu' = \sqrt{a}\nu$, $a = 0.707$, and $q = 0.3$ are based on a fit to the mass function of the numerical GIF simulations (Kauffmann et al. 1999), and $A = 0.322$ follows from the requirement that the integral of $f(\nu)$ over all ν should give unity. The halo mass M is related to the rms density fluctuations through the parameter

$$\nu \equiv \left[\frac{\delta_c}{D(z)\sigma(M)}\right]^2. \tag{10.11}$$

The mass function is accordingly

$$n(M, z)dM = \frac{\bar{\rho}}{M}\nu f(\nu)\frac{d\nu}{\nu}. \tag{10.12}$$

The typical halo mass that collapses at each redshift, $M_c(z)$, is defined by $\nu = 1$, i.e., $\sigma(M_c) = \delta_c/D(z)$.

We have used the above formalism to reproduce the evolution of halo abundances as shown by Mo & White (2002). The result is shown in Fig. 10.4, showing the number density of collapsed, dark halos as a function of redshift and (minimum) mass. The figure illustrates that the number density of collapsed halos of mass $> 10^{15}\ M_\odot$ are as frequent in the present-day universe, as halos of $> 10^{12}\ M_\odot$ at $z \sim 10$, and that locally halos of $> 10^{12}\ M_\odot$ are 4 orders of magnitude more abundant than those of $> 10^{15}\ M_\odot$.

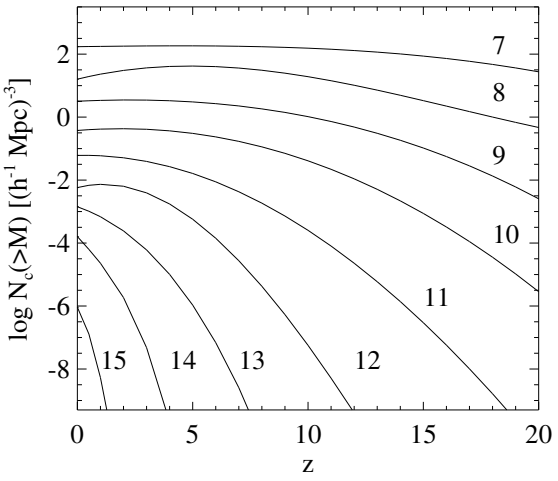

Figure 10.4 — Dark halo number densities as a function of redshift. The numbered lines indicate the cumulative abundance of halos of mass $\log(M/M_\odot)$.

10.3.4 Comparison between protocluster overdensities and halo abundances

In Fig. 10.5 we plot the predicted abundance of the progenitor halos of $10^{15}\ M_\odot$ halos, as a function of their linear overdensity and redshift (the predictions for $10^{14}\ M_\odot$ halos are shown as dotted lines). For your guidance, check that the number density corresponding to the linear collapse threshold of 1.686 (dashed line) at $z = 0$ is $\simeq 10^{-6}\ h^3$ Mpc^{-3}, consistent with the abundance of collapsed halos of this mass plotted in Fig. 10.4. The plot further shows that at $z \sim 2$, for example, the linear overdensity of such halos was ~ 0.8. Assuming that the protoclusters are the progenitors of $\sim 10^{15}\ M_\odot$ halos (see Table 10.1), how do their overdensities and number densities fit in with these model predictions? Unfortunately, the abundance of the protoclusters is largely unknown given the very few objects discovered to date and the complicated selection effects. However, we can place at least some constraints from the observed spread

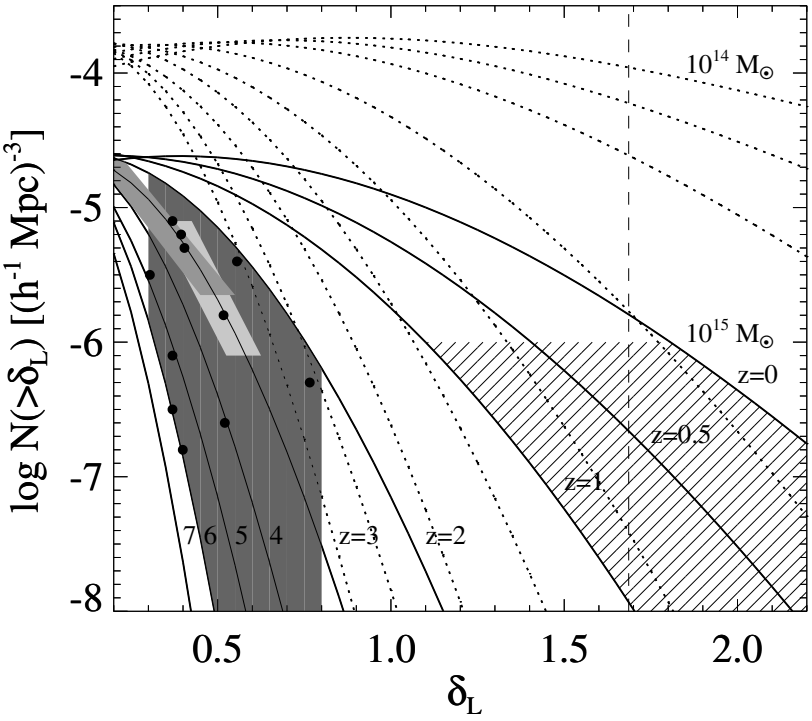

Figure 10.5 — The cumulative number densities of the progenitors of 10^{15} $M_\odot$ halos as a function of linear overdensity and redshift (numbered solid lines). Dotted lines are for dark halos of mass 10^{14} $M_\odot$. The points inside the dark shaded area indicate the range of overdensities ($\delta_L \sim 0.3 - 0.8$) measured at the corresponding redshifts of the protocluster targets of Table 10.1 and Fig. 10.3. Although there are few constraints on the abundance of protoclusters, we mark the approximate number density of powerful radio galaxies at $z \sim 3$ (medium shaded region), and the number density of protoclusters inferred by Steidel et al. (1998) based on the statistics of LBG redshift spikes (light shaded region). The vertical dashed line indicates the critical collapse threshold of 1.686. If radio galaxies, LBG spikes and the galaxy overdensities observed are associated with the progenitors of $\sim 10^{15}$ $M_\odot$ halos, their number densities of $\log N(> \delta_L) \sim -(5-6)$ h^3 Mpc^{-3} imply cluster virialization at $z \sim 0.5 - 0$ for the lower value, and no complete collapse by $z = 0$ for the higher value. The hatched area marks the observed number density of clusters at $z \lesssim 1$ with X-ray luminosities of $\gtrsim 5 \times 10^{43}$ erg s^{-1} (Rosati et al. 2002).

in (linear) overdensities of $\delta_L = 0.3 - 0.8$, and the corresponding redshifts of the protoclusters of $z = 2 - 6$ (points inside the dark shaded region in Fig. 10.5). Furthermore, we indicate the approximate number density of powerful radio galaxies at $z \sim 3$ as estimated[1] by Venemans et al. (2002) (indicated by the medium-dark shaded region, allowing for a factor 10 uncertainty in the number density). We also indicate the number density of $z \sim 3$ protoclusters as inferred by Steidel et al. (1998) based on the statistics of LBG redshift spikes (light shaded region, with a factor 10 uncertainty). If radio galaxies, LBG spikes and the range of structure overdensities observed all trace the same massive halos, their number densities are predicted to be in the range from $N(> \delta_L) = 10^{-6}$ to 10^{-5} h^3 Mpc^{-3}. Following the redshift evolution at these halo abundances using the lines in Fig. 10.5 imply cluster virialization by $z \approx 0.5$ for the overdensities at $z \simeq 4 - 6$. Some of the overdensities at $z \simeq 3$ seem too small for complete collapse even by $z = 0$.

We also indicated the observed number den-

[1]Based on the number density of radio galaxies at $2.7 < z < 3.4$ with luminosities exceeding 10^{33} erg s^{-1} Hz^{-1} sr^{-1} at 2.7 GHz, taking into account a radio source life-time of 10^7 yr. See Venemans et al. (2002) for details.

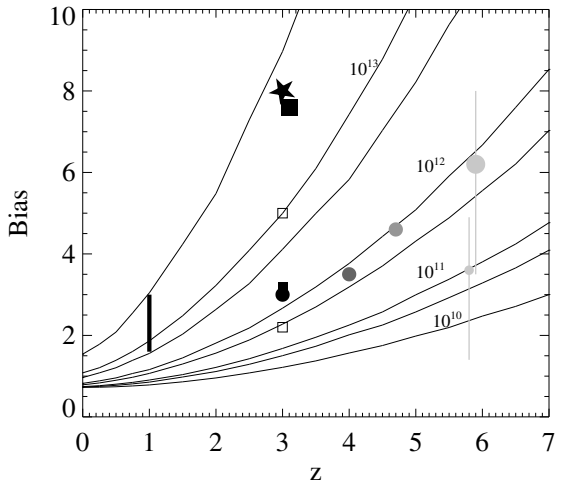

Figure 10.6 — The inferred bias of luminous radio galaxies (star) and LBG protoclusters (large square) based on their number densities derived by Venemans et al. (2002) and Steidel et al. (1998). Other populations shown are Lyman break galaxies at $z = 3 - 6$ (circles, taken from Ouchi et al. (2004) and chapter 8 of this thesis), near-infrared selected galaxies (relatively red objects (upper open square), blue objects (lower open square) and all objects (small filled square), from Daddi et al. (2003)), and luminous radio sources at $z \sim 1$ (bar, derived from chapter 2 of this thesis).

sity of clusters at $z \lesssim 1$ with X-ray luminosities of $\gtrsim 5 \times 10^{43}$ erg s^{-1} (hatched region in Fig. 10.5). For a massive cluster to collapse by $z \sim 1$, it is predicted to have $\delta_L \approx 0.7$ at $z \sim 4$. This is higher than observed for protoclusters at this redshift: TN J1338–1942 at $z = 4.1$, for example, has $\delta_L \approx 0.5$.

10.3.5 The bias of protoclusters and their $z = 0$ descendants

In the halo mass model given in Section 10.3.3, the bias of the dark halos is given by

$$b_{DH} = 1 + \frac{1}{\delta_c}\left[\nu'^2 + b\nu'^{(1-c)} - \frac{\nu'^{2c}/\sqrt{a}}{\nu'^{2c} + b(1-c)(1-c/2)}\right], \tag{10.13}$$

where $a = 0.707$, $b = 0.5$, $c = 0.6$ (Sheth et al. 2001). We have estimated the bias of protoclusters, by looking up the $b_{DH}(z = 3)$ corresponding to the number densities of luminous radio galaxies and LBG spikes at $z \sim 3$ given by Venemans et al. (2002) and Steidel et al. (1998). We find $b \sim 8$ (see Fig. 10.6). At this redshift, the bias corresponds to collapsed halos of $\sim 5 \times 10^{13}$ $M_\odot$. For comparison, we have also indicated in Fig. 10.6 the bias values found for several other classes of objects. At $z \sim 1$, luminous radio sources have $b \sim 2 - 3$, suggesting that they correspond to massive halos (see chapter 2 of this thesis). At $z = 3 - 5$, the clustering of bright ($L \gtrsim L_*$) LBGs indicate $b \sim 3 - 5$ and halo masses of $\sim 10^{12}$ $M_\odot$ (circles, from Ouchi et al. (2004)). Near-infrared selected galaxies at $z \sim 3$ show that the bias may strongly depend on colour (squares, from Daddi et al. (2003)). For completeness, we have also illustrated the (mild) constraints on the bias of i_{775}-dropouts at $z \sim 6$ derived in chapter 8 of this thesis.

Following Ouchi et al. (2004), we can extrapolate the bias measurements for these objects to $z = 0$ using (Sheth et al. 2001):

$$b^0_{DH} = 1 + \\ + \frac{D(z)}{\delta_c}\left[\nu'^2 + b\nu'^{(1-c)} - \frac{\nu'^{2c}/\sqrt{a}}{\nu'^{2c} + b(1-c)(1-c/2)}\right], \tag{10.14}$$

and by assuming that the bias of a given class of objects is representative of the bias of the dark halos hosting them, i.e., $b_g \simeq b_{DH}$. The results are shown in Fig. 10.7, where we plot the number densities of the present-day descendants of the objects in Fig. 10.6 as a function of halo mass. As previously shown by Ouchi et al. (2004), the descendants of all the classes of objects shown lie in the mass range corresponding to groups and clusters of galaxies. Albeit by construction, Fig. 10.7 illustrates that the number density of the $z = 0$ descendants of luminous radio galaxies and protoclusters at $z \sim 3$ implies masses well in the range for galaxy clusters,

10.3.6 Summary

There are several conclusions that follow from our analysis of the observed properties of protocluster candidates:
(1) We calculated the linear overdensities corresponding to the mass overdensities derived from the observations, finding $\delta_L \sim 0.3 - 0.8$.

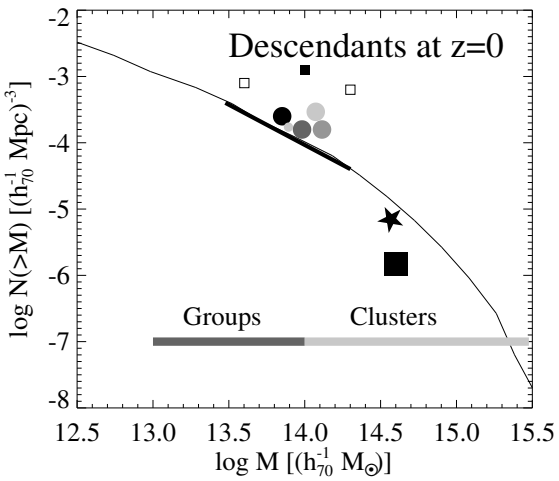

Figure 10.7 — The halo mass and number density of the $z = 0$ descendants of the populations shown in Fig. 10.6. The descendants of all of the high redshift populations shown are expected to end up in halos with masses ranging from those of groups to clusters, with the higher cluster-like masses clearly preferred by the descendants of radio galaxies and protoclusters.

(2) The observed overdensities are in approximate agreement with the amplitudes of massive halo progenitors at $z = 2 - 6$.
(3) The number densities of such massive dark halo progenitors agree approximately with the overdensities expected for luminous high-redshift radio galaxies (corrected for a radio source life-time of $\sim 10^7$ yr), and the estimated number density or protoclusters of Lyman break galaxies.
(4) The overdensities of the protocluster candidates are, on average, sufficiently large to form bound objects with masses of $10^{15}\ M_\odot$ at $z \lesssim 0.5$.
(5) The estimated number density of protoclusters implies $b \sim 8$ at $z \sim 3$, roughly twice as high as the bias of luminous galaxies at similar redshifts as measured by, e.g., Daddi et al. (2003) and Ouchi et al. (2004).

10.4 Part III: Modeling the history of the cluster red sequence

As detailed in the previous sections, the amplitudes and masses of the galaxy overdensities found suggest that they are likely progenitors of clusters. However, so far we have ignored the baryonic matter component of clusters altogether. Here, we shall construct a very simple 'toy model' for the star formation history of clusters. Because it is an established fact that most of the stellar mass contained in the cluster red sequence population was formed at redshifts similar to the redshifts of our protocluster candidates (see Blakeslee et al. 2006, and references therein), we will restrict our analysis to modeling of the red sequence of clusters. The goal of our simulations is to build a library of models that are able to reproduce the observed intrinsic scatters around the color-magnitude relation (CMR) as observed for massive high-redshift clusters, and compare the extrapolated star formation history of those models against the available protocluster data. For these simulations we shall use the observed CMR of three massive clusters chosen from literature. These are Cl 1358+6245 at $z = 0.33$ (van Dokkum et al. 1998), MS 1054–0321 at $z = 0.834$ (Blakeslee et al. 2006), and RDCS 0910+5422 at $z = 1.106$ (Mei et al. 2006). The main observational details for these clusters are summarized in Table 10.2.

10.4.1 The model

The first part of our procedure is similar to the method used by van Dokkum et al. (1998), Blakeslee et al. (2003, 2006) and Mei et al. (2006), who simulated the scatter around the CMR to estimate the mean ages of red sequence galaxies in a number of massive clusters at $z = 0.3 - 1.3$ observed with HST. We have used Bruzual & Charlot (2003,BC03) stellar population models to calculate template colors given a particular star formation history. We only consider the solar metallicity models with a Salpeter initial mass function and high resolution ("bc2003_hr_m62_salp_ssp"). We use the *truncated star formation* model for the star formation history of

Table 10.2 — Scatters of the color-magnitude relation in 3 massive clusters.

Cluster	z	$L^a_{bol,44}$ (erg s^{-1})	T^b_X (keV)	f^c_E	N^d_E	R^e_{max} (arcmin)	Color^f	σ^g_{int}	Refs.†
Cl 1358+6245	0.33	10.65	7.0	0.24	46	4	V_{606}–I_{814}	0.022 ± 0.003	1,2
MS 1054–0321	0.83	16.43	8.0	0.49	46	3	V_{606}–z_{850}	0.080 ± 0.015	3,4,5,6
RDCS J0910+5422	1.11	2.14	7.2	0.37	20	2	i_{775}–z_{850}	0.044 ± 0.010	6,7,8

[a]Bolometric X-ray luminosity in units of 10^{44} erg s^{-1}.
[b]X-ray temperature.
[c]Elliptical fraction.
[d]Number of ellipticals on the red sequence.
[e]Maximum radius for object selection.
[f]Color used for fitting the color-magnitude relation.
[g]Observed intrinsic scatter.
[†]References: (1) van Dokkum et al. (1998), (2) Fabricant et al. (1991), (3) Blakeslee et al. (2006), (4) Gioia et al. (2004), (5) Romer et al. (2000), (6) Postman et al. (2005), (7) Mei et al. (2006), (8) Stanford et al. (2002).

cluster galaxies, which assumes that stars form at a constant rate between $t = t_1$ and $t = t_2$, where t_1 and t_2 are randomly chosen to lie at $t_0 < t_1 < t_2 < t_{end}$ with t_0 the time at recombination and t_{end} the age of the universe at the redshift of the cluster.

We simulated 'clusters' by randomly creating 'galaxies' with different formation epochs and different burst durations. Instead of the standard procedure employed by Blakeslee et al. (2003) and Mei et al. (2006) of creating $\sim 10,000$ model galaxies per simulation (for statistical reasons), we limit the number of model galaxies to the actual number of red sequence galaxies observed on the CMR. For each randomly simulated cluster we evolve the star formation histories to the redshift (z_{obs}) or epoch (t_{end}) of observation, and calculate the average color and the scatter of the simulated population to test for the presence of a 'red sequence'. In case the scatter among the models in a particular simulation run are within the range of the scatters as observed for our three baseline clusters, we accept this ensemble of models to reflect a possible star formation history of the cluster red sequence. The formation epochs and star formation histories are saved to carry out step 2 of our simulation. In this step, the BC03 models are normalised so that the total stellar mass of the model at $z \sim 1$ amounts to the typical mass of red sequence galaxies. Given the set of models that yields an appropriate red sequence when evolved to the observed cluster redshifts, and the proper mass normalisation, the full star formation history of the simulated cluster is now fixed. It is straightforward to compute the total star formation rate or luminosity of the simulated 'clusters' at any redshift and in any bandpass. Summarizing, our toy model depends on the following input parameters or constraints:
(1) a global model form of star formation history (we assume constant star formation).
(2) N_e, the number of morphologically selected elliptical galaxies in the cluster CMR.
(3) M_e, the typical mass of cluster elliptical galaxies ($\sim 10^{11}\ M_\odot$).
(4) σ_{int}, the intrinsic scatter as observed in clusters at $z = z_{obs}$.

Note that the number of progenitor galaxies per red sequence galaxy is not a factor in our simulations. This is justified because we are only interested in modeling the evolution of the *total star formation rate*, and not the *number* of galaxies at different magnitudes (i.e., the luminosity function) as a function of redshift. It

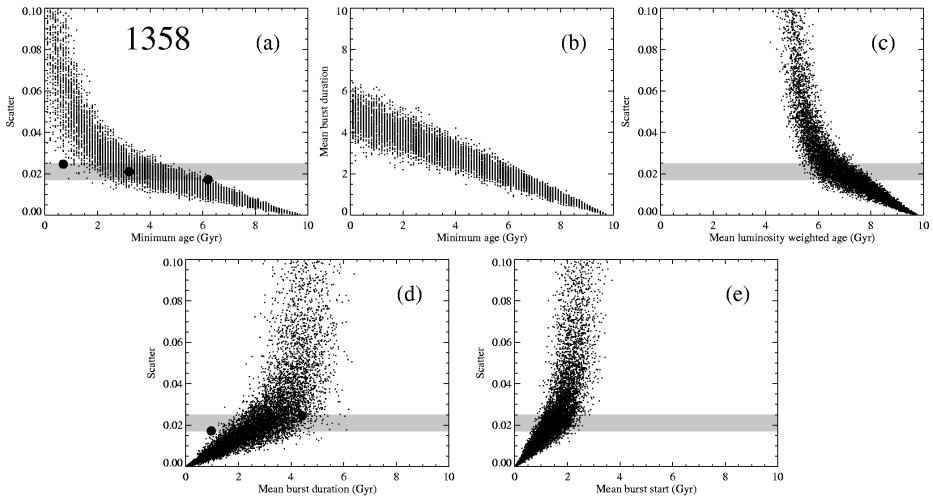

Figure 10.8 — Points show the scatter in the simulated color-magnitude relation at $z = 0.33$. Each simulation consisted of 46 model SEDs with constant formation of variable, random duration (from t_1 to t_2) between the age of the cluster (t_{end}) and the age of recombination (t_0). In (a), we show the scatter in V_{606}–I_{814} as a function of the minimum age at $z = 0.33$ (t_{end}). In (b), we illustrate how the increase in the minimum age of the models implies a decrease in the (mean) duration of the starburst, given the shorter time window allowed for star formation. In (c)–(e), we respectively plot the mean of the luminosity-weighted ages at $z = 0.33$, the mean duration of star formation ($\langle \Delta\tau \rangle = \langle t_2 - t_1 \rangle$), and the mean time of onset of the star formation ($\langle t_1 \rangle$) versus the scatter found in each of the simulations. Shaded regions indicate the $\pm 1\sigma$ range of the observed intrinsic scatter from van Dokkum et al. (1998). Large solid circles indicate the best fit model (middle circle in panel (a)), as well as a maximally young and a maximally old model that still fit the observed intrinsic scatter (left and right circles in panel (a), resp.). These three models are used in Fig. 10.11 to evaluate the star formation history of the red sequence galaxies at > 0.33.

is, however, implicitly assumed that the stellar mass that comprises a single galaxy at the observed cluster redshift, is coeval and formed with the same star formation history. This assumption is supported by simulations of the formation histories of cluster ellipticals. De Lucia et al. (2006) showed that there is a clear distinction between the epoch at which the stellar mass formed, and the epoch at which that mass was assembled into a single galaxy . The models also show that for massive cluster ellipticals, the number of equal mass progenitors is quite low ($\sim 2 - 3$). For such equal mass mergers to take place, it is conceivable that the two merging galaxies will roughly have comparable formation histories given that they have comparable mass at the time of the merger. Our model is independent of the exact mechanism that drives the star formation (e.g., induced by merger, monolithic collapse, AGN or superwind feedback, etc.). Although our model uses a very simplistic approach that should not be considered as an alternative for elaborate semi-analytical models or N-body simulations of cluster formation, it is sufficient for carrying out a rough order of magnitude comparison with the available data on protocluster candidates.

10.4.2 Model Results

For each simulation, we created N_e galaxies with randomly chosen t_1, t_2 (giving $\Delta\tau = t_2 - t_1$). $\Delta\tau$ was in the range 0.1–10.0 Gyr, with increments of 0.1 Gyr. Our three clusters 1358, 1054 and 0910 have respectively 46, 46 and 20 elliptical galaxies on the CMR. To aid the practicality, we simulated the model populations as a function of the minimum age, t_{min}, of galaxies at the cluster redshift. Figs. 10.8, 10.9 and 10.10 show the scatters calculated from the simulations (points), compared to the ob-

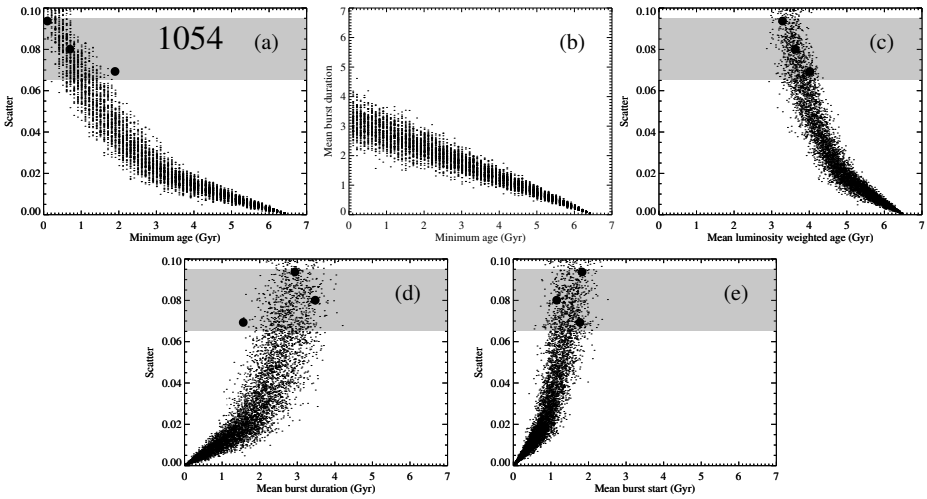

Figure 10.9 — Simulated scatters in V_{606}–z_{850} of the color-magnitude relation in the cluster MS 1054–0321 at $z = 0.834$. The shaded region indicates the $\pm 1\sigma$ range of the observed intrinsic scatter from Blakeslee et al. (2006). See the legend of Fig. 10.8 for further details.

Table 10.3 — Color-magnitude relation simulations.

Cluster	z	Model	σ	t^d_{min}	$\langle \tau_L \rangle^e$	$\langle t_1 \rangle^f$	$\langle \Delta\tau \rangle^g$
Cl 1358+6245	0.33	a	0.022	3.9	6.8	1.6	2.9
Cl 1358+6245	0.33	b	+	2.0	5.7	2.2	4.0
Cl 1358+6245	0.33	c	−	5.4	7.6	1.3	1.9
MS 1054–03	0.83	a	0.080	1.3	3.9	1.4	2.3
MS 1054–03	0.83	b	+	0.8	3.7	1.3	3.0
MS 1054–03	0.83	c	−	2.3	4.3	1.2	2.0
RDCS J0910+5422	1.11	a	0.042	1.0	3.3	1.0	2.2
RDCS J0910+5422	1.11	b	+	0.1	2.7	1.3	3.0
RDCS J0910+5422	1.11	c	−	2.1	3.8	0.9	1.7

[a] The best-fit model (see text for details).
[b] The 'maximally young' model (see text for details).
[c] The 'maximally old' model (see text for details).
[d] The minimum model age.
[e] The mean luminosity-weighted age.
[f] The mean start time of the star formation.
[g] The mean duration of the star formation.

served scatter and its 1σ error range (shaded regions). Our best-fit model for 1358 ($z = 0.33$) had a minimum age of 3.9 Gyr ($z > 0.9$), a mean luminosity-weighted age of 6.8 Gyr ($z \sim 2.2$), a mean burst duration of 2.9 Gyr, and a mean star formation starting time of 1.6 Gyr after recombination. For 1054 ($z = 0.83$), the minimum age was 1.3 Gyr ($z > 1.2$) and mean luminosity-

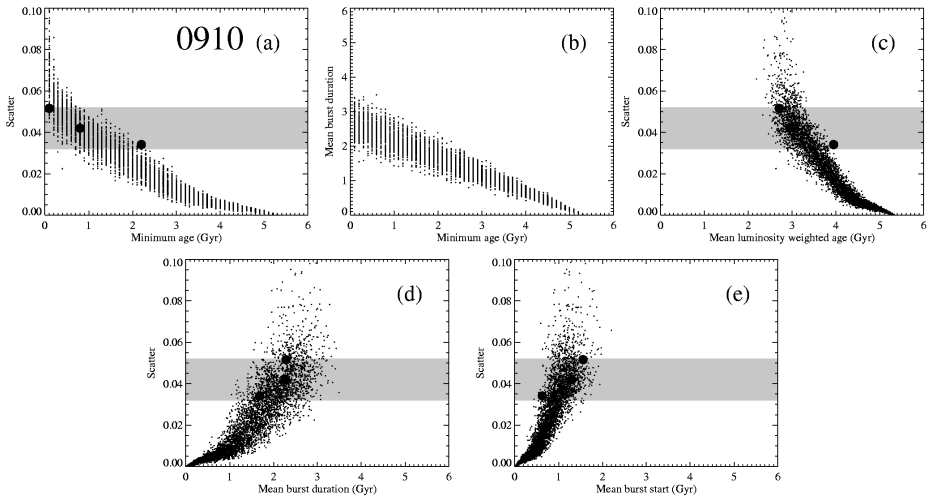

Figure 10.10 — Simulated scatters in i_{775}–z_{850} of the color-magnitude relation in the cluster RDCS 0910+5422 at $z = 1.106$. The shaded region indicates the $\pm 1\sigma$ range of the observed intrinsic scatter from Mei et al. (2006). See the legend of Fig. 10.8 for further details.

weighted age of 3.9 Gyr ($z = 2.4$). For 0910 ($z = 1.11$), the minimum age was 1.0 Gyr ($z > 1.5$) and the mean $\tau_L = 3.3$ Gyr ($z \sim 3.1$). The results are summarized in Table 10.3. Our results are in agreement with the results found by van Dokkum et al. (1998), Blakeslee et al. (2006) and Mei et al. (2006) for the same clusters.

Next, we rescaled the N_e SEDs belonging to the best-fit models so that at the epoch corresponding to the redshift of the clusters the total accumulated mass was $M_e = 10^{11}\ M_\odot$, suitable for cluster ellipticals. A schematic diagram of the star formation histories of the best-fit models are shown in Fig. 10.11. We then de-evolved the star formation histories to earlier times, and calculated the total cluster luminosity at rest frame 1500Å by adding up the luminosities of each of the N_e models. The result is our final model for the star formation history of each cluster, and is shown in Fig. 10.12. Also plotted are two alternative, extreme model outcomes that reproduced the observed intrinsic scatter (dotted lines). In these models, the star formation either shut off later (on average), or started earlier, compared to the best-fit model. We also indicated the effect of dust to the total luminosity (dashed line). The dust contents was assumed to be constant, and decoupled from redshift, taking $E(B-V) = 0.1$ and applying the dust law of Calzetti et al. (2002).

Our model shows (depending on the assumptions) that the massive end of the cluster red sequence may have formed its stars at a relatively constant rate of several hundred $M_\odot\ \mathrm{yr}^{-1}$ over the redshift range $\sim 10 - 2$.

10.4.3 Comparison with protocluster data

One of the main questions that motivated the analysis presented in this chapter is whether the total stellar mass observed at the brightest ~ 3 mag end of $z \lesssim 1$ cluster red sequences is consistent with being produced by the Lyman break galaxies (and Lyα emitters) observed in protoclusters at $z = 2 - 6$. Our models, as illustrated in Fig. 10.12, imply that such hypothesis would require an average SFR of several hundred to a thousand $M_\odot\ \mathrm{yr}^{-1}$ over this whole redshift range. An estimate of the measured SFR in protocluster fields due to the observed Lyman break and Lyα populations can be obtained by looking at the typical star formation rate of these objects. Lyα emitters have a typical SFR

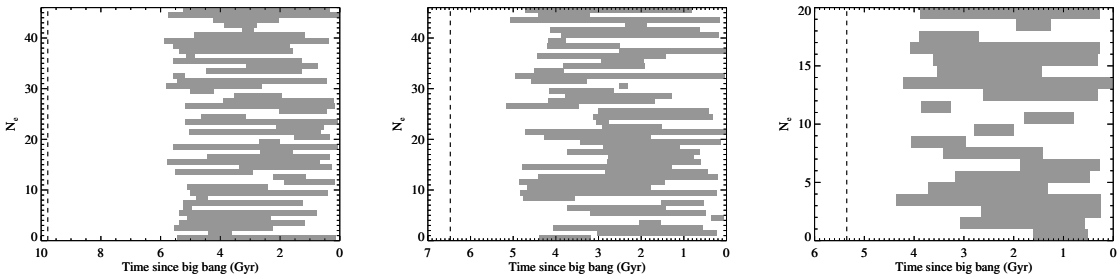

Figure 10.11 — The grey bars show the starting epoch and duration of constant star formation for each individual member among the set of simulated histories that best matched the observed intrinsic scatter of Cl 1358+6245 (left), Cl 1054–0321 (middle), and Cl 0910+5422 (right). The dashed vertical line indicates the age of the universe at the redshift of the clusters. See Table 10.2 for the model results.

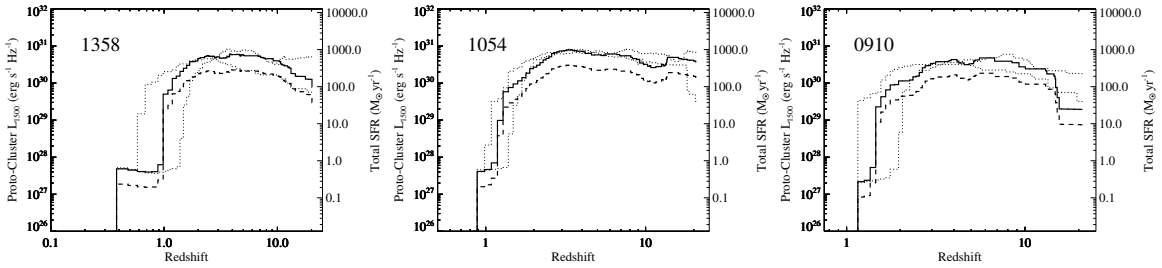

Figure 10.12 — The total combined star formation rate history of the red sequence populations corresponding to the star formation histories shown in Fig. 10.11. Each BC03 template was scaled so that the total stellar mass at t_{end} amounted to 10^{11} $M_\odot$. The model luminosities at rest frame 1500Å were traced back in time, and at each epoch the luminosities of the models were added to give an estimate of the total luminosity of the 'protocluster' (thick solid line). The luminosity at rest frame 1500Å was used as a proxy for the star formation rate using a conversion factor of 1 $M_\odot$ yr^{-1}= L_{1500} (erg s^{-1} Hz^{-1})/8×10^{27} from Madau et al. (1998). Dotted lines indicate the different evolution with redshift of the total cluster luminosity when we adopt the maximally young and maximally old models that still matched the observed scatter, as indicated in Figs. 10.8, 10.9 and 10.10. The dashed line shows the best-fit cluster luminosity evolution after applying a constant (with redshift) dust reddening factor of $E(B-V) = 0.1$ to the model luminosity.

of a few $M_\odot$ yr^{-1} (Venemans et al. 2005a), which multiplied by the typical number of $\sim 30-60$ found in protocluster regions gives about 100-200 $M_\odot$ yr^{-1}. This is still an underestimate of the total UV SFR, as field studies indicate that only about 25% of LBGs have a sufficiently large equivalent width in Lyα to be observed and detected as Lyα emitters according to the most common selection criteria. Evidence that this fraction is similar in protoclusters comes from the fact that we found large populations of LBGs in some of these fields (see chapters 5 and 8 of this thesis), indicating that the total UV star formation rate including dust correction could well be close to a thousand $M_\odot$ yr^{-1}. In this estimate we have not included the high star formation rates observed in the radio galaxies themselves of another several hundreds of $M_\odot$ yr^{-1}. Hence, the properties of the LBG and Lyα populations in the distant protoclusters are consistent with them being the progenitors of the evolved galaxies on the red sequence at $z \lesssim 1$.

10.5 Discussion and conclusions

We summarize our results as follows:

• The observed overdensities associated with

the protoclusters candidates listed in Table 10.1 are in rough agreement with those expected for massive halo progenitors at $z = 2 - 6$.
• The number densities of such massive dark halo progenitors are in rough agreement with the number density of luminous high-redshift radio galaxies (assuming a radio source lifetime of $\sim 10^7$ yr), and the estimated number density of LBG overdensities ('redshift spikes').
• The overdensities of the protocluster candidates are, on average, sufficiently large for forming a bound object with a mass of 10^{15} $M_\odot$ at $z \lesssim 0.5$.
• The estimated number density of protoclusters implies $b \sim 8$ at $z \sim 3$, roughly twice as high as the bias of luminous galaxies at similar redshifts as measured by, e.g., Daddi et al. (2003) and Ouchi et al. (2004).
• The total SFR of the LBG and Lyα populations in the distant protoclusters are consistent with them forming the stellar mass in the evolved galaxies on the red sequence at $z \lesssim 1$.

The main uncertainties in our conclusions are the following. Firstly, the mass overdensities were calculated from the observed surface overdensities of Lyα galaxies, and, in some cases, LBGs. These populations are known to be highly biased, and it is unclear if they are representative for the total mass overdensity. It is important that the mass overdensities are confirmed using other tracer populations (e.g. Pentericci et al. 2002; Kurk et al. 2004b; Steidel et al. 2005). Secondly, the galaxy overdensities that we used in our calculations are expected to be conservative estimates. We did not include information on the generally narrow velocity dispersion of the Lyα emitters, which, if it is narrower than that of similar galaxies in the field, could make the true overdensity in the protocluster region even higher. Thirdly, the exact volume that is occupied by the protocluster candidates has a large associated uncertainty. Fig. 10.5 demonstrates that the requirement for the observed overdensities to collapse within a finite time, becomes less stringent if the protoclusters have masses closer to 10^{14} $M_\odot$ than 10^{15} $M_\odot$ (dashed lines in Fig. 10.5), implying that the overdensities could be the progenitors of at least moderately rich clusters in the local universe. The largest overdensities observed are expected to have $\delta_L \approx 1.3 - 1.4$ at $z \approx 1$, implying that they can not be the progenitors of fully virialized clusters at $z = 1$. The X-ray luminous clusters discovered at $z \sim 1$ are probably, by selection, extreme clusters that are not representative of clusters in the local universe.

Our results are in excellent agreement with a recent study of protoclusters using N-body simulations (T. Suwa, private communications). Protoclusters were selected by picking up the particles belonging to clusters at $z = 0$ and tracing them back to high redshift. The simulations showed that clusters with masses of $> 10^{14}$ $M_\odot$ can be traced back to regions at $z = 4 - 5$ of 20–40 Mpc in size that are associated with overdensities of Lyα emitters and Lyman break galaxies of $\delta_g \sim 3$ and mass overdensities in the range 0.2–0.6. For randomly selected regions of the same size, the galaxy and mass overdensities were found to be mostly $\lesssim 0$, as expected due to the fact that massive halos are relatively rare. Although some of the overdense regions in the simulations having a similar overdensity as our protocluster candidates do not end up in clusters at $z = 0$, the simulations show that most regions with an overdensity on the order of a few at $z = 5$ will evolve into clusters more massive than 10^{14} $M_\odot$ ($\gtrsim 50\%$ for $\delta_g \gtrsim 2$).

It is interesting that the descendants of almost all of the classes of high redshift objects shown in Fig. 10.7 (such as radio galaxies, LBGs and DRGs) fall in the mass range corresponding to groups and clusters of galaxies when evolved to $z = 0$. This is a natural consequence of the bias of these highly luminous objects. This is further evidence that the descendants of the protoclusters candidates are likely to evolve into even rarer and more massive objects.

Although the protocluster regions contain large numbers of LBGs and Lyα emitters, their typical observed stellar masses are only a fraction ($\sim 1 - 10\%$) of those of early type cluster galaxies (see e.g., chapter 5), indicating that they

might accumulate more stellar mass through merging and continuous star formation as they evolve from the inhabitants of $z > 2$ protocluster regions into, possibly, $z \lesssim 1$ red sequence galaxies. It is highly important to also try to detect other high-z populations that one might expect, such as the 'distant red galaxies' found at $z < z < 4$ (Franx et al. 2003). Infrared observations with the *Spitzer Space Telescope* may be used to further constrain how the mass of the progenitors of cluster galaxies relate to the masses of galaxies in virialized clusters. The full sample of protoclusters described in this chapter provides a unique sample for studying cluster evolution at early epochs. Current wide-field optical and infrared surveys that search for clusters at $1 < z < 2$, as well as sensitive Sunyaev-Z'eldovich surveys are expected to further constrain the number densities of clusters as a function of redshift with a large dynamic range in mass. The study of how and when these structures and their galaxies were assembled will yield powerful clues to how the present-day large scale structure of the universe came about.

Acknowledgments

RAO is very grateful to Dr. Tamon Suwa for providing a preprint of his paper.

References

Adelberger, K. L., Steidel, C. C., Pettini, M., Shapley, A. E., Reddy, N. A., & Erb, D. K. 2005, ApJ, 619, 697
Bahcall, N. A., & Fan, X. 1998, ApJ, 504, 1
Bernardeau, F. 1994, ApJ, 427, 51
Best, P. N., Lehnert, M. D., Miley, G. K., Rïttgering, H. J. A. 2003, MNRAS, 343, 1
Blakeslee, J. P., et al. 2003, ApJ, 596, L143
Blakeslee, J. P., et al. 2003, ApJ, In Press (astro-ph/0603058)
Bruzual, G., & Charlot, S. 2003, MNRAS, 344, 1000
Carroll, S. M., Press, W. H., & Turner, E. L. 1992, ARA&A, 30, 499
Croft, S., Kurk, J., van Breugel, W., Stanford, S. A., de Vries, W., Pentericci, L., Röttgering, H. 2005, AJ, 130, 867
Daddi, E., et al. 2003, ApJ, 588, 50
De Lucia, G., Springel, V., White, S. D. M., Croton, D., & Kauffmann, G. 2006, MNRAS, 366, 499
van Dokkum, P. G., Franx, M., Kelson, D. D., Illingworth, G. D., Fisher, D., & Fabricant, D. 1998, ApJ, 500, 714
van Dokkum, P. G., Franx, M., Fabricant, D., Illingworth, G. D., & Kelson, D. D. 2000, ApJ, 541, 95
Ellis, R. S., Smail, I., Dressler, A., Couch, W. J., Oemler, A. J., Butcher, H., & Sharples, R. M. 1997, ApJ, 483, 582
Fabricant, D. G., McClintock, J. E., & Bautz, M. W. 1991, ApJ, 381, 33
Francis, P. J., et al. 2001, ApJ, 554, 1001
Franx, M., et al. 2003, ApJ, 587, L79
Holden, B. P., et al. 2005, ApJ, 620, L83
Kaiser, N. 1984, ApJ, 284, L9
Kaiser, N., 2002, *Elements of Astrophysics* (http://www.ifa.hawaii.edu/∼kaiser/)
Kauffmann, G., Colberg, J. M., Diaferio, A., & White, S. D. M. 1999, MNRAS, 303, 188
Bardeen, J. M., Bond, J. R., Kaiser, N., & Szalay, A. S. 1986, ApJ, 304, 15
Keel, W. C., Cohen, S. H., Windhorst, R. A., & Waddington, I. 1999, AJ, 118, 2547
Kurk, J. D., et al. 2000, A&A, 358, L1
Kurk, J. D., Pentericci, L., Röttgering, H. J. A., & Miley, G. K. 2004, A&A, 428, 793
Kurk, J. D., Pentericci, L., Overzier, R. A., Röttgering, H. J. A., & Miley, G. K. 2004, A&A, 428, 817
Lee, K., Giavalisco, M., Gnedin, O., Somerville, R., Ferguson, H., Dickinson, M. E., & Ouchi, M. 2005, Submitted to ApJ (astro-ph/0508090)
Madau, P., Pozzetti, L., & Dickinson, M. 1998, ApJ, 498, 106
Mei, S., et al. 2006, ApJ, 639, 81
Miley, G. K., et al. 2004, Nature, 427, 47
Mo, H. J., & White, S. D. M. 2002, MNRAS, 336, 112
Mo, H. J., & White, S. D. M. 1996, MNRAS, 282, 347
Möller, P., & Fynbo, J. U. 2001, A&A, 372, L57
Mullis, C. R., Rosati, P., Lamer, G., Böhringer, H., Schwope, A., Schuecker, P., & Fassbender, R. 2005, ApJ, 623, L85
Ouchi, M., et al. 2005, ApJ, 620, L1
Ouchi, M., et al. 2004, ApJ, 611, 685
Overzier, R. A., et al. 2006, Submitted to ApJ (astro-ph/0601223)
Overzier, R. A., et al. 2006, ApJ, 637, 58
Pascarelle, S. M., Windhorst, R. A., Driver, S. P., Ostrander, E. J., & Keel, W. C. 1996, ApJ, 456, L21
Peacock, J. A. 1999, Cosmological Physics, by John A. Peacock, pp. 704. ISBN 052141072X. Cambridge, UK: Cambridge University Press, January 1999.
Peebles, P. J. E. 1980, Research supported by the National Science Foundation. Princeton, N.J., Princeton University Press, 1980. 435 p.
Pentericci, L., et al. 2000, A&A, 361, L25
Pentericci, L., Kurk, J. D., Carilli, C. L., Harris, D. E., Miley, G. K., Röttgering, H. J. A. 2002, A&A, 396, 109
Press, W. H., & Schechter, P. 1974, ApJ, 187, 425
Postman, M., et al. 2005, ApJ, 623, 721
Rosati, P., della Ceca, R., Norman, C., & Giacconi, R. 1998, ApJ, 492, L21
Rosati, P., Borgani, S., & Norman, C. 2002, ARA&A, 40, 539
Sugiyama, N. 1995, ApJ, 100, 281
Sheth, R. K., Mo, H. J., & Tormen, G. 2001, MNRAS, 323, 1
Sheth, R. K., & Tormen, G. 2002, MNRAS, 329, 61
Sheth, R. K., & Tormen, G. 1999, MNRAS, 308, 119
Shimasaku, K., et al. 2003, ApJ, 586, L111
Stanford, S. A., et al. 2005, ApJ, 634, L129

Stanford, S. A., Holden, B., Rosati, P., Eisenhardt, P. R., Stern, D., Squires, G., & Spinrad, H. 2002, AJ, 123, 619
Steidel, C. C., Adelberger, K. L., Shapley, A. E., Erb, D. K., Reddy, N. A., & Pettini, M. 2005, ApJ, 626, 44
Steidel, C. C., Adelberger, K. L., Dickinson, M., Giavalisco, M., Pettini, M., & Kellogg, M. 1998, ApJ, 492, 428
Steidel, C. C., Adelberger, K. L., Shapley, A. E., Pettini, M., Dickinson, M., & Giavalisco, M. 2000, ApJ, 532, 170
Stiavelli, M., et al. 2005, ApJ, 622, L1
Tozzi, P., 2006, *Cosmological parameters from Galaxy Clusters: an Introduction* (astro-ph/0602072)
Venemans, B. P., et al. 2004, A&A, 424, L17
Venemans, B. 2005, Ph.D. Thesis, Leiden University
Venemans, B. P., et al. 2005, A&A, 431, 793
Venemans, B. P., et al. 2002, ApJ, 569, L11
Zheng, W., et al. 2006, ApJ, In Press (astro-ph/0511734)
Zirm, A. W., et al. 2005, ApJ, 630, 68

Hoofdstuk 11

Nederlandse samenvatting

1. Elementen van de sterrenkunde

Het heelal is bezaaid met miljarden sterrenstelsels die als eilanden van vele soorten en maten in een donkere oceaan van onvoorstelbare afmeting verspreid liggen (zie afbeelding 1). Deze sterrenstelsels (waarvan onze Melkweg er slechts één is) zijn opgebouwd uit miljarden sterren (zoals onze zon) en vermoedelijk bevinden vele sterren zich ook te midden van een systeem van planeten (zoals ons zonnestelsel). Het gezamenlijke licht van hun sterren geeft sterrenstelsels een aantal karakteristieke eigenschappen, zoals bijvoorbeeld hun helderheid (ook wel uitgedrukt in *magnitude*), hun afmeting (gemeten in *kiloparsecs*, 1 kpc is zo'n 200 miljoen maal de afstand van de aarde tot de zon), en hun kleur (het verschil in helderheid gemeten in verschillende golflengtegebieden, bijvooorbeeld ultraviolet, blauw, rood, infrarood of radio). Deze en nog vele andere eigenschappen zijn het gevolg van natuurkundige en chemische processen die zich in sterren en sterrenstelsels afspelen. De sterrenkunde bestudeert deze *astrofysische* processen.

Het licht van sterren en sterrenstelsels dat met telescopen versterkt wordt opgevangen is reeds in het verleden uitgezonden. Dit komt omdat de afstanden in het heelal erg groot zijn en licht zich niet oneindig snel voortplant. Zo heeft licht afkomstig van de zon bijvoorbeeld acht minuten nodig om de aarde te bereiken. Dus wil je weten hoe de zon er precies op dit moment uitziet? Kijk dan pas over acht minuten even naar buiten! De afstand tussen de zon en de aarde is - astronomisch gezien - een 'split-second'. Het licht van de dichtstbijzijnde sterren in onze Melkweg heeft enkele licht*jaren* nodig om ons te bereiken, en het licht van de sterren van andere sterrenstelsels heeft miljoenen of zelfs miljarden lichtjaren afgelegd alvorens de aarde te bereiken. Door sterrenstelsels op verschillende afstanden te bestuderen, komen sterrenkundigen dus meteen te weten hoe sterrenstelsels er vroeger uitzagen.

2. Kosmologie en de structuur van het heelal

De eigenschappen van het heelal worden echter niet alleen bepaald door de eigenschappen van de individuele sterrenstelsels. Als je kijkt naar de verdeling van sterrenstelsels door de ruimte, dan heeft het heelal een uiterst complexe structuur. Sterrenstelsels staan namelijk niet willekeurig door het heelal verspreid, maar vormen een 'kosmisch web' waarin kleine en grote groepen van sterrenstelsels met elkaar verbonden zijn door middel van dunne, draadvormige structuren van weer andere sterrenstelsels. Het kosmische web bestaat behalve uit de zichtbare materie van de sterrenstelsels ook uit zogenaamde 'donkere materie'. Deze mysterieuze materie is tot nog toe op geen enkele manier direct waargenomen, maar zijn aanwezigheid verraadt zich door zijn interactie met de sterrenstelsels via de onderlinge aantrekkingskracht die op talloze manieren uit sterrenkundige waarnemingen

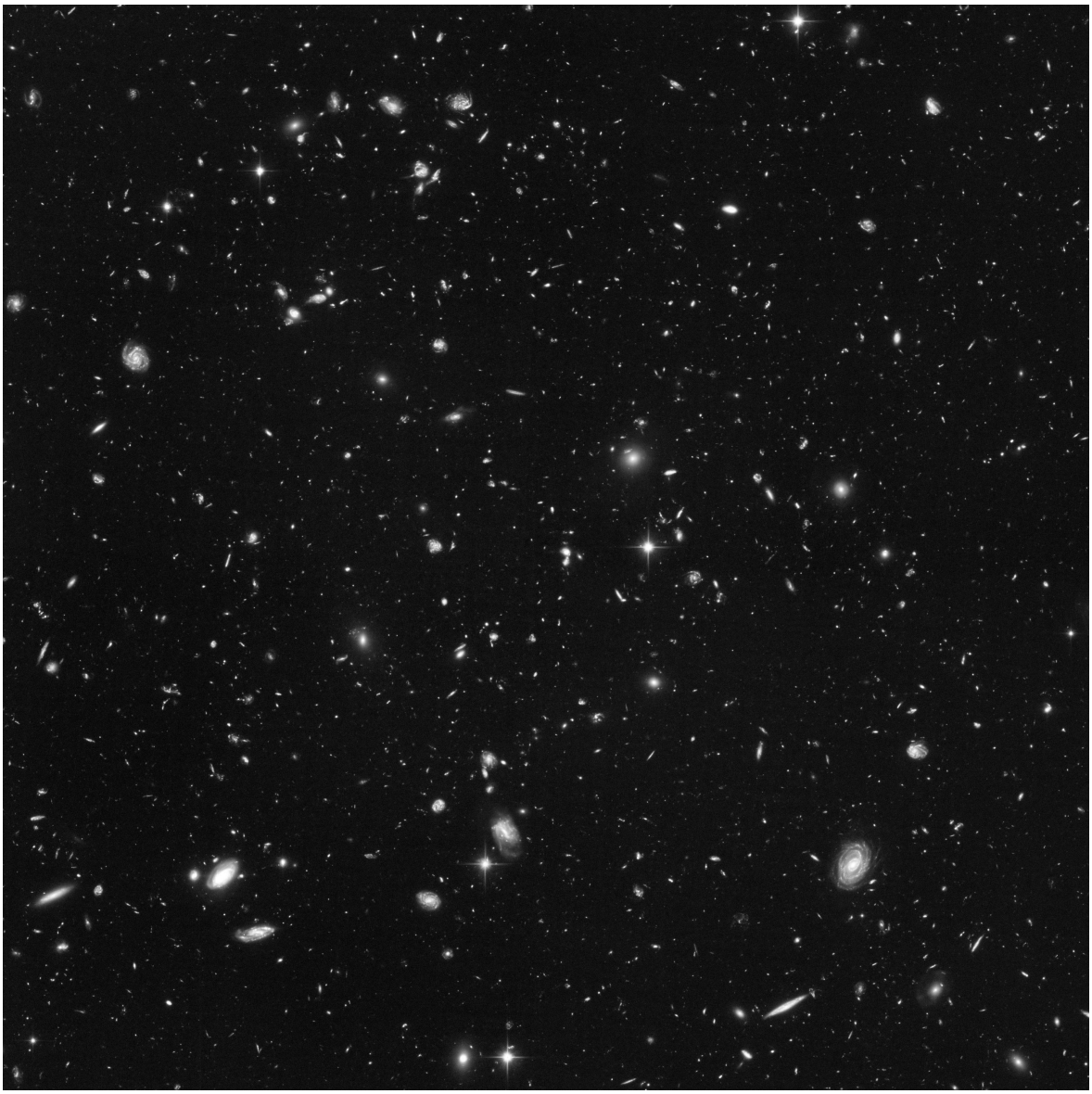

Afbeelding 1 – Sterrenstelsels in de 'Hubble Ultra Deep Field' (HUDF) gezien met de Hubble ruimtetelescoop. Deze opname, de diepste opname van het heelal ooit gemaakt, toont de verscheidenheid aan sterrenstelsels in een gebiedje ter grootte van *één-tien-miljoenste deel* van de gehele hemel. Bron: NASA, ESA, S. Beckwith (STScI) en het HUDF Team.

blijkt. De karakteristieke structuur van de sterrenstelsels en donkere materie tezamen noemen we de grote-schaal structuur van het heelal (zie afbeelding 2).

Uit metingen van de kosmische achtergrondstraling weten we dat de huidige grote-schaal structuur niet altijd hetzelfde is geweest. Zwakke microgolven uit alle richtingen van het heelal tonen aan

dat het heelal zo'n 14 miljard jaar geleden is ontstaan uit een zogenaamde 'oerknal'. In tegenstelling tot de grote variatie in de verdeling en de eigenschappen van sterrenstelsels in het huidige heelal, vertoont de microgolfstraling slechts hele kleine variaties in de intensiteit. Dit betekent dat vlak na de oerknal alle materie zeer gelijkmatig over het heelal verdeeld moet zijn geweest. De kosmologie houdt zich bezig met het zoeken naar astrofysische verklaringen voor hoe de huidige grote-schaal structuur uit de oerknal tot stand is gekomen. De observationele kosmologie, waarin men de grote-schaal structuur op steeds grotere afstanden van de Melkweg en dus tot ver in het verleden in kaart probeert te brengen, speelt hierin een belangrijke rol. Grote telescopen, zoals de Very Large Telescope (VLT) in Chili en de Hubble ruimtetelescoop, gebruiken grote spiegels om het licht van de uiterst zwakke sterrenstelsels op miljarden lichtjaren afstand op te vangen, zodat de structuur van het heelal ook op die afstanden bestudeerd kan worden.

3. Het ontstaan van sterrenstelsels en clusters

De wijze waarop de structuur van het heelal zich ontwikkeld heeft kan in grote lijnen door de kosmologie verklaard worden, maar vele details zijn onbekend. De gangbare theorie beschrijft hoe kleine variaties in de materiedichtheid kort na de oerknal onder de invloed van zwaartekracht uitgroeiden tot steeds grotere concentraties van de donkere materie, en hoe vervolgens in het centrum van deze concentraties de eerste sterren en sterrenstelsels ontstonden. De eerste generaties sterren bestonden enkel uit die elementen die na de oerknal aanwezig waren, waterstof en helium. Alle andere elementen die we van het periodiek systeem kennen zijn het gevolg van (astro-)fysische processen tijdens de evolutie van sterren. De leeftijden (jong of oud), magnituden (helder of zwak), kleuren (blauw of rood) en morfologische kenmerken (elliptisch, spiraalvormig of onregelmatig, groot of klein) van de sterrenstelsels die we waarnemen zijn het gevolg van de evolutie van zowel de sterren als de sterrenstelsels zelf. Aangenomen wordt dat vooral in de beginfase van de ontwikkeling van het heelal kleine sterrenstelsels zijn gegroeid door samen te smelten met andere sterrenstelsels. Op deze manier moet het heelal uiteindelijk zijn huidige samenstelling en hiërarchische structuur gekregen hebben.

Gebieden in het jonge heelal waar de fluctuaties in de materiedichtheid het grootst waren, groeiden gedurende miljarden jaren uit tot de grootste concentraties van donkere materie en sterrenstelsels. De meest extreme voorbeelden hiervan zijn de clusters van sterrenstelsels. Clusters bestaan uit vele honderden sterrenstelsels die dichtbijeengepakt in een enorme wolk of 'halo' van donkere materie en gas bewegen. De totale massa van zulke halo's bedraagt honderd tot duizend maal de massa van de Melkweg. Alhoewel de eigenschappen van sterrenstelsels tot diep in het heelal bestudeerd kunnen worden, blijkt de ontwikkeling van clusters van sterrenstelsels veel moeilijker te onderzoeken. Dit komt doordat clusters uiterst zeldzaam zijn in het heelal. Bovendien waren de dichtheidverschillen tussen clusters en hun omgeving vroeger vele malen kleiner en daardoor zijn ze moeilijk te onderscheiden in de overvloed aan voor- en achtergrondstelsels. De meest verre clusters die tot nu toe gevonden zijn, staan op een afstand van ongeveer negen miljard lichtjaar. Dit toont aan dat zelfs sommige van de allergrootste structuren in het heelal zich al vrij vroeg ontwikkelden. Door hun grote massa, gigantische afmeting en hoge leeftijd zijn deze objecten uitermate geschikt om de theorie voor de ontwikkeling van de grote-schaal structuur van het heelal te testen.

Omdat clusters grote groepen van relatief rode, oude sterrenstelsels bevatten zal hun licht gemeten in een rood filter duidelijk afsteken tegen dat in een blauw filter. Een veel gebruikte methode om clusters van sterrenstelsels te vinden is dus om waarnemingen te doen over een groot gebied aan de hemel in zowel een blauw als een rood filter en te zoeken naar groepen van vooral rode objecten. Deze techniek is echter moeilijk toepasbaar voor het zoeken naar clusters op de allergrootste afstanden. Ten eerste verschuift ten gevolge van de uitdijing van het heelal het licht van ver weg gelegen objecten naar langere (rodere) golflengten. Hoe verder weg de objecten staan, hoe groter

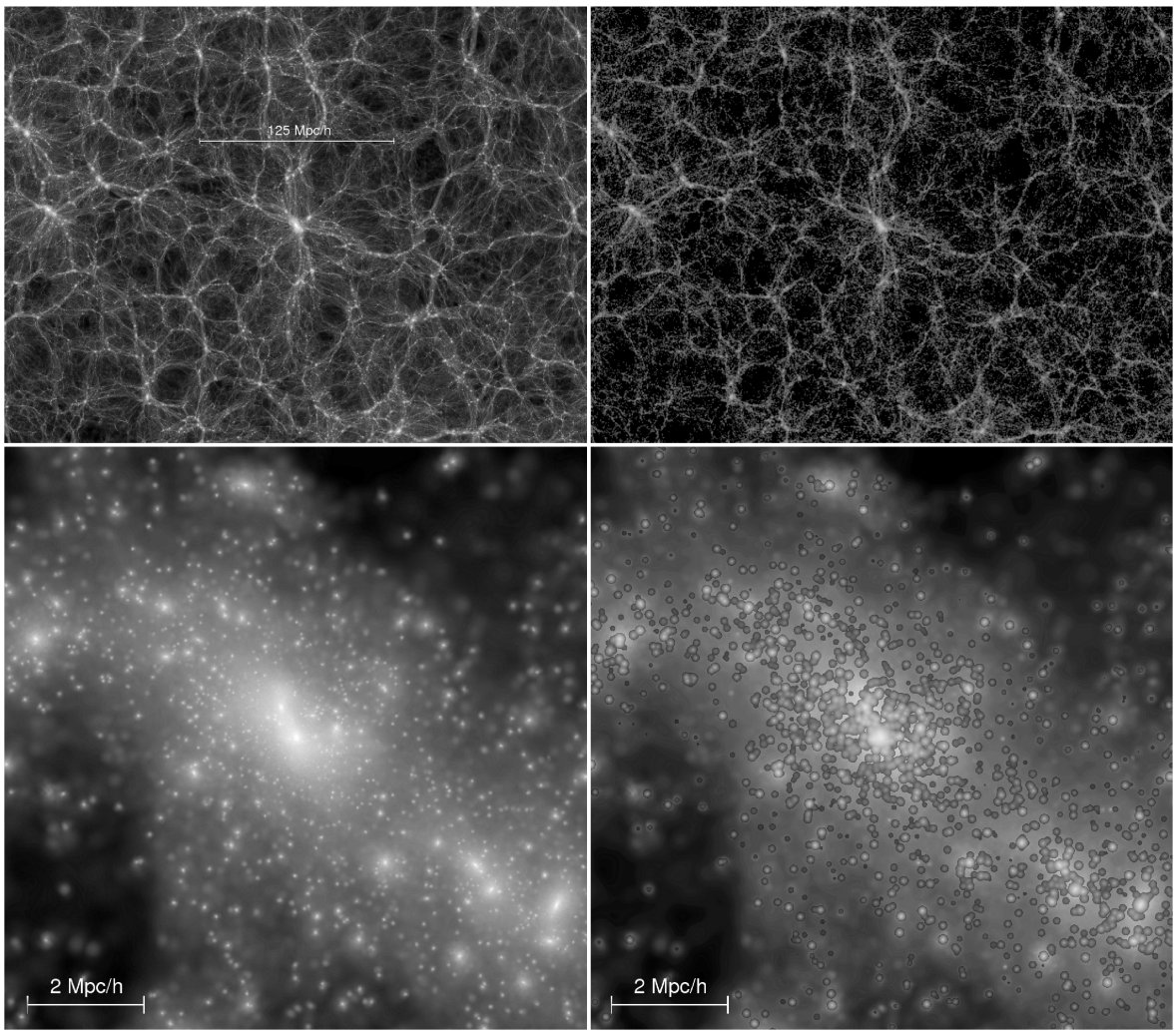

Afbeelding 2 – De grote-schaal structuur van het heelal, geïllustreerd aan de hand van computersimulaties. De bovenste afbeeldingen tonen de verdeling van de donkere materie (links) en de sterrenstelsels (rechts, aangegeven met de circels) in een groot gebied rondom een cluster. De onderste afbeeldingen tonen een uitvergroting van deze cluster. Bron: V. Springel et al., *Nature*, 435, 629, (2005).

deze 'roodverschuiving' (de wet van Hubble). Voor de clusters die het verst weg liggen moeten de waarnemingen gedaan worden op infrarode golflengten, wat technisch gezien relatief moeilijk is. Ten tweede verwacht men dat naarmate de clusters verder weg staan (en dus jonger zijn), ze nog geen karakteristieke rode stelsels hebben maar vooral blauwe, jonge stelsels die veelvuldig voorkomen in het heelal, ook buiten clusters. Een andere techniek om ver weg gelegen clusters te vinden maakt gebruik van de karakteristieke röntgenstraling die uitgezonden wordt door het zeer hete clustergas van ongeveer 10 miljoen graden. Op deze manier heeft men met satellieten die gevoelig zijn voor röntgenstraling een aantal van de grootste en meest verre clusters gevonden. Ondanks het feit

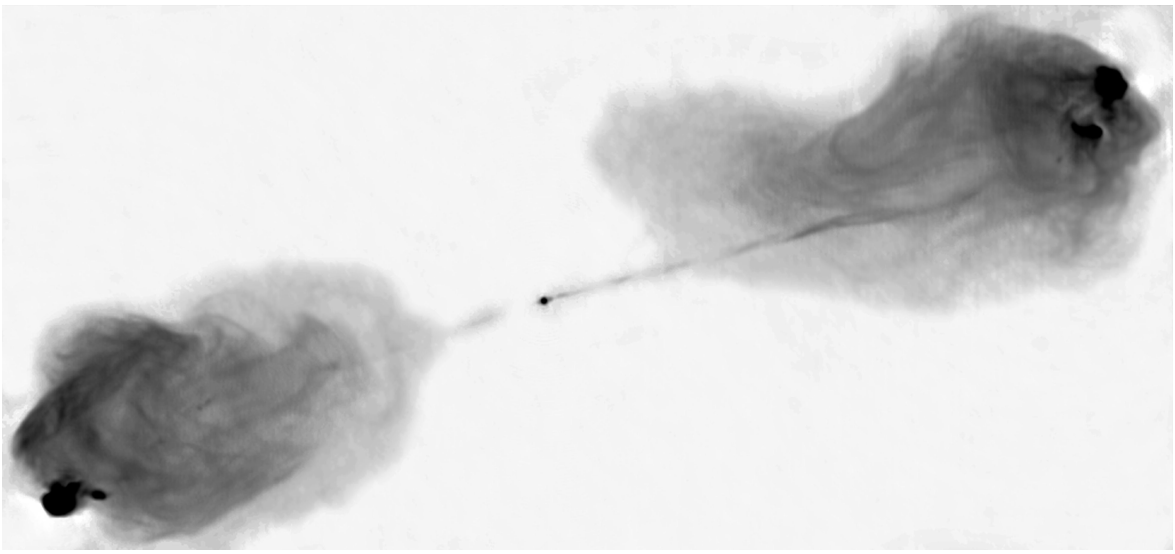

Afbeelding 3 – Het radiosterrenstelsel 'Cygnus A'. De enorme radiostraling is afkomstig van een zwart gat in het centrum van het sterrenstelsel. Het sterrenstelsel zelf is niet veel groter dan het zwarte stipje in het midden. Bron: R. Perley, C. Carilli & J. Dreher (NRAO/AUI).

dat men met deze twee technieken vele interessante ontdekkingen met betrekking tot clusters heeft gedaan, zijn de mogelijkheden om clusters te vinden in het nog vroegere heelal zeer beperkt.

4. Radiosterrenstelsels en protoclusters

Radiosterrenstelsels behoren tot het type sterrenstelsels met een zogenaamde 'aktieve kern'. In het centrum van deze stelsels bevinden zich de grootste zwarte gaten die in het heelal bestaan. De massa van deze zwarte gaten is vergelijkbaar met die van een klein sterrenstelsel, maar de afmeting is oneindig klein. Rondom deze zwarte gaten vinden hoogenergetische processen plaats, die onder andere krachtige radiostraling kunnen veroorzaken (zie afbeelding 3). Deze straling is tot diep in het heelal waarneembaar, bijvoorbeeld met de radiotelescopen in Westerbork. Nader onderzoek van radiosterrenstelsels heeft aangetoond dat ze behoren tot de meest massieve stelsels in het vroegere heelal. In het nabije heelal zien we dat de centra van clusters bevolkt worden door hele zware stelsels (zie ook afbeelding 2) en deze stelsels hebben, net als de radiosterrenstelsels, massieve zwarte gaten in hun kern. Deze overeenkomsten in eigenschappen zouden kunnen duiden op een verband tussen radiosterrenstelsels en het ontstaan van clusters. Een van de theoretische voorspellingen voor het ontstaan van clusters is dat deze ontstonden rondom de grootste objecten die er tot dan toe in het heelal waren en dat deze stelsels bovendien een fase van kernaktiviteit doormaakten door de toestroom van materiaal naar het zwarte gat. Waarnemingen van verre radiosterrenstelsels hebben aangetoond dat in de buurt van deze stelsels zich inderdaad vaak grote groepen van kleinere stelsels ophouden. Het is waarschijnlijk dat deze objecten, de zogenaamde 'protoclusters', de voorouders van clusters van sterrenstelsels zijn. De studie van de protoclusters maakt het dus mogelijk om het ontstaan van enkele van de meest spectaculaire objecten in het heelal tot op vele miljarden jaren terug in de tijd te traceren.

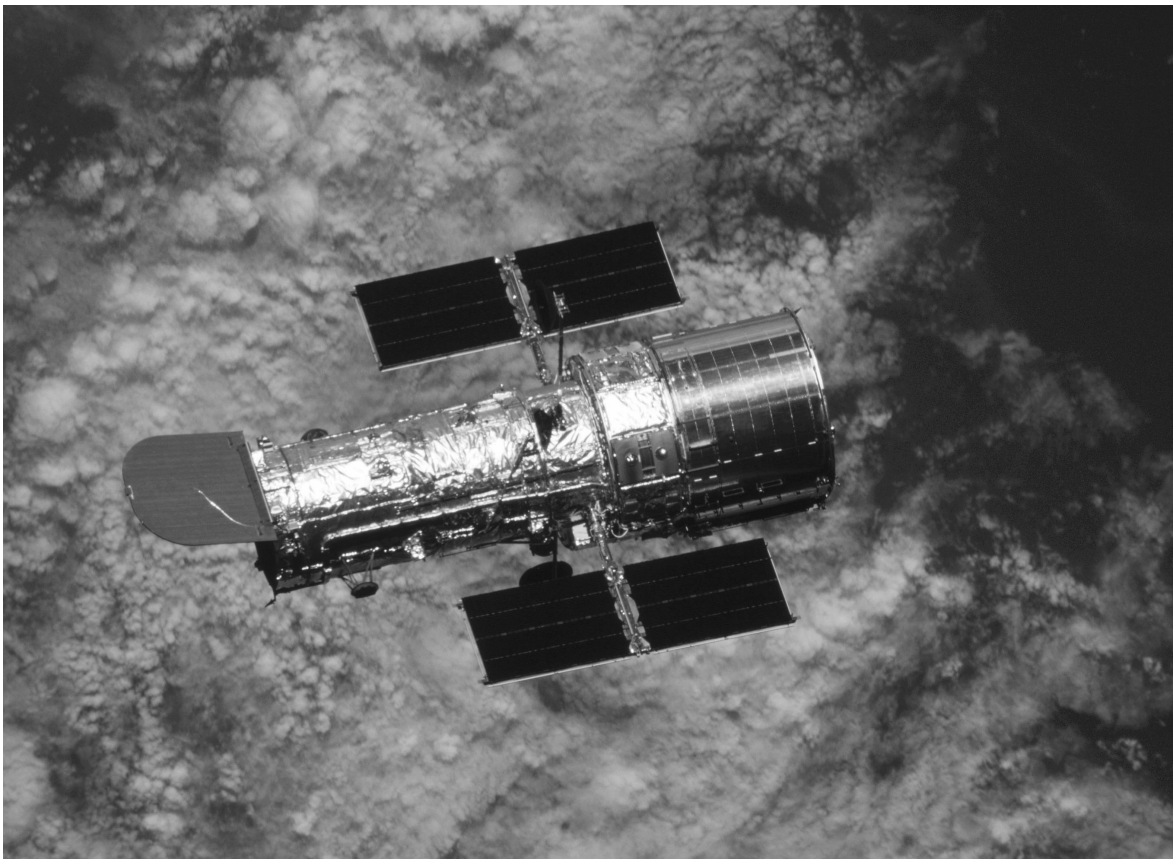

Afbeelding 4 – Een foto van de Hubble ruimtetelescoop in zijn baan om de aarde. Bron: NASA.

5. De "Advanced Camera for Surveys" van de Hubble ruimtetelescoop

In maart 2002 werd met de Space Shuttle Columbia een nieuwe camera naar de Hubble ruimtetelescoop (zie afbeelding 4) gebracht en door de astronauten tijdens een ruimtewandeling geïnstalleerd. Omdat de telescoop zich buiten de dampkring van de aarde bevindt kunnen sterrenkundigen met behulp van de "Advanced Camera for Surveys" (ACS) ongekend scherpe en gevoelige foto's maken van sterrenstelsels op vele miljarden lichtjaren afstand. Het merendeel van het onderzoek dat beschreven is in dit proefschrift is gebaseerd op opnamen met de ACS. We bestudeerden onder andere de eigenschappen van enkele ver weg gelegen radiosterrenstelsels en zochten naar protoclusters van sterrenstelsels in hun directe omgeving. Foto's door verschillende filters werden gebruikt om een selectie te maken van sterrenstelsels die ruwweg in de omgeving van de radiostelsels staan. Het licht van ver weg gelegen stelsels wordt tijdens de lange weg naar de aarde gedeeltelijk geabsorbeerd door tussenliggende gaswolken. Hoe langer de reis, hoe meer licht er wordt geabsorbeerd. Deze verzwakking van het licht door het intergalactische medium vindt bovendien voor elke roodverschuiving op een specifieke plek in het spectrum plaats, zodat met strategisch gekozen filters sterrenstelsels op de gewenste roodverschuiving (en dus afstand) gezocht kunnen worden. Ook stelden deze waarnemingen ons in staat om de eigenschappen van reeds eerder geïdentificeerde radiostelsels en hun protoclusters te onderzoeken. Dit project is onderdeel van een omvangrijk on-

derzoek naar de oorsprong van clusters van sterrenstelsels, een relatief jong onderzoeksgebied met nog talloze onopgeloste vraagstukken.

6. De inhoud van dit proefschrift

Hieronder geven we een kort overzicht van de inhoud van elk van de hoofdstukken in dit proefschrift.

Hoofdstuk 2 – In dit hoofdstuk onderzoeken we de clustering, of samenklontering, van radiosterrenstelsels op kosmologische afstanden. Radiosterrenstelsels zijn sterker geclusterd dan normale (d.w.z. niet aktieve) sterrenstelsels. Dit duidt erop dat radiosterrenstelsels een speciale positie binnen de grote-schaal structuur innemen. Mogelijk bevinden ze zich vooral op plaatsen waar men relatief grote sterrenstelsels en/of groepen of clusters van sterrenstelsels vindt.

Hoofdstuk 3 – In dit hoofdstuk beschrijven we waarnemingen van verre radiosterrenstelsels met de *Chandra* röntgensatelliet. De röntgenstraling van deze radiosterrenstelsels wordt voor een belangrijk deel veroorzaakt doordat fotonen (lichtdeeltjes) afkomstig van de microgolfachtergrondstraling door middel van een verstrooiingsproces energie 'stelen' van electronen afkomstig van de radiobron en daardoor een kortere golflengte krijgen. We zoeken ook naar de aanwezigheid van heet gas en quasars (aktieve sterrenstelsels), omdat beide een indicatie voor jonge clusters in de omgeving van de radiostelsels kunnen zijn, maar hebben daarvoor nog geen aanwijzingen gevonden.

Hoofdstukken 4 & 5 – In deze hoofdstukken tonen we de resultaten van een grote studie met de ACS van een van de beste voorbeelden van een protocluster rond radiosterrenstelsels: TN J1338–1942. Naast de objecten die eerder gevonden waren door middel van een karakteristieke waterstoflijn in hun spectrum op dezelfde roodverschuiving als het radiostelsel, vinden we een grote hoeveelheid aan nieuwe objecten op ruwweg dezelfde afstand. Deze objecten, waarvan de afstand echter niet exact kan worden bepaald, vertonen een sterke clustering rond het radio stelsel en zijn extra bewijs dat in dit veld een massieve cluster in aanbouw is. We bepalen de typische stervormingsnelheden, afmetingen, morfologieën en massa's van deze objecten. De eigenschappen van TN J1338–1942 zouden representatief kunnen zijn voor de eigenschappen van clusters die in een zeer vroeg stadium van hun evolutie verkeren.

Hoofdstuk 6 – In dit hoofdstuk bestuderen we enkele bijzondere astrofysische processen die zich afspelen in het radiosterrenstelsel TN J1338–1942. De grote mate waarin dit stelsel sterren vormt en het feit dat het in een protocluster omgeving ligt (zie hoofdstukken 4 & 5) kunnen betekenen dat dit stelsel het dominante clusterstelsel in wording is. Het totale systeem bestaat uit een paar afzonderlijke stelsels die elk de afmeting van een klein sterrenstelsel hebben. De stervorming in dit stelsel wordt mogelijk veroorzaakt door de wisselwerking tussen de radiostraling en het aanwezige gas. We vinden ook aanwijzingen voor de uitstroom van gas in een zogenaamde 'superwind', een proces waarbij de straling afkomstig van hevige stervorming in sterrenstelsels gas tot op grote afstanden buiten het stelsel blaast. De superwind en de interactie tussen het gas en de radiostraling zijn voorbeelden van ingewikkelde terugkoppelingen die mogelijk belangrijk zijn tijdens het ontstaan van massieve sterrenstelsels.

Hoofdstuk 7 – Hier bestuderen we het verst bekende radiosterrenstelsel, TN J0924–2201, met een roodverschuiving van 5.2. Foto's met de ACS tonen aan dat dit stelsel, afgezien van zijn radiostraling, niet zo veel verschilt van andere (niet-aktieve) sterrenstelsels op deze roodverschuiving. De oppervlaktedichtheid van stelsels in de omgeving van het radiosterrenstelsel is ongeveer twee keer

zo hoog als men voor een willekeurig veld zou verwachten. Dit is in overeenstemming met de eerdere ontdekking van zes stelsels met een waterstoflijn op de roodverschuiving van het radiostelsel en dus dat dit stelsel deel uitmaakt van een grote structuur van stelsels.

Hoofdstuk 8 – De ACS heeft de detectie van sterrenstelsels op een roodverschuiving van 6 relatief eenvoudig gemaakt. Deze enorme roodverschuiving correspondeert met een zo grote afstand dat we de sterrenstelsels zien zoals ze er uitzagen toen het heelal slechts zo'n $\sim 7\%$ van zijn huidige leeftijd had! We meten de mate van clustering van ongeveer 500 van deze objecten en vinden dat zelfs in het vroege heelal sterrenstelsels al aanzienlijk geclusterd zijn. Deze blauwe, sterrenvormende stelsels op roodverschuiving 6 zijn mogelijk de voorlopers van relatief oude, massieve stelsels die later in het heelal (en dus dichterbij) te vinden zijn.

Hoofdstuk 9 – We zoeken in de omgeving van een krachtige radiobron op roodverschuiving 6 naar begeleiders die kunnen duiden op grote-schaal structuur rond deze quasar. Het aantal stelsels dat we vinden op ongeveer dezelfde roodverschuiving is groter dan het verwachte aantal van dit soort stelsels in willekeurige velden. Onze bevinding is in overeenstemming met recente simulaties van het ontstaan van clusters, die voorspellen dat de eerste tekenen van het ontstaan van clusters van sterrenstelsels mogelijk rond heldere quasars op zeer hoge roodverschuiving te vinden zijn. Het feit dat de door ons ontdekte stelsels zo zwak zijn maakt het helaas moeilijk om een fysische relatie met de quasar definitief aan te tonen.

Hoofdstuk 10 – In dit hoofdstuk geven we een uitgebreid overzicht van de tot nu toe gevonden bewijzen voor vormende clusters zeer vroeg in het heelal. We laten zien dat de structuren die gevonden zijn rondom radiostelsels en in enkele andere velden over het algemeen voldoen aan de eigenschappen die men verwacht voor 'protoclusters' op grond van de theorie voor het ontstaan van massieve clusters van sterrenstelsels. We laten zien dat de hoge mate van stervorming in de protoclusters in overeenstemming is met het totaal aantal sterren waargenomen in oude, rode stelsels in volgroeide clusters.

About the author

I was born in 1978 in Rotterdam (The Netherlands) to Jeanne Overzier-Koppers and Harry Overzier. After attending the Erasmiaans Gymnasium, I decided to study Astronomy ("Sterrenkunde") at the University of Leiden in order to pursue further one of my biggest childhood fascinations. Despite some transitional difficulties in the beginning, I nonetheless managed to obtain my "propedeuse" at the end of the first year. My interest for research started through my first undergraduate research project ("klein sterrenkundig onderzoek") with Dr. Huub Röttgering. We analysed spectroscopic observations of a distant radio galaxy obtained with the Very Large Telescope in Chile. Our results lead to my first scientific publication, and I presented the results at a conference on Isla Mujeres (Mexico), supported by a travel grant from the Leids Universitair Fonds (LUF). For my graduate research project ("groot sterrenkundig onderzoek"), under the supervision of Dr. Huub Röttgering and Dr. Roeland Rengelink, I studied the large-scale, cosmological structure as probed by extragalactic radio sources. By studying the statistical distribution of hundreds of thousands of radio sources in the sky, we were able to study their gravitational clustering to unprecedented detail. I obtained my Master degree in November 2001.

In January 2002, I started as a Ph.D. student ("promovendus") working with Prof. George Miley on the study of galaxies in the environments of distant radio galaxies. I made two observing visits to the Very Large Telescope (Chile), and spent the month May both in 2002 and 2003 at the Harvard-Smithsonian Center for Astrophysics in Cambridge (United States) working with Dr. Daniel Harris on the analysis of X-ray observations of distant radio galaxies obtained with the Chandra satellite. The main part of my Ph.D. project was based on observations by the Science Team of the Advanced Camera for Surveys (ACS) on the Hubble Space Telescope (HST). This superb camera was installed during an upgrade of the HST by astronauts of the space shuttle Columbia's 27th flight (STS-109) in March 2002. The results of these research projects are presented in the current thesis, parts of which have also appeared as separate publications in *Astronomy & Astrophysics*, *The Astrophysical Journal*, and *Nature*.

During my Ph.D. I spent one and a half years working with the ACS Science Team in Baltimore (United States). I further participated in the 21st winterschool on galaxy formation in Jerusalem (Israel) and in meetings, conferences or workshops in London and Edinburgh (United Kingdom), College Park and Aspen (United States), Poelgeest and Dwingeloo (The Netherlands), Granada (Spain), and Heidelberg (Germany).

At Leiden Observatory ("Sterrewacht Leiden") I was a teaching assistant for the course Galaxies ("Sterrenstelsels") given by Dr. Jan Lub and Prof. Marijn Franx. I was a member of the Social committee, the Public Outreach committee, and the Annual Report committee.

In September 2006, I will continue my research in astronomy through a joint postdoctoral fellowship at The Johns Hopkins University in Baltimore (USA) and the Max Planck Institute for Astrophysics in Garching (Germany).

Acknowledgments

Congratulations! You have found the most important page of this thesis. I can finally set aside all frustrations and express gratitude towards those whose help and company I treasured along the way.

I am grateful to Leiden Observatory for providing the means and a friendly environment to carry out my work, from my start as an undergraduate research student to the end. I thank the directors, and the institute manager, Dr. Jan Lub, for their support. I owe great gratitude to the secretarial and computer support staff of both Leiden Observatory and the Johns Hopkins University (JHU) in Baltimore, in particular to Sharon Busching and Alex Framarini whose personal dedication made my many visits to JHU run smoothly.

I thank Rychard Bouwens, Nick Cross, Dan Harris, Simona Mei, Bram Venemans, Wei Zheng and Andrew Zirm for the interesting projects we shared. I further thank the entire Advanced Camera for Surveys Team for their support, the Aspen meetings, and the research that came to be my thesis. I have very much appreciated the extensive, and - most importantly - always positive feedback that I received on each draft paper or proposal. I hope that I will be able to do the same for future colleagues and students. In addition I would like to thank John Blakeslee and Gerhardt Meurer for their pipeline support, and Prof. Myang Li for the exciting experiments. In the Leiden 'cosmos' group I have had the good fortune of working with Carlos, Laura, Jaron, Bram, Richard, Andrew, Michiel, Cyril, and Huib, who proved to be good colleagues both professionally and personally. Maria, Dominic, Andrew, Bram, Ricardo, Carolina and Niruj: you made excellent office mates and friends; Keep up with the good work wherever you go next!

My greatest thanks go to my friends and family. Suzanne, Eefje, Marije, Maurits, Bartel, Rogier, Laura, and Isa, I have been lucky to have you as my friends. I hope you will forgive my periods of 'seclusion' when overwhelmed by work or other circumstances. I have very much appreciated the warmth and hospitality of Matthijs, Yvonne and Jacob in Zutphen, and of Mario & Deisy in Leiden. I have never had so many nice friends as I had at JHU in Baltimore. I will never forget the lunches at the BMA, Levering and the president's garden, the insightful friday afternoon teas at the Eisenhower library, the squirrels (they are just like the universe: cute and furry), and the many adventures and parties with our 'United Nations': Ricardo, Michele, Boryana, Valentin, Nick, Manu, Victor, and Isa: thank you! My dear parents, my brother Marnix, Natasja, and Isa, thank you for your never-tainting support of my academic 'extravaganzas'. It would not be worth it without having that.

Finally, I would like to give special thanks to an important group often missed in the acknowledgments: the galaxies, without which this thesis could not have been written. Their light has always been there for me in the darkness. Some of them will have ceased their flickering long by now, while others have yet to acquire their luminous wealth. Millions of civilisations have come and gone within the tiny stretch of space that I spied on during my research. Despite the impossibility of direct contact due to the laws of physics, some of them were perhaps even aware of the likeliness that others, as myself, watched them laboriously from our astronomical observatories. May your galactic homes become immortalized by the images in this thesis, a family portrait of the deep, deep space.